LEVEL 12

RADC-TR-78-272
Final Technical Report
January 1979

ARRAY SCANNING FOR IMAGE TRANSMISSION

Harris Corporation

Dr. W. C. Adams, Jr.
Dr. T. R. Bader
Dr. J. J. Knab
Dr. E. B. Knick, Jr.
Dr. C. A. Shuman

MAR 13 1979

APPROVED FOR PUBLIC RELEASE; DISTRIBUTION UNLIMITED

This report has been reviewed by the RADC Information Office (OI) and is releasable to the National Technical Information Service (NTIS). At NTIS it will be releasable to the general public, including foreign nations.

RADC-TR-78-272 has been reviewed and is approved for publication.

APPROVED: *Leonard E. Converse, jr.*

LEONARD E. CONVERSE, Jr.
Project Engineer

APPROVED: *76 Davi*

HOWARD DAVIS
Technical Director
Intelligence & Reconnaissance Division

FOR THE COMMANDER: *John P. Huss*

JOHN P. HUSS
Acting Chief, Plans Office

REPORT DOCUMENTATION PAGE		READ INSTRUCTIONS BEFORE COMPLETING FORM
1. REPORT NUMBER RADC-TR-78-272	2. GOVT ACCESSION NO.	3. RECIPIENT'S CATALOG NUMBER
4. TITLE (and Subtitle) ARRAY SCANNING FOR IMAGE TRANSMISSION		5. TYPE OF REPORT & PERIOD COVERED Final Technical Report Sep 77 - Sep 78
		6. PERFORMING ORG. REPORT NUMBER N/A
7. AUTHOR(s) Dr. W. C. Adams, Jr. Dr. E. B. Knick, Jr. Dr. T. R. Bader, Dr. C. A. Shuman Dr. J. J. Knab		8. CONTRACT OR GRANT NUMBER(s) F30602-77-C-0181
9. PERFORMING ORGANIZATION NAME AND ADDRESS Harris Corporation/Government Systems Group Communications Systems P.O. Box 37 Melbourne FL 32901		10. PROGRAM ELEMENT, PROJECT, TASK AREA & WORK UNIT NUMBERS 62702F 62441082
11. CONTROLLING OFFICE NAME AND ADDRESS Rome Air Development Center (IRRP) Griffiss AFB NY 13441		12. REPORT DATE January 1979
		13. NUMBER OF PAGES 384
14. MONITORING AGENCY NAME & ADDRESS(if different from Controlling Office) Same		15. SECURITY CLASS. (of this report) UNCLASSIFIED
		15a. DECLASSIFICATION/DOWNGRADING SCHEDULE N/A

16. DISTRIBUTION STATEMENT (of this Report)

Approved for public release; distribution unlimited.

17. DISTRIBUTION STATEMENT (of the abstract entered in Block 20, if different from Report)

Same

18. SUPPLEMENTARY NOTES

RADC Project Engineer: Leonard E. Converse (IRRP)

19. KEY WORDS (Continue on reverse side if necessary and identify by block number)

Array Scanning	MTF Correction
Image Transmission	REARCS
Image Bandwidth Compression	CCD Signal Processing
Two-Dimensional Filtering	
Image Enhancement	

20. ABSTRACT (Continue on reverse side if necessary and identify by block number)

This study effort evaluates the feasibility of utilizing one or two-dimensional arrays of image sensing and recording elements rather than a single sensing and recording element in image transmission systems. This array scanning concept facilitates the implementation of many sophisticated image processing functions including bandwidth compression, image enhancement, modulation transfer function correction, and two-dimensional filtering. Extensive computer simulation of these processing functions and subjective analysis of the resulting imagery, along with the results of the array sensing and array

DD FORM 1473   1 JAN 73

recording feasibility evaluation, are used to formulate the trade-offs necessary to provide a conceptual system design and implementation. The conceptual design that is presented fully exploits the nature of the array scanning. Various practical aspects and system considerations regarding the conceptual design are treated.

ACCESSION for

NTIS   White Section

DDC   Buff Section

UNANNOUNCED

JUSTIFICATION

BY

DISTRIBUTION/AVAIL   IAL

Dist.   AVAIL

TABLE OF CONTENTS

TABLE OF CONTENTS (continued)

TABLE OF CONTENTS (continued)

LIST OF ILLUSTRATIONS

LIST OF ILLUSTRATIONS (continued)

LIST OF ILLUSTRATIONS (continued)

LIST OF ILLUSTRATIONS (continued)

LIST OF ILLUSTRATIONS (continued)

LIST OF TABLES

EVALUATION

The final report on this study effort provides information which can be utilized for the development of a system for transmitting imagery or in evaluating tradeoffs for scanning and recording image information, compressing image data, and restoring and enhancing image data. This forms a basis for meeting the objectives of RADC TPO #R2C, which is concerned with each of the above image related problems.

Leonard E. Converse, Jr.

LEONARD E. CONVERSE, JR.
Project Engineer

1.0   INTRODUCTION

This final report contains the documentation
of the results of the Array Scanning for Image Transmission
Study performed in accordance with RADC contract number
F30602-77-C-0181 during the contract period September 16, 1977
to September 20, 1978.

In this introduction we provide an overview
and description of the nature of the study effort, followed
by a description of the study approach we have followed.
This is followed by a summary of the organization of the
final report. The introduction concludes with a summary of
the conclusions of the study.
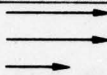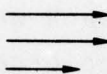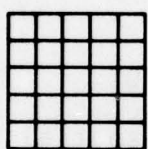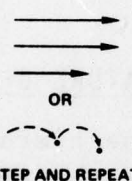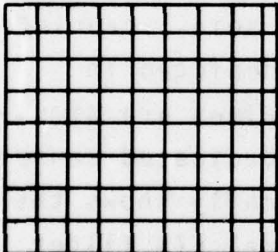
1.1   AN OVERVIEW OF THE NATURE OF THE STUDY

Figure 1.1-1 shows the hierarchy of spatial
sampling or scanning techniques of increasing generality
and complexity ranging from the conventional point scanning
method of Figure 1.1-1 (a) to the situation depicted in
Figure 1.1-1 (d) in which all of the pixel values are simul-
taneously available, i.e., there exists one dedicated sensor
for each image pixel. Figure 1.1-2 schematically shows the
implementation of a generalized two-dimensional FIR filter
which operates on the output of a two-dimensional sensor
array whose pixel output values are all simultaneously avail-
able.

The motivation for this study of Array Scanning
for Image Transmission Systems is two-fold:

(1) Array scanning has the potential for
increasing the throughput rate for image transmission systems
that are not channel bandwidth limited.

1

METHOD OF SPATIAL SAMPLING	METHOD OF SCANNING	ENCODED SIGNAL DESCRIPTION	INHERENT PROCESSING CAPABILITY
a.		POINT SCANNED	ONE-DIMENSIONAL PROCESSING
b.		LOCAL NEIGHBORHOOD VECTOR SCANNED	SEPARABLE TWO-DIMENSIONAL LOCAL NEIGHBORHOOD IMAGE PROCESSING
c.	OR STEP AND REPEAT	LOCAL NEIGHBORHOOD MATRIX SCANNED	GENERAL NONSEPARABLE TWO-DIMENSIONAL LOCAL NEIGHBORHOOD IMAGE PROCESSING
d.	NONE	FULL IMAGE SCANNED	GENERAL TWO-DIMENSIONAL IMAGE PROCESSING

10320-33

Figure 1.1-1

An Hierarchy of Image Spatial Sampling Techniques
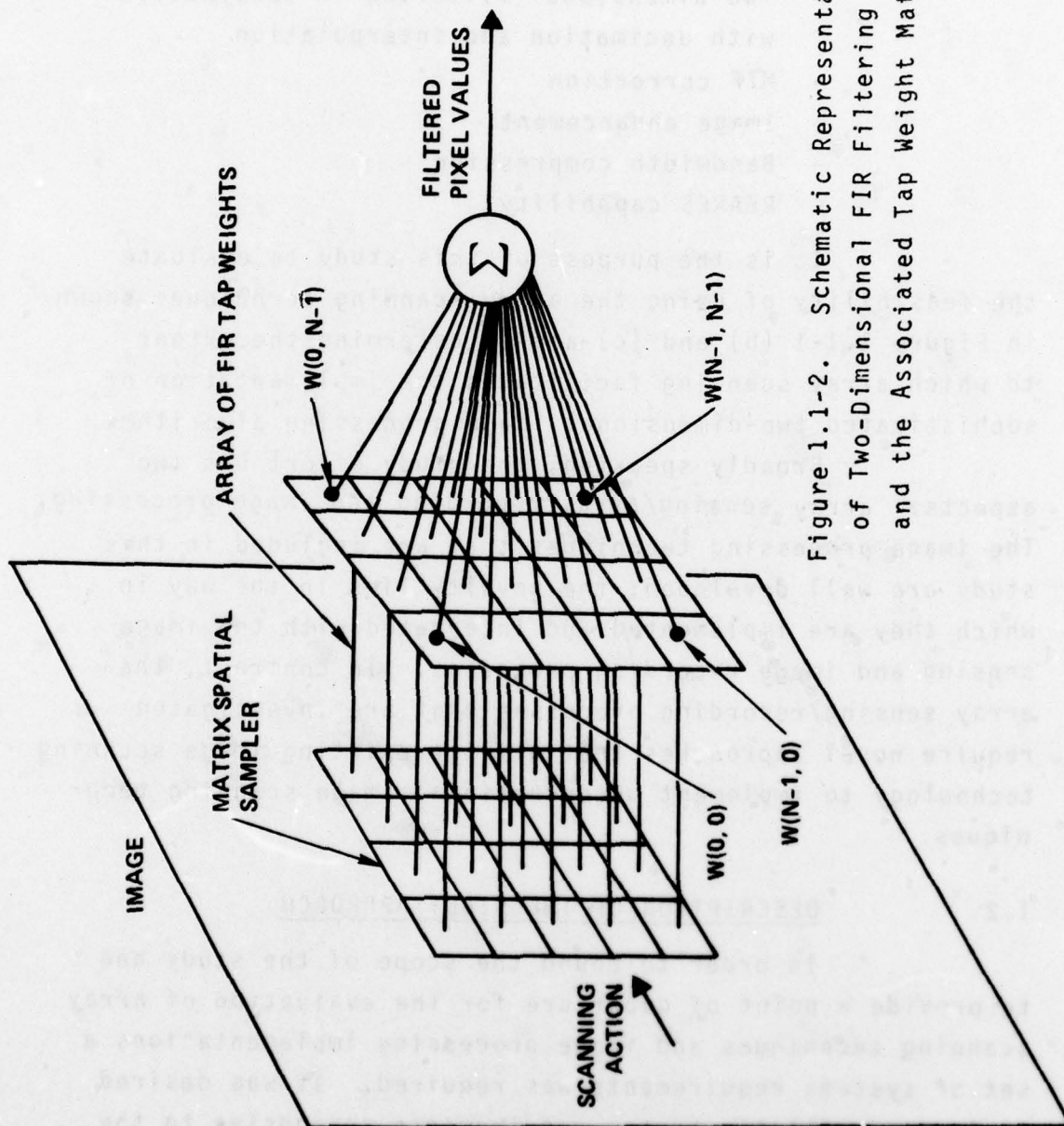
Figure 1.1-2. Schematic Representation of Two-Dimensional FIR Filtering and the Associated Tap Weight Matrix

(2) Array scanning greatly facilitates implementation of certain two-dimensional image processing tasks, including:

- Two-dimensional filtering in conjunction with decimation and interpolation
- MTF correction
- Image enhancement
- Bandwidth compression
- REARCS capability

It is the purpose of this study to evaluate the feasibility of using the array scanning techniques shown in Figure 1.1-1 (b) and (c) and to determine the extent to which array scanning facilitates the implementation of sophisticated two-dimensional image processing algorithms.

Broadly speaking, the study effort has two aspects: array sensing/array recording and image processing. The image processing techniques that are included in this study are well developed; the novelty lies in the way in which they are implemented and integrated with the image sensing and image recording processes. In contrast, the array sensing/recording processes that are investigated require novel approaches that utilize existing image scanning technology to implement unconventional image scanning techniques.

1.2 DESCRIPTION OF THE STUDY APPROACH

In order to bound the scope of the study and to provide a point of departure for the evaluation of array scanning techniques and image processing implementations a set of systems requirements was required. It was desired to impose realistic system requirements responsive to the current needs of the military regarding image dissemination;

4

toward this end we selected the system requirements correspond-
ing to the Intra-Theater Image Transmission System (IITS),
which are well-understood by Harris Corporation. These
requirements are enumerated elsewhere in this report.

Figure 1.2 shows the organization of the study
approach. The array sensing and array recording subtasks
were delegated to study team members having the requisite
in-depth knowledge and experience in electro-optical tech-
nology. Because of the unconventional nature of array scanning
techniques, careful attention was given to the implementation
risks associated with array scanning. The image processing
aspect of the study effort was broken into several inter-
related subtasks which were performed by personnel having
appropriate expertise and experience. During the performance
of the study every effort was made to maintain communication
between the personnel performing the electro-optical task
and those performing the image processing task in order to
arrive at a system architecture and conceptual design that
fully exploits the relationships that exist among the various
systems. For example the MTF correction could be inherent
in the lowpass filtering required prior to decimation and the
lowpass filter operation can itself be an integral part of the
electro-optical array sensing process.

Although two-dimensional image filtering plays
either an explicit or implicit role in all of the image
processing subtasks, each of these subtasks is treated
separately in the report. The differing roles of filtering
in each of these subtask topics is fully developed in each
of the corresponding sections of the final report. Computer
simulation of the two-dimensional FIR filters used for MTF
correction, image enhancement, presampling (decimation),
and reconstruction (interpolation) played a central role
in this study. Because of the subjective nature of image
quality evaluation, the computer simulation of the various

5

Figure 1.2. Organization of the Study Effort

The diagram shows a hierarchy:

System Architectures and Conceptual Design
- Electro-Optics
  - Array Sensing
  - Array Recording
- Image Processing
  - Bandwidth Compression
  - MTF Correction
  - Image Enhancement
  - Decimation Interpolation and REARCS
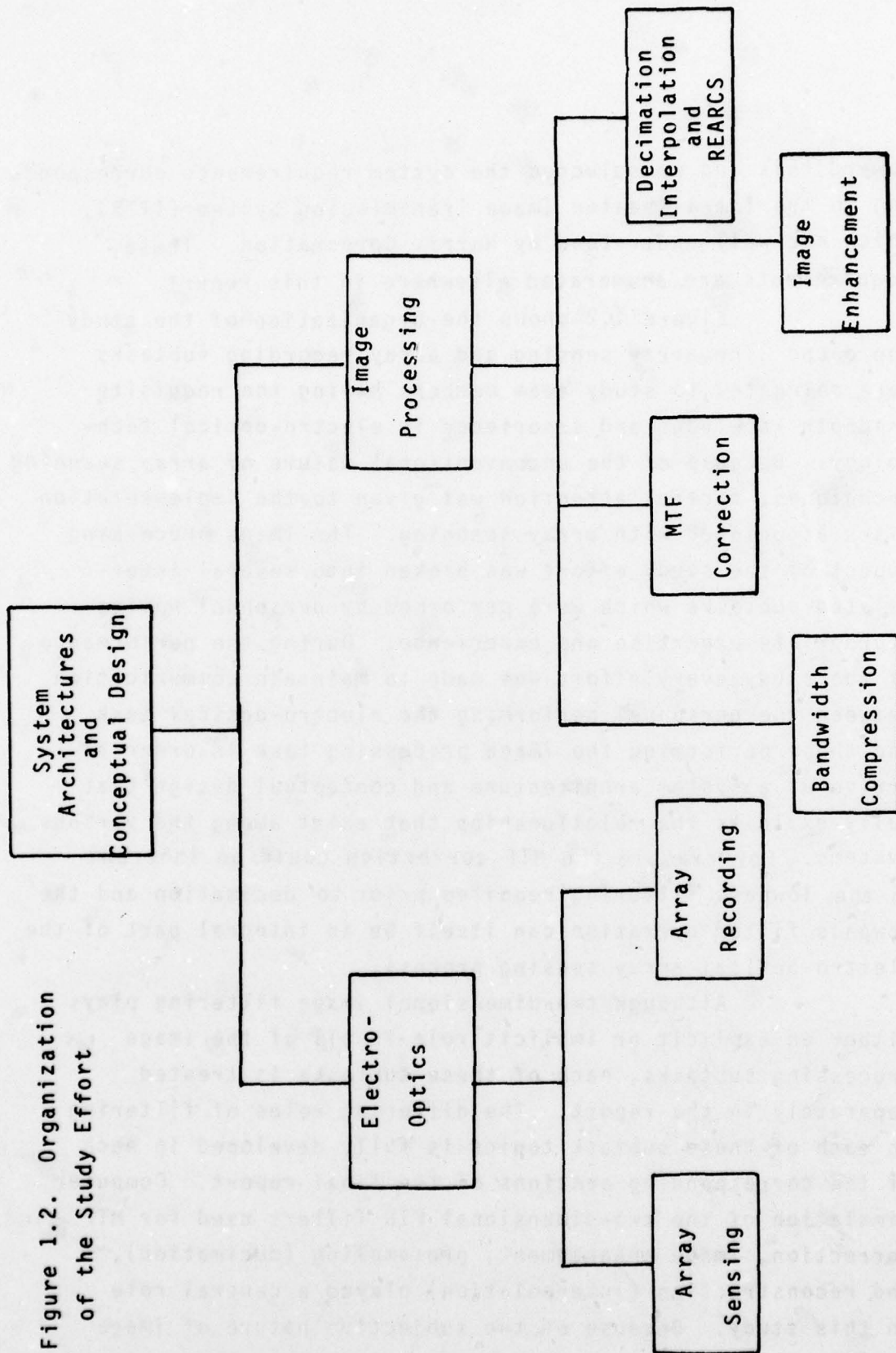
image processing algorithms was of paramount importance in
performing the subsystem tradeoffs. The study philosophy
regarding the image processing tasks has been to first
thoroughly develop the analytical or theoretical aspects
of the issues relating to aliasing, decimation, interpolation,
MTF correction, and image enhancement, and then use computer
simulation to provide the data required to perform subjective
evaluation of the system or subsystem tradeoffs. We feel
that this approach is appropriate and that it has served
the purposes of this study effort well. Wherever appropriate
in this report we have included half-tone reproductions of
computer processed imagery developed on 3M 7771 heat-pro-
cessed dry silver photographic paper. The source image
used in all the computer simulation experiments was a composite
image that we constructed using an aerial photograph con-
taining both natural and man-made features, a quarter of a
frequency wedge, and selected typewritten text. This com-
posite image has proved to be quite useful for our experiments--
especially the frequency wedge portion since this allowed
us to accurately compare both aliasing content (evidenced as
moire patterns) and in-band frequency content of the images
after various filtering operations. It is worthy of comment
that the source image was scanned at 125 lines-per-inch (lpi)
whereas the system requirements we assumed for this study
mandated 384 lpi as the maximum possible resolution. We
chose to use 125 lpi resolution for our experiments because
this allowed us to properly perform the subjective evaluation
of the various filtering operations while maintaining a
manageable computer run time requirement. In spite of this,
the run times of some of the experiments were very long and
were accomplished on an overnight or over-weekend-run basis.
For example, a single 31 x 31 FIR filtering operation without
decimation or interpolation required 11 hours and 43 minutes
for the 350 x 350 pixel source image we used; the same

source image scanned at 384 lpi would have required 110.5 hours (4.6 days), which is clearly prohibitive in view of the large number of filtering simulations that we felt were necessary.

The decimation/interpolation experiments constituted the bulk of the simulation effort. The decimation/ interpolation filters that were simulated included 31 x 31, 15 x 15, and 9 x 9 FIR quarter- and half-bandwidth filters, both separable and nonseparable, with Kaiser window parameter $\beta = 3, 1,$ and 0. This permitted a thorough evaluation of the tradeoffs among stopband attenuation, transition bandwidth, passband ripple, aliasing, inband image detail, and implementation complexity. The MTF correction, image enhancement, and bandwidth compression simulations received less attention because of the limited number of parameter tradeoffs involved. The theoretical and practical limitations of array sensing and array recording techniques were thoroughly examined. The final phase of the study effort draws upon the results and tradeoffs of all the subtasks in order to synthesize several candidate ASITS architectures, whose advantages and disadvantages are discussed and traded off. The result is a final conceptual design whose proposed architecture is evaluated.

1.3   ORGANIZATION OF THE STUDY FINAL REPORT

Following the introductory paragraph 1.0, the final report is organized as follows.

Paragraph 2.0 documents the results of the array sensing subtask in which both theoretical and practical limitations on array sensing implementation and performance were explored. The tradeoffs among the various parameters of the array sensing technique are displayed graphically.

8

Paragraph 3.0 describes the tradeoffs and reports the achievable limits regarding array recording implementation and performance. Again, the tradeoffs are presented graphically in order to facilitate an intuitive understanding of the complex relationships among array recording parameters. Although some of the technologies required for array recording are the same as those required for array sensing, the applications of the technologies are sufficiently different that array sensing and array recording warranted separate paragraphs in the final report.

Paragraph 4.0, Data Collection and Processing, contains all of the theoretical and computer simulation results regarding two-dimensional decimation, interpolation, lowpass filtering, MTF correction, and image enhancement. In addition, the theoretically derived performance limitations resulting from using nonideal or defective CCD's for FIR implementation are reported in this section in the form of computer-generated graphical plots.

Paragraph 5.0 presents a tutorial overview of the bandwidth compression techniques of interest in the ASITS application. The implementation tradeoffs involved for bandwidth compression algorithms using array scanning techniques are reserved for the following paragraph, 6.0.

Paragraph 6.0, Candidate Systems, treats the complexity versus performance tradeoffs for array scanning systems of various complexity. In this paragraph we show top-level implementation diagrams for array scanning systems having complexity ranging from that of minimal capability systems to those having full IITS-type capability.

Paragraph 7.0 details the conceptual design and expected performance for the candidate system of paragraph 6.0 deemed most cost-effective for the ASITS application.

The summary, conclusion, and recommendations of the study effort are contained in paragraph 8.0.

Appendices have been included as deemed appropriate to the presentation of the study results.

1.4   CONCLUSIONS AND RECOMMENDATIONS

The results of this study indicate that an array scanning image transmission system is both feasible and advantageous when compared to a conventional single point scanning image transmission system. The study effort focussed upon array scanning implementations and tradeoffs and the implementation of sophisticated processing algorithms using the CCD technology that is so well suited to array scanning techniques. It was found that the state-of-the-art of electro-optics technology supports one-dimensional sensing and recording arrays and that two-dimensional sensing arrays can be easily synthesized from one-dimensional sensing arrays. After evaluating many candidate systems, we present a conceptual design for a sophisticated ASITS whose implementation is built entirely around two commercially available CCD's. Based upon the results of this study, we recommend a multiphase follow-on study effort. Section 8.0 contains a more detailed description of the study conclusions and recommendations.

2.0 ARRAY SENSING

The function of a scanning system is to extract data from a source image and prepare it for transmission. This usually implies that a minimum configuration will consist of a scanning method, an illumination source, and a detection system, with appropriate electronic control functions synchronizing their operation. Requiring the system to be capable of array scanning places an additional demand on the optical system: either the illumination source or the optical receiver (or both) must be capable of distinguishing a number of different positions for each scan location. In addition, the requirement to resolve simultaneously a number of pixels can place restrictions on the nature of the scanning technique, because of the larger apertures required and the size of the array devices themselves.

There are a number of techniques that can be used to provide multichannel or multidimensional array scanning capabilities. These include acousto-optic devices, fiber-optic arrays, photodiode detector arrays, and LED arrays. Each of these approaches can be combined with conventional scanning techniques to provide an array scanning/image dissection system. Among conventional scanning techniques, the most successful and generally useful for tactical imagery applications are galvanometer scanners and rotating drum scanners. Galvo scanners, which move only the optical beam in relation to the stationary document, can provide the significantly greater speeds required in some applications. Drum scanners, however, are particularly relevant to array scanning applications, since their use of stationary sources and detectors can support more complex optical configurations as

required in many array techniques.

In this section we will provide a discussion of
the tradeoffs and implementation considerations associated
with currently accessible array technologies, including
both basic introductions to the capabilities and limita-
tions of specific components, and conceptual system descrip-
tions of some viable array scanning systems. After several
systems have been described briefly, some more specific
goals (as to formats, data rates, etc.) will be assumed
and used as the basis for some detailed tradeoff considera-
tions of a specific array scanning system design. The sec-
tion will conclude with some discussion of alternative
approaches to meeting the specific goals of the main scan-
ner system.

Emphasis in this section will be placed on the
scanning of one-dimensional linear arrays, in preference to
the block matrix approach. There are two reasons for this
emphasis: first, the linear devices currently have signifi-
cant cost and implementation advantages over matrix-oriented
systems, often without sacrificing much in the way of per-
formance; second, the development of two-dimensional input/
output devices is not yet adequate to support the multiple,
field-operational units which would be required for a useful
imagery transmission network.

Finally, it should be noted that many of the de-
vices and techniques discussed in this section are also rele-
vant to array recording; thus additional data and tradeoff
discussions on these components may be found in Section 3.0.

2.1   COMPONENTS FOR ARRAY SCANNING

A necessary precondition to an understanding of the array scanning system approaches to be discussed in this section (and the reporting techniques of the following section) is a familiarity with the electro-optical components which compose these systems. In this subsection we will present brief introductions to each key concept and technique to be used in the subsequent system descriptions.

2.1.1   Scanning Techniques

Since very large format area sensing devices are not currently available (or on the horizon), a means is required to scan the operational area of a smaller sensor across the width of the image to be transmitted. For most image transmission systems, drum and galvanometer based scanners have proven to be the most successful; also, in small-format, high-speed applications, acousto-optic devices have many attractive features, especially their speed capabilities and the absence of moving parts. These three types of scanning devices will be used extensively in the system descriptions to follow; accordingly a brief summary of their nature and capabilities is appropriate here.

2.1.1.1   Galvanometer Scanners

A galvo scanner is a moderate-speed, random access device based on the motion of a coil within a changing magnetic field. One end of the coil armature shaft supports a thin mirror which moves with the shaft. Thus, electrical inputs to the driving field can control mirror position and hence beam angle. A simple illustration of this situation is shown in Figure 2.1.1.1.

13

MIRROR

MOVING
COIL
ROTOR

STATOR
MAGNETS

10312—16
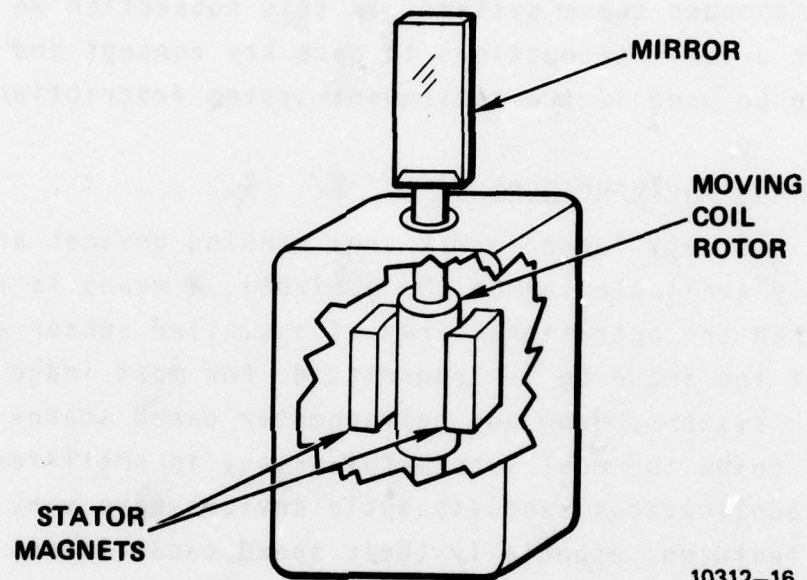
Figure 2.1.1.1

Basic Moving - Coil Galvanometer Structure

Some of the capabilities and limitations of galvo scanners include the following parameters.

- Peak-to-peak optical scan angles of up to 60°.

- Scan frequencies of from 0 to 25,000 Hz (but with higher frequencies achievable only with smaller scan angles).

- Resolution capability of up to 2000 spots, extensible to over 10000 using optical feedback techniques.

- Good repeatability of better than 0.05%.

- Moderate cost.

- Ability to respond to many input control waveforms: sine wave, sawtooth, ramp, random step, etc.

Galvanometer scanners have been used successfully in many facsimile transmission systems, as well as digital data storage and retrieval systems and image display systems.

2.1.1.2   Drum Scanners

In many applications, the requirement to scan an optical beam over a wide area, as is done with the galvo-based systems, places uncomfortable restrictions on some key optical components (e.g., the detector system). This problem is eliminated by scanning techniques in which the scanned medium is moved past a stationary optical beam in one of the two dimensions; the major technique in this category is the drum scanner. Such a system is illustrated in simplified form in Figure 2.1.1.2. The optical beam
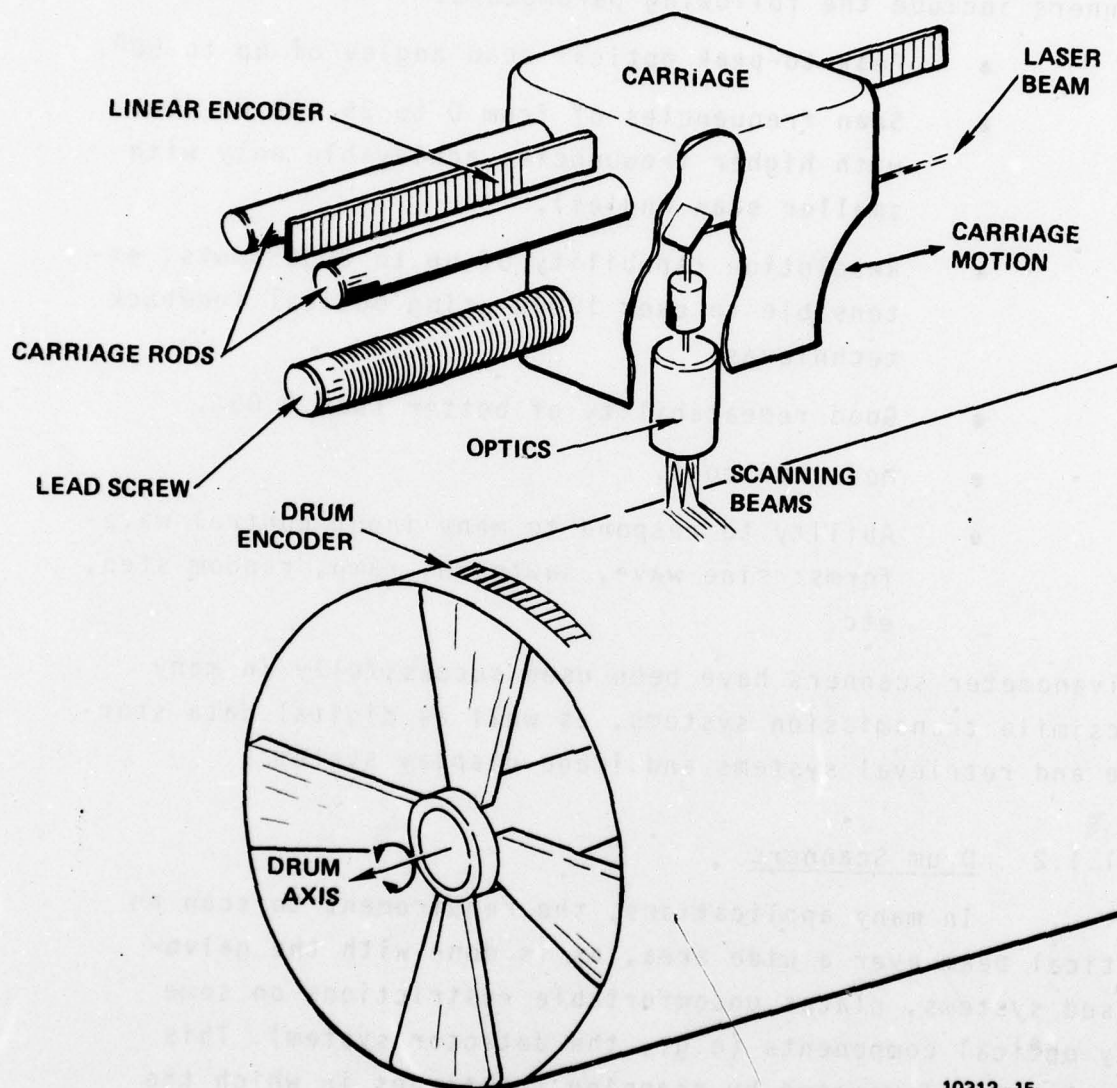
15

Figure 2.1.1.2
Multi-Beam Drum Scanning Configuration

(which for an array scanning may be a multiple beam) is
translated parallel to the drum axis by a moving optical
head, while the drum rotates the scanned document perpendicu-
lar to the beam's motion, creating an X-Y raster scan of the
drum surface. The advantage of such a system is that, since
the beam-forming optics do not have to participate in sat-
isfying a wide-area scanning constraint, they are better able
to produce a complex beam structure, as would be required
in an array scanning application. Also, since the beam/sur-
face interaction area is small, a smaller detector can be
used, permitting higher speed devices and/or higher sensi-
tivities and consequently reduced input light level require-
ments.

The capabilities of drum scanners currently avail-
able include the following:

- Capacity for fairly large documents, up to
  ∿14 inch length.

- Speeds up to about 1800 RPM.

- Resolution of up to 500-700 lines per inch.

- Good reliability compared to more complex
  scanning mechanisms.

Applications of drum scanners have included primarily fac-
simile image transmission systems; a few data storage and
retrieval systems have also been drum-based.

2.1.1.3   Acousto-Optic Devices

In many applications requiring fast, small field
scanning, acousto-optic devices are useful. An acousto-optic
device is a block of transparent material (various types of

17

glass, for example) through which we pass the laser beam that we want to modulate or deflect. In the crystal, the light beam encounters the acoustic wave. These devices typically operate in the "Bragg" diffraction mode, which implies that they behave like thick gratings rather than thin diffraction gratings. This mode produces two main output beams as shown in Figure 2.1.1.3. One beam, the undiffracted component, has not interacted with the acoustic wave and is usually discarded. The other beam, the diffracted component, has interacted with the acoustic wave. Temporal modulation of the acoustic wave amplitude can be used to temporally modulate the amplitude of the diffracted light wave; more importantly for scanning applications, frequency modulation of the acoustic wave will produce angular variation of the light wave, since the diffraction angle is proportional to the spatial frequency of the acoustic wave. The acoustic wave is introduced into the crystal by means of an electromechanical transducer which is bonded to one face of the crystal, and which in turn is connected to an appropriate source of RF electrical energy and associated control circuits for amplitude or frequency modulation.

When used to produce angular scanning of a beam, an acousto-optic device is known as an acousto-optic beam deflector (AOBD). Some of the pertinent capabilities of AOBD scanners include the following:

- Peak-to-peak optical scan angles of up to 2^0.

- Scan frequencies greater than 250 kHz.

- Up to 2000 resolvable spots.

- Capability to respond to a variety of waveforms: sine wave, sawtooth, ramp, random step, etc.

DIFFRACTED
BEAM

UNDIFFRACTED
BEAM

θ_B

TRANSDUCER

ACOUSTIC
BEAM

θ_B

INCIDENT OPTICAL BEAM
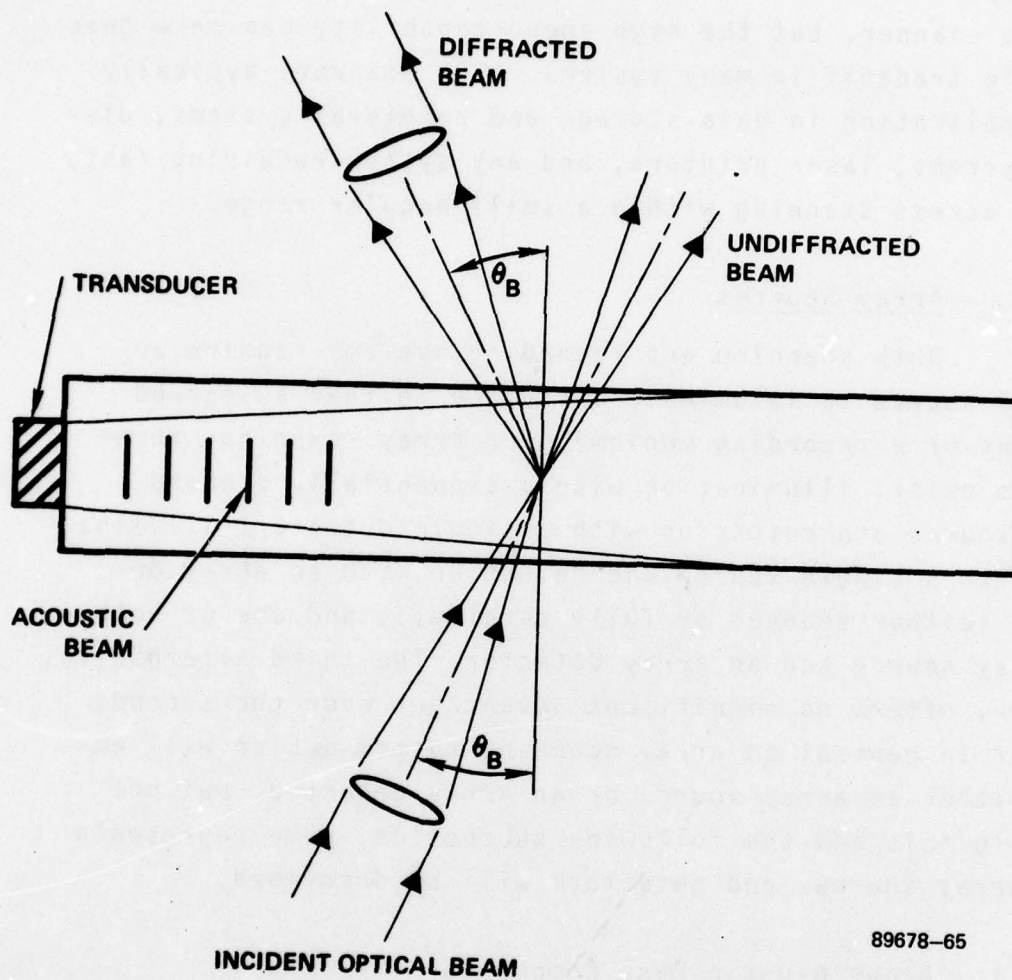
89678-65

Figure 2.1.1.3
Details of Acousto-Optic Interaction

19

This type of scanner is usually somewhat more costly than
a galvo scanner, but the high speed capability can make this
a viable tradeoff in many systems. AOBD scanners typically
find application in data storage and retrieval systems, dis-
play systems, laser printers, and any system requiring fast,
random access scanning within a small angular range.

2.1.2   Array Sources

Both scanning and recording systems require an
optical source to illuminate a surface (either a scanned
document or a recording medium). For array scanning, three
options exist: illumination with a sequentially scanned
array source and detection with a single detector; illumina-
tion with a single source and detection with an array de-
tector (either scanned or fully parallel); and use of both
an array source and an array detector. The third alternative,
however, offers no significant advantages over the second,
so that in general an array scanning system design will em-
ploy either an array source or an array detector, but not
both. In this and the following subsection, some representa-
tive array sources and detectors will be described.

2.1.2.1   Acousto-Optic Page Composers

In the previous subsection, a description of the
functioning of acousto-optic devices was given, and it was
noted that, if the drive frequency is held constant, such
a device can be used as a modulator simply by varying the
amplitude of the input signal. When an array of such modulat-
ing transducers is placed on a single crystal to form a modu-
lating array, the resultant device is known as an acousto-

20

optic page composer (AOPC). A schematic drawing of an AOPC
is shown in Figure 2.1.2.1. When illuminated by a line of
laser light, the diffracted beams from the AOPC's trans-
ducers form a fully parallel, high performance linear array
source. AOPC's with up to 128 channels have been fabricated,
providing total data throughput rates of up to 780 Mbits/s.
The specifications of a 32-channel device are given in Table
2.1.2.1, and provide a representative example of the capa-
bilities of this type of array source.

Table 2.1.2.1. Specification of a 32-Channel AOPC

No. of Channels	32
Transducer Size	100 μm
Center-to-Center Spacings	250 μm
Rise Time (10-90%)	20 ns
Beam Use Efficiency	30%
Crosstalk Isolation	-33 dB
Center Frequency	150 MHz
Material	TeO_2

Because of their high speed capability and potential for
operation with high power lasers, AOPC's are used in a wide
variety of optical storage and processing applications, in-
cluding holographic recorders, direct spot recorders, data
processors, display systems, etc.

2.1.2.2   Light-Emitting Diode Arrays

A semiconductor diode in which a proper energy
gap exists between the valence band and the conduction band
in the P-type material can be made to emit light when bias-
ed in the forward direction. The wavelength emitted depends

21

INCIDENT LIGHT

UNDIFFRACTED LIGHT

LIGHT WEAKENED BY DIFFRACTION

DIFFRACTED LIGHT SHOWING BITS

LIGHT SOURCE

TRANSDUCERS
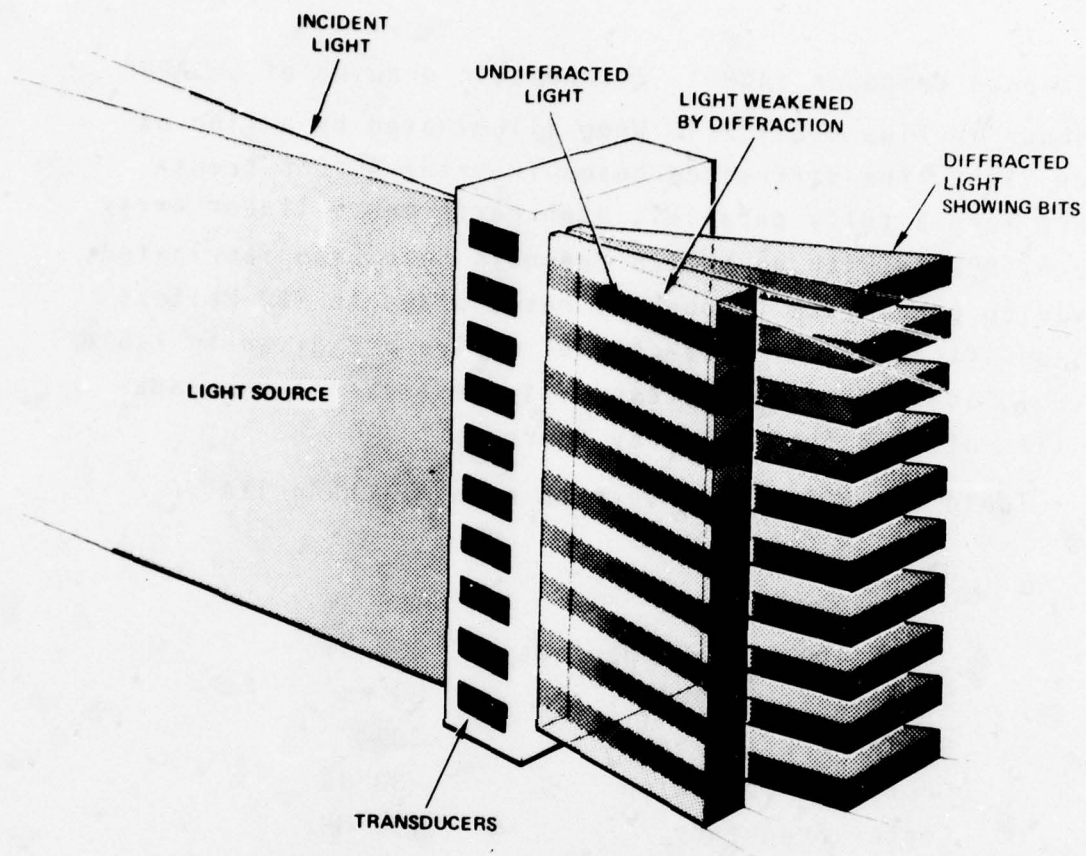
88589-2

Figure 2.1.2.1

Acousto-Optic Page Composer

22

on the energy gap width, and the efficiency of the device is controlled by the tendency of the electrons in the material to emit photons rather than phonons (vibrations) as they fall from the excited state. Light emitting diodes (LED's) are available in most areas of the visible spectrum, as well as the near infrared. Both single element and array sources have been constructed and delivered, with good reliability and flexibility of configuration.

LED's can be used in any optical system in which a relatively low-power, incoherent source is acceptable. Linear array devices have been constructed with some or all of the following characteristics:

- Output wavelength: 660 nm

- Output power: 1 µW/mA drive

- Maximum output: 400 µW pulsed, 40 µW continuous

- Number of elements: hundreds

- Array output uni-
  formity: $\pm$30%

- Rise time: 50 ns

- Commutation rate: 200 kHz

Additionally, progress in element spacings is continuing, with 7.5 mils achieved and 2 mils projected for the near future. This combination of capabilities make LED arrays potentially attractive as a source for the array scanning application.

LED arrays have chiefly found use in document scanners, film annotation, alpha-numeric readout, pattern recognition and display systems.

2.1.2.3   AOBD Techniques

The acousto-optic beam deflector, or AOBD, as described above in Paragraph 2.1.1.3, is a convenient means of achieving rapid, narrow-angle scanning. Another potential use of such a device is in the production of multiple beams from a single beam. By inputting simultaneously several drive frequencies, a number of acoustic frequencies can be produced within the crystal, each frequency capable of deflecting some light in a different direction. In this case, the frequencies are held constant (so that no angular motion of the beams takes place), and the beams can be individually intensity modulated by controlling the strength of each input frequency. This technique will be described in more detail in Paragraph 3.0, where it will be used as the basis of an array recording system.

An additional AOBD technique, in which the various beams are not all present simultaneously, is not a true array technique, but will be of importance for the system design to be presented in a later section of this paragraph; this technique will be described in sections 2.1.4 and 2.3.3.2.

2.1.3   ARRAY DETECTORS

As previously described, one viable option for the production of array information involves the use of a scanned array source and a single detector; in that case, an array detector is not used. In the other possible systems, however, scanned or parallel array detectors are necessary. The two most useful of the current devices in this category are fiber-optic/discrete detector arrays, and scanned integrated detector arrays.

2.1.3.1 Fiber-Optic/Discrete Detector Arrays

One effective way to acquire array information at high speeds is through the use of an array of optical fibers and discrete detectors, as shown in Figure 2.1.3.1. By imaging the linear area to be scanned onto the input surface of the fiber-optic linear bundle, information from each pixel location can be conducted to a discrete detector for amplification and processing. The use of discrete detectors permits advanced integral preamplifier designs to be used and thus increases the speed and SNR achievable by the system. Fiber arrays with several hundred elements can be constructed; some other readily achievable array parameters are as follows:

- Fiber diameters: $\geq$5 mils
- Fiber transmission: >75%
- Transmission uni-
    formity: $\pm$5%
- Crosstalk: < -45 dB
- Per-channel data
    rate: 10 Mb/s

Typical applications of fiber-optic/discrete detector arrays include high-speed optical data storage and retrieval systems and document scanners.

2.1.3.2 Integrated Detector Arrays

Although not as fast or as adaptable to parallel output systems as the discrete approaches, integrated detector arrays are another important option for array detection. These devices include charge-coupled devices (CCD's),

DISCRETE
PHOTODETECTORS

OPTICAL CONNECTOR

SINGLE FIBER-OPTIC
ELEMENT

FIBER-OPTIC
LINEAR
BUNDLE
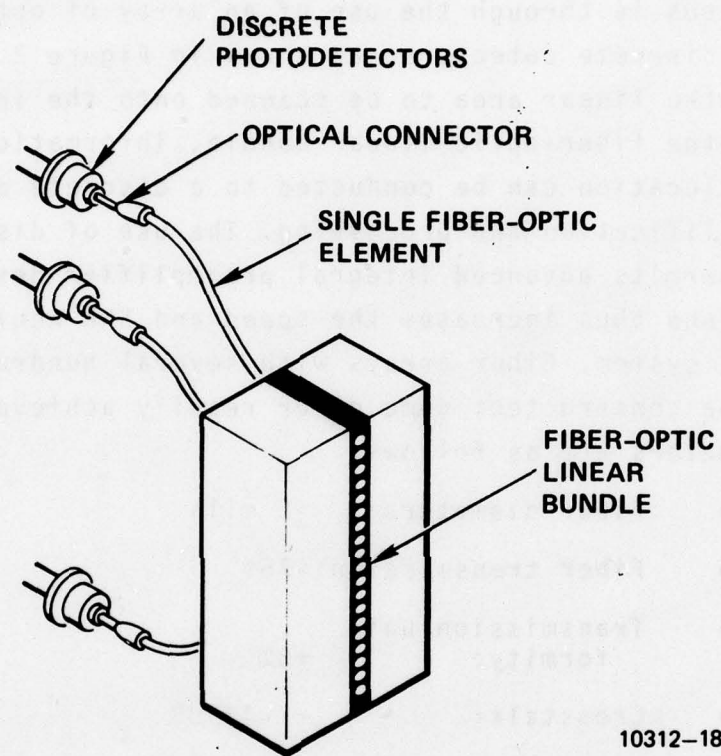
10312—18

Figure 2.1.3.1

A Linear Fiber-Optic Array

charge-injected devices (CID's), phototransistor arrays (PTA's) and others. The primary advantage of such devices is that they can accommodate both a number of photosensitive areas and a preamplification stage on the same substrate; this makes possible low-noise amplification of the received signals and thus enhances the SNR and speed capabilities of the units. The space problems associated with placing multiple amplifiers on the substrate with the photosensors make the scanned approach much more common. In this approach, signals from the photosites are serially gated through a common amplifier prior to leaving the chip. Parallel-output integrated photosensitive arrays are less common, and generally provide poorer SNR performance because of the off-chip signal amplification; however, such devices do exist, and are capable of much greater information throughput rates than are the serially scanned arrays.

The following table illustrates the capabilities of two typical, serially scanned, wide field integrated photo sensors.

Table 2.1.3.2. Integrated Photo Sensor Characteristics

	Device 1 (Fairchild)	Device 2 (Reticon)
Array Size	1728X1	1024X1
Cell Size	0.51X0.67 mils	1 X 1 mil
Cell Center Spacings	0.51 mils	1 mil
Operational Method	CCD buried channel	Silicon gate MOS
Dynamic Range	500:1 @ 1 MHz	1000:1
Max. Clock Rate	1 MHz	10 MHz
Saturation Exposure	0.5 $\mu J/cm^2$	0.11 $\mu J/cm^2$

Applications of these devices include page scanning, facsimile readers, optical character recognition, process control, film reading, and spectroscopy. Self-scanned integrated photosensors are also available as matrix arrays in sizes up to about 400 x 400.

2.1.4 PSEUDO-ARRAY GENERATION

To achieve the full speed capabilities of array scanning, parallel generation of the picture elements is required. However, in many cases, such as when system bandwidth is limited by a data transmission link, speed is not the prime concern, and other methods of obtaining information for array processing may be considered. In particular, if the data associated with an array of picture elements can be generated serially and stored in analog form, parallel processing can then be done as if they were generated simultaneously.

One approach to achieving the required array information is to buffer entire scan lines until enough lines are stored to cover the matrix of interest. This approach is straightforward, but requires (for all but the smallest scan formats) an uncomfortably large buffer, e.g., N lines times several thousand pixels for arrays of size N by N. Another approach, which will be discussed in detail in Section 2.3.3 below, involves vertical dithering of a horizontal raster, so that the N^2 pixels of a matrix array are scanned out contiguously, rather than N in each full line.

In both approaches, a method of storage of information is required, to allow serial scanning and parallel processing both to be accomplished. When full lines of data

must be buffered, digital storage is currently the only
practical approach. For the smaller, dithered raster scan
technique, however, analog storage is feasible. Two tech-
niques which may be used to accomplish such analog storage
are an electrical tapped analog delay line (TAD) and an
acousto-optic delay line (AODL).

2.1.4.1   Electrical Delay Line

Storage and shifting of analog values has become
economically viable with the recent introduction (primarily
by Reticon, Inc.) of TAD devices in integrated form. In
these devices, analog values are represented by quantities
of charge stored on capacitive nodes in a transistor gate
network. By adjusting the potentials in the semiconductor
material properly the charge can be shifted from node to
node at each clock pulse. Also, taps at each node make the
values available in parallel to the outside world for simul-
taneous processing. These TAD devices can achieve clock
rates of 5 MHz and can have up to 32 stages (much longer de-
vices have been built, but without the feature of parallel
output taps). Additional discussion of TAD devices and test
results of a particular unit are provided in section
2.3.3.3.3.

2.1.4.2   Acousto-Optic Delay Line

Electrical TAD devices provide a flexible, inte-
grated package, but have limitations in the areas of pulse
fidelity and number of output taps. By using an acousto-
optic device, some of these problems can be overcome. The
technique is a standard one in acousto-optics: modulating

the analog samples onto an RF carrier and inputting them to
an acousto-optic crystal via a piezo-electric transducer.
As the pressure waves, whose intensities represent the
analog values, propagate down the crystal, they are avail-
able for simultaneous illumination by a laser source, and
hence parallel processing. The primary limitations of such a
system are the available crystal sizes and the F/numbers in
the optical system itself. Additional details on acousto-
optic devices are provided in sections 2.1.1.3 and 2.3.3.3.1,
while the use of the AODL in serial-to-parallel conversion
is central to the system described in section 2.4.2.

2.1.5   Direct Electronic Fourier Transformation

Another type of component which can be of sig-
nificant use in array scanning systems is the direct elec-
tronic Fourier transform (DEFT) device. This is a device
which can produce as an output the Fourier transform of
an image projected on its surface; thus it provides the
capability for a variety of two-dimensional filtering and
bandwidth compression operations with minimal hardware
complexity. Because of these filtering applications, the
DEFT device could validly be described in the section of
this report dealing with filtering and bandwidth compression;
by placing it here, however, we can more easily see its
relationship to some other array sensing techniques, as
well as its usefulness for array scanning.

There has been considerable effort expended since
1972 toward the development of a "Fourier Transform Camera",
which would generate a set of time-sequential electrical
signals corresponding to the Fourier Transform of an image
projected upon it. This effort has been supported at

30

Syracuse University by RADC under Contract numbers F30602-
72-C-0403 and F30602-73-C-0277. The results of this re-
search are contained in two final reports:

> Direct Electronic Fourier Transforms of Optical
> Images, RADC-TR-73-254, August 1973[2] and

> DEFT: Progress on Direct Electronic Fourier Trans-
> forms of Two-Dimensional Images, RADC-TR-74-244,
> October 1974[3].

Additional research on this topic has been funded by the U.S.
Aramy Night Vision Laboratory, Ft. Belvoir, Va., again
at Syracuse University, under Contract No. DAAG53-76-C-0162.
An interim report for the period 10 June 1976, through
9 June 1977 is entitled Two-Dimensional Direct Electronic
Fourier Transform (DEFT) Devices: Analysis, Fabrication,
and Evaluation[4].

In this section we trace the progress of this
research as reported in the above reports and evaluate the
applicability of present state-of-the-art DEFT devices to
an image compression and transmission system.

The research reported in [2] deals with theoretical
aspects of two-dimensional surface acoustics, image recon-
struction, and motion detection, and describes the experi-
mental aspects of the design and construction of a one-
dimensional CdS surface acoustic wave (SAW) "camera".

The SAW camera utilizes the elastophotoconductiv-
ity of the semi-conducting CdS film deposited onto a glass
substrate to correlate the impinging light pattern with the
SAW launched into the glass substrate by the transducer.

An electrical current proportional to the photo-
conductivity of the CdS film is sensed phase-synchronously

to provide a voltage output corresponding to the particular
Fourier spatial frequency component. The spatial frequency
of this Fourier Transform component is related to the sinu-
soidal frequency driving the electrical transducer through
the velocity of propagation of the surface strain wave in
the substrate. Different Fourier spatial frequency compo-
nents can be obtained by varying the wavelength of this sur-
face strain wave. Sweeping the frequency of the generator
driving the electrical transducer provides a time-serial
output sequence of the various Fourier transform spatial
frequency components of the incident light pattern. A one-
dimensional DEFT camera was fabricated and tested for sever-
al simple test illumination patterns consisting of alter-
nating strips of light and dark. The experimental results
demonstrated the validity of the approach for the one-
dimensional SAW camera. The remainder of the report dealt
with various theoretical aspects concerning the two-dimension-
al DEFT camera.

The research for the following year was reported
in RADC-TR-74-244[3], and described the experimental re-
sults obtained using a two-dimensional DEFT camera. The
experimental setup that was used is shown in Figure 2.1.5-1
taken from [3]. The sensors used exhibited improved sensi-
tivity and resolution compared to previous devices. The two-
dimensional DEFT camera utilized 100 sensors in parallel
which were fabricated by deposition of interdigital contacts
on a square CdS film. This DEFT camera was used in extensive
focus detection and motion detection experiments with en-
couraging results. Also reported was the building and test-
ing of an elastobirefringent light valve for one-dimensional

TO PHASE SYNCHRONOUS DETECTOR

CURRENT SENSOR

ACOUSTIC ABSORBING TAPE

CdS FILM

INTERDIGITAL INDIUM CONTACTS

LIME GLASS SUBSTRATE

TRANSDUCER

PLEXIGLAS WEDGE

SWEEP FREQUENCY GENERATOR
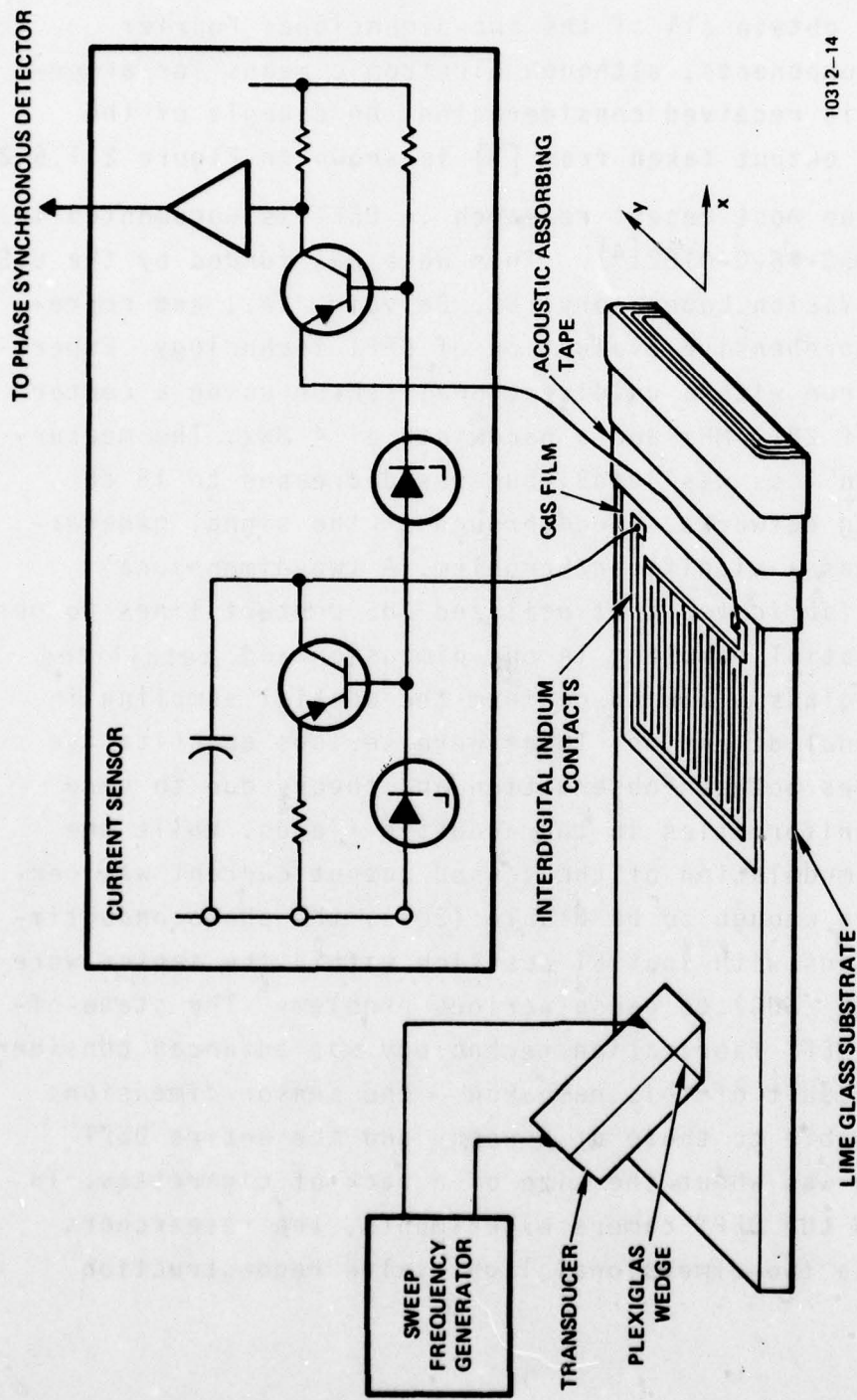
10312-14

Figure 2.1.5-1

Two-Dimensional Interdigitated Elastophotoconductive Sensor

reconstruction. In the work reported for this phase of the research, mechanical rotation of the image was required in order to obtain all of the two-dimensional Fourier transform components, although electronic means for accomplishing this received consideration. An example of the DEFT camera output taken from [3] is shown in Figure 2.1.5-2.

The most recent research in DEFT is documented in Report DAAG53-76-C-0162[4]. This work was funded by the U.S. Army Night Vision Laboratory, Ft. Belvoir, Va., and represents a comprehensive evaluation of DEFT technology. Experiments were run with a unidirectional sensor using a center frequency of 28.2 MHz and a bandwidth of 4 MHz. The measured insertion loss was 40 dB, but was decreased to 18 dB via matching networks. Feedthrough of the signal generator source was a significant problem. A two-dimensional sensor was fabricated that utilized CdS contact lines to perform the spatial sampling in one dimension and metallized lines on a glass plate to perform the spatial sampling in the orthogonal dimension. There were serious quantitative discrepancies between observation and theory due to very strong nonuniformities in the acoustic fields. While the AO-induced modulation of the sensed output current was certainly large enough to be usable (20%), the photoconductivity variations with spatial position within the sensor were large enough (50%) to cause serious problems. The state-of-the-art of DEFT fabrication technology was advanced considerably as a result of this research -- the sensor dimensions were comparable to those of a penny and the entire DEFT camera size was about the size of a pack of cigarettes. In addition to the DEFT camera experiments, the researchers fabricated a two-dimensional light valve reconstruction
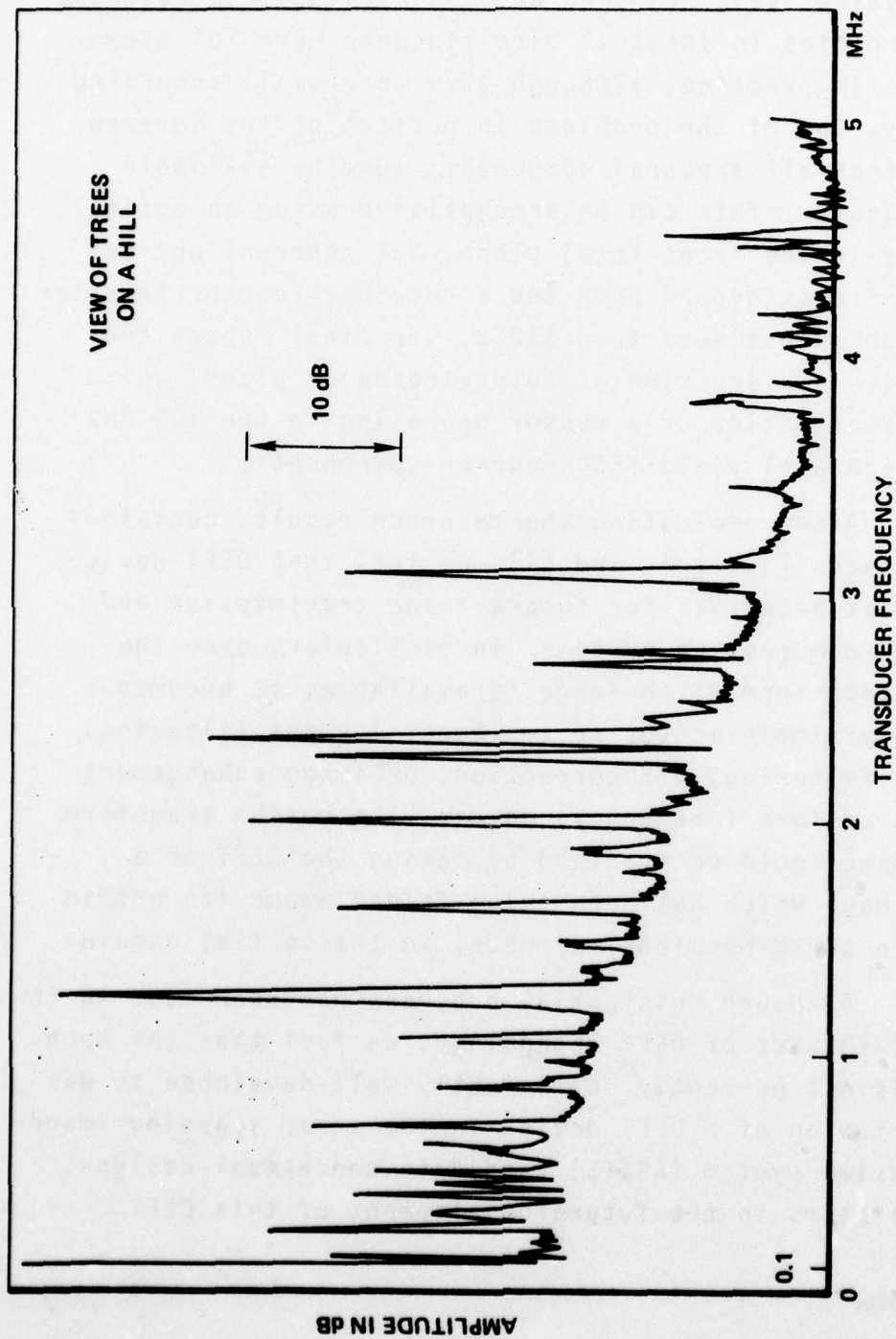
Figure 2.1.5-2

Output Magnitude From a High-Sensitivity DEFT Sensor.
Overcast Outdoor Scene.

device that relied upon strain-induced birefringence in
a light valve "sandwich". No data is available because the
nonuniformities in internal birefringence were 100 times
too large in practice, although they were small according
to theory. One of the problems in performing the inverse
DEFT is that all spectral components must be available
simultaneously. This can be accomplished using an optical
modulator in the front focal plane, but coherent optical
modulators cost around $40K and a complete Fourier inverter
system would cost more than $100K. The final report con-
cludes with a discussion of future research plans, which
include fabrication of a sensor operating in the 100 MHz
range which will yield 1500 Fourier components.

After evaluating the research results contained
in references [2], [3], and [4], we feel that DEFT devices
offer great potential for future image transmission and
bandwidth compression systems. In particular, once the
Fourier transform of an image is available, it becomes a
relatively simple matter to implement lowpass filtering,
bandpass filtering, MTF correction, or image enhancement
in the transform (frequency) domain. The cosine transform
of an image could be obtained by taking the DEFT of a
source image which has been twice-folded about its origin
to obtain two-dimensional symmetry in the spatial domain.

Although substantial progress has been made in the
state-of-the-art of DEFT technology, we feel that the tech-
nology is not presently sufficiently well-developed to war-
rant inclusion of a DEFT device in the array scanning image
transmission system (ASITS) candidate conceptual designs.
Critical items in the future development of this DEFT

technology appear to be increased uniformity of the Cds
film spatial responsivity and the fabrication of a usable
reconstruction device at a reasonable cost.

2.2   ARRAY SCANNING SYSTEM CONCEPTUAL DESIGNS

Having established as a background the nature
and capabilities of many of the components which can be
used in an array scanning system, we now turn our atten-
tion to the tradeoffs that are encountered in designing
a system using these components. As a method of covering
this subject, we will give brief descriptions of several
array scanning systems which can be configured from some
of the components described above, describing as we go
the advantages and disadvantages of each type of system.
In the absence of any specific parametric design goals,
only fairly qualitative and conceptual design choices can
be made; this will, however, allow adequate presentation
of the features of each system, and will form a basis
for the following section, where specific design goals
will be adopted and more quantitative tradeoff studies
described.

2.2.1   Drum-Scan/LED System

The details of the optical receiving head of
an array scanner based on the combination of Light-Emitting
diodes (LED) with drum scanning techniques are given
in Figure 2.2.1. The LED array is a linear array of from
5 to 50 emitters aligned transverse to the plane of the
figure.

LED DRIVE ELECTRONICS   LED ARRAY   DETECTOR ELECTRONICS   PHOTO-DETECTOR

FIBER-OPTIC LIGHT PIPE

FIBER SUPPORT

DRUM SURFACE

DRUM ROTATION

10312–12
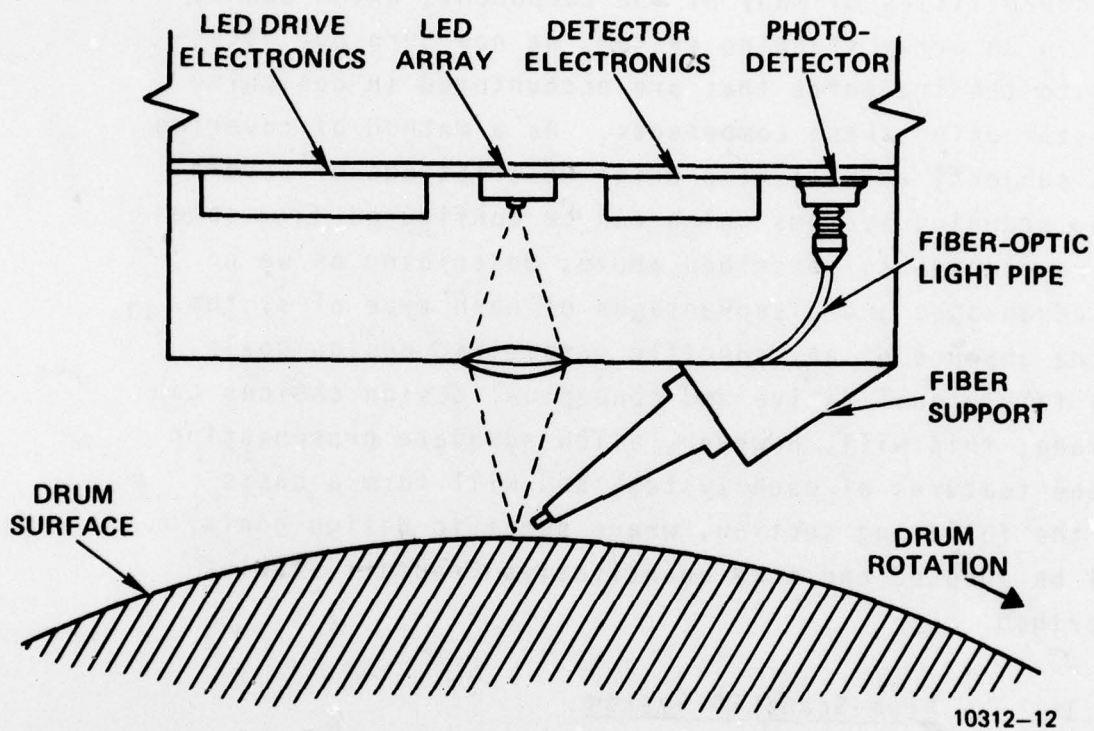
Figure 2.2.1

Details of Optical Scanner Head for

Drum-Scan/LED System

38

The diodes are imaged to the surface of the drum, which
supports the document to be scanned. For most systems
of interest, the resolution will be high enough and the
number of elements small enough that a single light-con-
ducting fiber-optic element can be used to receive the light
reflected from the document's surface, independent of
which diode is illuminated. This means that a single,
fast detector can be used, greatly simplifying the system
structure and cost.

To produce information using this system, the
LED's are sequentially scanned as the drum rotates. The
scan rate of the diodes is sufficiently greater than that
of the drum that a vertical line of pixels is scanned
out while the drum moves laterally one pixel distance. Thus
for an LED array length of N, each N-pixel distance traversed
by the drum completes a new NXN matrix pseudo-array in the
manner described in Sections 2.1.4 and 2.3.3.2. Some form
of analog stroage for the N^2 pixels must be provided, as
shown in Section 2.1.4; however, details of the storage
mechanism will not be discussed here, except as needed
to assure compatibility with system data rates. The
additional components required in the scan head are the
commutation electronics for the LED array, and the biasing
and post-amplification circuitry associated with the photo-
detector.

To determine the performance capabilities of
the described system, operating parameters will be chosen
which are well within the current state of the various arts
involved, thus assuring that the resulting configuration
is feasible. The starting point will be the resolution and
light budget. For small arrays, LEDs on 2 mil centers are
possible, so we will take the required resolution to be

400 lines (pixels)/inch. Thus an array of 1.5 mil square
LEDs on 2.5 mil centers would be required for use with a
one-to-one imaging system (for maximum light collection
efficiency). If we assume an array size of 20 x 20,
then the length of the scanned array will be about 50
mils or 1.27 mm. Thus a standard 1.25 mm diameter light
pipe can be used with good collection efficiency for the
whole array. First, consider the output capabilities of
the LEDs: a diode of about 2 mil^2 area can be safely
driven at up to 100 mA on a pulsed basis; furthermore,
about 1 µW of optical output will be generated for each
1 mA of current input; thus about 100 µW of signal (at a
wavelength of 660 nm) would be produced from a typical
LED at the 5% duty cycle envisioned for a 20-element array.

Next, we consider the lens and fiber collection
efficiencies. The minimum feasible F/# of the imaging
lens is around F/2. This means its efficiency can be as
high as about 3%, as given by

$$\eta = \frac{\Omega}{2\pi} = 1 - \frac{2F\#}{\sqrt{1+(2F\#)^2}} = .0298 \qquad (2-1)$$

If the collection fiber is located 75 mils from the pixel
center, then it will be an F/1.5 system and collect about
5% of the scattered light. Allowing an additional 3 dB
of loss for the combined effects of paper reflectivity
off-axis collection, and fiber-detector interface loss,
we find an expected signal at the detector of approximately
75 nW. For a detector such as the RCA C30914E (an aval-
anche photo-diode with integral light pipe) this would pro-
duce about 10 mV of signal, and the detector NEP of about 0.1
pw $\sqrt{Hz}$ would provide adequate SNR up to around 500 Khz,

40

which is consistent with a system pixel transmission rate
of up to 25 KHz. Furthermore, this rate is compatible
with the capabilities of the analog storage devices des-
cribed in Section 2.1.4. Since this analysis is very
preliminary, and does not include the important noise
considerations involved in the design of the circuitry
required to process the detector output, it may be somewhat
optimistic; nevertheless, the utility of such a system
design for a rather broad class of array scanning applica-
tions (perhaps even up to the requirements of the IITS
system) has been clearly demonstrated.

A summary of the parameters of the system
just described is provided in Table 2.2.1.

Table 2.2.1. Parameters for Drum-Scanned LED Array System

Number of Elements	20
Array Size	20 x 20
LED Size (mils)	1.5
LED Centers (mils)	2.5
LED Commutation Rate (kHz)	500
Resolution (pixels/inch)	400
Pixel Transmission Rate (kHz)	25
Drum Speed (r/min)	180
SNR (Detector Only) (dB)	30

The chief advantage of this system is its compact-
ness, reliability, and the simplicity of its optical design.
This is a result of the use of the drum scan technique,
which eliminates the wide optical scan/detection require-

ments of other systems, as well as the limitation of system speed, which makes the low power/efficiency of the LED/ fiber collector acceptable. For higher speed systems, the parallel data reception scheme of the following subsection may be more appropriate.

2.2.2   Drum-Scan Fiber-Optic Array System

Another drum-based system concept that is appropriate for consideration in medium to high speed array scanning applications is that of Figure 2.2.2. In this system, which superficially resembles that of the previous section, several important changes have been made in pursuit of a specific goal: to shift the burden of pixel separation from the light source to the detector. By passing a laser beam (from a laser mounted external to the scan head) through a series of shaping optics, a line source of light can be produced to illuminate the scanned document at the drum's surface. Then the scattered light is used to image the line onto a linear array of fiber-optic elements, each of which conducts the light from a different pixel to a discrete detector for detection and processing. In the previous system, any non-uniformities caused by the optical configuration could be eliminated by varying the drive to the various LEDs in a compensatory manner; in this system, the analagous procedure (to handle the truncated Gaussian profile of the laser beam, for example) is simply to vary the sensitivity of the individual photodetectors such that a uniform input document results in a uniform output.

To analyze the capabilities of this system, we first note its fundamental difference from the previous system: the pixels in the linear array are generated simultaneously rather than serially. Thus the commutation rate

DISCRETE
DETECTOR ARRAY

DETECTOR
ELECTRONICS

LASER
BEAM

FIBER-OPTIC
ARRAY

FORMING
OPTICS

COLLECTION
LENS

DRUM
SURFACE

DRUM
ROTATION

10312–11
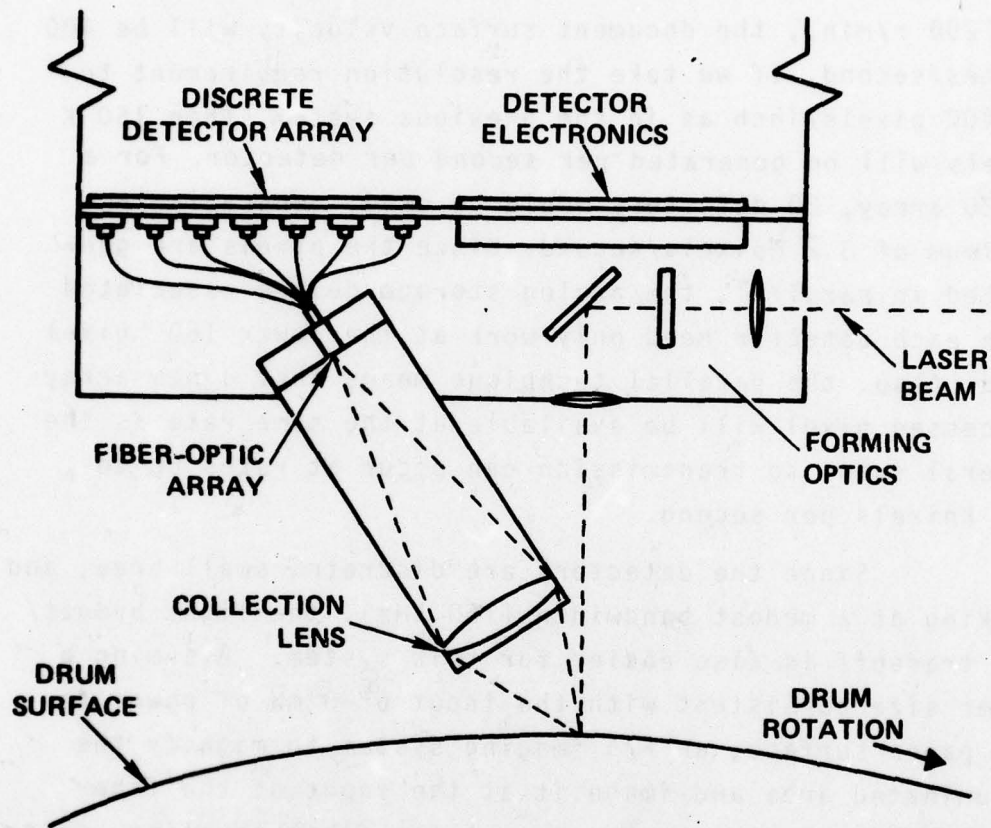
Figure 2.2.2

Scanner Head Details for

Drum-Scan/Fiber-Optic Array System

(bandwidth in this case) of the detectors is also the lateral pixel rate of the drum's surface. We may thus expect that this system will be capable of much higher speeds, and that the speed limiting component will be the drum itself. Assuming a drum diameter of 6.4 inches and a rotation rate of 1200 r/min., the document surface velocity will be 400 inches/second. If we take the resolution requirement to be 400 pixels/inch as in the previous system, then 160 K pixels will be generated per second per detector. For a 20x20 array, 20 detectors would be used, generating a maximum of 3.2 Mpixels/second. Since the pixels are generated in parallel, the analog storage device associated with each detector need only work at the lower 160 Kpixel rate. Also, the parallel technique means that a new array processed pixel will be available at the same rate as the lateral scan, so transmission can occur at rates up to 160 Kpixels per second.

Since the detectors are discrete, small area, and working at a modest bandwidth (160 kHz), the light budget/ SNR tradeoff is also easier for this system. Assuming a laser size consistent with the input of 5 mW of power to the paper surface, an F/5 imaging system to magnify the illuminated area and image it at the input of the fiber array, and a 3 dB loss to account for fiber coupling, paper reflectivity, etc., we can expect to see approximately 0.6 µW of optical power reaching each detector. This is in a range where at least a 35 dB SNR can be supported by many available detector/amplifier combinations, so further analysis will not be done in this cursory tradeoff consideration.

A summary of the parameters which appear to be readily supportable by an array scanning system of this type is given in Table 2.2.2.

44

Table 2.2.2.   Parameters for Drum-Scanned
Fiber-Optic Array System

Number of Elements	20
Array Size	20x20
Resolution (pixels/inch)	400
Detector Bandwidth (kHz)	160
Pixel Generation Rate (MHz)	3.2
Processed Pixel Transmission Rate (Kpixels/s)	≤ 160
Drum Speed (r/min.)	1200
SNR (dB)	≥ 35

The capability to support considerably higher system data
rates is the chief advantage of this system. It also relaxes
the speed requirements on the detectors and analog storage
devices (as compared to the previous system). The price paid
for this relaxation, of course, is the need for multiple
detectors and storage devices, as well as the use of a laser
and a somewhat more complex optical system. For small arrays,
however (up to 25X25 or so), this added complexity would not
incur too steep a cost penalty; thus this scheme should be
attractive for applications requiring high-speed, medium
resolution array scanning.

2.3   GALVO-SCAN/AOBD SYSTEM - DETAILED TRADEOFFS

In the brief descriptions of the two systems of the
previous section, we have seen that a drum-scanner based
approach to the array sensing problem offers several advan-
tages in the areas of design simplicity and speed. For a
variety of reasons, including compatibility with previous
formats and the desire for wider fields or larger matrix
arrays, other system designs may be desirable. In this sec-
tion we will provide a detailed tradeoff study of the com-
ponent interrelationships involved in such a system. This

45

will provide an opportunity both to introduce the characteristic applications of some components not present in the systems of the previous section, and to exhibit in some detail the kind of tradeoff calculations which must be performed in the preliminary design of the electro-optic portions of an array scanning system. We will first adopt a set of parametric goals toward which a system can be designed, then select an approach compatible with those goals, and finally launch into the detailed tradeoff analyses needed to characterize the performance of the system.

2.3.1   Adoption of Parametric Goals

Since the components and techniques that support array scanning systems have a broad range of capabilities, a more detailed design study cannot be undertaken until a set of system goals is defined with respect to which the components can be evaluated. For this purpose we have adopted the technical requirements of the Intra-Theater Imagery Transmission System (IITS) as the goals for the current array scanner. This selection was made because the IITS (although not presently in active procurement) appears to be a representative example of the current and near future imagery transmission systems needed by the image analysis community.

The goal of the IITS is a high resolution system which can achieve a minimum transmission time over limited bandwidth data links. Thus the technical parameters specified in the IITS design are relevant to both the scanning/recording portion of the Array Scanning program and the data compression and processing portion. The following table lists

46

the system parameters which define the required performance of the scanner system.

Table 2.3.1. IITS System Requirements (Scanner)

Scan Width (inches)	9.0
Scan Time (msec)	13.5
Digitization (bits/pixel)	4.0
Resolution (lines/inch)	384.0
Data Compression Ratio	4:1
Transmission Rate (kb/s)	32.0
MTF (@ 7.6 cycles/mm)	0.5
SNR (dB)	35.0

Additional system requirements included the ability to handle both opaque and transparent input documents, a pixel registration accuracy of $\pm$0.10 pixel, and a less than 5 minute warmup time.

When the focus of attention is narrowed to those systems and techniques which can support these goals, the design requirements for an array scanner become clearer. Specifically, a straightforward extension of the system proposed by Harris for the IITS, based on the use of an acousto-optic beam deflector and analog serial-to-parallel conversion, meets the array scanning requirements and offers several attractive features not available from the unmodified system. The details of a design tradeoff study of this array-scanning-modified system are given in the following paragraphs.

2.3.2   Approach Selection

The driving requirement in the system requirements described above is the field width of 9 inches. Except for a

47

few sophisticated (and relatively expensive) techniques such as the acousto-optic travelling wave lens scanners, the only scanning technique compatible with such a wide field is the galvanometer scanner. Since galvo scanning can also satisfy the scan time and resolution requirements of the system, it becomes the first component selected for the current system. To provide array sensing capability across a wide field requires either a sophisticated optical system to "descan" the reflected light so that it can be collected at a stationary array detector, or the use of a serially-scanned matrix array approach, with a single long detector and a form of storage to permit simultaneous processing of all pixels in the matrix. The latter technique offers lower risk and cost, and provides a good contrast to the schemes detailed in the previous section; it is therefore the selected approach.

2.3.3 Description of Selected Approach

After a design approach to be taken to produce an ITTS-oriented array scanning system had been selected, a number of specific investigations of the approach were conducted. These included preliminary tradeoff analyses to verify the feasibility of the approach, analyses of the performance of the systems key components, and brief experimental testing of several of the recommended devices which were available during the study. In this paragraph, we report on the results of these analyses, beginning with a description of the scanning system and the recommended dithered raster scanning technique.

2.3.3.1   Scanner System Description

The large scan size of the projected system (384 lines/inch over 9 inches) can be achieved by only a limited number of scanning techniques. One possibility is the system proposed for the IITS: a position-corrected galvo scan technique. This technique, which has been proven capable of resolving 10,000 single-Rayleigh spots across a 10-inch field, can be modified in several possible ways to support an array scanning requirement. The advantage of doing so is clear: since the basic scanner has been shown to be applicable to the system requirements, we may concentrate our evaluation on those areas and components required to modify the system to perform the array scanning functions.

The optical portion of the basic scanner is shown in Figure 2.3.3.1. The output from a low-power Helium-Neon laser is folded by a roof prism and divided into two beams by an integral beamsplitter. One of these beams passes through an acousto-optic device, which can be used to vary the light intensity or beam direction as required. The un-deviated part of the beam passing through the acousto-optic device is removed by a dc stop. The two remaining beams are then folded and overlapped by a second roof prism; the prism also sends a small portion of the second beam to a detector to monitor the laser's power output.

After the beam passes through the second prism, the beam expansion optics enlarge it to provide the required resolution at the film plane; these optics also image the overlap plane (after the second prism) to the galvo mirror plane, minimizing the required mirror size, and hence, providing the fast response time required by the system.

TRANSMISSIVE DETECTOR

FILM PLANE

REFLECTIVE DETECTOR

GRATING

MIRROR

FOLD PRISM/ BEAM COMBINER

FLAT FIELD LENS

BEAM EXPANSION OPTICS

DC STOP

GALVO MIRROR

AOM

FEEDBACK DETECTOR

LASER

FOLD PRISM/ BEAM SPLITTER
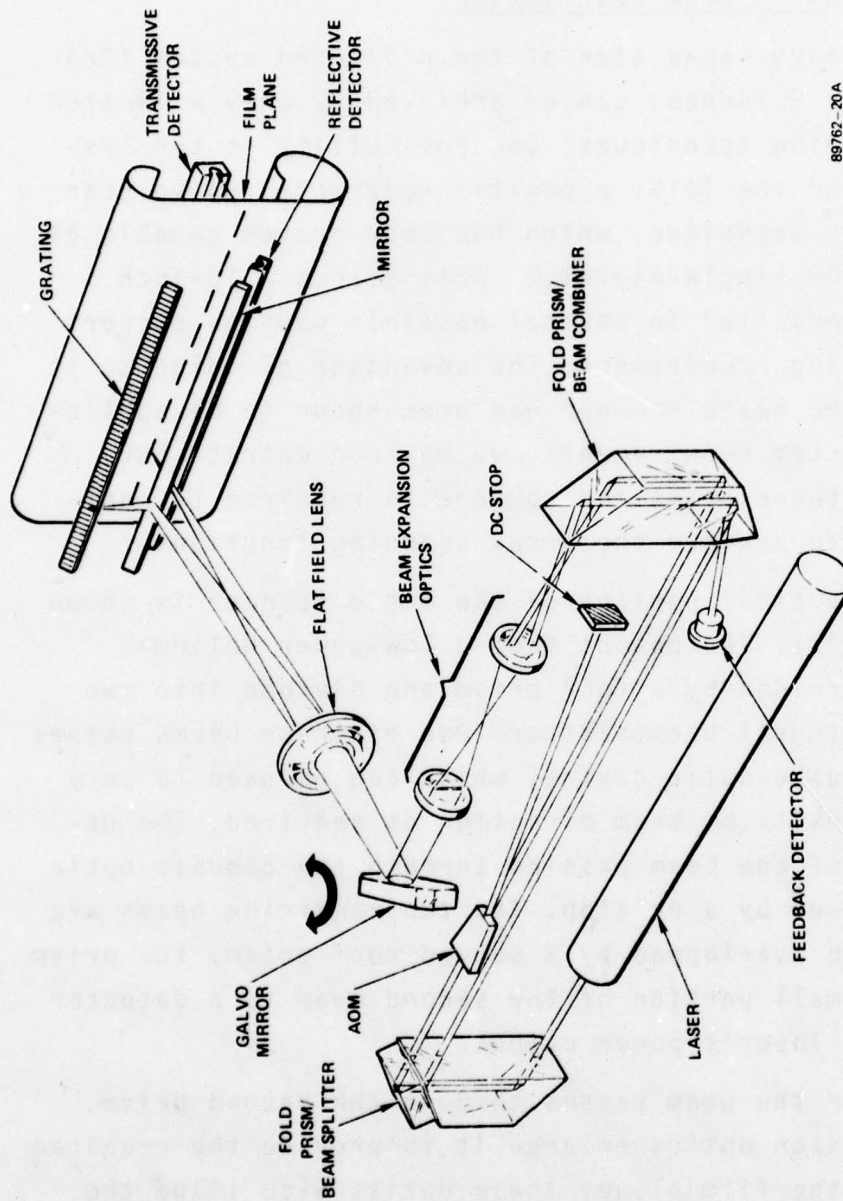
89762-20A

Figure 2.3.3.1

Scanner System Optical Layout

Angular scanning is then imparted to the beam by the galvanometer, and the flat field lens produces a small scanned spot across the wide field with adequate depth of focus to permit easy input copy positioning in the film plane. A second function of the flat field lens is to separate the two beams in the region of the input copy plane. If the input copy is opaque, the scanning beam is reflected from it onto a long, narrow photodetector; this signal is then converted to a digital signal that carries the information relating to the imagery. (For transparencies, a second detector, located behind the film plane, would perform this function.) The second beam is reflected by a mirror and focuses onto a transparent grating which is attached to an additional long, narrow photodetector. The addition of this beam produces several important and unique performance improvements which are central to the production of a high-resolution galvanometer-based scanner.

Since the grating is configured to be in the same (equivalent) plane as the input copy, the result is two focused beams scanning simultaneously, one being used to determine the reflectance at each pixel location, the other in passing through the grating, providing information about the exact location of the pixels. Thus the grating detector provides a grating clock which is used to synchronize the data handling electronics to the received data. There are three primary design advantages to the grating clock approach. First, in spite of the nonlinear scan velocity produced by the geometry of the flat field scan, the grating clock information can be used to remove all velocity errors and simulate a completely linear scan; thus the distortion and image size tolerances can easily be met. Second, the start-of-scan

51

uncertainty exhibited by conventional galvo scanners ("galvo jitter") can be eliminated using the grating clock approach; thus a conventional galvo scanner can be made compatible with a high resolution system requirement. Third, the mid-scan angular velocity changes which are exhibited by some galvo scanners can also be effectively eliminated by the grating clock technique.

As discussed to this point, the scanner is essentially identical to that used in various linear-raster scanning applications. We will now turn our attention to the modifications necessary to enable it to support the array scanning requirement, while still providing the capabilities required of the IITS system.

2.3.3.2   Dithered Raster Scanning

One convenient way of obtaining data for array-format processing is dithered raster scanning. This technique, which avoids both the full-line buffering required of linear raster scanners and the development of complex multichannel components needed for true matrix scanners, is based on a scanning pattern illustrated in Figure 2.3.3.2-1. The main raster scan travels in the x-direction as always, but with a vertical oscillation added. The downward strokes of the vertical motion carry the beam across N pixels (5 in the figure), after which a retrace stroke restores it to the top of the next N-element column. After N columns have been scanned in this manner, all the data associated with an NxN array have been obtained and may be immediately processed, provided they have been converted from serial to parallel format in some sort of storage device.

52

SCANNING SPOT

PIXEL LOCATIONS

Y-SCAN (DITHER)

RETRACE

X-SCAN (RASTER)
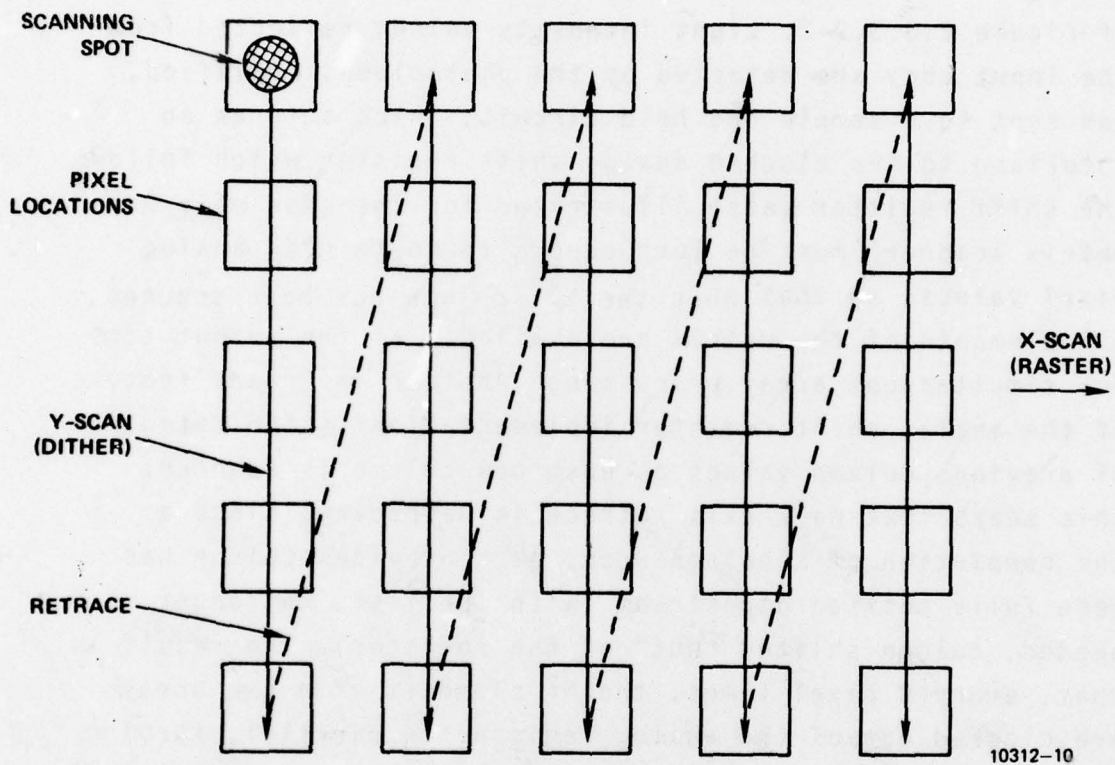
10312-10

Figure 2.3.3.2-1

Dithered Raster Scanning Pattern

53

Thus a key to the success of the dithered raster technique in array scanning is the use of an analog shift register and serial-to-parallel converter.

The operation of a dithered raster scanner with analog pixel storage is illustrated in the block diagram of Figure 2.3.3.2-2. Light intensity values reflected from the input copy are detected by the photodiode, amplified, and sent to a sample and hold circuit, which acts as an interface to the clocked analog shift register which follows. The shift register (also illustrated for the case of a 5x5 matrix scanner) must be long enough to contain N^2 analog pixel values, so that when the Nth column has been scanned, all elements of the matrix are available at the output taps for simultaneous array processing. Another important feature of the analog shift register implementation is the retention of previous column values as each new column is scanned; this means that no x-axis retrace is necessary, since at the completion of a column scan, each previous column has been fully shifted downstream (with the last, no longer needed, column shifted "out" of the register). The result is that, every N pixel times, the N^2 elements of a new array are clocked out of the analog register in parallel, forming a pseudomatrix indistinguishable from the output of a true matrix scanner.

The cost of achieving the simplicity and flexibility of dithered raster scanning comes in terms of the speed at which the components must operate. Since the pixel values are generated serially, the detector and other components must be capable of operation at the pixel rate, rather than the array rate as would be the case for a true array scanner. Note, however, that, because of the column storage

54
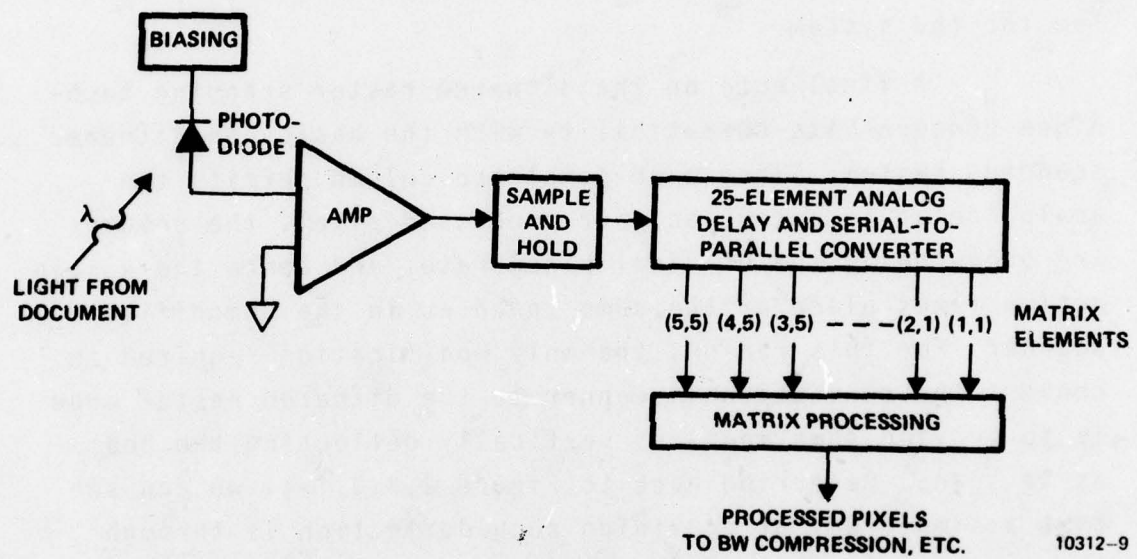
Figure 2.3.3.2-2

Matrix Formatting of Scanned Information

55

performed by the analog shift register, its rate need be
only N times the array rate (as opposed to N^2 for a non-
shifting storage device). As we shall see in the design
tradeoff analyses to follow, the high speed components re-
quired to permit the application of the dithered raster
approach to the current system goals are currently avail-.
able as standard or custom devices; thus the speed require-
ment imposed by the technique will not be a serious prob-
lem for the system.

A final note on the dithered raster scanning tech-
nique concerns its compatibility with the basic non-dithered
scanning system. Since each completed column permits the
analog delay to output another processed pixel, the columns
are produced at the original pixel rate, and hence the x-scan
action takes place at the same speed as in the unmodified
scanner. For this reason, the only modification required to
convert the conventional scanner to the dithered raster mode
is to provide some means of vertically deflecting the beam
as it scans. Referring back to Figure 2.3.3.1-1, we can see
that a simple way of providing such deflection is through
the use of the acousto-optic device. If this device is con-
figured as an acousto-optic beam deflector (AOBD), then it
can provide an angular deflection of the beam in the plane
between the two prisms; and since a Fourier relationship
exists between that plane and the film plane, the angular
deflection will produce a corresponding positional change
of the scanning beam at the film. By proper orientation of
the AOBD, we can insure that the deflections so produced
will be vertical, producing a dithering of the raster as it
sweeps horizontally across the film. Thus we have shown that
a simple modification of the grating-feedback galvanometer

scanning system can produce a dithered raster system com-
patible with the array scanning requirement but requiring
no full line buffer memory. In the paragraphs to follow, we
will investigate the tradeoffs and limitations affecting the
design of such a system, with emphasis on determining the
maximum array size feasible with currently available compo-
nents.

2.3.3.3   Key Component Tradeoffs

The optical design of the system under considera-
tion involves relatively simple components, and will not have
any impact on the system's performance; thus the performance
limitations of the system will be set by the active compo-
nents: the laser, AOBD, galvo, detector, and analog shift
register. Two of these will receive only minimal considera-
tion in the following analyses: the laser, a reliable low-
power device, will only provide a light intensity value for
use in the SNR and light budget calculations; also, the
galvo, since its requirements are identical to those in orig-
inal application (the IITS, whose goals we have adopted),
will not be considered. The remaining devices will be thor-
oughly covered, particularly in terms of their abilities to
support the necessary pixel rate, which we have seen to be
the critical factor affecting the dithered raster design
approach.

2.3.3.3.1 AOBD Tradeoffs

An acousto-optic device is a block of transparent
material (various kinds of glass or crystal, for example)
to which is bonded an electromechanical transducer. By driving

the transducer with an appropriate source of RF energy, travelling pressure waves can be created within the crystal which are capable of deflecting a light beam. This occurs because the changes in pressure in the crystal are accompanied by changes in the index of refraction, making the crystal appear to the light beam as a phase-only diffraction grating. The light diffracted from this grating can be rapidly controlled by controlling the RF input: amplitude variations can change the beam's intensity, while frequency variations can change its angle of diffraction. The latter effect is the basis of operation of an acousto-optic beam deflector (AOBD).

The design of the AOBD for the dithered raster scanner will affect the achievable performance in several key areas. The risetime of the deflector, because it represents the minimum time between pixel locations for the scanning beam, will set a limit on the system's speed. The diffraction efficiency of the device will impact the amount of input light required to provide a given SNR at the detector, and hence the system light budget and detector bandwidth trade-offs will be affected. Finally, the bandwidth of the AOBD itself, because it controls the number of resolvable spots the device can produce in a given time, will directly place an upper limit on the size of the matrix array achievable in the system.

The optical system required to produce angular deflection in the collimated beam between the two prisms is shown in Figure 2.3.3.3.1. The beam is assumed to be initially 1 mm in diameter, and is demagnified by the two input lenses to minimize the risetime in the AOBD. After
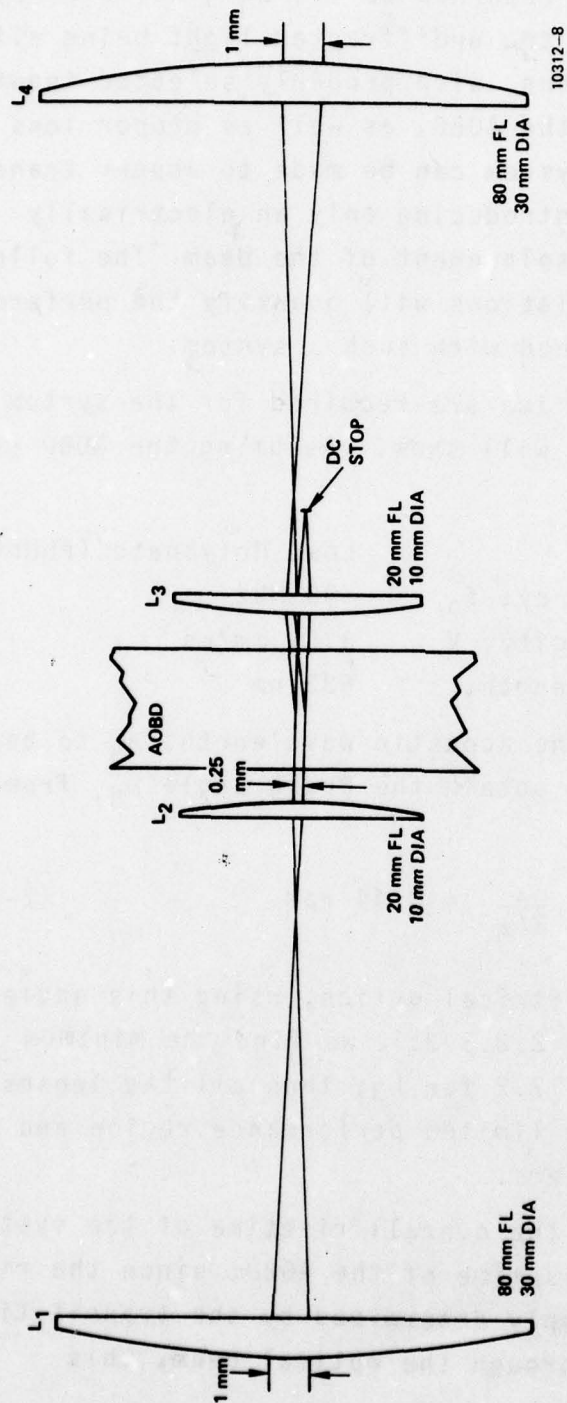
Figure 2.3.3.3.1

AOBD Optical Design

deflection, the beam is returned to its original size by the output lenses, with the undiffracted light being eliminated at a dc stop. Thus, with properly selected input and output surfaces on the AOBD, as well as proper lens positioning, the AOBD system can be made to appear transparent to the system, introducing only an electrically controllable angular displacement of the beam. The following simple design calculations will quantify the performance which may be obtained with such a system.

Optics. No critical optics are required for the system, as a simple calculation will show. Assuming the AOBD parameters are as follows

Material	Lead Molybdate ($PbMoO_3$)
Center Frequency, f_0	500 MHz
Acoustic Velocity, V	3.61 mm/μs
Optical Wavelength, λ	633 nm

then we can calculate the acoustic wavelength, Λ_A to be about 7.2 μm, and thus obtain the Bragg angle Θ_B, from the approximation

$$\Theta_B \approx \sin \Theta_B = \frac{\lambda}{2\Lambda_A} = 0.44 \text{ rad.} \qquad (2-2)$$

By straightforward geometrical optics, using this angle in the system of Figure 2.3.3.3.1, we find the minimum F# in the system to be 17.2 for L_3; thus all the lenses are used in the diffraction limited performance region and pose no optical design problems.

Risetime. To minimize the overall risetime of the system, we must minimize the risetime of the AOBD; since the risetime of the AOBD is simply determined by the transit time of the acoustic wave through the optical beam, this

means a narrow optical beam is required. However, to provide a positional deflection at the film plane, the AOBD must be located in a collimated beam, so focusing through the AOBD to minimize risetime is not an available option. As illustrated in the figure, the beam may be demagnified by about a factor of four using two lenses; for greater demagnifications, the diffraction spreading of the small beam would re-expand the beam before it reached the acousto-optic interaction region, defeating the attempt to achieve a smaller risetime in a collimated beam. Assuming a four-to-one reduction is used as illustrated, and a 20 mm distance from the second lens to the center of the crystal, the optical beam interacting with the acoustic wave will be approximately 258 μm in diameter. Therefore the minimum risetime achievable will be given by

$$T_r = \frac{258 \ \mu m}{3.61 \ \mu m/ns} \cong 71 \ ns. \tag{2-3}$$

Time-Bandwidth Product.   An additional consideration in the design of the AOBD is the bandwidth of the device. For operation in the Bragg mode (for high efficiency), the acoustic "Q" of the device should be at least 4π. Here Q is defined as

$$Q = \frac{2\pi\lambda L f_0^2}{n V^2} , \tag{2-4}$$

where L is the transducer length and n is the index of refraction. For lead molybdate and the previously specified parameters, setting Q equal to 4π gives

$$L f_0^2 = 101.3 \ \mu m(GHz)^2. \tag{2-5}$$

Then if we select a center frequency, f_o, of 500 MHz, which is near the upper limit of current standard acousto-optic practice, we get the required transducer length, L, to be 405 mm. Finally, using the relation

$$\Delta f_b = \frac{1.8 \cos\Theta_o (2\pi f_o)}{Q} \qquad (2-6)$$

We can find the 3 dB bandwidth of the device to be given by Δf_B= 450 MHz. Since the number of spots resolved by the AOBD will be equal to the time-bandwidth product, i.e., $N \le T_r \Delta f_B$, we arrive at the constraint

$$N \le (0.45) T_r, \qquad (2-7)$$

where T_r has been expressed in nanoseconds.

Diffraction Efficiency

For later use in the light budget calculations, we now determine the efficiency of the projected AOBD using the equation

$$\eta = \sin^2 \frac{\pi}{\lambda} \frac{M_2 L}{2H} , \qquad (2-8)$$

where M_2 is the figure of merit of the acoustic material (36.1×10^{15} m^2/W for lead molybdate), H is the transducer height, and 1 watt of acoustic input power has been assumed. Taking H = 250 µm to match it to the size of the optical beam, we get

$$\eta = 56\% \qquad (2-9)$$

62

Summary

The brief analyses presented above have shown
that an AOBD can be designed which can support the array
scanning/dithered raster system with risetimes as low as
71 ns and efficiencies as high as 56% per watt. Having
determined that the projected design is feasible, we now
need only check the compatibility of the achieved parameter
values with the other constraint analyses (risetimes,
light budget, etc) to follow.

2.3.3.3.2   Detector Tradeoffs

Another key component in the dithered raster
scanner is the long scan detector which receives the light
reflected from the surface of the input document. Currently,
only one device, the UDT-Pin-L9 detector, is capable of
supporting both the scan length (9 inches) and speed
requirements of the system being analyzed. Because the
system's feasibility depends on the performance of this
device, detailed analyses of its bandwidth and sensitivity
were performed, as well as some preliminary experiments to
verify the detector's performance at high speeds. The
following paragraphs summarize the results of these in-
vestigations.

Bandwidth-Noise Relationship

The nominal specifications of the PIN-L9 detector
are given by the manufacturer as

NOISE EQUIVALENT POWER (nW/ MHz)	50
BANDWIDTH (MHz)	2
INPUT CAPACITANCE, 50V BIAS (pF)	900
RESPONSIVITY (A/W)	0.3

To determine the performance to be expected of this device in practice, we must analyze it in combination with an appropriate preamplifier circuit. The model circuit chosen for analysis is shown in Figure 2.3.3.3.2-1. The detector input capacitance, C_i, has been included, as well as the transfer impedance, R, and the current and voltage noise figures of the amplifier. In this situation the primary noise sources and their values are:

NOISE SOURCE	EXPRESSION
Photodiode Noise Current	$(NEP) \times r \sqrt{B}$
Resistor Thermal Noise Current	$\sqrt{4kTB/R}$
Amplifier Noise Current	$i_n \sqrt{B}$
Amplifier Noise Voltage	$e_n \sqrt{B}$

Here, B is the bandwidth as limited by the filter, k is Boltzmann's constant, and T is the temperature in $^{\circ}$K. According to this model, the photodiode detector is seen as a current source; its impedance is a large value of resistance shunted by a capacitor. The system bandwidth is determined by the associated circuitry.

The signal-to-noise ratio may be determined by finding the equivalent noise input current of the system and comparing it with the signal current. Simple circuit analysis of the circuit in Figure 2.3.3.3.2-1 shows that the input noise current equivalent to the noise voltage of the amplifier is given by

$$i_{eq}^2 = e_n^2 \left(\frac{1}{R_i^2} + \omega^2 C_i^2 \right), \qquad (2\text{-}10)$$

64

BAND
LIMITING
FILTER

AMP

$i_n\sqrt{B}$

$e_n\sqrt{B}$

R

$(NEP)_r\sqrt{B}$

C_i

DETECTOR

BIASING
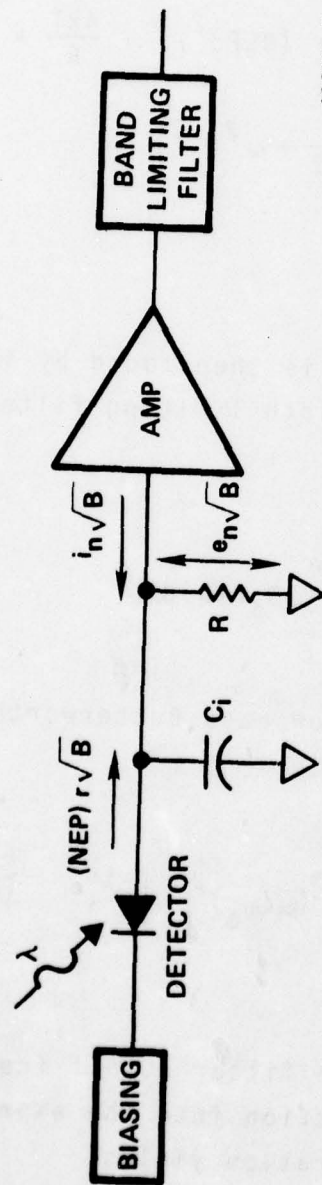
10312-7

Figure 2.3.3.3.2-1

Model Circuit for Detector Analysis

where ω is the radian frequency and R_i is the total input resistance. Then the total input noise current spectral density will be given by:

$$S_i = \frac{d(i_i^2)}{d\omega} = (NEP)^2 r^2 + \frac{4kT}{R} + i_n^2$$

$$+ e_n^2 \left(\frac{1}{R_i^2} + \omega^2 C_i^2 \right). \tag{2-11}$$

The total input noise current is then found by integrating over frequency with the bandwidth limiting filter function as a weighting factor, i.e.,

$$i_i^2 = \frac{1}{2\pi} \int_0^\infty S_i F(\omega) d\omega. \tag{2-12}$$

If the filter has an n-pole low pass Butterworth characteristic, then

$$F(\omega) = \left[1 + (\omega/\omega_0)^{2n} \right]^{-1}, \tag{2-13}$$

where $\omega_0 = 2\pi f_0$ and f_0 is the filter cutoff frequency. Substituting this filter function into the expression for i_i^2 and performing the integration yields

$$i_i^2 = \left[(NEP)^2 r^2 + \frac{4kT}{R} + i_n^2 + \frac{e_n^2}{R_i^2} + K_1 (2\pi B_n C_i e_n)^2 \right] B_n \qquad (2\text{-}14)$$

where we have defined

$$B_n \triangleq f_0 / \text{sinc}(1/2n) \quad \text{and} \quad K_1 \triangleq \left[\text{sinc}^3(1/2n) \right] / 3\text{sinc}(3/2n)$$

and

$$\text{sinc}(x) \triangleq \frac{\sin(\pi x)}{(\pi x)} \quad .$$

This final equation for e_i^2 relates the input noise current to the noise sources and the noise bandwidth.

To make this result useful for our tradeoff study, we will now assume the use of a specific device, so that the expression for i_i may be simplified. For a low-noise J-FET device of type LF-157, the following conditions hold: $e_n = 15 \times 10^{-9}$ V; $i_n = 1 \times 10^{-14}$ A; high input impedance implies that $R_i = R$. For the detector under study, we also have $C_i = 900$ pF, NEP = 50 nW MHz, r = 0.3 A/W; we will further assume that R = 1.1 kΩ. Inserting these values into the expression for i_i yields

$$i_i \simeq (2.06 \times 10^{-11}) \sqrt{B_n} \sqrt{1 + (1.69 \times 10^{-11}) K_1 B_n^2}. \qquad (2\text{-}15)$$

In this expression, the $K_1 B_n^2$ term becomes significant as B_n approaches 500 kHz; since we are interested in the high frequency performance limits, we may further simplify to obtain

$$i_i \cong (8.4 \times 10^{-17}) \sqrt{K_1} \; B_n^{3/2}. \tag{2-16}$$

Finally, if we assume the use of a 2-pole Butterworth filter, and express i_i in microamperes and B_n in Megahertz, we obtain

$$i_i \cong (0.076) \; B^{3/2}. \tag{2-17}$$

This result will be of use in a subsequent determination of the system SNR and light budget.

Detector Collection Efficiency

The light reflected from the input document propagates in all directions, and can therefore be only part-ially collected by the scan detector. The amount that can be detected is an important consideration for the system efficiency calculations to come. Therefore we will briefly consider the geometrical restrictions imposed by the detector size and limitations. Figure 2.3.3.3.2-2 shows a schematic of the PIN-L9 detector unit; the dimensions are specified by the manufacturer as L=9.0 inches, W=0.5 inches, and d=0.1 inch. Figure 2.3.3.3.2-3 is a model of the situation which will be used for calculation. To simplify the calculation, the model assumes that the detector lies on the surface of a cylinder which surrounds the scan line. From the surface of the input document, the reflected light goes into 2π steradians. Futhermore, for the worst case (as illustrated)
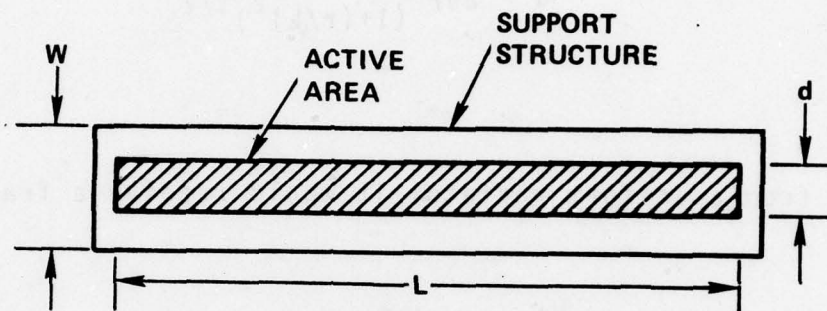
Figure 2.3.3.3.2-2

Scan Detector Geometry
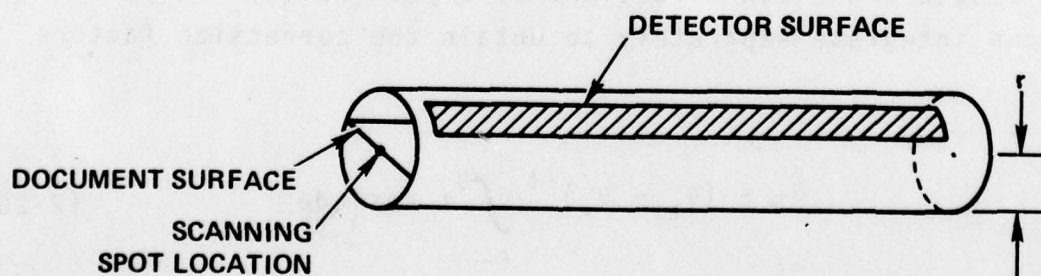
10312—6

Figure 2.3.3.3.2-3

Model for Collection Efficiency Calculation

where the scanning spot is at the end of the detector, the angular subtense of the detector as seen at the spot is

$$\Omega_d \simeq \frac{d}{2\pi r} \frac{2\pi}{(1+(r/L)^2)^{1/2}} \qquad (2\text{-}18)$$

so from a uniform radiator it would receive a fraction

$$\frac{\Omega_d}{2\pi} \simeq \frac{d/2\pi r}{(1+(r/L)^2)^{1/2}} \qquad (2\text{-}19)$$

of the light. Since the reflected light will not be uniform, but will approximately obey Lambert's Law (i.e., proportionality to the cosine of the angle from the scattered direction to the surface normal), we must add another correction factor to account for the detector's average direction. By treating the length and width directions as approximately independent, we can integrate separately to obtain the correction factors

$$C_W = (\theta_+ - \theta_-)^{-1} \int_{\theta_-}^{\theta_+} \cos\theta \, d\theta \qquad (2\text{-}20)$$

$$C_L = (\theta_L)^{-1} \int_0^{\theta_L} \cos\theta \, d\theta , \qquad (2\text{-}21)$$

70

where $\theta_{\pm} \triangleq \tan^{-1} (W \pm d/2r)$ and $\theta_L \triangleq \tan^{-1} (L/r)$. Thus the total collection efficiency is approximately

$$\eta_d \simeq \frac{1}{2\pi} \Omega_d \; C_W C_L . \tag{2-22}$$

For the PIN-L9 (UDT) detector, $W=0.5"$, $L=9"$, $d=0.1"$, and we will assume $r=0.25"$. This gives

$$\eta_d \simeq 6.1\%, \tag{2-23}$$

or with a 90% reflective paper,

$$\eta_{TOTAL} \simeq 5.5\% . \tag{2-24}$$

A final consideration is derived from experience with facsimile systems, where it has been found that the use of a mirror at each end of the scan can approximately double the collected light. Accordingly we will adopt for further calculation a final detector collection efficiency value of

$$\eta \simeq 10\%. \tag{2-25}$$

Detector Experiments

Having established that the PIN-L9 detector could theoretically support reasonably high rates of scanning, we next tested an available unit for verification of these results. The circuit shown in Figure 2.3.3.3.2-4 was used

71
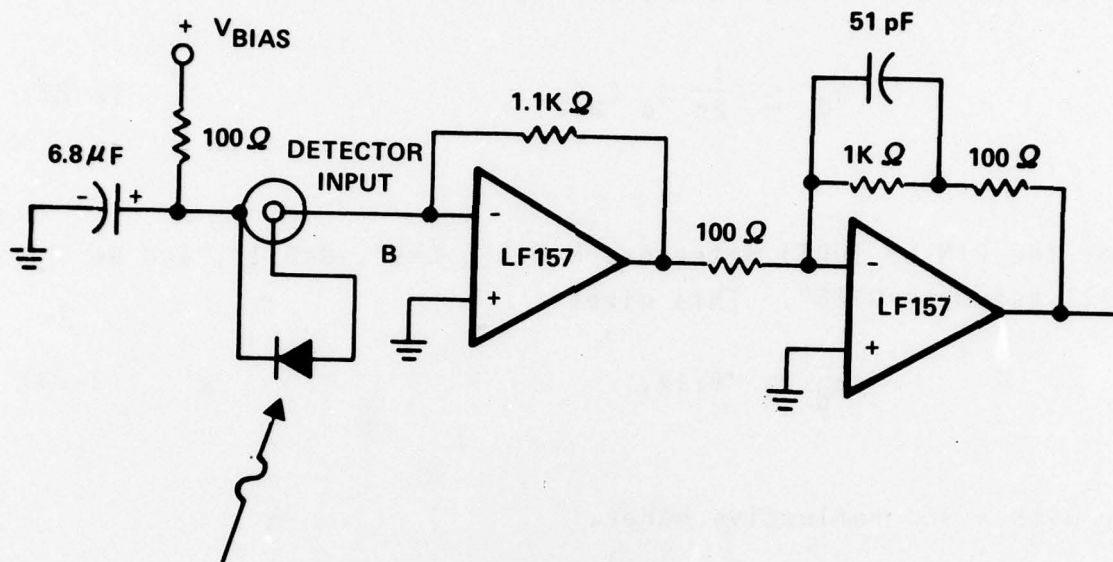
Figure 2.3.3.3.2-4

... st Circuit for PIN-L9 Detector
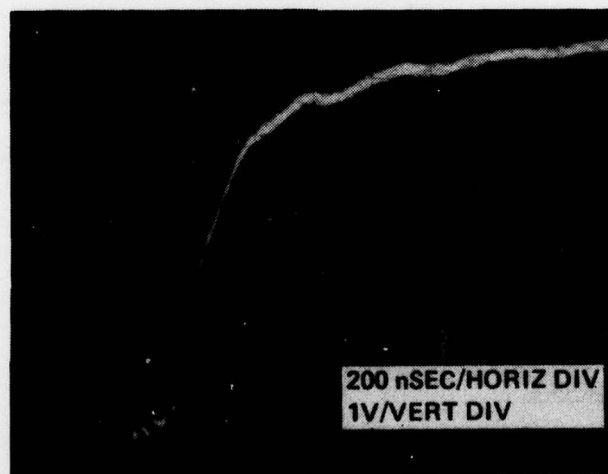
Figure 2.3.3.3.2-5

Detector Step Response

for the test; the detector was used in conjunction with a
pair of LF-157 amplifiers. For input, the detector was il-
luminated with a laser beam which was modulated by an acousto-
optic modulator. In this way the risetime of the detector
could be measured and its corresponding frequency response
calculated. The step response measured in this way is shown
in Figure 2.3.3.3.2-5. By measuring the amplitude values
shown for various time locations, a set of data was collected
for input to a Fourier transform program to determine the
frequency response. The result of this computation is shown
in Figure 2.3.3.3.2-6. The 3 dB bandwidth of the detector
is seen to be only about 700 KHz; however, the detector
response remains monotonic until about 1.1 MHz, at which
point its signal is down by about 7 dB. Thus there is hope
that a frequency-compensating filter network can be constructed
to flatten the detector response out to slightly above 1 MHz.
This experiment does indicate, however, that the detector's
specification (2 MHz) appears to be optimistic, and that a
lower value should be used for any critical system design.

2.3.3.3.3   TAD Performance

        Because it is a central element in the scanning
system, a brief examination of the performance of a currently
available tapped analog delay (TAD) device was made; this
paragraph will document both specifications and conceptual
operation of the device, as well as the results of the ex-
periments conducted with it.

        The device to be tested was the TAD-32, a
product of the Reticon Corporation, along with the associated
circuitry of the TC-32 Evaluation Circuit Card. The TAD-32
is described by Reticon as follows:

73
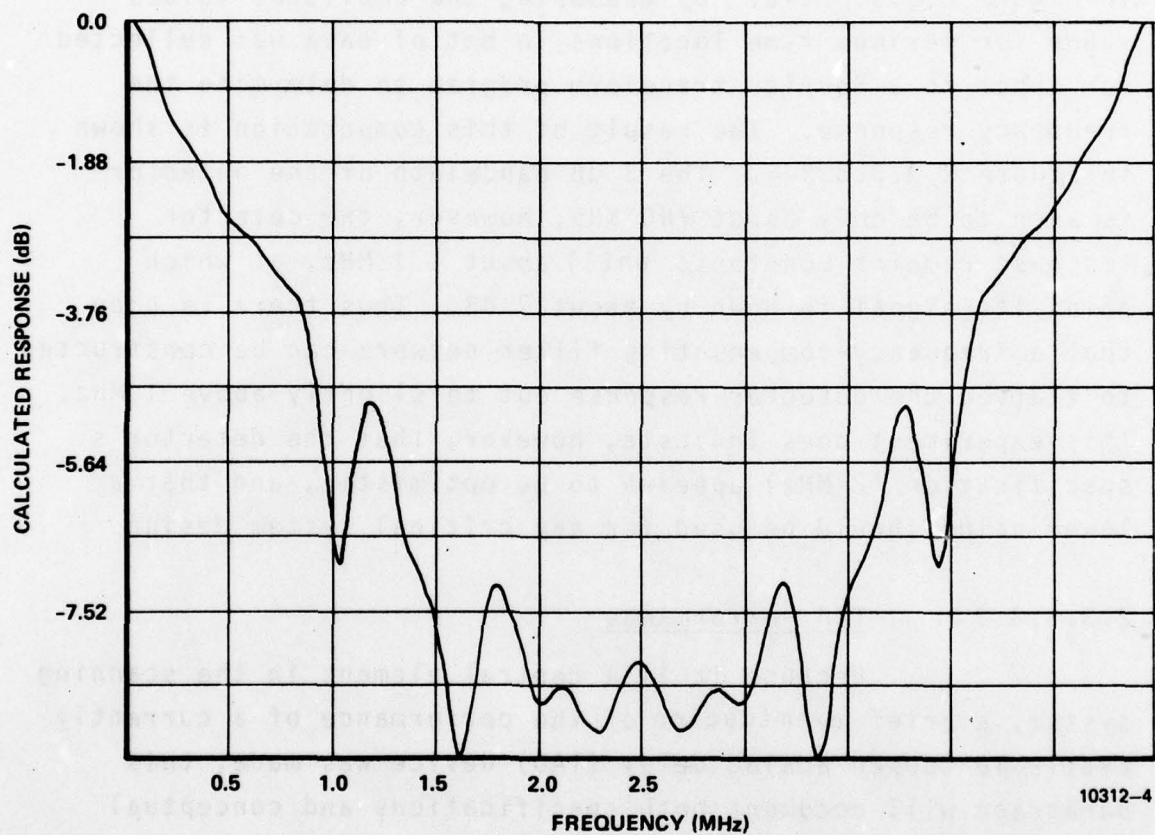
Figure 2.3.3.3.2-6

Detector Frequency Response Calculated

From Step Response

TAD-32 is a 32-stage charge-transfer device
which permits the storage of analog signals
with recovery of the signals at multiple
separate outputs at successive delay times
later. The taps on each stage are brought
to the outside through buffer amplifiers.
Each buffer amplifier output appears as a
source follower, thus permitting variable
loading of the taps in order to create various
tap-weight functions. The taps are spaced
one sample time apart along the delay. An
additional special feed-forward output tap is
provided so that multiple devices may be cas-
caded without causing discontinuity in the
spacing of the taps from one device to the
next. With this arrangement, timing integrity
is maintained. The ability to cascade devices
permits the user to build processors (such as
transversal filters) with more than 32 taps.

The device specifications (from the manufacturer's 1976
documentation) include

No. of Taps	32
Clock Frequency Range	1 KHz - 5 MHz
Max. Power Requirement	700 mW
Dynamic Range	60 dB
Sensitivity (for SNR $\simeq 1$)	4 mV p-p

Thus the TAD device appears ideally suited to the serial-in,
parallel-out shifting and weighting of analog pixel values
as required for the dithered raster scanner.

Since a TC-32 Evaluation Circuit Card (which
inlcudes all necessary support circuitry, tap weighting

resistors and switches, etc.) was available within Harris,
some brief tests were conducted to evaluate its applicability
to the array scanning requirement. The first test concerned
the key parameter of clocking speed. A video signal from a
television camera was input to the TAD-32 and its output was
fed to a standard monitor. The tap weights were adjusted
to represent various types of transversal filters (bandpass,
lowpass, etc.) and the clock rate was varied over a wide range.
The result showed good video fidelity at clock rates up to
10-15 MHz, well above the 5 MHz specification; it should be
noted, however, that the frequency response required for vis-
ually acceptable video information is considerably less than
that needed in the array scanning system; thus the accuracy
of the analog samples being shifted by the device at high clock
rates was not completely determined by this test. Neverthe-
less, since clock rates at or below the 5 MHz specification
would be required for a IITS-type array scanner, this result
is encouraging.

A second test was made of the pulse fidelity
transmitted by the device. For this test, a single pulse
was repetitively input to the device and examined as it passed
each output tap. During this test, considerable pulse dis-
persion was observed: at the 32nd tap, the pulse has lost
up to 20% of its initial voltage, while the pulses leading
and trailing the main pulse had grown to about 20% of the
initial pulse height (with the leading pulse voltage being
negative). Discussions with Reticon Corporation after this
test was completed confirmed the problem, and disclosed that
a technique of compensating for it has been published by J. J.
Brady of the Applied Research Lab at the University of Texas
at Austin. In that publication [1](ARL-TP-77-13), it was shown

76

that the use of discrete transistors to provide a low impedance
to ground at each tap could greatly reduce the pulse disper-
sion effect. An additional consideration is that the pulse
dispersion effect may be of minor importance in the array
scanning application. A computer simulation (documented
elsewhere in this report) has shown this to be the case for
a realistic choice of parameters and applications.

The performance of the TAD-32 device appears
capable of supporting the array scanning application in
many important cases. An additional important fact is that,
for non-adjustable filter applications, analog delay lines/
transversal filters have been constructed (by Reticon and
others) with as many as 512 stages, indicating that pulse
dispersion and other problems can indeed be made negligible
in custom devices. In summary, the TAD appears to be a
viable component for inclusion in the dithered raster scanning
system described above.

2.3.3.3.4   Light Budget and SNR

With estimates of the efficiencies of the
various active components in the system now complete, we
are in a position to evaluate the ability of the system to
produce an acceptable SNR for a given amount of input light.
Since the scanning system is identical to that of the IITS
system (except for the replacement of the AOM by the AOBD),
we will adopt and modify the original light budget calculation,
reproduced in Table 2.3.3.3.4. Replacing the AOM efficiency
(65%) with the AOBD efficiency, η, and assuming a 5 mW laser
source, we find approximately that the light expected at the
detector, I, is given by

$$I = \begin{pmatrix} \text{detector} \\ \text{collection} \\ \text{efficiency} \end{pmatrix} \times (\eta) \times (2.5 \text{ milliwatts}) \qquad (2\text{-}26)$$

77

Table 2.3.3.3.4. Detailed Light Budget

Exposing Beam

Optical Element	Efficiency Percent
BS Prism Surface 1	0.998
BS Prism Surface 2	0.85
BS Prism Surface 3	0.998
AOM (includes reflection losses)	0.65
Folding Prism Surface 1	0.96
Folding Prism Surface 2	0.998
Telescope: Lens 1	0.98
Telescope: Lens 2	0.98
Galvo Mirror	0.90
Flat Field Lens	0.96
Transmission and Truncation	0.80
Total	0.35
Available exposing power (5 mW Laser)	1.76 mW

Grating Beam

Optical Element	Efficiency Percent
BS Prism Surface 1	0.998
BS Prism Surface 2	0.15
BS Prism Surface 3	0.998
Folding Prism Surface 1	0.998
Folding Prism Surface 2	0.998
Telescope: Lens 1	0.98
Telescope: Lens 2	0.98
Galvo Mirror	0.90
Flat Field Lens	0.96
Fold Mirror	0.99
Transmission and Truncation	0.80
Total	0.10
Available grating beam power (5 mW Laser)	0.50 mW

Modulation Feedback Detector

	Efficiency Percent
BS Prism Surface 1	0.998
BS Prism Surface 2	0.85
BS Prism Surface 3	0.998
AOM (includes reflection loss)	0.65
Folding Prism Surface 1	0.04
Transmission and Truncation	0.80
Total	0.02
Available Power (5 mW Laser)	0.09 mW

78

so with a collection efficiency of 10%, we get

$$I = 250\eta \; \mu W. \tag{2-27}$$

From the previous AOBD calculations we have

$$\eta = \sin^2\left\{ \frac{\pi}{\lambda} \sqrt{\frac{M_2 L}{2H}} \right\}; \tag{2-28}$$

thus using the values $\lambda = 633$ nm, $V = 3.61$ mm/μs, $L = 0.405$ mm, $M_2 = 36.1 \times 10^{15}$ m^2/W, $H = VT_r$, we get

$$\eta = \sin^2\left\{ \frac{7.0197}{\sqrt{T_r}} \right\}. \tag{2-29}$$

Thus, for a silicon detector with a responsivity of 0.3 A/W, the expected signal current is

$$i_s = (0.3)I = 75 \sin^2\left(\frac{7.0197}{\sqrt{T_r}} \right) \mu A. \tag{2-30}$$

As shown in the detector analysis above, for a PIN-L9 photodetector in conjunction with an LF-157 amplifier and a 2-pole Butterworth filter, the expected noise current for wideband operation is given by

$$i_n \simeq \left(B^{3/2} \right)/13.2,$$

79

where B is the bandwidth of the external filter. Therefore the current SNR is

$$\text{SNR} = i_s/i_n = (B^{-3/2})990 \sin^2(7.0197/\sqrt{T_r}). \qquad (2\text{-}32)$$

The (arbitrarily selected) SNR requirement for the system is 35 dB, which implies a current ratio of 56.2. If we increase this to 60 to allow some margin, we can find the bandwidth/ risetime relationship from the above equation, i.e.,

$$B = \left| 16.5 \sin^2(7.0197/\sqrt{T_r}) \right|^{2/3} \text{ MHz}. \qquad (2\text{-}33)$$

Thus, finally, the risetime of the detector circuit can be related to the AOBD risetime using

$$T_d = 350 \left| 16.5 \sin^2(7.0197/\sqrt{T_r}) \right|^{-2/3} \text{ ns}. \qquad (2\text{-}34)$$

This value can now be used in the overall system risetime calculation.

2.3.3.3.5 Risetimes

Within each pixel time, T_p, must be included the risetimes of all the active components; this includes the AOBD risetime, T_r, the detector risetime, T_d, and the sample/hold risetime $T_{s/h}$. We will assume that these rise-times can be combined in a root-sum-square way, via the inequality

$$T_p^2 \geq T_r^2 + T_d^2 + T_{s/h}^2. \tag{2-35}$$

The pixel time, T_p, is derived from the IITS system require-ments as follows. Within one 13.5 ms scan time, 3,456 pixel columns must be completed. For an N x N matrix array scanner, each column will contain N pixels. Thus the pixel time is

$$T_p = \frac{13.5 \text{ ms}}{3456 \, N} = \frac{3.906 \, \mu s}{N} . \tag{2-36}$$

Now, if we substitute for T_p, T_d, and $T_{s/h}$ in the above in-equality, we get the constraint

$$N \leq 3906 \left\{ (35)^2 + T_r^2 + (350)^2 \left[16.5 \, \sin^2 \left(\frac{7.0197}{\sqrt{T_r}} \right) \right]^{-4/3} \right\}^{-1/2} \tag{2-37}$$

where we have used for $T_{s/h}$ the value of 35 ns, which is typical of currently available devices, It should be noted that this constraint inequality was derived under the as-sumption that the maximum theoretical bandwidth, as given in the previous sections, could be used. We have seen experimen-tally, however, that compensation of the detector under con-sideration for use at very high bandwidths (above 1 MHz) will be a difficult task. Therefore, it is also useful to state the risetime constraint as it would appear if we achieve not the maximum bandwidth, but some lower value, B (MHz). In that case, the constraint is simply

$$N \leq 3906 \left[(35)^2 + T_r^2 + (350/B)^2 \right]^{-1/2}. \qquad (2\text{-}38)$$

It should be noted also that T_r as used in these inequalities is the AOBD transit time only when a random-access type scanning is being done; however, this is appropriate to the current scanner provided that, to simplify the analog sample delay line process, we require that all pixels be generated at regular time intervals (as opposed to burst-and-wait type sampling).

The constraint of equation (2-38) can now be used to define the sizes of matrix arrays which the dithered raster technique as described above can support. This will be done by way of the constraint summary graph presented in the following section.

2.3.3.4 Constraint Summary

Four basic constraints on the feasible size of the matrix array in the dithered raster scanner can be defined. The first and simplest, the matrix constraint, can be expressed as $N \geq 3$, and results from the desire to have an odd-edged square array to preserve the uniqueness of the central point. Second is the optics constraint: to produce beam deflection at the film, the AOBD must be in a Fourier plane of the scanning spot, and thus its input beam cannot be focused to minimize risetime; with 20 mm between AOBD and input lens, the minimum beam diameter (due to Gaussian beam diffraction) is 180 μm (50 ns risetime); restriction to 71 ns keeps the required optical F#'s reasonable, thus $T_r \geq 71$ ns. Third is the AOBD design constraint, which arises from the time-band-width product of the device; with a state-of-the-art bandwidth of 450 MHz, this produces the relation $N \leq 0.45\, T_r$.

82

Finally, the detector speed and SNR constraint as derived above requires $N \leq 3906 \left[(35)^2 + T_r^2 + (350/B)^2 \right]^{-1/2}$. With plenty of optical power available to achieve the required SNR, the goal is to trade it for detector bandwidth (and hence, risetime). The result is a coupling of system risetime, detector bandwidth and SNR.

The constraints above have been derived in terms of the AOBD risetime, T_r, so that it may act as a common parameter against which the array size may be plotted. The result of this is shown in Figure 2.3.3.4. The upper curved line is the risetime constraint obtained when it is assumed that the detector response can be equalized out to the maximum bandwidth for which the SNR is adequate. The lower curves are based on constant bandwidth values lower than the maximum (and hence these curves describe increasing SNR as T_r increases). Because of the experimental performance of the PIN-L9 detector, the maximum bandwidth curve is not likely. As a more practical upper bound, a bandwidth of 1 MHz seems readily achievable, and 1.6 MHz should be attainable with proper detector selection and compensation. From this we may conclude that array sizes up to 11 x 11 are definitely feasible and that arrays up to 17 x 17 are conceivable with careful design. Thus, the dithered raster system with analog shift register can support, at adequate speed, SNR, and resolution levels, all but the largest of array scanning requirements, and this can be done with only relatively minor modification to the proven scanning system concept as exemplified in the (proposed) IITS system.
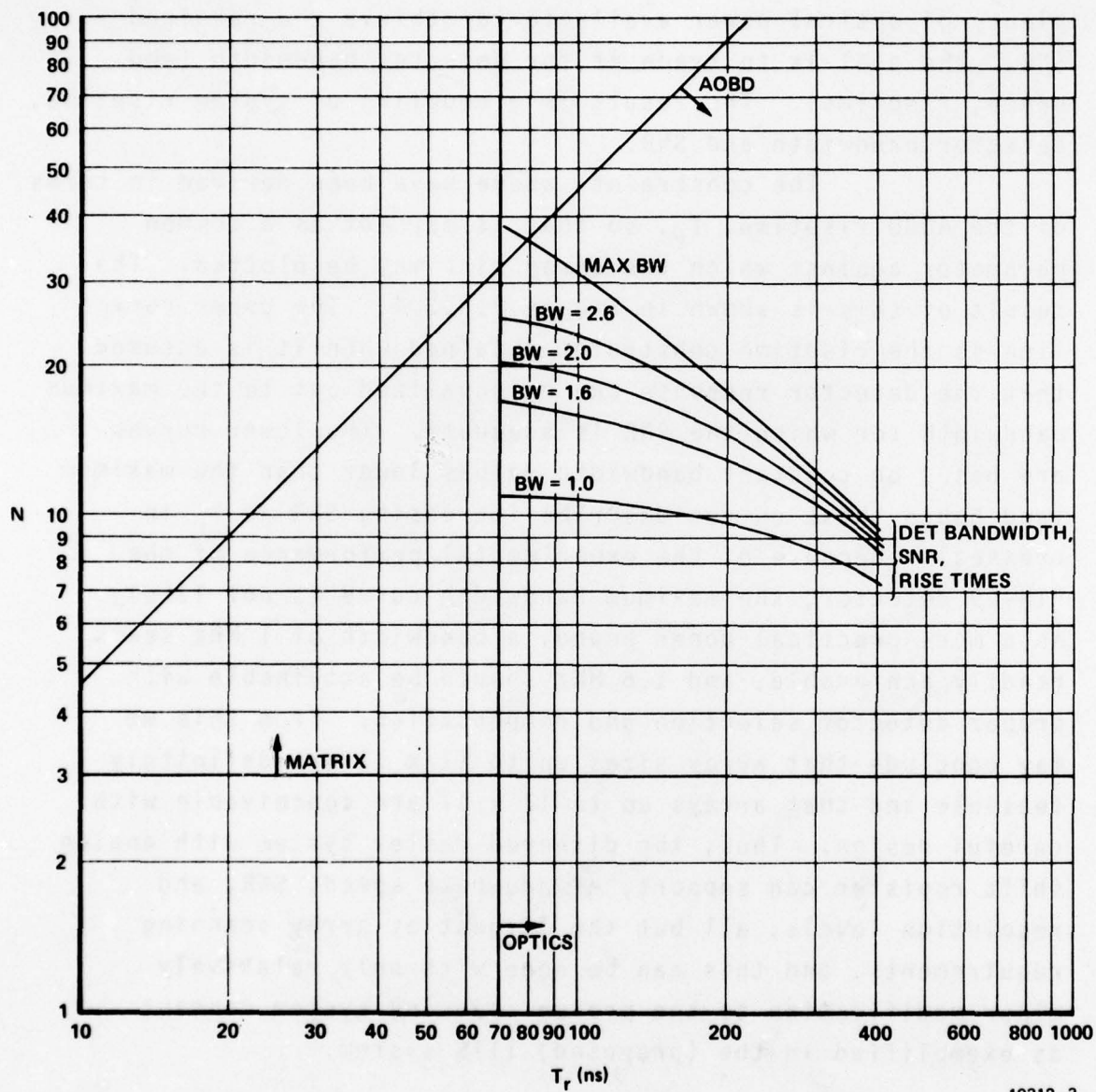
Figure 2.3.3.4

Array Size Constraint Summary

84

2.4   ALTERNATIVE APPROACHES

During the investigation of the dithered raster
array scanner described above, several additional approaches
to the specific problem addressed in section 2.3 were iden-
tified which show promise for future study. Although not
examined thoroughly to this point, these approaches appear
to have some advantages (and disadvantages) with respect to
the main system concept which would make them particularly
useful in some system scenarios. We will now briefly document
two of these approaches.

2.4.1   Weighted Linear Array with Column Memory

In the main system of Paragraph 2.3, the scanning
was done by a single, dithered beam, with the pixel values
of each column of the array being stored in the tapped
analog delay line for later parallel processing. The price
paid for the design simplicity of that system was the high
speed required to generate serially the N^2 pixels of the
array. A more complex, but potentially much faster, tech-
nique involves the scanning of multiple beams in a linear
array. If true array scanning is employed, both the input
array and the detector array (required to separately detect
each channel) are complex devices; however, an interesting
alternative is made possible by the use of the tapped
analog delay: linear array scanning with a single detector.
In this case (see Figure 2.4.1-1), a linear array of spots
from a multi-element source, such as an acousto-optic page
composer, is scanned across the page. The scattered light
from all the spots is collected into a single detector,
which produces a summation process. If the pixel weights

COLUMN
ARRAY OF
SCANNING
SPOTS

SCANNED
DOCUMENT

SCAN
DIRECTION

LIGHT
FROM SPOTS
IN COLUMN
STRIKES
DETECTOR

TO ELECTRONICS

SCAN DETECTOR

LINEAR
ARRAY
SOURCE
IN
OPTICAL
SYSTEM

MULTIBEAM
ILLUMINATION

10312–2
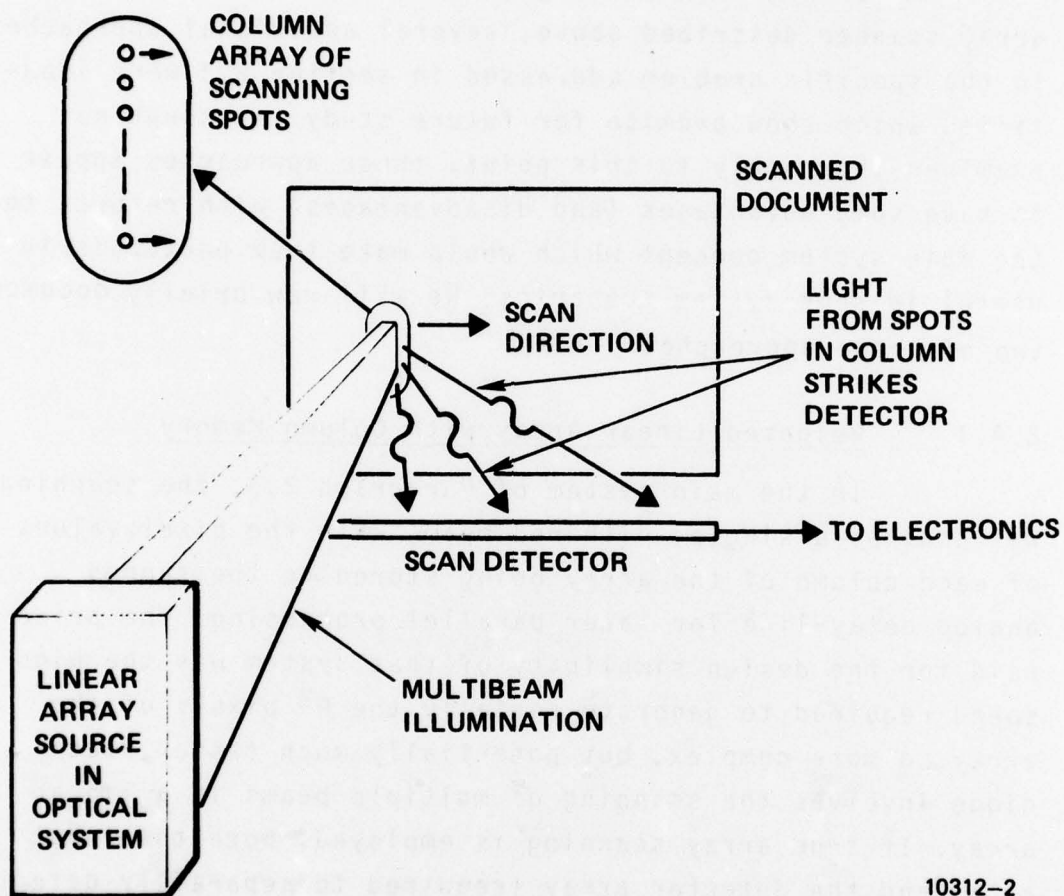
Figure 2.4.1-1

Array Scanning With Single Scan Detector

(document reflectances) are called the a_{ij}, then the detector would generate for each column the sum

$$S_i = \sum_i a_{ij}c_i, \qquad (2\text{-}39)$$

where the c_i are intensity weighting coefficients assigned to the input beams according to the desired MTF response in the vertical direction. After detection, the succession of weighted column sums would be stored in a TAD to permit weighting of the columns via the external resistors. This situation is depicted schematically in Figure 2.4.1-2. Also indicated is the use of two TADs with a 1 pixel delay between them, whose outputs are later subtracted; the purpose of this is to allow for the use of negative weights on the column values, which is not possible with the simple optical detection scheme. By assigning weights c_j to the TAD taps, the summation would generate finally

$$S_2 = \sum_j \sum_i c_i c_j a_{ij}, \qquad (2\text{-}40)$$

which is the desired weighted array value to be assigned to the transmitted pixel. It will be observed that this scheme somewhat restricts the class of filter functions available to the array processor; specifically, since the rows and columns are weighted separately, only separable filter functions of the type $f(x,y) = f_1(x)f_2(y)$ can be realized. However, this should be only a minor problem for large matrices, and is in fact exactly what is needed for certain important image processing tasks.

The chief advantage of this technique is that it can support higher system speeds because of its generation of N pixel values simultaneously in column form. Thus both

87
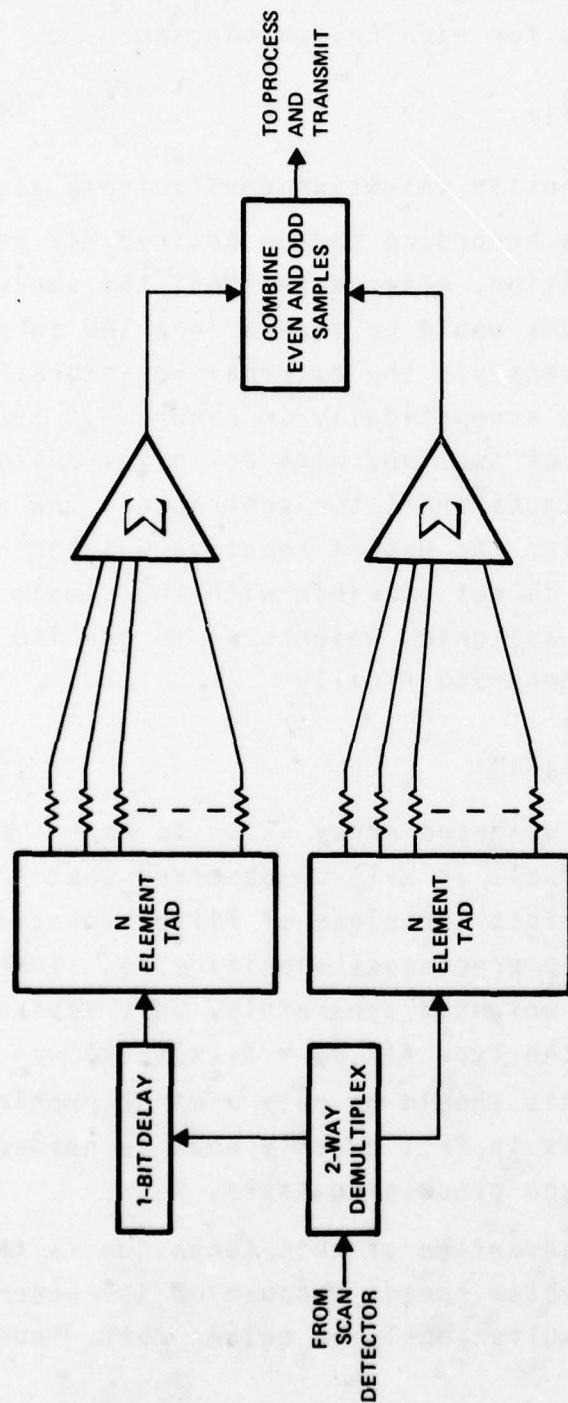
10312-17

Figure 2.4.1-2

Column Storage And Processing Via TAD Devices

the detector and the TAD are operated N times slower for a given array size than was required in the previous system. The need for an AOBD has been eliminated, but it has been replaced by another complex device, the acousto-optic page composer(AOPC) which generates the multichannel scanning beam. However, current AOPC designs are easily capable of supporting the required rates and array sizes. In summary, the weighted linear array scanner appears to provide a good compromise design, combining the speed advantages of a multichannel input device with the simplicity and flexibility of a single channel output device and analog storage register.

2.4.2 Optical Convolution System

One of the potential drawbacks of systems based on the use of the TAD is the pulse dispersion problem discussed in Paragraph 2.3.3.3.3. Although some techniques have been found which appear to eliminate the dispersion, an approach not using this device would provide added confidence in the viability of array scanning systems. Such a system is detailed in the optical schematic of Figure 2.4.2. The input to this system is assumed to be the same as that described for the dithered raster system in Paragraph 2.3.3.2; i.e., the serial pixel values from each N pixel column across the scan. In the new approach, the TAD has been replaced by an acousto-optic delay line; after modulation onto an RF carrier, the pixel values are used to drive the transducer of an acousto-optic device. Because of the finite propagation time of the acoustic waves down the crystal, many values can be present in the crystal simultaneously. When the N^2 pixel values representing an array to be processed are present in
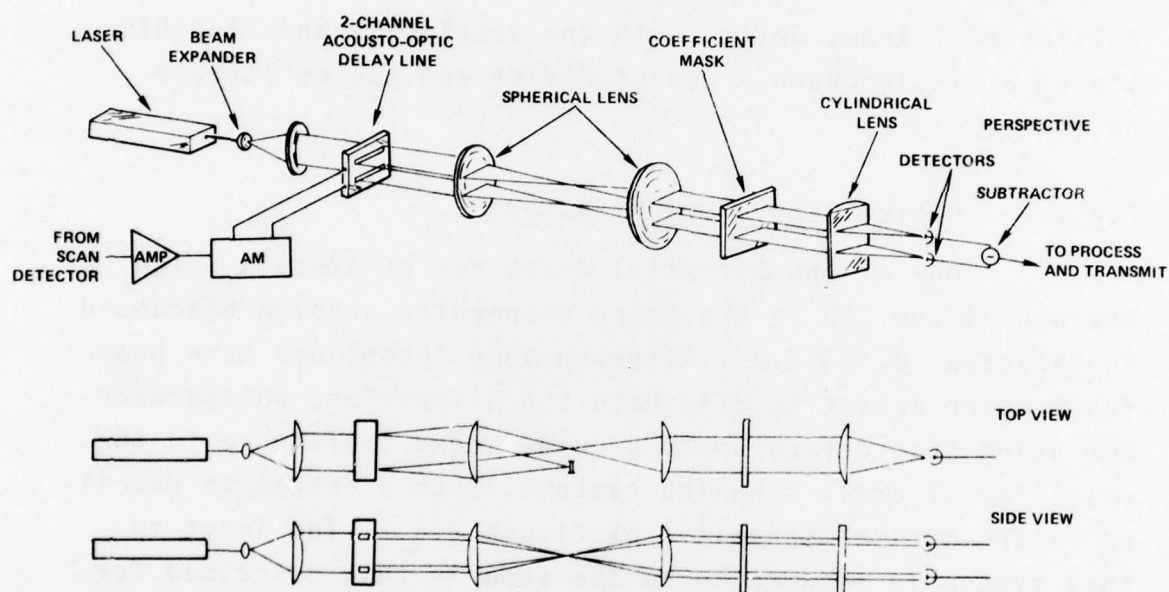
Figure 2.4.2
Convolutional System For Temporal
Transversal Filtering

90

the crystal (and hence in the light exiting the crystal),
they are imaged onto a coefficient mask where each is
effectively multiplied (weighted) by the local transmit-
tance of the mask. Then the weighted values are collected
and summed in a single detector. As in the previous sys-
tem, to obtain negative weights, we perform the above·pro-
cedure in two channels, using one channel of the mask to
provide the positive weights and the other the negative
weights. The two channels are then electrically subtracted
to produce the processed output.

The key tradeoff of a system of this type is the
capacity of the accusto-optic delay line. For practical
acousto-optic materials, the minimum acoustic velocity is
about 0.6 mm/μs. Also, a maximum practical crystal length
of about 60 mm is currently available. Thus about 100 μs of
delay can be achieved, which limits the storage in an AO
delay channel to about 100 times the pixel time (e.g., at
1 Mp/s, to $N \leq 100$). For the IITS requirements, this would
restrict the array size to around 11x11 when full data link
rates are needed. Other systems, however, may have re-
quirements which make this technique compatible with larger
arrays. Another potential method of achieving larger arrays
is to increase the number of channels in the AO delay de-
vice. For example, a very feasible device of only 8 chan-
nels would support array sizes up to around 19x19 even at
the IITS speed and resolution values. In summary, a system
based on optical convolution can provide most of the advan-
tages of the previous systems while eliminating the need
for the TAD device.

3.0 ARRAY RECORDING

In the following paragraphs we analyze the operating parameters of several techniques suitable for array recording. The five techniques that have been identified are two approaches to multifrequency acousto-optic beam deflector (AOBD) recording, scanned AOBD recording, multitransducer acousto-optic page composer (AOPC), and LED array recording.

The two major motivations for array recording are (i) the ability to record block-encoded data without the requirement for large buffers and (ii) speed. Scanning and recording systems generally are required to be capstan-driven raster systems rather than drum devices except in those circumstances permitting the inconvenience of drum systems. A galvanometer reflector, typically used for the raster deflection, is limited to about 500 K pels/s (or 40 seconds to record a 9" x 9" image at 500 pel/in). By simultaneously recording N lines for each galvanometer sweep the recording time can be reduced by 1/N.

3.1 AOBD MULTIFREQUENCY RECORDING

An acousto-optic beam reflector is most commonly used as a spot scanner, a mode to be discussed in the next paragraph, by inducing into the acoustic medium a single, but changing, frequency. An alternate mode is to drive the AOBD with a multiplicity of frequencies, individually modulated so that a block of N pixels in the image plane can be recorded in parallel. In principle this can be accomplished in two ways. These are briefly described below separately to enumerate their individual characteristics. The data rate and block size analysis that follows applies to both multifrequency approaches.

3.1.1 Multiple Oscillator Technique

Figure 3.1.1(a) illustrates the basic approach, in which N discrete frequencies, derived from N oscillators or in any other manner, but where the frequencies are equally spaced, are individually modulated according to the values of the N pixels in the array to be recorded. These signals are added together and mixed with a carrier to drive an AOBD. A lens forms an optical Fourier transform of the N optical waves diffracted from the AOBD cell. The resulting intensity pattern corresponds to the desired array pattern to be recorded. The chief attraction of this technique is the requirement for only one acousto-optic device; no separate modulator is needed. Another advantage, as we will see later, is that higher data rates and larger array block sizes are attainable compared with the AOBD spot scanning techniques. The chief difficulty is the implementation of the array of frequencies, most particularly when the array is large. Another problem is that at very high data rates pixel-to-pixel distortions arise from the coherent addition of the randomly phased pixel amplitudes in the overlap areas. At lower data rates the difference in the frequencies causes the coherent effects to wash out, leaving the incoherently added intensity patterns. However, another source of distortion is the intermodulation terms associated with the diffraction of light from a complex phase-modulated grating, such as an AOBD. This can force the requirement to limit the diffraction efficiency of the device to 10% or less, in order to adequately suppress these distortions. The optical efficiency of the system is thus affected and influences in turn the size of the laser required for the system.

3.1.2 Fourier Transform AOBD

An approach to multifrequency recording that requires only the carrier oscillator is sketched in Figure 3.1.1(b), where the
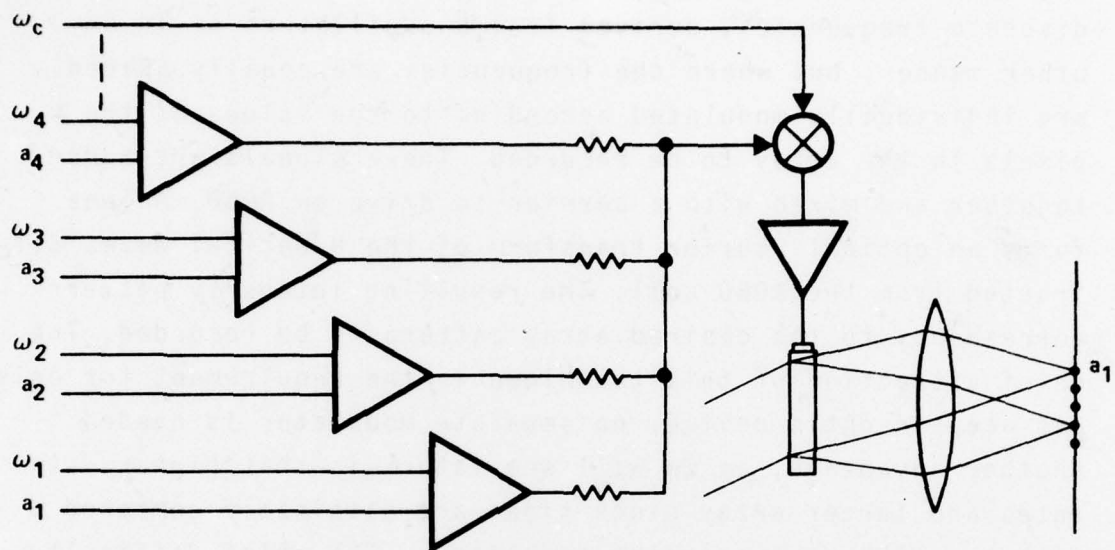
a. MULTIPLE FREQUENCY
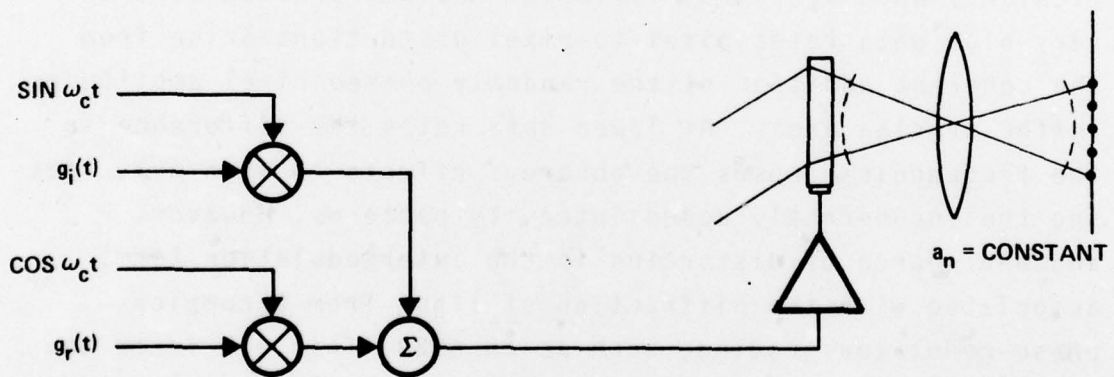
b. CHIRP FOURIER TRANSFORM

10304-1

Figure 3.1.1
Multifrequency Techniques

94

real and imaginary parts of the Fourier transform of the pixel
array are mixed, respectively with $\cos \omega_c t$ and $\sin \omega_c t$ which
are then added to drive the AOBD. A lens performs an optical
transform to reconstruct the pixel array. The original pixel
values, however, must be weighted by a unit modulus complex
amplitude with a quadratically changing phase. The reason for
this is that the Fourier transform of an array of real constant
pixel values has a strong spike at zero frequency and smaller
amplitude structure at higher frequencies. This would result in
an acoustical wave traveling through the AOBD such that most of
the energy was contained in a narrow pulse. This concentration
of power makes extremely inefficient use of the dynamic range
of the acousto-optic medium and results in low optical effic-
iency and severe nonlinearities.

Figure 3.1.2 contains a simplified block diagram of a
possible system configuration. As it is shown here the mode
of operation is that of high speed multichannel recording
without block processing. The scanner and recorder are both
included to illustrate overall signal train. Linear array
scanned data is log companded for human visual response
correction, converted to digital form, corrected for the
recording medium nonlinear D-log E response, and raised to
the ½ power to correct for square law recording. At this
point we still have real positive pixel values, so that a
chirp spread spccturm cosine transform is generated and trans-
mitted. If $a(n)$ are the corrected pixel values

$$g_r(m) = \sum_{n=1}^{N} a(n) \cos (\pi n^2/N) \cos (2\pi nm/N)$$

$$g_i(m) = \sum_{n=1}^{N} a(n) \sin (\pi n^2/N) \cos (2\pi nm/N)$$

(3-1)
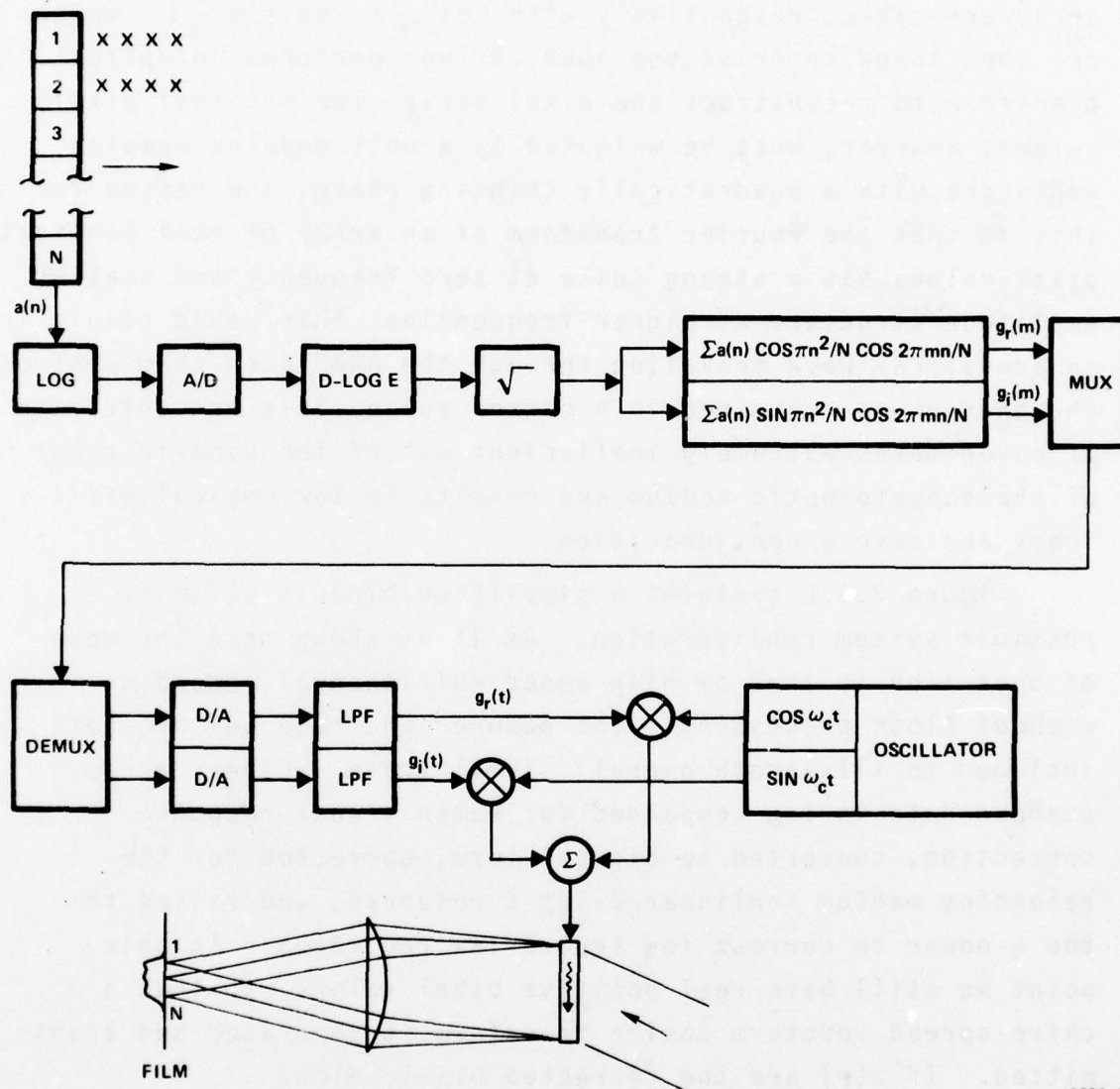
Figure 3.1.2
Acousto-Optic Fourier Transform Array Recording

In the receiver the two components of the signal are converted to analog form with appropriate interpolation smoothing with low-pass filters having frequency response q(f) and impulse response p(t) to yield

$$g_r(t) = \sum_m g_r(m) \, p(t-mT_o)$$

$$g_i(t) = \sum_m g_i(m) \, p(t-mT_o) .$$

(3-2)

The signal driving the AOBD is

$$s(t) = g_r(t) \cos \omega_c t + g_i(t) \sin \omega_c t$$

(3-3)

The refractive index of the acoustic medium is

$$n = n_o \, S(t-x/v)$$

$$= n_o \sum_{m,n} a(n) \cos (2\pi mn/N) \cos \left[\pi n^2/N + \omega_c (x-vt)/v \right]$$

$$\times p \left[(x/v) - t + mT_o \right] , \quad (3-4)$$

where we have used Equations 3-1, 3-2, and 3-3 and some manipulation. We will take that part of Equation 3-4 corresponding to one diffraction order to describe the diffracted light amplitude (assuming offset incident reference wave exp $(-ik_c x)$,

97

$$A(x) = A_o e^{ik_c x} \sum_{m,n} a(n) \cos 2\pi mn/N$$

$$\times e^{-i\pi n^2/N - i\omega_c(x-vt)/v} p\left[(x/v)-t+mT_o\right].$$

The amplitude in the image plane is

$$B(k) = \int A(x) e^{ikx} dx$$

$$= cA_o \sum_{m,n} a(n) \cos 2\pi mn/N$$

$$\times e^{-i\pi n^2/N} e^{ik_c vt + ik(vt - mT_o v)} q(k)$$

$$= cA_o e^{i(k_c+k)vt} \sum_n a(n) e^{i\left[\pi n^2/N + 2\pi(n/N) - kvT_o\right]}.$$

$$\times \frac{\sin\left[(NkvT_o/2)+\pi n\right]}{\sin\left[(NkvT_o/2)+\pi n\right]/N}$$

$$\approx c'A e^{i\phi_o(t)} \sum_n a(n) e^{i\left[\pi n^2/N + 2\pi(n/N) - kvT_o\right]}$$

$$\times \mathrm{sinc}\left[(NkvT_o/2)+\pi n)\right]$$

$$= c'A e^{i\phi_o(t)} a(kD/2\pi) e^{i\left[\pi(kDN/2\pi)^2/N\right]}$$

where we have optically selected only positive k.

The exposure in the image plane is

$$\left|B(k)\right|^2 = K\left|q(k)\right|^2 \left|a(kD/2\pi)\right|^2,$$

98

which is the desired result, since the low-pass response $q(k)$ can be made flat over the array field.

This technique, like the previous multifrequency technique, requires only a single acousto-optic device and has wider bandwidth capability than the scanned AOBD technique. It has the additional advantage that the chirp spectrum spreading permits higher optical efficiency with lower phase distortion, especially at high data rates. For variable recording speeds, coefficients would have to be stored in a temporary memory device and clocked out at a fixed rate. Only the input rate to this memory device would vary. A question yet to be dealt with is the proper technique for pixel leveling; a precise control for this is necessary to avoid raster banding in the recorded copy, to be discussed later. Pixel leveling, required to compensate for variations in diffraction efficiency, for example, from pixel-to-pixel, must be carefully dealt with in any array scanning or recording system.

3.1.3 Data Rate Analysis

In analyzing the operational characteristics of a multi-frequency AOBD we will use the following quantities:

v_a	acoustic velocity
D	optical aperture of the AOBD
λ	optical wavelength
Λ	acoustical wavelength at the center of the band

$T = D/v_a$	acoustic transit time
f_c	center frequency
Δf	signal bandwidth
f_s	sampling frequency in raster direction
N	number of pixels in array
Θ	acoustic divergence
d	transducer width (optical-acoustical interaction distance)
Γ	acoustic attenuation coefficient
n	refractive index of material

Acoustic Divergence Limits

The number of resolvable elements of an AOBD is given by the product of the bandwidth Δf of the device and the transit time D/v_a. Therefore, the resolution increases with the length and bandwidth of the device. However, as the frequency range is extended several factors combine to limit the usable optical aperture. First, higher frequencies imply shorter acoustic wavelengths, and therefore, if the thickness of the acoustic grating remains constant, a more constrained angular range of diffraction is permitted by the Bragg effect. Thus the grating thickness is made smaller (by decreasing the size of the transducer) to maintain a constant fractional bandwidth $\Delta f/f_c$; in other words, the Q value is made constant, where

$$Q = \frac{2\pi d\lambda}{n\Lambda^2} \tag{3-5}$$

100

However, as the transducer gets smaller the divergence of the acoustic wave increases as

$$\Theta = \Lambda/d \tag{3-6}$$

The wave envelope spreading is usually acceptable up to the point where

$$D\Theta \leq d, \tag{3-7}$$

beyond which the wave begins to spread rapidly and the Bragg properties deviate significantly from the desired behavior. From Eqs. 3-6 and 3-7

$$D \leq \frac{d^2}{\Lambda} \tag{3-8}$$

Combining Eq. 3-8 and Eq. 3-5 and noting that

$$v_a = f_c \Lambda,$$

and

$$D = v_a/f_s = Nv_a/\Delta f, \tag{3-9}$$

we find

$$N \leq \frac{1}{3}\left(\frac{Qnv_a}{6\pi\lambda}\right)^2 \frac{1}{(\Delta f)^2}, \tag{3-10}$$

where we have taken a fractional bandwidth $\Delta f/f_c = \frac{1}{3}$, a mildly conservative constraint to ensure no more than about 3 dB loss at the band edges.

Attenuation Limits

The attenuation coefficient for acousto-optic materials is proportional to some power m of frequency, generally between one and two, depending on the material. If the acoustic wave is permitted to decay 3 dB, we have

$$\Gamma f_{max}^m \, D \leq 3dB \qquad\qquad (3-11)$$

Since $f_{max} = f_c + \Delta f = (\frac{7}{2})\Delta f$, then, using Eq. 3-7,

$$N \leq \left(\frac{2}{7}\right)^2 \frac{3}{\Gamma v_a (\Delta f)^{m-1}} \qquad\qquad (3-12)$$

$Te O_2$, $PbMoO_4$, SF-8 glass, SF-59 glass and Te glass have [5, 6, 7, 8], respectively, m = 2, 2, 1.4, 1.25, and 1.32. The limits for these materials have been plotted in Figure 3.1.3 along with the divergence limits of Equation 3-10. Also plotted are the N vs. Δf lines for values of f_s and AOBD size.

3.2 AOBD SCANNED RECORDING

In its normal mode of operation an acousto-optic beam deflector is driven by a linear frequency ramp (or chirp), which induces a sound wave with changing frequency to propagate through the acousto-optical medium. The frequency of the acoustic wave at any instant determines the angle at which the incident laser beam is diffracted, and therefore, the position of the focused spot. A periodic chirp drive, therefore, results
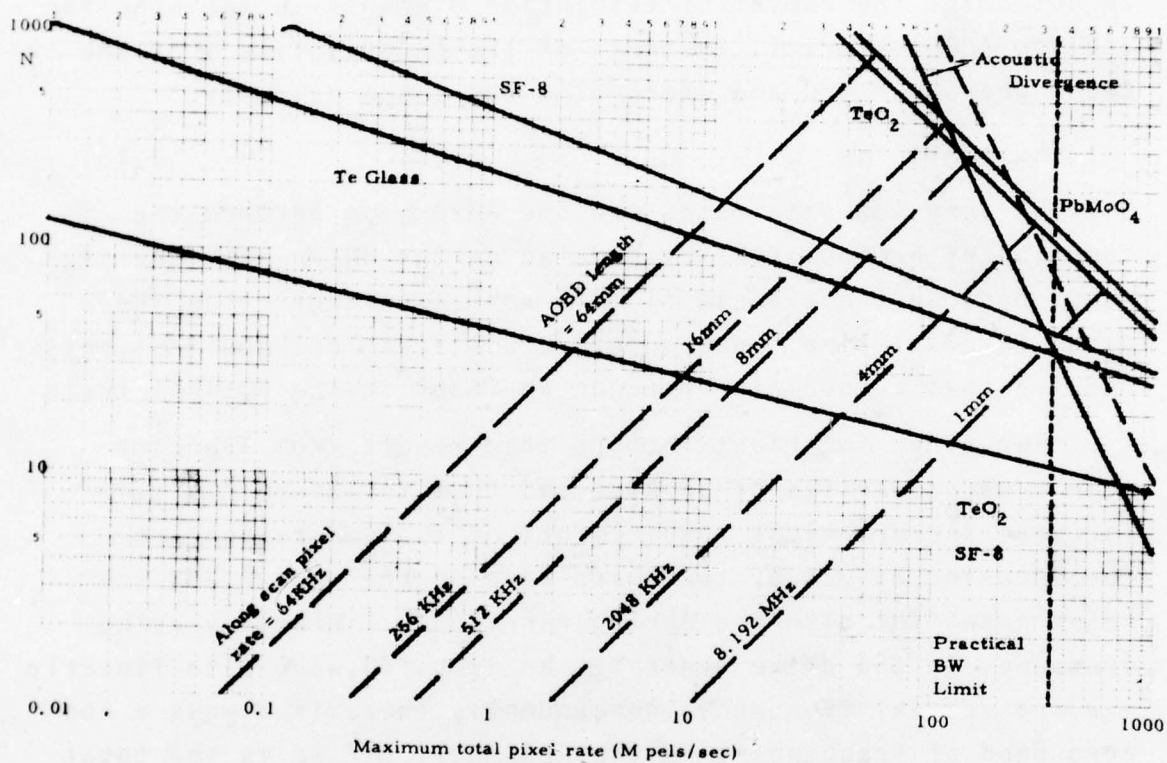
Figure 3.1.3
Device Tradeoff Curves for an AOBD Used
in the Frequency Mode in Array Recording Applications

103

in a raster scan of the focussed spot with a repetition rate
equal to that of the chirp. The bandwidth Δf of the chirp,
which determines the angular range of deflection and the dis-
tance the focussed spot travels, and the length D of the
AOBD, which determines the size of the focussed spot, combine
to determine the number of resolution elements in the scan for
a given AOBD material. In terms of the transit time τ of the
AOBD, where $\tau = v/D$ and where v is the sound velocity,

$$N_o = \Delta f \tau \tag{3-13}$$

Only at very low data rates can the AOBD also perform the
function of a modulator (by modulating the chirp with the sig-
nal), because the transit time is normally larger than the
pixel-to-pixel time. Consequently, all practical applications
require that a modulator precede the AOBD in the optical train.

Two other important factors that result from the high
scan rate properties of an AOBD and that influence the per-
formance and practical requirements of implementation are
the focusing effect of the chirp wave in the medium and the
requirement for blanking during retrace. A linearly varying
frequency in the drive generates an acoustic wave with linearly
varying spatial frequency; consequently there is always a non-
zero band of frequencies in the AOBD cell. If Δf is the total
bandwidth of the chirp, then a band $\Delta f/N_o$ is associated with
one resolution element; that is, as the range of frequencies
within the cell shifts by $\Delta f/N_o$ the focused spot shifts posi-
tion by one resolution element. Furthermore, if the band with-
in the cell changes width by $\Delta f/N_o$, the spot spreads over two
resolution elements. This is a defocussing property that can
only be corrected by optical means (e.g., altering the posi-
tion of a lens). To estimate the range within which the chirp
repetition rate can be varied without requiring a focus

104

correction, we note that the absolute value of the change in bandwidth within the cell resulting from a factor γ change in chirp duration T is

$$\pm \frac{\tau}{T} \Delta f \mp \frac{\tau \Delta f}{\gamma T} \; . \tag{3-14}$$

If α is the spot growth factor acceptable (usually.about 0.1), then the above expression is set equal to $\alpha \Delta f / N$ to obtain, after some algebra,

$$\gamma = \frac{\mp 1}{\frac{\alpha T}{N^2} \pm 1}$$

Substituting for τ,

$$\gamma = \frac{\mp 1}{\frac{\alpha T \Delta f}{N^2} \mp 1} \tag{3-15}$$

Let us take the IITS raster rate of 256 k pels/sec, and assume we wish to maintain this horizontal scan rate (which is approaching the limit for a galvanometer in the application) and increase the recording (or scanning) data rate by an orthogonal N-pixel AOBD to 256 x N k pels/sec. The largest reasonable bandwidth for an AOBD in this type of an application is about 250 MHz. Since T = 1/256 kHz, the range of variability in the sweep time is only ±10% for N = 32, and becomes even smaller for larger block sizes and/or lower chirp bandwidth. For N = 16, we find $0.72 \leq \gamma \leq 1.6$. For N = 10 and smaller blocks the range becomes infinite on the top side (scans may be made exceedingly slow) but remain constrained for low values of γ. The data is summarized in

105

Figure 3.2-1, which shows the upper and lower limits for γ corresponding to several horizontal pixel frequencies, the fastest of which is that of IITS. The conclusion is that unless block sizes are very small, or slow overall scanning/recording rates are acceptable, then variable scan rates of useful range can be obtained only with optical focus compensation, and this is generally a rather difficult task, particularly it scan rates must be altered within an image.

The optical configuration for raster recording with an AOBD is illustrated in Figure 3.2-2, which includes (a) slow scan operation, (b) the defocus effect discussed above, and (c) the transition region during which the end of one chirp leaves the cell and the beginning of the next chirp enters it. During this time the modulator must be turned off, since the light distribution in the image plane consists of blurred spots at the extremes of the scan field, a result of an effectively reduced optical aperture for these frequencies. This blanking has a direct influence on the usable block size and bandwidth properties of a scanning AOBD. To analyze the data rate characteristics of this technique we observe that the useful bandwidth of the AOBD is

$$\Delta f' = \Delta f(1 - \tau/T).$$ (3-16)

This reduces the actual useful block size to

$$N = \Delta f' \tau$$
$$= \Delta f \tau \left(1 - \frac{\tau}{T}\right)$$
$$= N_0 \beta,$$ (3-17)

where N_0 is the number of resolution elements in a scan for the limiting case of very slow scan ($T \to \infty$), and

$$\beta = 1 - \tau/T$$ (3-18)

106
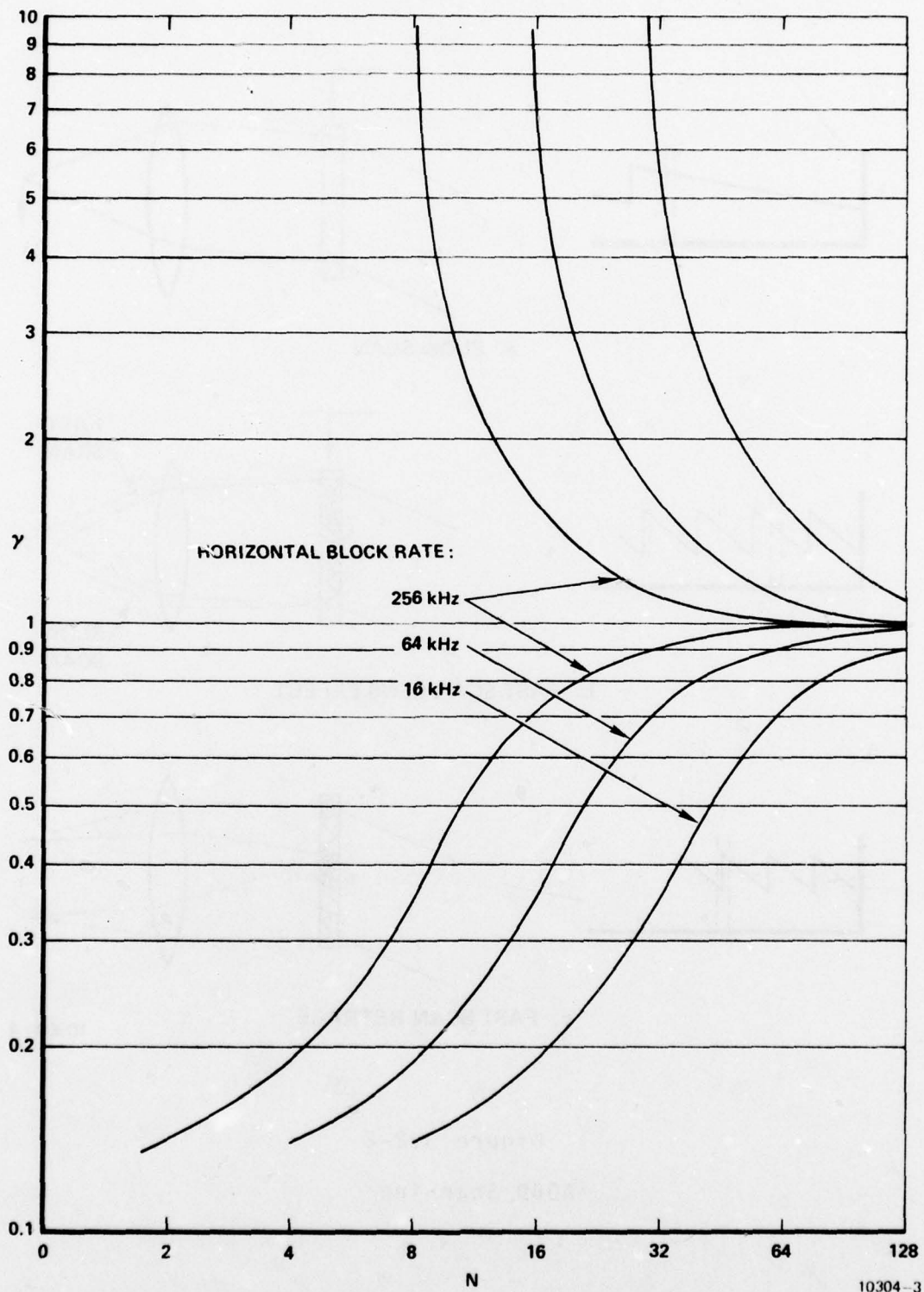
Figure 3.2-1. Chirp Rate Variation Factor Vs. N

107

a. SLOW SCAN

b. FAST SCAN LENS EFFECT

c. FAST SCAN RETRACE
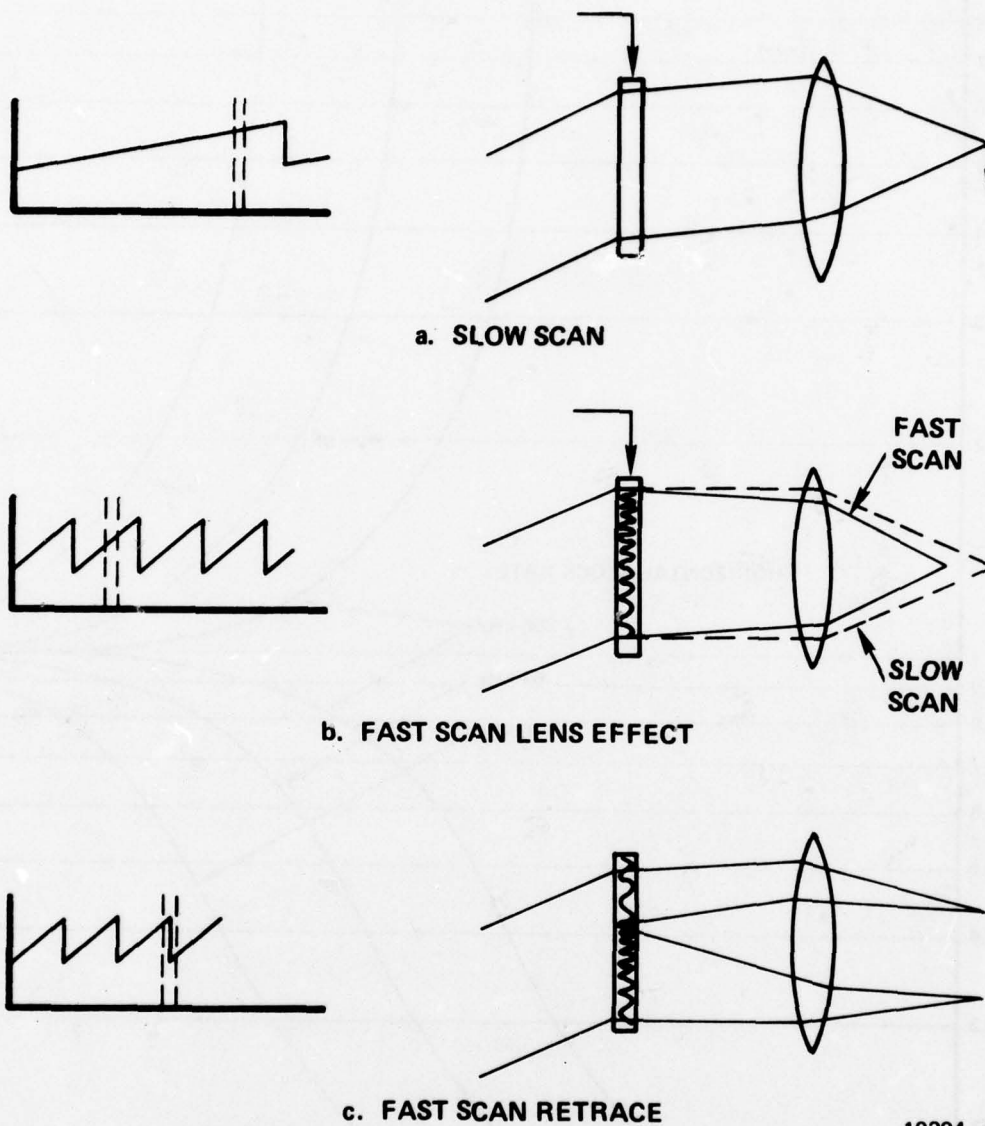
10304—4

Figure 3.2-2

AOBD Scanning

is the duty factor of the scanner. If we assume the chirp drive retrace time is negligible, the average pixel rate is

$$\frac{N}{T} = \beta(1 - \beta)\Delta f. \qquad (3-19)$$

It is apparent that the maximum obtainable data rate is $\Delta f/4$, which occurs when $\beta = \frac{1}{2}$. Note, however, in this case that only $N_o/2$ pixels are available, and that, because of the 50% blanking, a 50% exposure loss must be accepted. Figure 3.2-3 summarizes the transition constraints on an AOBD. Usually it is possible and prudent to accept a lower data rate for a larger duty factor. Figure 3.2-4 shows the block size and bandwidth characteristics of an AOBD scanner with the duty factor $\beta = 3/4$ chosen to provide a reasonable compromise in the high data rate limit. The most noteworthy aspects of Figure 3.2-4 are the acoustic divergence and attenuation limits; we moved to lower frequencies and slightly down in the N coordinate compared with the curves for the AOBD in a multi-frequency mode. It is evident that data rates and block rates are considerably more constrained at high data rates for recording with a scanning AOBD than in a multifrequency mode.

3.3 MULTICHANNEL ACOUSTO-OPTIC MODULATOR (AOPC)

This technique is rather straightforward and consists simply of simultaneously modulating an array of transducers in a multichannel modulator and imaging the acousto-optical interaction plane onto the film. The beneficial aspect of this method of array recording is that it is capable of extremely high data rates. In the linear array mode the transducers can be made very small and therefore capable of very wide-band operation; as was mentioned earlier, the state of the art today is about 500 MHz of modulation bandwidth for a single channel. A multichannel device, therefore, is fundamentally

$$\frac{\Delta f'}{\Delta f} = \beta (1 - \beta)$$

OPTICAL EFFICIENCY

N_0

N

10304-5
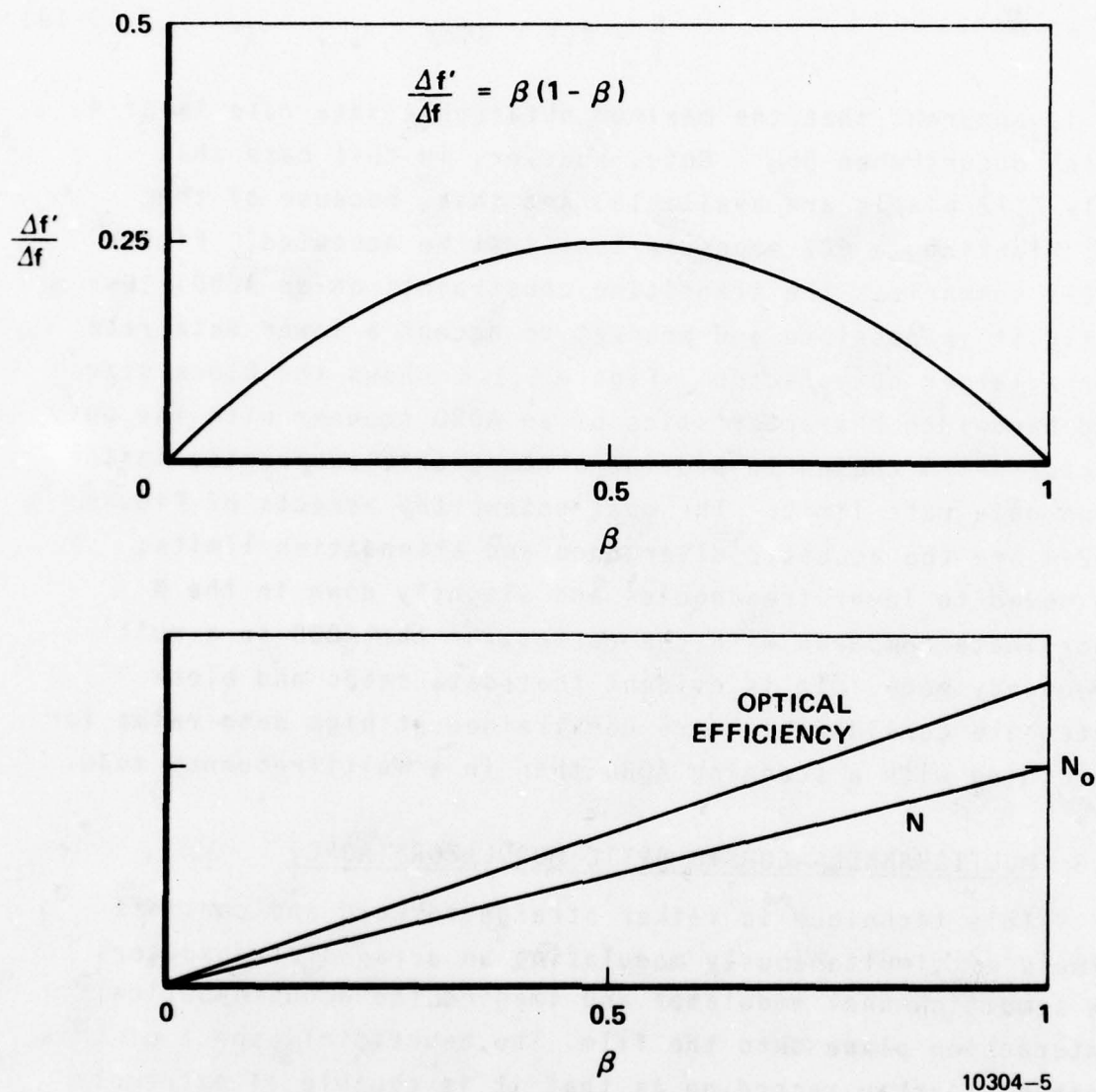
Figure 3.2-3

Operational Parameters Vs. Duty Factor For AOBD Scanner

110
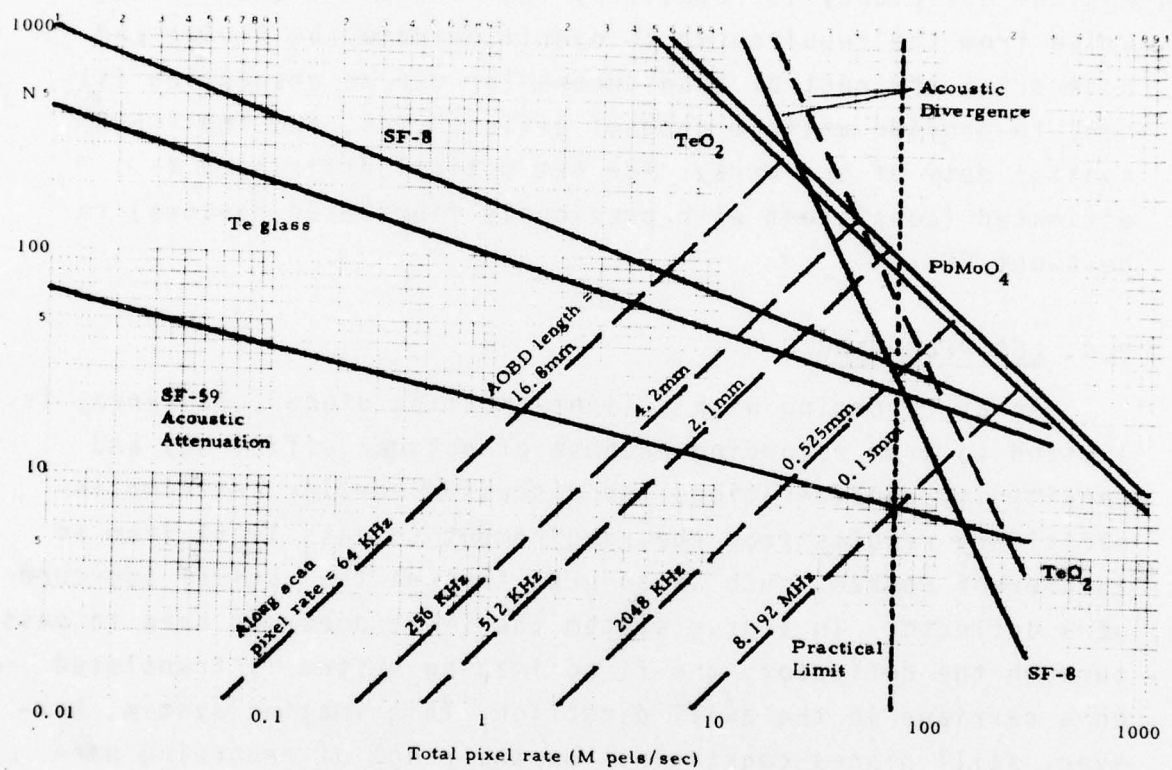
Figure 3.2-4
Device Tradeoff Curves for an AOBD Used
in the Scanning Mode in Array Recording Applications

111

capable of recording at rates far beyond any requirement en-
visioned. (350 MHz per channel is probably the largest prac-
tical bandwidth in this application).

The drawbacks of multichannel modulators are that they
are physically complex, and therefore quite expensive, and the
optical efficiency is relatively low. The efficiency losses
arise from the requirement to overilluminate the device and
underdrive the central transducers (or use an absorption fil-
ter) to provide uniform channel efficiencies, and the ($\sim$50%)
spatial duty of the array. The net optical efficiency is
estimated (consistent with previously fabricated devices) to
be about 20%.

3.4 LED RECORDING

Array recording with a light-emitting diode (LED) array is
limited to drum recording because of optical efficiency and
sensitivity considerations. As discussed earlier, extreme in-
efficiency results from the requirement to pass light from an
incoherent source, such as an LED, through the optical aperture
of a deflector. In a drum system the light does not have to pass
through the deflector; the fixed imaging system is translated
on a carriage in the axial direction. This imaging system, how-
ever, still places constraints on the range of recording par-
ameters achievable.

LED array technology is still in a developing stage, ori-
ented primarily toward visual displays. The state of the art for
LED arrays applicable for the present purpose consists of single
unit arrays with a maximum length of about 1 inch and a minimum
center-to-center spacing of about 0.003 inch, with an 80%
spatial duty factor. Larger LED element areas and spacings are
readily achievable, but the 1-inch length is constrained by
fabrication considerations. Larger sizes can, in principle, be

112

obtained by abutting smaller arrays, but this is a very expensive procedure with considerable risk in providing sufficiently accurate spacing at the abutment to avoid visual banding in the recorded image.

The light emitted from an LED can be adjusted in wavelength by suitable doping to be in the visible region (LEDs normally emit in the infra-red) to match the spectral sensitivity of recording materials. The response time of an LED is generally no more than a few nanoseconds. At 655 nm an LED emits about 12.5 mwatts/mamp/cm^2 up to a heat-limiting maximum of about 200 mamps of drive current. Assuming a 50% margin for diode-to-diode levelling, etc., a maximum radiant emittance of about

$$R = 1.25 \times 10^6 \ \mu watts/cm^2 \qquad (3-20)$$

is radiated nearly as a Lambert source in the forward hemisphere. Therefore, if, as in Figure 3.4 a lens of size L and focal length F forms an image of an LED element of side D with magnification M,

$$M = d/D = S_2/S_1 . \qquad (3-21)$$

then the power collected by the lens is

$$P = \frac{RD^2}{2\pi} \int_{\phi=0}^{2\pi} \int_{\theta=0}^{\theta_M} \sin\theta \cos\theta \, d\theta$$

$$= \frac{RD^2}{2} \sin^2\theta_M$$

$$= \frac{RD^2}{2} \frac{1}{\left[1 + (2S_1/L)^2\right]} . \qquad (3-22)$$

113

FOCAL LENGTH = F
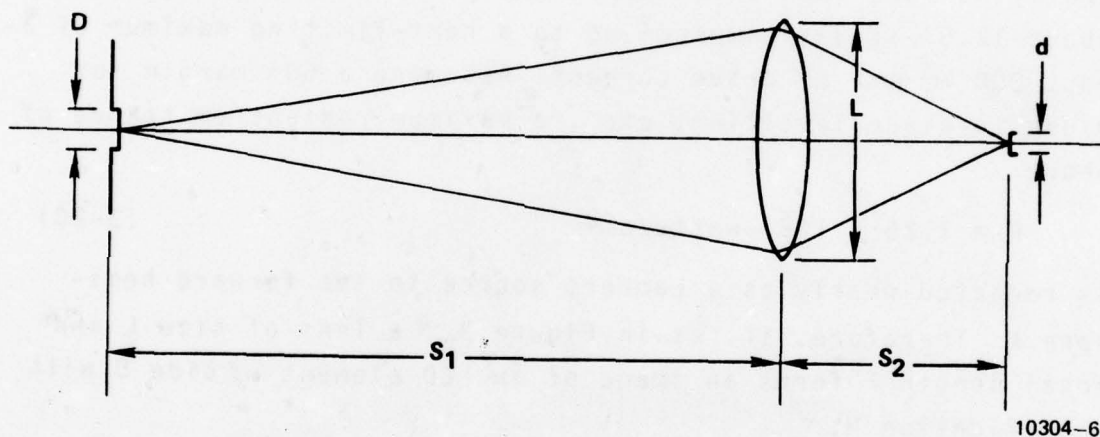
Figure 3.4
LED Imaging Optics

114

From the lens formula

$$\frac{1}{F} = \frac{1}{S_1} + \frac{1}{S_2} \qquad (3-23)$$

and Eq. $(3-21)$ we find

$$\frac{2S_1}{L} = \frac{2(M+1)}{M} \; (f/No.), \qquad (3-24)$$

and Eq. $(3-22)$ becomes

$$P = \frac{RD^2}{2} \; \frac{1}{[1 + 4(M+1)^2(f/No)^2/M^2]} \; . \qquad (3-25)$$

The irradiance of the film is

$$I = P/d^2$$

$$= \frac{R}{2M} \; \frac{1}{[1 + 4(M+1)^2 \; (f/No)^2/M^2]} \; . \qquad (3-26)$$

115

Let r be the instantaneous pixel rate. The exposure of
the film is

$$E = I/r. \tag{3-27}$$

The block rate is

$$\frac{r}{N} = \frac{R}{2EM^2} \frac{1}{\left[1+4 \ (M+1)^2 \ (f/No)^2/M^2\right]} \tag{3-28}$$

Let us take the example of a typical recording material used in
image transmission systems, 3M type 7771 dry silver paper, re-
quiring a maximum exposure of about 20 µj/cm. Using this expo-
sure and Eqs. 3-20 and 3-28, the maximum block rate for an
$f/N_0 = 2$ lens (about the minimum practical imaging lens) with
magnification M = 0.37 is

$$\frac{r}{N} = 1036. \tag{3-29}$$

The assumed magnification corresponds to an LED spacing of
0.007 inch reduced to the IITS line spacing of 0.0026 inch.
At the IITS data rate of 256 K pels/sec, the minimum block
size is

$$N = 247 \tag{3-30}$$

The size of the LED array is 1.73 inches. The number of elements
in the array is too large for most applications and the physic-
al size requires very costly fabrication. Reducing the element
spacing and simultaneously increasing the magnification pro-
duces a smaller array length but a larger number of elements.
On the other hand, reducing the magnification and increasing
the block size means a longer array length. Reduction of the

pixel rate requirement brings the parameters within the range of practical fabrication. For example, reducing the pixel rate by a factor of ten (corresponding to a total recording time of about 10 minutes), reduces the minimum block size to 25 elements with a total length of 0.175 inch (for M = 0.37)

The performance and implementation tradeoffs involve multiple variables, primarily resolution, pixel rate, block size and array length. The general conclusion that can be made is that LED recording is limited to systems with longer recording times or lower resolution than the IITS configuration. A further disadvantage of LED array recording is that tight positioning tolerances of the surface of the recording material must be held to maintain a constant spot size, due to the strong convergence of the incoherent light. Finally, the applications are limited to those using array scanning/recording for block encoding rather than image enhancement (filtering) or high speed.

3.5 FIBER OPTIC LIGHT GUIDES

Fiber optics are generally most useful for transporting light through an unusual optical path, such as relaying reflected light along a line or a scanned photograph to a single small photodetector by means of a ribbon of fibers spindled at one end, or to an otherwise remotely located detector. For array recording fiber optics can be used instead of an imaging lens to bring the LED light to the photosensitive film surface. By using tapered fiber bundles (readily available from fiber-optic manufacturers), magnification and demagnification of the light spots is possible. These fiber optic links may be made somewhat more efficient than a lens system in some cases, but generally the fiber surface at the recording medium must be held

117

extremely close to the surface (on the order of a line spacing) at all points. This places a severe constraint on the design and film-holding tolerances that is even worse than for the lens-imaging system. Alternate techniques can generally be identified that are superior to fiber-optic coupled LED recording.

3.6 SUMMARY

Array recording is generally useful for high speed recording and for recording of two-dimensionally encoded data. Array scanning, on the other hand, is performed for these purposes and also to perform image enhancement operations, such as spatial filtering, which provides a single output pixel for a block of scanned pixels. For this latter operation, the recorder need only be a single line raster recorder. Although array recording is of more limited use than array scanning, it is generally less difficult to perform. There are two principal sources of difficulty in array scanning that are not present in array recording. These are the low bandwidths associated with optical detectors generally suitable for scanning applications, and the difficulty in handling efficiently the light that is diffusely scattered from a scanned object. Thus there are a number of techniques for array recording that are compatible with block sizes and data rates attainable with array scanning techniques. The considerably larger block sizes and data rates available may be used to record images stored in memory, as a means of retrieving imagery stored in a mass memory, for example, or for reducing the number of terminals required at a receiving station having large throughputs.

A summary of the principal array recording techniques that have been identified is given in Table 3.1. The AOBD scanned recording technique seems to be the least complicated approach overall and can perform well at any pixel rate or block size

118

Table 3.1 Summary of Array Recording Techniques

Technique	Pixel Rate	Block Size (N)	Principal Application	Optical Efficiency	Comments
Multiple Oscillator	<350 Mpels/s	<1500	High Speed	~30%	Difficult electronic implementation. Coherent distortions at high pixel rates.
Fourier Transform	<350 Mpels/s	<1500	High Speed	~40%	High pixel rate may be expensive to implement electronically. May be directly compatible with block DFT or DCT coding. Lowest optical cost.
AOBD Scanned Recording	<75 Mpels/s	<1500	High Speed	~50%	Least electronic complexity. Lowest overall cost. Difficult to implement speed change.
AOPC Multichannel Recording	<350N Mpels/s (<500N Kpels/s for galvo)	<64	Very High Speed	~20%	Cost effective only at very high pixel rates.
LED	<250 Kpels/s	<25	Block Encoding	(~3%)	Light power & array length limited. Drum recording only.

119

required to be compatible with array scanning. The remaining complication, which applies to all the array recording techniques listed, is the requirement to provide optical efficiencies that are sufficiently corrected over the scan to avoid observable banding in the image.

4.0 DATA COLLECTION AND PROCESSING

The data collection and processing operations that are the subject of this paragraph include resolution selection (via REARCS), image enhancement, and MTF correction. Two-dimensional filtering operations are inherent in all three of these operations and therefore have received a substantial amount of attention during the course of the study effort.

Although resolution reduction reduces the required image transmission bandwidth the selectable resolution capability is, for the purposes of this study, considered to be primarily a data collection and processing operation rather than a bandwidth compression technique and therefore is not addressed in paragraph 5.0, Bandwidth Compression Techniques.

The remainder of this paragraph deals with the theory and implementation of the two-dimensional filtering operations involved in selectable resolution, image enhancement and MTF correction and describes the results of computer simulation experiments in these three areas.

4.1 THE IMPLICATIONS OF ELECTRONICALLY SELECTABLE RESOLUTION

Selectable resolution is a useful feature for many image transmission systems, depending upon the end use of the transmitted images. The REARCS approach to image coding and transmission described below is particulary useful in military image systems in which some portions of an image are much more important than others for tactical reasons. If each source image is constrained to be transmitted with the same (selectable) resolution throughout the image, the desired resolution could be simply obtained by mechanically adjusting the scanning spot size and spatial

sampling rate. However, when two or more resolutions may
be required within the same image, electronic resolution
selection becomes very attractive for either single spot
scanning systems or array scanning systems. Electronic
control of image resolution has far-reaching implications;
these considerations are the subject of the next section.

4.1.1   REARCS and Its Impact Upon System Design

          The REARCS (Redundant Area Coding System)
approach to image bandwidth compression and transmission
is best described by reference to Figure 4.1.1, in which
so-called nonredundant or target areas, indicated by shaded
blocks, are transmitted with little or no bandwidth compression
at the highest spatial resolution while all remaining one-
inch squares (background or redundant areas) are transmitted
at a lower resolution after considerable bandwidth compression.
While it is obvious that transmitting designated strips
rather than designated blocks at the higher resolution
would greatly simplify the system implementation, this ap-
proach would greatly diminish the attainable overall
compression ratio. For such a system as REARCS in which
two spatial resolutions can be present in the same image,
electronic resolution reduction of high resolution imagery
becomes more feasible than mechanically de-focussing a
lens, especially at the higher image throughput rates.
The increase in implementation complexity due to imposing
a REARCS requirement will become evident in this and
subsequent paragraphs.

LOCATING NONREDUNDANT AREAS ON GRID
FOR REARCS TRANSMISSION
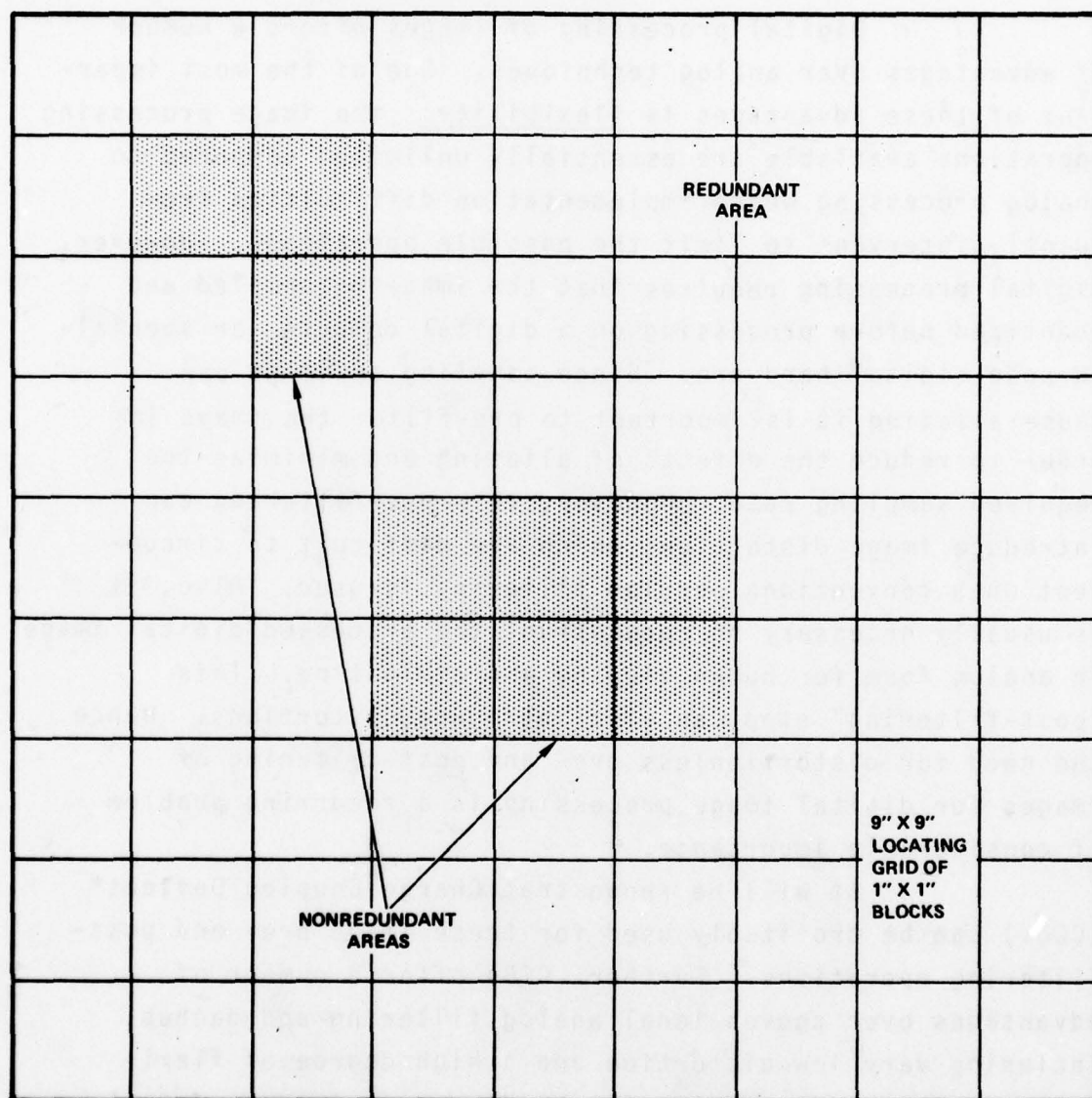
Figure 4.1.1
REARCS Concept

4.1.2   Distortion and Aliasing Considerations
             in Sampled Imagery

4.1.2.1   Introduction

        Digital processing of images offers a number
of advantages over analog techniques. One of the most impor-
tant of these advantages is flexibility: the image processing
operations available are essentially unlimited compared to
analog processing where implementation difficulties fre-
quently intervene to limit the possible operations. However,
digital processing requires that the image be sampled and
quantized before processing on a digital computer or special-
purpose digital hardware. Since sampling an image can
cause aliasing it is important to pre-filter the image in
order to reduce the effects of aliasing and minimize the
required sampling rate. However, this pre-filtering can
introduce image distortions which are difficult to circum-
vent when conventional analog filtering is used. Also, it
is usually necessary to reconstruct the processed digital image
in analog form for human viewing and evaluating. This
"post-filtering" step can also introduce distortions. Hence
the need for distortionless pre- and post-filtering of
images for digital image processing is a recurring problem
of considerable importance.

        It will be shown that Charge-Coupled Devices*
(CCDs) can be profitably used for these image pre- and post-
filtering operations. Further, CCDs offer a number of
advantages over conventional analog filtering approaches,
including very low distortion and a high degree of flexi-
bility. These advantages will be discussed in more detail
subsequently.

---

*Here, the term "CCD" is used to denote any device which stores
 and transfers charge to represent sampled analog signals.

4.1.2.2   Image Processing Model

        Figure 4.1.2.2 shows a model for a typical
digital image processing system. The image $I(x,y)$ is scanned
by a raster scan device which converts the 2-D image into
a series of "lines". The raster scan device also effectively
filters the image $I(x,y)$, where the effective filter impulse
response (also called the "point-spread function") is
determined by the optics of the scanner and is denoted by
$g(x,y)$. The scanned lines are then passed through a conven-
tional analog LPF for bandlimiting purposes. After sampling
and A/D conversion, the digitized image is processed by
a digital computer to yield a processed image (for example,
the processing might involve contrast enhancement, bandwidth
compression, etc.) In order to convert the digital image
back to analog form, the processed image is fed in raster
format to a "boxcar" D/A converter (sample-and-hold). The
analog raster scans out of the D/A drive an optical device
which generates a photographic film of the processed image.
This optical device has a 2-D point-spread function denoted
by $g'(x,y)$.

4.1.2.3   Sources of Image Distortion

        Distortions exist at a number of places in the
system of Figure 4.1.2.2. Ideally, the optics of the raster
scan device used to input the image should have an impulse
point-spread function. In practice, it does not, and the
result is image distortion. The analog LPF used to band-
limit the raster scans before sampling does not have in-
finite rejection above its cut-off frequency, hence some
aliasing always results from the sampling process. Con-
versely, it is usually desirable to minimize the sampling
rate required, so the LPF is designed with a cutoff frequency
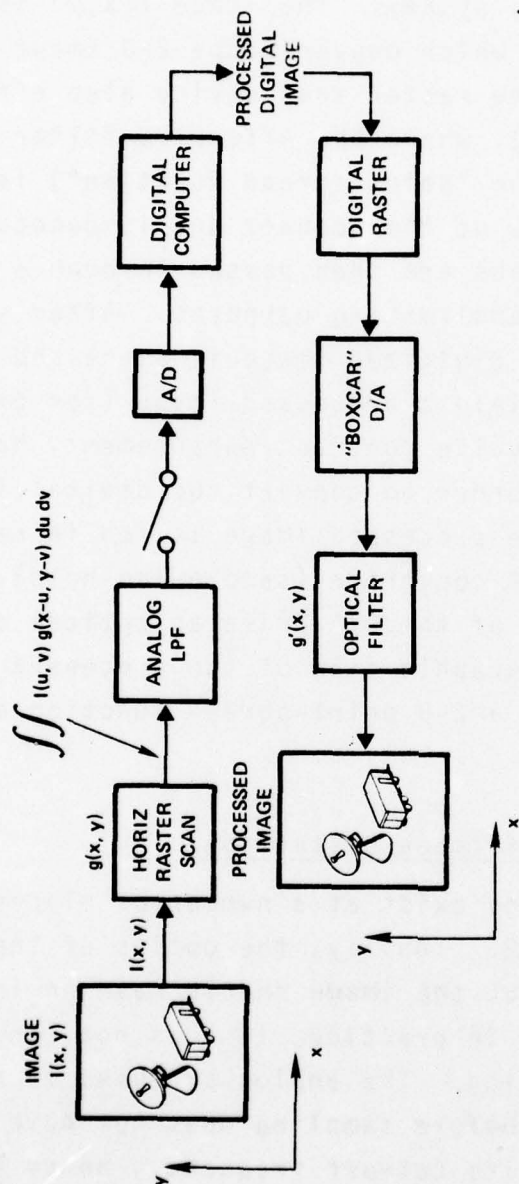
Figure 4.1.2.2

Model of Typical Image Processing System

10320—31

126

which may in fact eliminate some of the image's high frequency content. In addition, the analog LPF is usually of Chebyshev or Elliptic design in order to achieve steep skirts. These types of filters have highly non-linear phase (or equivalently non-constant group delay) and poor step response, which contributes to distortion of the image and blurring of edges. After processing in the digital computer the image is reconstructed with a boxcar D/A converter, which amounts to filtering the digital samples with a sinc (f/f_s) lowpass filter (where f_s is the sampling rate and sinc $(x) =$ $\frac{\sin (x)}{x}$). The phase of this filter is linear, but it has considerable amplitude droop and high sidelobes. The amplitude droop and high sidelobes can be compensated for by adding a compensating filter, but this will introduce phase non-linearities. Finally, the effective optical filter at the system output has a point-spread function $g'(x,y)$ which further distorts the image by degrading the MTF.

4.1.2.4   CCD Filters

CCD filters can be used to reduce these system distortions. CCD's can be used as analog shift registers to implement Finite Impulse Response (FIR) filters. Since FIR filters have linear phase and better step response than comparable lumped element analog designs, less image distortion and blurring will result. In addition, the amplitude versus frequency response of these analog shift register filters can be readily adjusted to compensate for undesirable effects of the optical filters $g(x,y)$ and $g'(x,y)$ in Figure 4.1.2.2. This is accomplished by adjusting the CCD tap weights to achieve the desired frequency response. Hence the CCD FIR filter offers linear phase and good step response characteristics, and can be tailored to compensate for the

127

point-spread distortions of the optics in the system. It
can be difficult or impossible to achieve similar character-
istics with conventional analog filters.. The relative
merits of FIR and IIR CCD filters are discussed in Section
4.1.4.

4.1.2.5   Conventional Analog Design

As an example, consider the pre-sampling filter
specifications shown in Figure 4.1.2.5-1. An in-band ripple
of 0.1 dB is desired, and the stop-band rejection is speci-
fied to be at least 40 dB in order to suppress the effects
of aliasing. It can be shown that a 6-pole Chebyshev filter
will meet these specifications at a sampling rate (f_s)
of 2.82 times the filter bandwidth (B). Figure 4.1.2.5-2(a)
and 4.1.2.5-2(b) show the step response and group delay of
this filter, respectively. Note the ringing in the step
response, and the variation in group delay with frequency.

For image reconstruction, the system of Figure
4.1.2.2 uses a boxcar D/A. Figure 4.1.2.5-3 shows the fre-
quency response of this boxcar reconstruction filter. The
filter has linear phase (hence constant group delay) but
considerable amplitude droop (roughly 4 dB at the half
sampling frequency) which attenuates the high frequency
content of the image. Also, the first side-lobe of the
filter is down only 13 dB, which will cause the reconstructed
image to be contaminated with aliased image content. While
it is possible to compensate for the amplitude droop and high
sidelobes by cascading a compensating filter, this filter
will introduce phase non-linearities.

Note also that compensation for the point-
spread functions in Figure 4.1.2.2 would complicate the con-
ventional filter design and synthesis problem considerably.
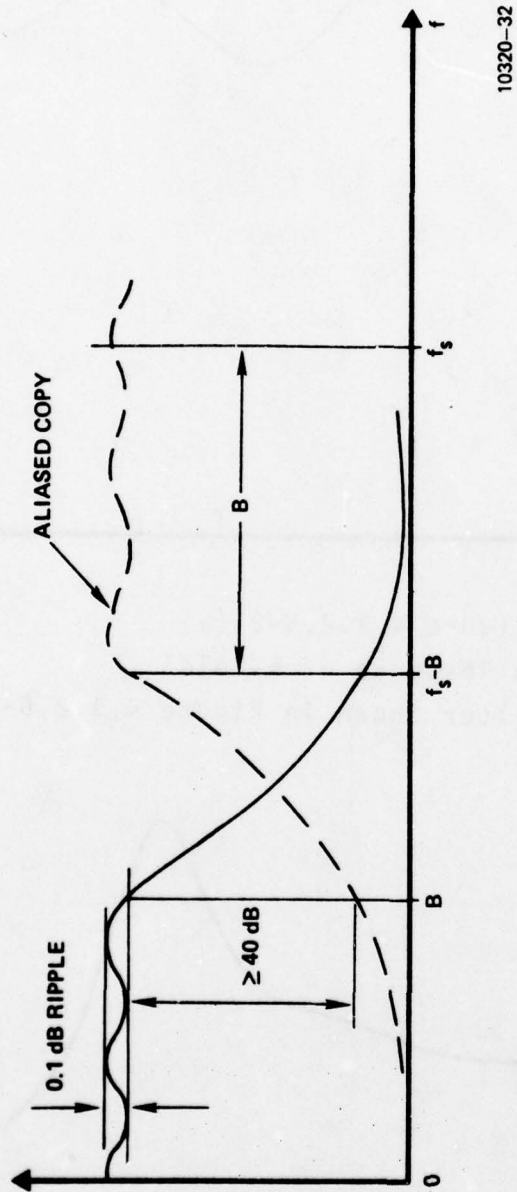
Figure 4.1.2.5-1

Conventional Analog LPF of CHEBYSHEV Design Showing Effect of Aliasing

10320-32

129
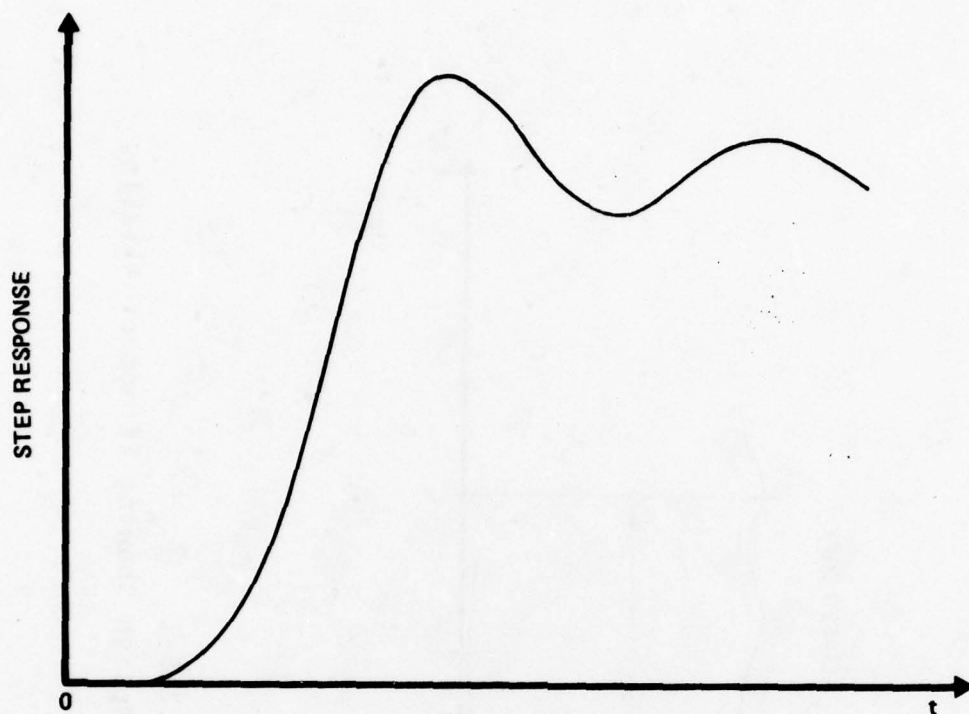
10320—29

Figure 4.1.2.5-2 (a)
Step Response of 6-Pole
Chebyshev Filter Shown in Figure 4.1.2.5-1
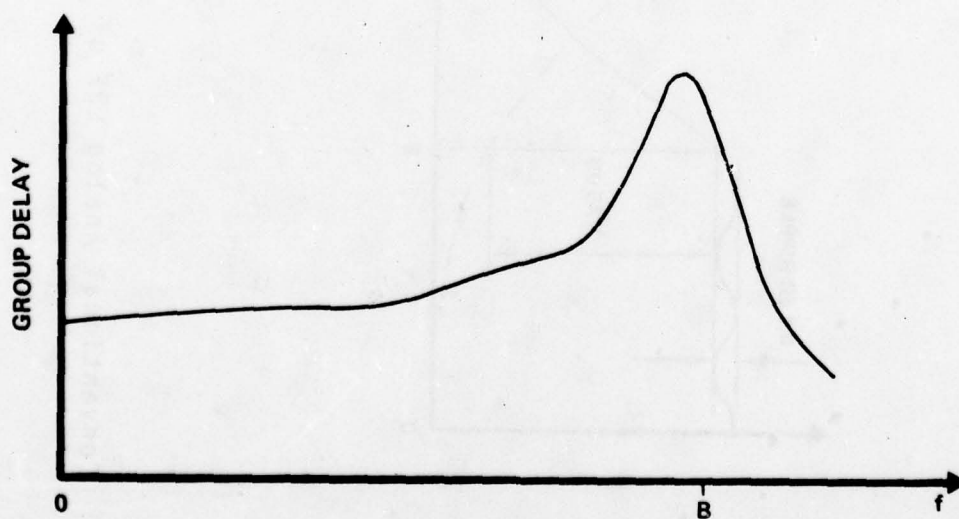
10320—30

Figure 4.1.2.5-2 (b)
Group Delay of 6-Pole
Chebyshev Filter Shown in Figure 4.1.2.5-1
130
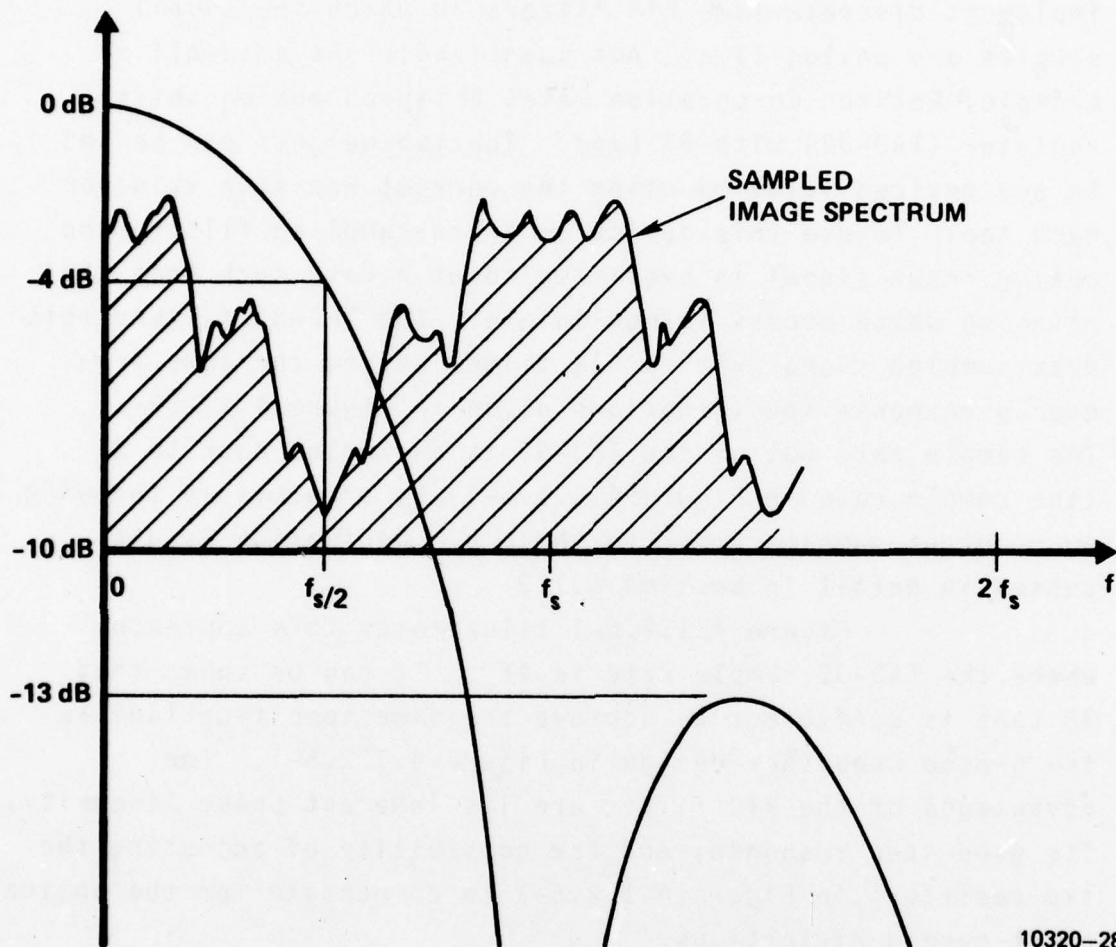
Figure 4.1.2.5-3

Frequency Response of Boxcar D/A

131

4.1.2.6   CCD Design

As discussed previously, CCDs can be used to implement discrete-time FIR filters in which the signal samples are analog (i.e., not quantized). As a specific example, Reticon Corporation makes a tapped analog shift register (TAD-32) with 32 taps. The tap weights can be set to any desired value by using the correct resistor value on each tap. To use this device as a pre-sampling filter, the analog input signal is over-sampled at a rate such that the aliasing which occurs is negligible. The TAD-32 filters this over-sampled signal with a FIR filter having the same frequency response specifications given in Figure 4.1.2.5-1. The sample rate out of the TAD-32 is decimated back to f_s (the sample rate in Figure 4.1.2.5-1) by effectively throwing away output samples prior to the A/D. Decimation is discussed in detail in Section 4.1.3.

Figure 4.1.2.6-1 illustrates this approach, where the TAD-32 sample rate is $4f_s$. It can be shown that 32 taps is sufficient to achieve the same specifications as the 6-pole Chebyshev design in Figure 4.1.2.5-1. The advantages of the FIR filter are its inherent phase linearity, its good step response, and the possibility of adjusting the tap resistors in Figure 4.1.2.6-1 to compensate for the optical point-spread distortions.

Figure 4.1.2.6-2 shows the step response of the 32-tap FIR filter. For comparison, the step response of the 6-pole Chebyshev design is also shown. Note the smaller overshoot for the FIR filter, and its rapid approach to steady-state conditions. The group delay of the FIR filter is constant, of course, as compared to the variable group delay of the 6-pole Chebyshev filter shown in Figure 4.1.2.5-2 (b).

132
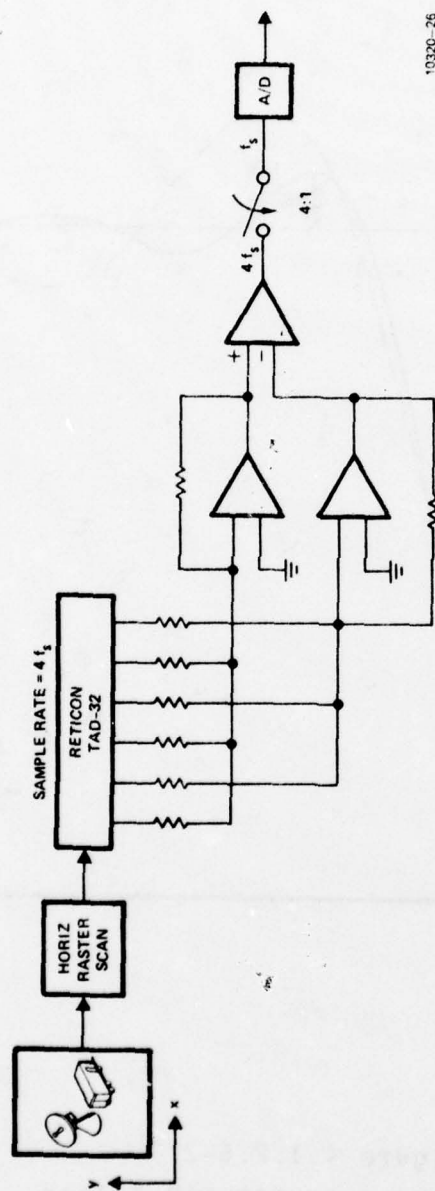
Figure 4.1.2.6-1
Use of Reticon TAD-32 For
Pre-Sampling Filter

133
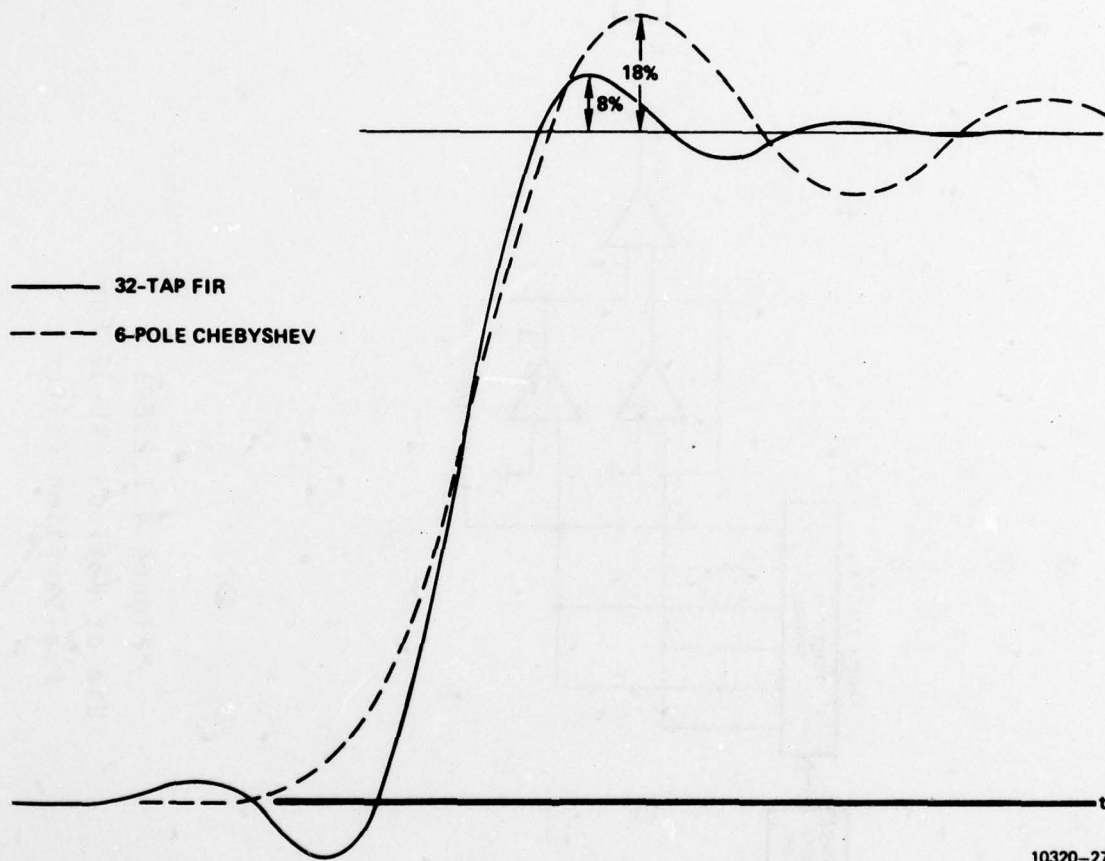
Figure 4.1.2.6-2
Step Response of 32-TAP FIR Filter

134

Figure 4.1.2.6-3 shows how the processed digital image can be reconstructed using the TAD-32 to implement an FIR filter. The digital image samples are fed raster-fashion to a boxcar D/A converter at a rate of $4f_s$ samples/second, where three zero samples have been interleaved between each pair of image samples. The TAD-32 shift register takes samples at a rate of $4f_s$ (3 out of every 4 samples are zero). The FIR filter then filters out the spectrum copies at 0, $4f_s$, $8f_s$, etc,. as shown in Figure 4.1.2.6-3. Hence the TAD-32 is used here as a FIR interpolator to increase the sample rate into the optical output device; interpolation is discussed in Section 4.1.3. Note that the first boxcar D/A converter in Figure 4.1.2.6-3 causes a droop of 0.22 dB at the half-sampling frequency. The second boxcar D/A converter in Figure 4.1.2.6-3 will also cause a droop of 0.22 dB, yielding a net droop of 0.44 dB at the half-sampling point. Actually, the tap resistors of the TAD-32 could be adjusted to compensate for the small amplitude droop and still maintain linear phase; MTF correction is discussed in Section 4.3. With or without MTF correction, the reconstruction approach of Figure 4.1.2.6-3 does an excellent job of preserving high frequency content, and has linear phase throughout.

4.1.2.7 Conclusions

In the foregoing discussion it was shown that CCD tapped analog delay line filters offer some advantages over conventional analog filters when used as pre-sampling and reconstruction filters, including linear phase and good step response. Also, the response of these filters can be easily adjusted to compensate for optical point-spread distortions. The basic idea is to oversample the scanned image
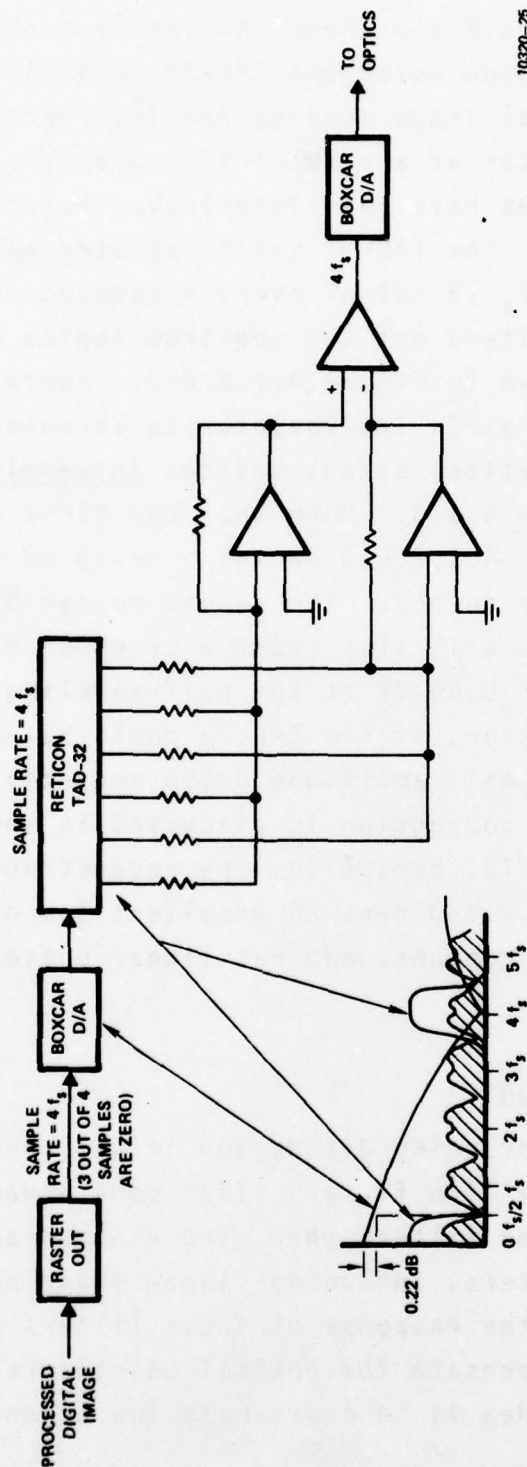
Figure 4.1.2.6-3

Use of TAD-32 Filter For Image Reconstruction

and then use the CCD as a FIR filter before reducing the
sample rate.

While these characteristics of CCD filters
seem clearly desirable on a priori grounds, the final proof
of the value of these features must rest on experimental
processing of images. Do the resulting images appear less
distorted, blurred, noisy, etc., than conventionally filtered
images? Also, the computed CCD filter responses were based
upon the assumption that the CCD filters correspond to ideal
FIR filters. In practice, such effects as charge transfer
inefficiency, tap resistor inaccuracies, etc., will cause
the CCD filter characteristics to deviate from the ideal
response computed above. The deviations from ideal perfor-
mance are best investigated by a combination of device model-
ling and analysis and experimental testing of actual devices.

The possibility of compensating for optical point-
spread distortions is a very valuable feature of the CCD
approach. However, this capability must also be demonstrated
experimentally by measuring the point-spread function of the
optics, computing the compensating filter characteristics
required, implementing these characteristics in an actual
CCD filter, and measuring the compensated point-spread func-
tion.

This section has served as a brief introduction
to and overview of the distortion and aliasing considerations
inherent in any digital image processing systems. The problem
of ringing in an image due to the nonlinear phase response
of presampling filters was described and a solution based
upon the use of linear phase FIR sampled-data filters was
proposed. The example that was presented in this section
served as a convenient vehicle to introduce the important
concepts of decimation and interpolation in image transmission
systems. When the analog presampling filter in the example

137

was replaced by a FIR sampled-data filter the sampling rate
was increased to prevent significant aliasing. Consequently, at
the <u>output</u> of the FIR filter the signal frequency content
was such that the samples were required less frequently,
and decimation was appropriate. Similarly, the interpolation
process at the other end of the channel reduced the MTF
degradation due to the boxcar effect of the D/A converter.
The theory of decimation and interpolation and its role in
the ASITS is discussed in detail in Sections 4.1.3, 4.1.5,
and 4.1.6.

It should be noted that oversampling the source
image by a factor of D and then decimating the output of the
presampling filter by a factor of D results in no net re-
duction of computational burden. The advantage lies in the
fact that linear phase FIR filters can be used to minimize
aliasing without introducing image distortion due to nonconstant
group delay. However, if subsequent additional decimation
is utilized in order to achieve electronically reduced spatial
resolution, then the reduced frequency content of the de-
cimating filter output implies that a lower sampling rate
can be employed without violating the Nyquist criterion. The
computational burden can then be reduced by the square of the
decimation ratio without degradation to system performance.
For the decimation ratios considered for the ASITS, viz.,
D=2 and D=4, this means a four-fold or sixteen-fold reduc-
tion in required computation at these reduced system resolu-
tions.

138

4.1.3   Decimation and Interpolation

4.1.3.1   Introduction

The need for decimation and interpolation is a
direct result of having a selectable resolution capability.
While selectable resolution in an imaging system could be
easily implemented via mechanical or optical means if the
resolution were constant throughout the image, the additional
resolution flexibility required by REARCS makes electronic
resolution reduction of a high resolution image the most attrac-
tive approach for obtaining multiple resolutions within a
single image.

Perhaps the most straightforward approach to
reducing the resolution of an image by a factor of n is to
retain every n^{th} pixel of every n^{th} scan line, ignoring all
others. After these retained pixels have been transmitted
to the receiver, the receiver could then repeat each received
pixel value n times along each scan line and repeat each such
scan line n times. As might be expected, this straightforward
approach yields worse image quality than more sophisticated
approaches. The remainder of this section is devoted to
explaining the important issues involved in decimation and
interpolation of imagery.

The straightforward but trivial decimation
and interpolation process described above leads to unsatis-
factory results. Figure 4.1.3.1-1 shows the original image
used in this study, while Figure 4.1.3.1-2 shows the result
of a 4-to-1 trivial decimation/interpolation process. As
can be seen, the reconstructed image is blocky as would be
expected.

139
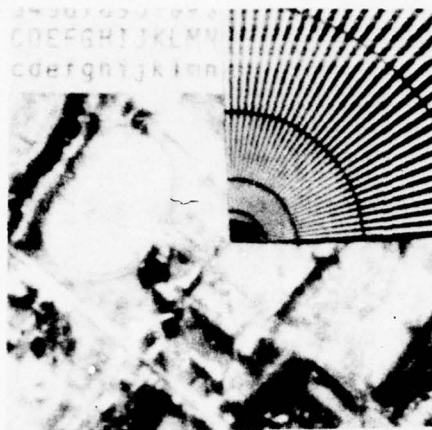
Figure 4.1.3.1-1
Original

Figure 4.1.3.1-2
4:1 D/I Only

Figure 4.1.3.1-3
Decimation/Interpolating
Using LP Filters

Figures 4.1.3.1-1, 4.1.3.1-2
and 4.1.3.1-3

140

Fortunately, it is possible to generate a recon-
structed image superior to that of Figure 4.1.3.1-2 by first
filtering the original image before decimation and then "in-
terpolating" between the sampled values at the reconstruc-
tion. Interpolation is defined as the generation of pixel
values between the decimated values. Figures 4.1.3.1-2 uses
trivial interpolation, i.e., repeating the previous point n
times in each dimension. This report will investigate more
sophisticated interpolation techniques using low pass filters.
To illustrate that dramatic improvement is possible, Figure
4.1.3.1-3 shows the decimated and interpolated image for a 4-
to-1 decimation when the correct type of decimation and
interpolation is used. The details of these filters will
be given below.

Basically, one must first low pass filter (LPF)
the original image with a filter whose bandwidth is $(1/n) \times f_s/2$
before the decimation by n and then put n-1 zeros between
each output of the decimation filter (f_s is defined as the
sampling frequency). This sequence of data and interspersed
zeros is then put through the same LPF as was used for deci-
mation. The theory describing this decimation/interpolation
(D/I) will now be given.

4.1.3.2   Decimation

The discussion to follow will be given for one-
dimensional signals. All of the concepts, however, are easily
extended to two-dimensional imagery. The one-dimensional
analysis is given here in order to simplify the presentation.
The analysis given here is taken from an excellent paper by
Schafer and Rabiner [33].

Consider a signal $\hat{x}(t)$ with Fourier transform

$$\hat{X}(\omega) = \int_{-\infty}^{\infty} \hat{x}(t)e^{-j\omega t} \, dt \ . \qquad (4-1)$$

141

Let the signal $\hat{x}(t)$ be sampled at intervals T to generate

$$x(n) = \hat{x}(nT) . \qquad (4-2)$$

The Fourier transform of the sampled data impulse stream is

$$X(\omega) = \sum_{-\infty}^{\infty} x(n)e^{-j\omega nT} \qquad (4-3)$$

It can be shown that

$$X(\omega) = \frac{1}{T} \sum_{k=-\infty}^{\infty} \hat{X}(\omega+k\frac{2\pi}{T}) . \qquad (4-4)$$

This means that the original spectrum is repeated ad infinitum with copies of $\hat{X}(\omega)$ repeated every $\frac{2\pi}{T} = f_s$ where f_s is the sampling frequency. This is illustrated in Figure 4.1.3.2-1, in which it is assumed that $X(\omega)$ is bandlimited. Figure 4.1.3.2-1 also illustrates the important concept of aliasing. In general, aliasing occurs when the copies of $\hat{X}(\omega)$ overlap in the repeated spectrum. If aliasing does not occur, it is possible to recover $\hat{X}(\omega)$, i.e. $\hat{x}(t)$, by using a low pass filter of radian bandwidth π/T [33]. Aliasing will not occur only for signals bandlimited to Ω and provided that $T \leq \frac{\pi}{\Omega}$. But if aliasing occurs, it is not possible to recover $\hat{X}(\omega)$ since $X(\omega)$ will have aliased detail as shown in Figure 4.1.3.2-1.

Suppose that it is desirable to undersample (decimate) $\hat{X}(\omega)$ with $T' > \pi/\Omega$ where Ω is the radian bandwidth of $\hat{X}(\omega)$. According to the above, aliasing will occur. If, however, $\hat{X}(\omega)$ is prefiltered with an ideal LPF of radian bandwidth $\Omega' = \pi/T'$, then aliasing will not occur when undersampling
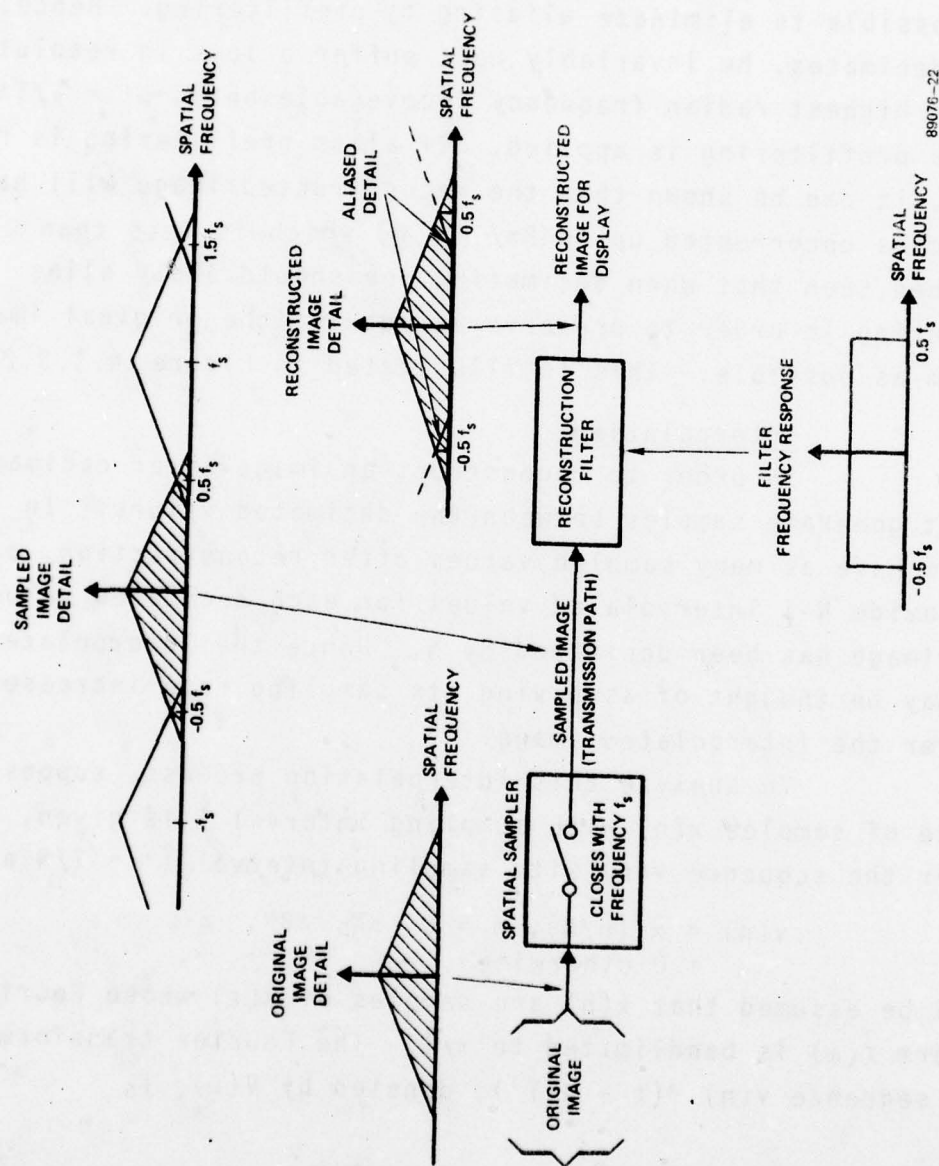
142

Figure 4.1.3.2-1

Sampled Imagery System With Aliasing

143

with $T' > \pi/\Omega$. It will then be possible to reconstruct the fil-
tered version of $\hat{x}(\omega)$ by passing the sampled values through an
ideal LPF of radian bandwidth $\Omega' = \pi/T'$. It should be noted
that it is not possible to recover $\hat{X}(\omega)$ when undersampling but
it is possible to eliminate aliasing by prefiltering. Hence,
if one decimates, he invariably must suffer a loss in resolution
with the highest radian frequency recoverable being $\Omega' = \pi/T'$
if alias prefiltering is applied. If alias prefiltering is not
applied, it can be shown that the reconstructed image will have
frequencies uncorrupted up to $(2\pi/T' - \Omega)$ which is less than Ω'.
It is then seen that when decimating one should apply alias
prefiltering in order to preserve as much of the original image
spectrum as possible. This is illustrated in Figure 4.1.3.2-2.

4.1.3.3   Interpolation

In order to reconstruct an image after decimation,
one must generate samples between the decimated values. In
order to have as many sampled values after reconstruction, one
must provide N-1 interpolated values for each decimated value
if the image has been decimated by N. Hence the interpolated
image may be thought of as having its sampling rate increased
by N over the interpolated image.

To analyze this interpolation process, suppose a
sequence of samples x(n) with sampling interval T is given.
Consider the sequence v(n) with sampling interval $T' = T/N$ and
with
$$v(n) = x\ (n/N), \quad n = 0, \pm N, \pm 2N,$$
$$= 0 \text{ otherwise}$$
It will be assumed that x(n) are samples of $\hat{x}(t)$ whose Fourier
transform $\hat{X}(\omega)$ is bandlimited to π/T. The Fourier transform
of the sequence v(n) $\delta(t - n\ T')$, denoted by $V(\omega)$, is

$$V(\omega) = \sum_{k = -\infty}^{\infty} v(k)e^{-j\omega T'k} \qquad (4-5)$$

144
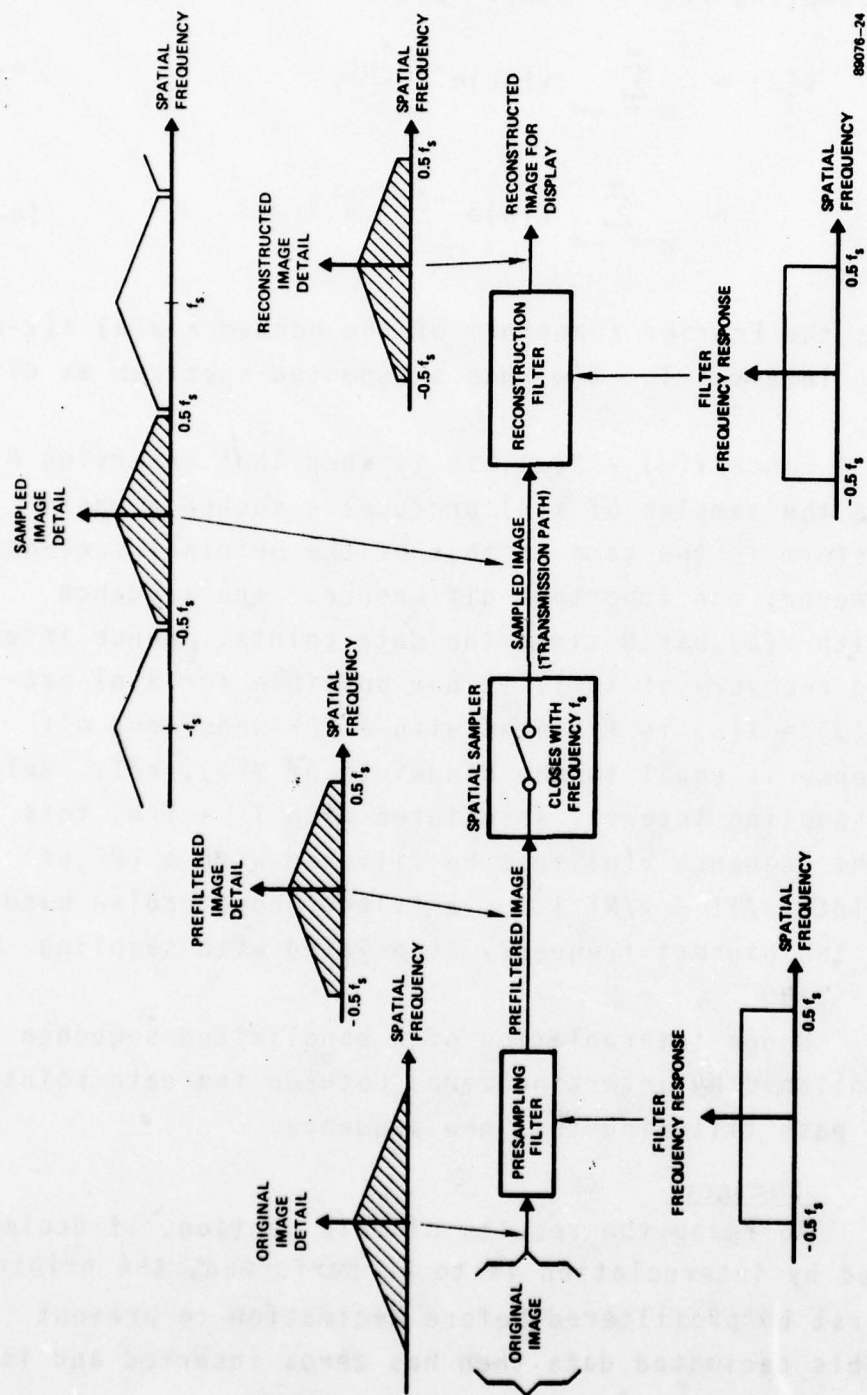
Figure 4.1.3.2-2

Sampled Imagery System, Prefiltered to Prevent Aliasing

Note that sampling interval $T' = T/N$ is used for $V(\omega)$, i.e., N times the sampling rate of $x(n)$. Let $k = nN$ and $V(\omega)$ becomes

$$V(\omega) = \sum_{n = -\infty}^{\infty} v(nL)e^{-j\omega\frac{T}{L}nL} \tag{4-6}$$

$$= \sum_{n = -\infty}^{\infty} x(n)e^{-jnT} = X(\omega) \tag{4-7}$$

where $X(\omega)$ is the Fourier transform of the sequence $x(n)\ \delta(t-nT)$ with sampling interval T. $X(\omega)$ has a repeated spectrum as discussed above.

Since $V(\omega) = X(\omega)$, it is seen that inserting N-1 zeros between the samples of $x(n)$ produces a sequence whose Fourier transform is the same as that of the original sequence. There is, however, one important difference: the sequence associated with $V(\omega)$ has N times the data points. Hence interpolation (and recovery of $\hat{X}(\omega)$) is now possible for $x(n)$ provided that $V(\omega) = X(\omega)$ is filtered with a LPF whose cut off radian frequency is equal to the bandwidth of $\hat{X}(\omega)$, π/T. Relative to the sampling interval associated with $T' = T/N$, this means that the sequence $v(n)$ must be filtered with a LPF of radian bandwidth $\pi/T' = \pi/NT$ i.e., a filter whose radian bandwidth is 1/N the highest frequency associated with sampling interval $T' = T/N$.

Hence interpolation of a bandlimited sequence can be accomplished by inserting zeros between the data points, and then low pass filtering this new sequence.

4.1.3.4   Summary

To recap the results of this section, if decimation followed by interpolation is to be performed, the original data must first be prefiltered before decimation to prevent aliasing. This decimated data then has zeros inserted and is

146

filtered by a filter whose bandwidth is equal to that of the
decimation filter. In this way, the interpolated image is a
filtered version of the original image. The various
filtering actions and sampling spectra associated with the
decimation/interpolation process are summarized in Figure
4.1.3.4.

4.1.4   <u>FIR vs IIR Sampled Data Filters and</u>
         <u>FIR Filter Parameter Tradeoffs</u>

A two-dimensional digital filter is characterized
by the two-dimensional z transform

$$H(z_1, z_2) = \frac{\sum_{i=0}^{p} \sum_{j=0}^{q} a_{ij} z_1^{-i} z_2^{-j}}{\sum_{i=0}^{p} \sum_{j=0}^{q} b_{ij} z_1^{-i} z_2^{-j}}$$

where the set of a_{ij} and b_{ij} are constants and $b_{00}=1$. The
difference equation for this filter is of the form

$$y(n_1, n_2) = \sum_{i=0}^{p} \sum_{j=0}^{q} a_{ij} x(n_1-i, n_2-j)$$

$$- \sum_{\substack{i=0 \\ 0=i \neq j=0}}^{p} \sum_{j=0}^{q} b_{ij} y(n_1-i, n_2-j) \qquad \begin{array}{l} 0 \le n_1 \le \infty \\ 0 \le n_2 \le \infty \end{array}$$

147
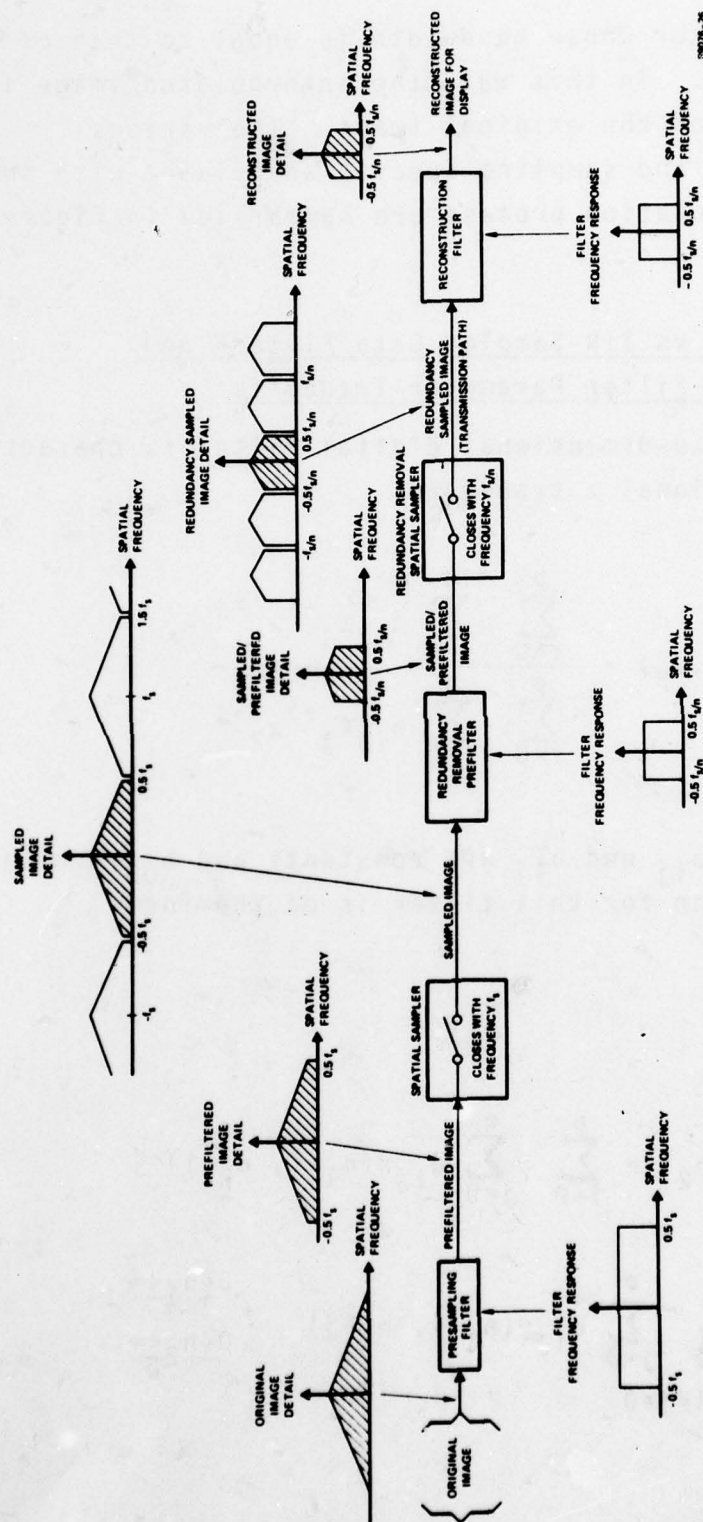
Figure 4.1.3.4

Summary of the One-Dimensional
Decimation and Interpolation Process

where the filter recursion is in the $(+n_1, +n_2)$ direction, i.e., the filter is casual.

In the equations above, $a_{ij} \equiv 0$ corresponds to IIR filters and $b_{ij} \equiv 0$ corresponds to FIR filters.

There are formidable problems associated with using two-dimensional IIR filters. These are best explained with an excerpt from Rabiner and Gold[29]:

> To design infinite impulse response filter, we must be able to choose the filter coefficients a_{ij}, b_{ij} to approximate some desired response and then we must be able to ensure that the resulting filter is stable. Both these aspects of the design problem have met with considerable difficulty to the extent that no simple design technique is readily available. It is worth discussing the sources of difficulty before proceeding to the design of two-dimensional FIR filters. As far as the filter problem is concerned, an important property of one-dimensional z transforms is the ability to factor higher-order polynomials into a product of lower-order polynomials. Thus the polynomial
>
> $$P(z) = z^4 + \alpha_1 z^3 + \alpha_2 z^2 + \alpha_3 z + \alpha_4$$
>
> can be factored into
>
> $$P(z) = (z-\beta_1)(z-\beta_2)(z-\beta_3)(z-\beta_4)$$
>
> The importance of this factorization cannot be minimized. It enables the designer to determine the stability of a high-order filter from simple criteria on the lower-order polynomials. Furthermore it provides a convenient means for realizing the filter as a cascade of lower-order filters, thereby greatly reducing certain coefficient sensitivity problems inherent in realizing high-order polynomials.

149

In two dimensions this factorization property is <u>not</u> preserved. Thus the general two-dimensional polynomial $P(z_1, z_2)$ has no simple lower-order factors. The main implication of this inability to perform factorization is that it is almost impossible to test the stability of an IIR filter, except for some simple cases. Furthermore it implies that an unstable filter cannot be stabilized by cascading an appropriate all-pass filter with the unstable filter. The final implication is that two-dimensional IIR filters cannot be realized using a cascade configuration of lower-order filters. Thus even if one could design a stable high-order IIR filter, it would be quite difficult to realize it in an efficient way.

However, in spite of these difficulties with two-dimensional IIR filters, there is one special case involving IIR filters that could be of interest: separable two-dimensional transfer functions for which

$$H(z_1, z_2) = H_1(z_1) \, H_2(z_2).$$

In this case the two-dimensional transfer function can be realized using two one-dimensional filters, where the filters could be both FIR, both IIR or one of each.

The discussions in the remainder of this section will deal with one-dimensional filters which, as just pointed out, can be used to realize two-dimensional separable transfer functions. In addition, a procedure to be described later exists for generating two-dimensional nonseparable transfer functions from one-dimensional FIR filter designs.

150

Given the need for decimation and interpolation filters, one must evaluate the relative merits of FIR and IIR sampled data filters. Generally speaking, FIR filters have exactly linear phase and thus there is no group delay signal distortion. On the other hand, IIR filters have nonlinear phase which gives rise to signal distortion, but IIR filters are generally easier to implement than FIR filters with comparable frequency transfer function magnitude response. For the purposes of this discussion ease of implementation of discrete-time filters will be measured in terms of the number of multiplies per sample. Since the importance of linear phase in image filtering is well established [12] it is of some interest to determine the magnitude of the implementation complexity penalty that results when choosing FIR filters over IIR filters. Some valuable work in this area has been reported in [13] in which quasi-equiripple FIR filters were compared to elliptic IIR filters realized as a cascade of second-order filter sections. For equivalent FIR and IIR filter designs, i.e., both having the same values of δ_1, δ_2, F_p, and F_s as defined in Figure 4.1.4-1, equivalent implementation complexity is obtained when the number of IIR multiplies per sample is equal to the number of FIR multiplies per sample:

$$\left[\frac{3n+3}{2} \right] = \left[\frac{N+1}{2} \right] \tag{4-12}$$

or

$$\frac{N}{n} \approx 3 + \frac{1}{n} \tag{4-13}$$

151
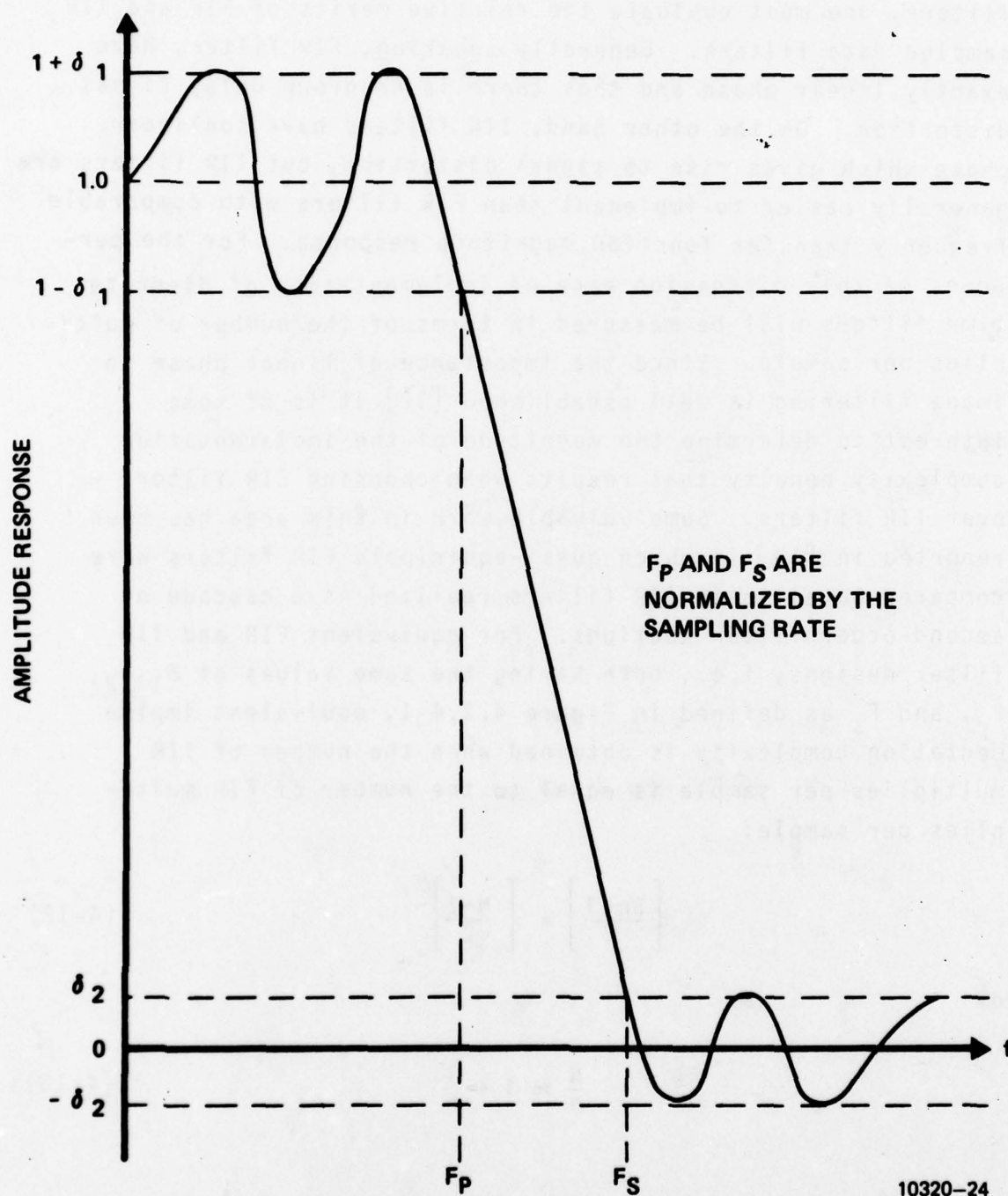
Figure 4.1.4-1
Filter Terminology

152

where

$$N = \text{number of FIR stages}$$
$$n = \text{order of IIR filter}$$

and

$$[\cdot] = \text{integer part of.}$$

Rabiner et. al measured N/n as a function of n for filter designs with a wide variety of values for F_p, F_s, δ_1, and δ_2. In general, it was found that large values of δ_1, small values of δ_2, and large transition bandwidths ($F_s - F_p$) led to FIR designs that compared favorably with IIR designs in terms of complexity. More specifically, they observed that

(1) For $F_p \geq 0.3$, N/n > 3+1/n for all values
    of δ_1, δ_2, and n

(2) For $n \geq 7$, N/n > 3+1/n for all values
    of δ_1, δ_2, and F_p

(3) The smaller the value of F_p, the larger
    the range of δ_1, δ_2, and n for which N/n <
    3+1/n

For the decimation ratios of interest in ASITS, e.g., 2 and 4, F_p = 0.25 and 0.125, respectively, so condition (1) above implies that there exist some choices of δ_1, δ_2, and $N \approx 3n+1$ for which FIR designs are less complex than IIR designs. Condition (2) implies that for N > 22, all FIR designs will be more complex than IIR designs, regardless

153

of δ_1, δ_2, and F_p. Computer simulation experiment results described in Section 4.1.7 and for which N=9, 15, and 31 indicate that N > 22 is highly desirable in the FIR filters used for decimation and interpolation. Consequently, it appears that the required FIR filters will require more multiplies per sample than equivalent IIR filters. However, the fact that the break-even point occurs for a vlaue of N as high as N=22 indicates that the additional FIR filter complexity compared to IIR filter complexity may not be of consequence for the values of N likely to be used in ASITS. Therefore, the advantage of having linear phase filters is obtained for a modest increase in computational complexity.

Given that FIR filters are appropriate for the ASITS application, the trade-offs among the various FIR filter parameters are of interest. Using the empirical relationship $\left[13\right]$:

$$N = \frac{-10 \log_{10}(\delta_1 \delta_2) -15}{14(F_s - F_p)} +1$$

these filter parameter trade-offs can be displayed graphically as shown in Figures 4.1.4-2 and 4.1.4-3. In both of these figures, $\delta_1 = \delta_2$ was assumed. An alternative method of displaying these tradeoffs that yields more insight is given in Figure 4.1.4-4.

154
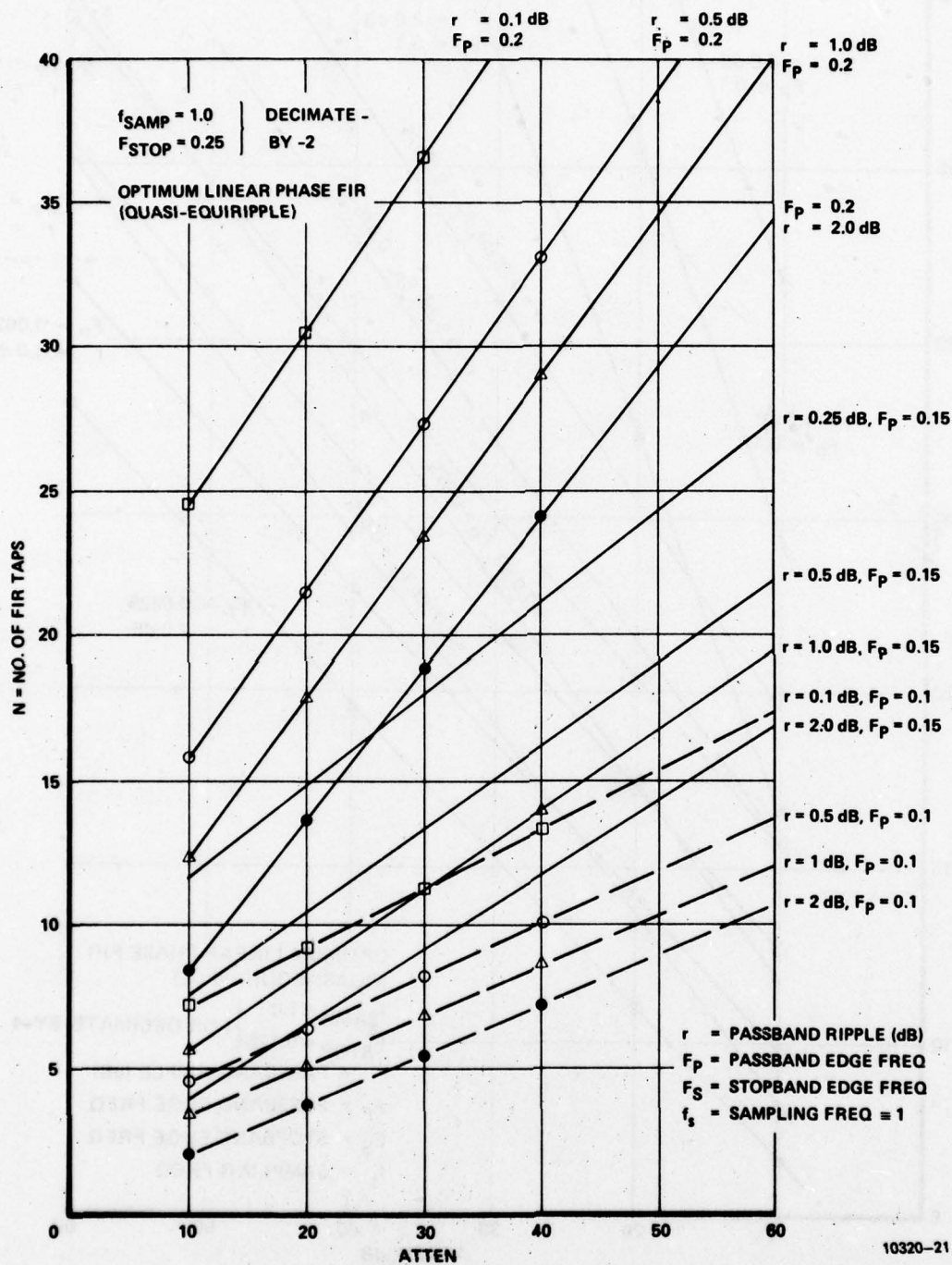
Figure 4.1.4-2

Filter Tradeoffs for D/I-by-2

155
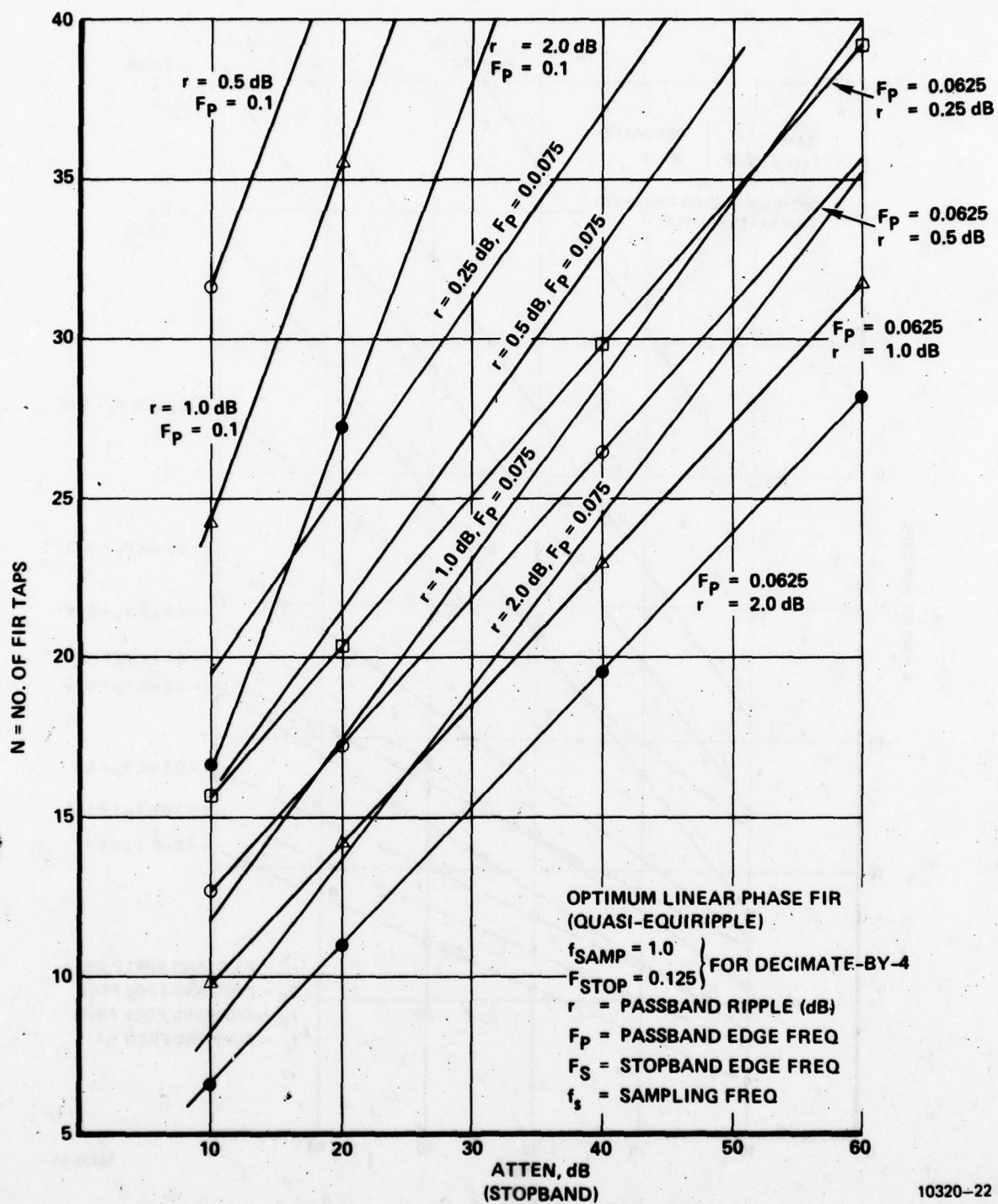
Figure 4.1.4-3

Filter Tradeoffs for D/I-by-4

156
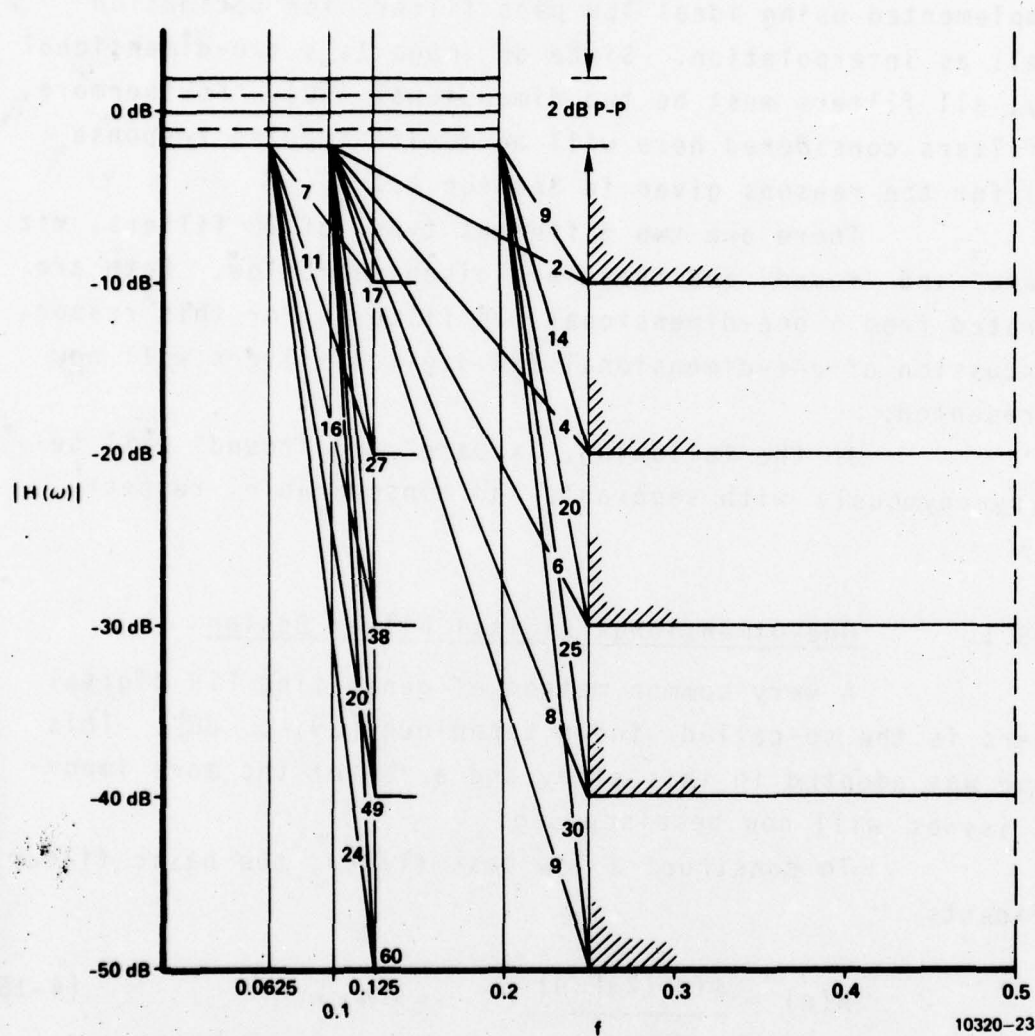
Figure 4.1.4-4

Alternative Method of Displaying

FIR Filter Trade-Offs

157

4.1.5   Two-Dimensional Filters

As discussed in Section 4.1.3, the D/I process
is implemented using ideal low pass filters for decimation
as well as interpolation. Since an image is a two-dimensional
array, all filters must be two dimensional (2D). Furthermore,
all filters considered here will be finite impulse response
(FIR) for the reasons given in Section 4.1.4.

There are two different types of 2D filters, viz.,
"square" and "round" and these are discussed below. Both are
generated from a one-dimensional FIR filter. For this reason,
a discussion of one-dimensional FIR digital filters will now
be presented.

In the following, "square" and "round" will be
used synonymously with separable and nonseparable, respect-
ively.

4.1.5.1   One-Dimensional Digital Filter Design

A very common method of generating FIR digital
filters is the so-called window technique [29, p. 88]. This
method was adopted in this study and a few of the more impor-
tant issues will now be discussed.

To construct a low pass filter, the basic filter
coefficents

$$h(n) = \frac{\sin (2\pi F n)}{\pi n}, \qquad -\infty < n < \infty \qquad (4-15)$$

are multiplied by a window $w(n)$ for $-(\frac{N-1}{2}) \leq n \leq (\frac{N-1}{2})$ where N
is an odd number for all the filters to be considered here.
The window $w(n)$ to be used here is the Kaiser window and is
given by

$$w(n) = \frac{I_0 (\beta\sqrt{1-[2n/(N-1)^2]})}{I_0(\beta)} \qquad (4-16)$$

158

for $-\left(\frac{N-1}{2}\right) \le n \le \left(\frac{N-1}{2}\right)$. The parameter β is a constant that specifies a frequency response tradeoff between the peak height of the side lobe ripples (stopband attenuation) and the width of the transition band (see Figure 4.1.5.1-1); $I_0(x)$ is the zeroth-order Bessel function. Table 4.1.5.1 presents the tradeoff between the transition bandwidth and stopband attenuation as β is varied.

TABLE 4.1.5.1

β	D	Stopband ripple (dB)
2.120	1.5	-30
3.384	2.23	-40
4.538	2.93	-50
5.658	3.62	-60
6.764	4.32	-70
7.865	5.0	-80
8.960	5.7	-90
10.056	6.4	-100

Transition bandwidth is $D/(N-1)$.

The filters designed by this technique have two properties worth noting: they have linear phase, which is extremely important for image processing, and the space (time) response $h(n)\,w(n)$ is symmetric about $n = 0$.

An example of a filter designed with this technique is shown in Figure 4.1.5.1-2, which gives the frequency response in dB. The parameters for this filter are indicated on the plot: the order of the filter (number of points) is 31, the Kaiser parameter β is 3.0, and the bandwidth ρ is 0.42.
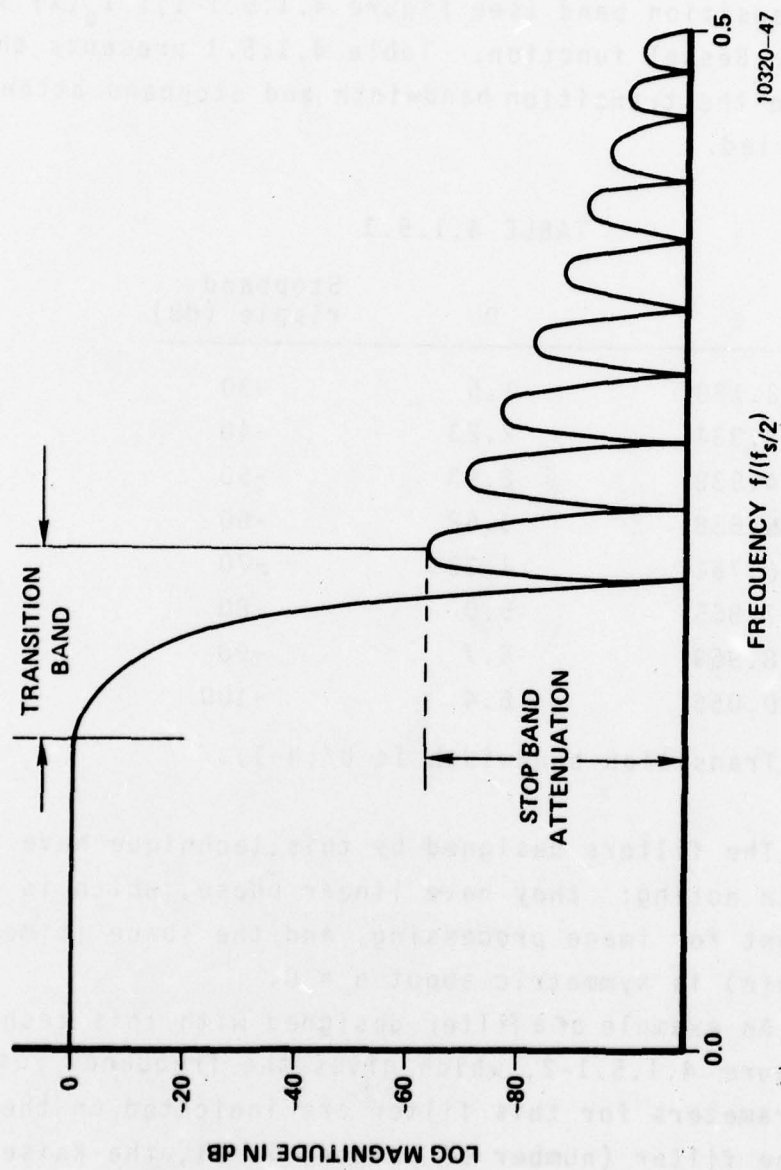
Figure 4.1.5.1-1
Definition of Filter Parameters

LOW PASS FILTER DESIGN USING SAMPLING OF SIN(T)/T WITH KAISER WINDOW

FREQUENCY DOMAIN RESPONSE

BANDWIDTH = 4200   ORDER = 31   KAISER PARAMETER = 3.0000

COMMENT 29 JUN-78   KAISER WINDOW

```
  116 ┤
-9.733 ┤
-19.583 ┤
-29.432 ┤
-39.282 ┤
-49.131 ┤  P
        │  O
-58.980 ┤  W
        │  E
-68.830 ┤  R
        │
-78.679 ┤  I
        │  N
-88.529 ┤  d
        │  B
-98.378 ┤
       1.000    512.750      1024.500      1536.250     2048.000
          256.875      768.625      1280.375      1792.125
                          FREQUENCY
```
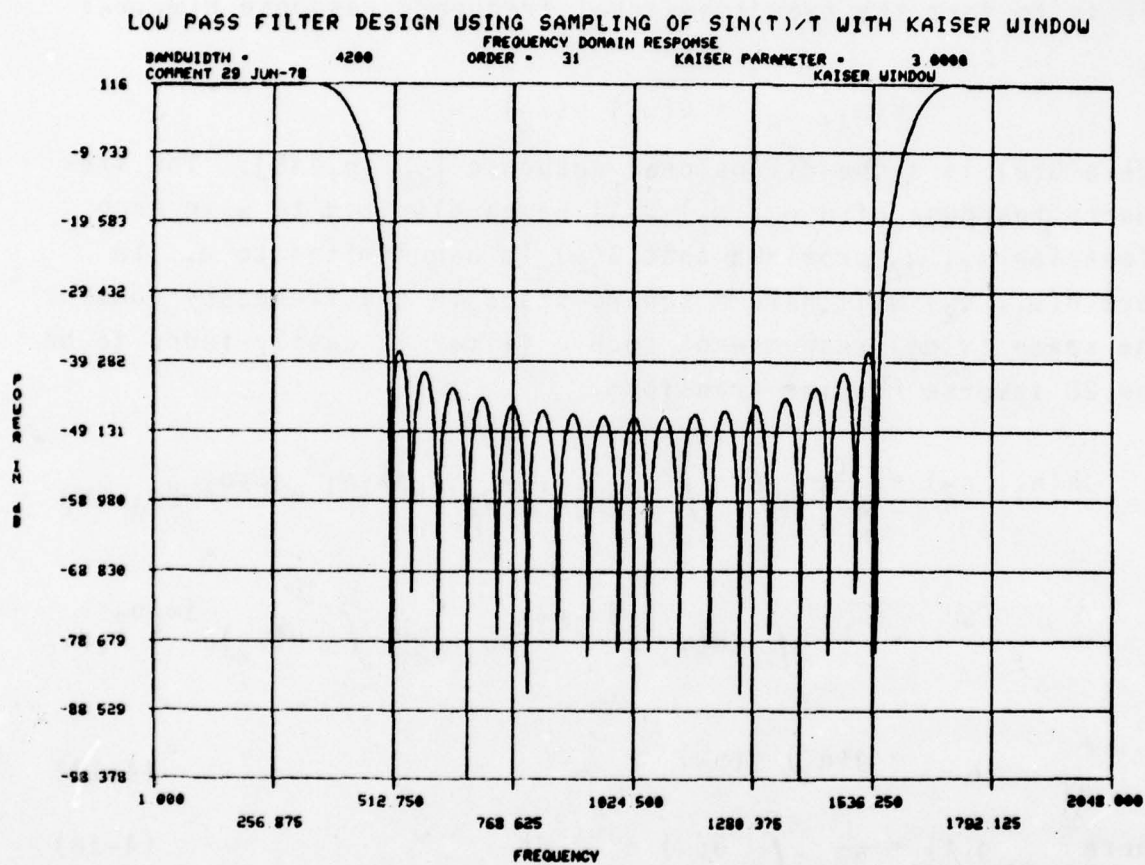
Figure 4.1.5.1-2

One-Dimensional LP Filter

161

4.1.5.2   Two-Dimensional Digital Filter Design

The one-dimensional FIR filters described above were used to construct two-dimensional filters. There are two filter classes of interest: the "square" filter and the "round" filter.

The simplest way to generate a two-dimensional LPF is to form the two-dimensional frequency response $H(\omega_1, \omega_2)$ as

$$H(\omega_1, \omega_2) = G(\omega_1) G(\omega_2)$$

where $G(\omega)$ is a one-dimensional response [2S, p.445]. The frequency response of $H(\omega_1, \omega_2)$ will be bandlimited to Ω in each dimension ω_1, ω_2 provided that $G(\omega)$ is bandlimited to Ω. In fact $H(\omega_1, \omega_2)$ will have a square shape in the frequency domain. The space (time) response of such a filter is easily found to be the 2D inverse Fourier transform.

$$h(n_1, n_2) = \frac{1}{4\pi^2} \int_{-\Omega}^{\Omega} \int_{-\Omega}^{\Omega} H(\omega_1) H(\omega_2) e^{j\omega_1 n_1} e^{j\omega_2 n_2} d\omega_1 d\omega_2$$

$$= \frac{1}{2\pi} \int_{-\Omega}^{\Omega} H(\omega_1) e^{j\omega_1 n_1} d\omega_1 \quad \frac{1}{2\pi} \int_{-\Omega}^{\Omega} H(\omega_2) e^{j\omega_2 n_2} d\omega_2$$

$$= g(n_1) g(n_2) \tag{4-17}$$

$$\text{where} \quad g(t) = \frac{1}{2\pi} \int_{-\Omega}^{\Omega} G(\omega) e^{j\omega t} dt \tag{4-18}$$

is the space (time) response of the low pass filter $G(\omega)$.

To implement such an approach, one merely generates the $g(n)$ response using the window technique described above for one-dimensional filters. This is then used to generate

$$h(n_1, n_2) = g(n_1) g(n_2) \tag{4-19}$$

162

for $-(\frac{N-1}{2}) \leq n \leq \frac{N-1}{2}$. $\qquad$ (4-20)

Of course, such a filter has a square shaped frequency response. Figure 4.1.5.1-2 shows a 1D frequency response generated using the window technique while Figure 4.1.5.2-1 shows a perspective plot of the 2D square (nonseparable) filter response generated from the 1D filter. As can be seen from this perspective plot, the passband of such a filter is square in nature.

The response in the horizontal and diagonal direction in the frequency domain for square filters is easily calculated. Since

$$H(\omega_1, \omega_2) = G(\omega_1) G(\omega_2) \qquad (4-21)$$

and for LP filters, $G(o) = 1$, it can be seen that the horizontal response is

$$H(\omega_1, o) = G(\omega_1) \cdot 1 = G(\omega_1). \qquad (4-22)$$

Furthermore the diagonal response is seen to be

$$H(\omega,\omega) = G(\omega) G(\omega)$$
$$= G^2(\omega) \qquad (4-23)$$

Hence the diagonal response in the frequency domain is down twice as many dB as the horizontal response for square filters. This can be seen by examining Figure 4.1.5.2-1.

Since imagery has no preferred direction in the frequency domain, it seems that a square filter would not be desirable since its response is not the same in all directions. For this reason, another type of 2D filter was designed and implemented. This is the so-called round filter, developed by McClellan [34]. Basically, this approach transforms a 1D FIR filter into the 2D frequency domain using the transformation

$$\text{Cos } \omega = \frac{1}{2} [\text{Cos } \omega_1 + \text{Cos } \omega_2 + \text{Cos } \omega_1 \text{ Cos } \omega_2 -1] \quad (4-24)$$

163
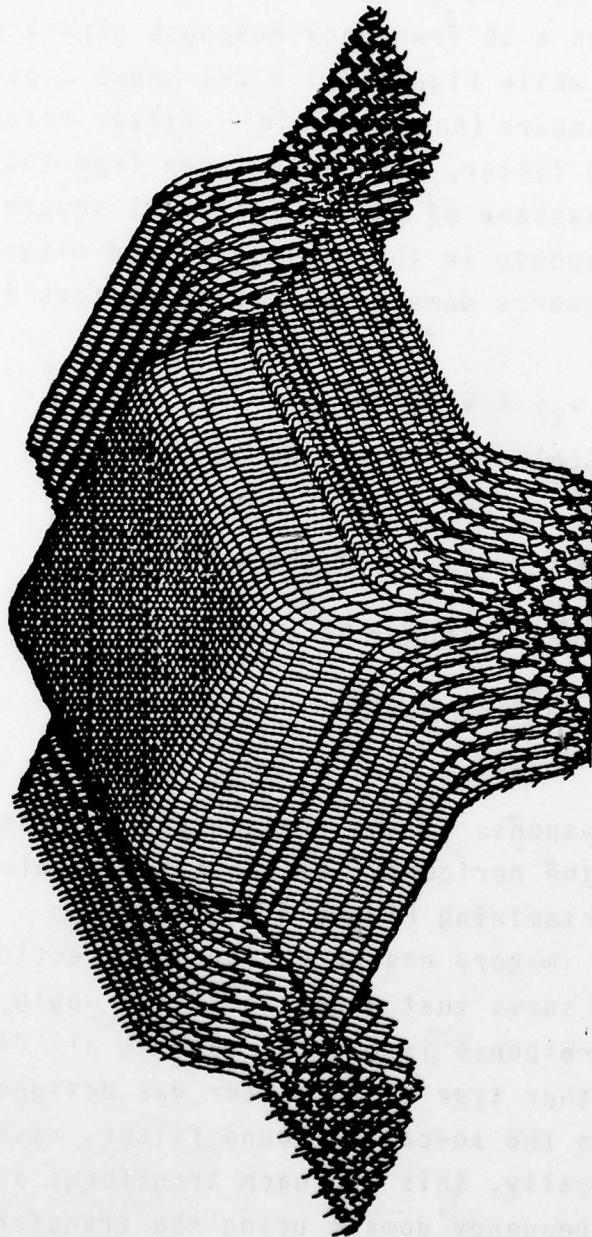
Figure 4.1.5.2-1

Two-Dimensional Square Filter, Generated
Using Filter of Figure 4.1.5.1-2

164

where ω is the radian frequency of the 1D filter while (ω_1, ω_2) are the radian frequency variables of the 2D frequency domain. This transformation generates a nearly circular frequency response. The details of this transformation are given in [29, p. 472]. An example of the 2D frequency response is given in Figure 4.1.5.2-2 which was generated from the 1D filter of Figure 4.1.5.1-2. Note the circular passband response.

These 2D filters were applied to imagery in the space domain using 2D convolution. Since the response of these filters is symmetric about the center element, 2D convolution is equivalent to multiplying the 2D response $h(n_1,n_2)$ times each pixel value and summing. This sum is the convolution. This process is repeated for each pixel value in the image. When interpolation is performed, the image is considered to consist of the decimated values along with the added zeros as discussed in Section 4.1.3.

4.1.6   <u>Two-Dimensional Decimation/Interpolation Experiments</u>

In order to evaluate the performance of the decimation/interpolation (D/I) filters described in Sections 4.1.3 and 4.1.5, computer simulations were used. Many 2D filters, both square and round, were applied to the original image of Figure 4.1.6 (A). The original is a composite image consisting of alpha-numeric characters, an aerial view, and a frequency wedge. The frequency wedge is very useful in showing the cut-off response of the low pass filters used, as well as showing aliasing effects.

The filters were applied in the space domain by using 2D convolution. Filters of three sizes were applied: 31 x 31, 15 x 15, 9 x 9. Furthermore, the Kaiser parameter β
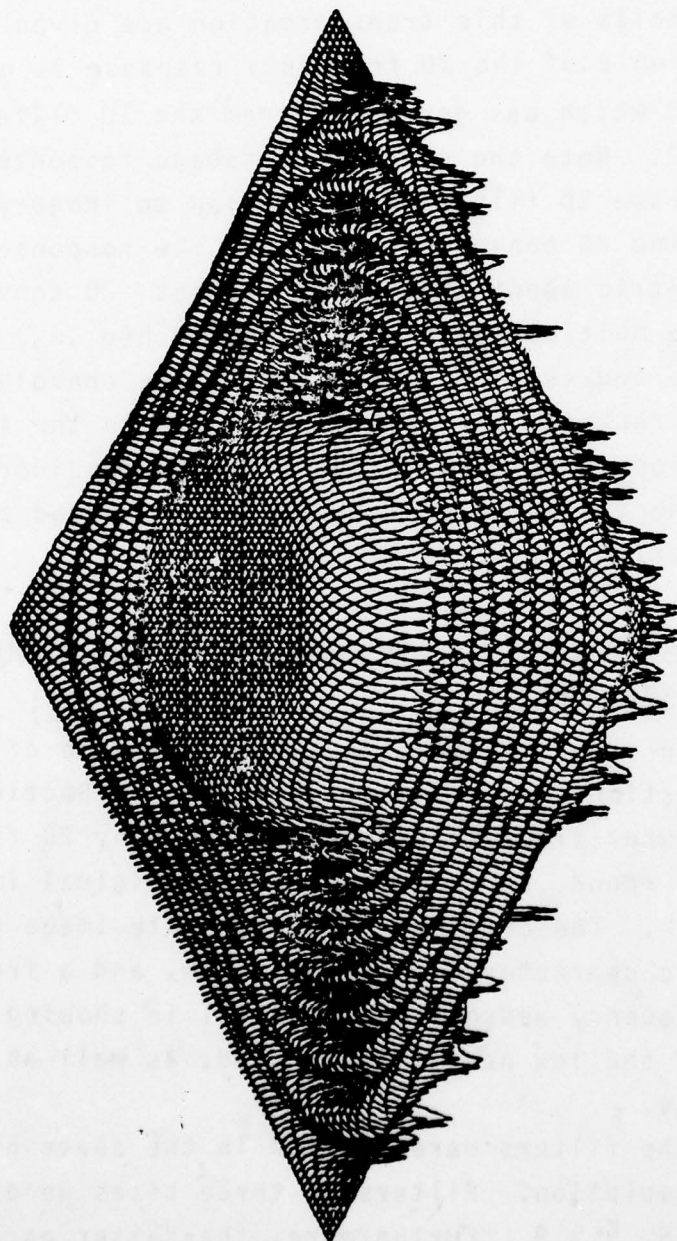
Figure 4.1.5.2-2
Two-Dimensional Round Filter, Generated
Using Filter of Figure 4.1.5.1-2

(A) Original

(B) 2:1 Decimate Only
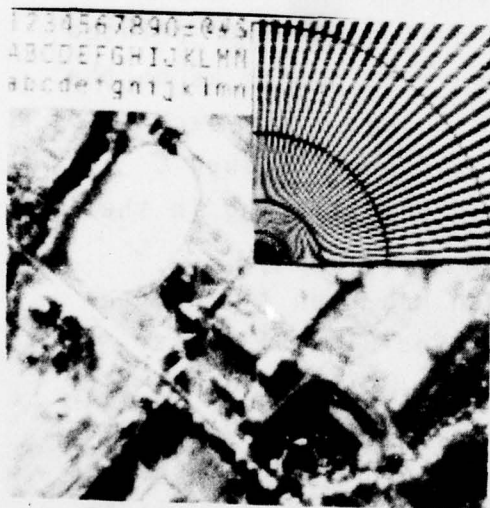
(C) 2:1 D/I Only

(D) LPF only - Round
31x31 β=1.0 ρ=0.46

Figure 4.1.6
2:1 Decimation/Interpolation Computer Simulation Results

167

was varied from 0.0 to 3.0 giving a stopband attenuation of between -20 dB and -36 dB. The bandwidth of the filters was also varied where $0 \leq \rho \leq 1.0$: when $\rho = 1.0$, the bandwidth of the filter is $f_s/2$, i.e., the maximum frequency. As described in Section 4.1.5, a 2D filter may be generated from a 1D filter. Appendix I gives all the 1D filters used here. Both square and round filters were applied to the original image. In all cases, the same filter used for decimation was also used for interpolation, unless otherwise noted.

Since filtering is implemented using 2D convolution, the boundary points will not have as many points for the convolution calculation: hence these points are not reproduced and the filtered image will always be smaller than the original.

4.1.6.1   Two-to-One Decimation/Interpolation

Figure 4.1.6. (B) through (P) shows various images for the 2-to-1 (2:1) decimation/interpolation (D/I) experiments. Figure B shows a typical decimated image printed at full resolution. There are ¼ as many data points as on the original A. If trivial interpolation is used, i.e., each point is repeated once and each line is repeated once, Figure C results. Note the blocky appearance and the aliasing in the frequency wedge.

Figure D is an image which has been filtered only--no decimation/interpolation. A round 31 x 31 filter, with Kaiser parameter $\beta = 1.0$ and bandwidth $\rho = 0.46$ was used. For an ideal LP filter, ρ should equal 0.5 for 2:1 D/I; however, when using filters of finite order, ρ can be adjusted to control the placement of the transition and stopband. It is felt that D more or less represents the best possible image that can result when doing 2:1 D/I, since only low pass filtering has been applied. If the D/I low pass filters are per-

(E) 2:1 D/I Round
31x31 β=1.0 ρ=0.46

(F) 2:1 D/I Square
31x31 β=1.0 ρ=0.46

(G) 2:1 D/I Round
31x31 β=0.0 ρ=0.45

(H) 2:1 D/I Round
31x31 β=3.0 ρ=0.42

Figure 4.1.6 (continued)
2:1 Decimation/Interpolation Computer Simulation Results

(I)   2:1 D/I Square
31x31 β=3.0 ρ=0.42

(J)   2:1 D/I Round
15x15 β=1.0 ρ=0.4

(K)   2:1 D/I Square
15x15 β=3.0 ρ=0.35

(L)   2:1 D/I Round
15x15 β=0.0 ρ=0.41

Figure 4.1.6 (continued)
Decimation/Interpolation Computer Simulation Results

(M) 2:1 D /I Round
9x9 β=0.0 ρ=0.37

(N) 2:1 D/I Round
9x9 β=1.0 ρ=0.355
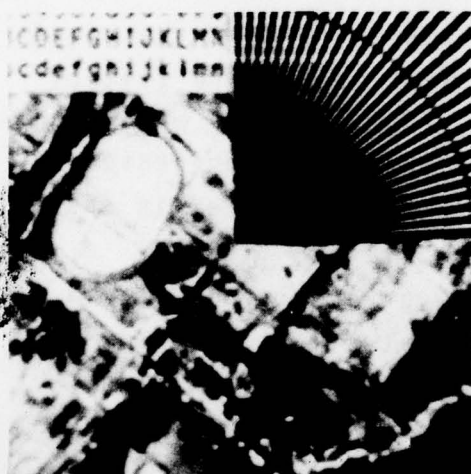
(O) 2:1 D/I Square
9x9 β=1.0 ρ=0.355

(P) 2:1 D/I Round
9x9 β=3.0 ρ=0.21

Figure 4.1.6 (continued)
2:1 Decimation/Interpolation Computer Simulation Results

171

forming correctly, then no aliasing would result and the reconstructed image would be a low pass version of the original; hence, D is the best possible image (notwithstanding the finite size of the 31 x 31 filter). Note the frequency wedge is filtered equally in all directions since a round 2D filter was used.

Figure E shows a 2:1 D/I when using a round 31 x 31, β = 1.0, ρ = 0.46 filter, the same filter as for D. These images are essentially the same; hence a 31 x 31 filter appears to be a large enough filter for 2:1 D/I.

Figure F is a square 31 x 31, β = 1.0, ρ = 0.46 filter. Hence the E and F filters differ only in that one is round and the other is square. Note that the images are virtually identical - only the frequency wedge appears different with the diagonal frequencies attenuated at a higher frequency than the horizontal (or vertical) frequencies. (It should be noted that the passband of a square LP filter is $\sqrt{2}$ greater in the diagonal direction than in the horizontal or vertical directions).

In these experiments it was found that the round filter was virtually indistinguishable from the square filter, all other parameters being equal: only the frequency wedge shows any difference with higher diagonal frequencies being passed. This is an important observation since a square filter is easier to implement as will be shown in Section 4.1.7

Figures G through I show a veriety of 31 x 31 filters and these demonstrate the fact that slight changes in the bandwidth and attenuation of the filters do not significantly affect the D/I performance for a 31 x 31 filter.

172

Figures J through L show a variaty of 15 x 15 filters. They appear to be somewhat degraded from the 31 x 31 filters.

Figures M through P show a veriety of 9 x 9 filters. Note that if the bandwidth ρ of the filter is too small, the interpolated image is blurred (see Figure P). Otherwise, a 9 x 9 filter generates an interpolated image somewhat lower in quality than the larger filters.

From these 2:1 D/I experiments, the following conclusions can be drawn:

a) A 31 x 31 filter is more than adequate for 2:1 D/I

b) A square filter can be used

c) A 9 x 9 square $\beta = 1.0$ $\rho = 0.355$ filter yields good performance, slightly degraded from the optimum LP filter.

4.1.6.2   <u>Four-to-One Decimation/Interpolation</u>

Figure 4.1.6.2 B through AA shows a wide variety of 4:1 D/I experiments. Figure A is a 4:1 decimated image only; it contains 1/16th as many data points as the original of Figure 4.1.6 A. If trivial interpolation is used, i.e., each point is repeated 3 additional times and each line is repeated 3 additional times, figure B results. Note the extreme blockiness and the severe aliasing in the frequency wedge.

Figure C is an image which has been filtered only--no D/I. A 31 x 31 filter was used and represents the best possible D/I image possible, notwithstanding the finite size of the 31 x 31 filter. (For 4:1 D/I ρ should equal 0.25 when using an ideal LPF: it may differ from this for a finite order filter.) It is felt that C represents the best possible

173

image that can result when doing 4:1 D/I since only low pass
filtering has been applied. The remainder of the images of
Figure 4.1.6.2 involve both decimation and interpolation.

Figures D through K give a variety of 31 x 31
filters varying the same parameters as for the 2:1 D/I experi-
ments above. It will be noted that ρ = 0.25 and β = 1.0, 3.0
give the best results. A smaller ρ or smaller β gives a blurred
image; a larger ρ (figure K) gives a blocky image due to the
fact that aliasing is occurring.

It will be noted that the round and square filters
are virtually indistinguishable from each other: only the fre-
quency wedge is filtered differently with the square filter al-
lowing higher diagonal frequencies to pass. This result is
true for all size filters and is important since square filters
are easier to implement than around filters (see Section 4.1.7).

Figures L through P show the 15 x 15 filtered
images. Note that ρ = 0.25 and β = 1.0, 3.0 give the best re-
sults. If ρ is smaller the image appears blurry (filter re-
jecting too much information); if β = 0, the image appears blocky
(filter allowing aliasing).

Figures Q through X show the 9 x 9 filter images.
The best image appears to be the β = 3.0 with a low bandwidth
of ρ = 0.01. This is because a 9 x 9 filter has a very wide
transition bandwidth and if ρ is any larger, aliasing will occur.
This is verified by the reconstructed images. If ρ is small
and β = 1.0, then aliasing will dominate since a β = 1.0 filter
gives only about -26 dB stopband attenuation as opposed to -36
dB for β = 3.0. This is seen in Figure W, X.

174
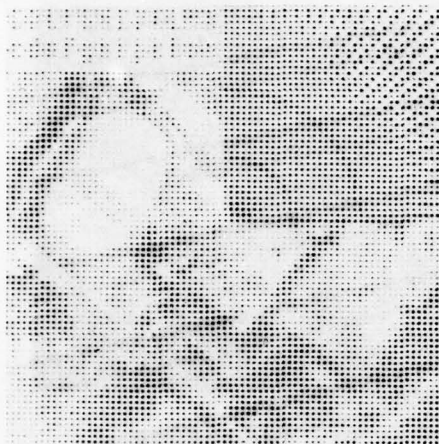
(A) 4:1 Decimate Only
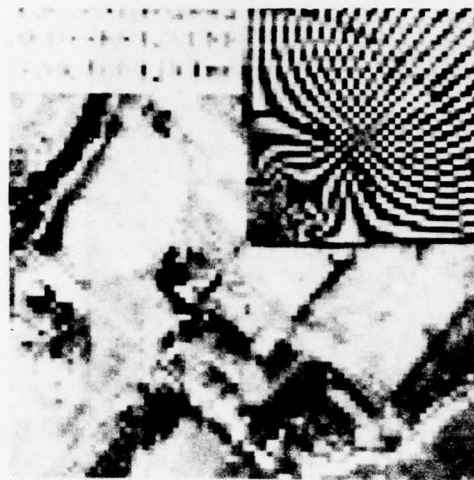
(B) 4:1 D/I Only
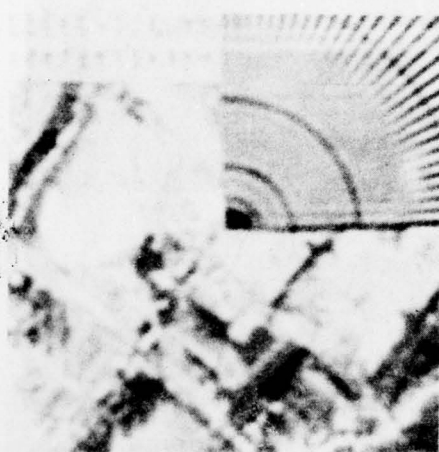
(C) LPF Only Round
31x31 β=1.0 ρ=0.25
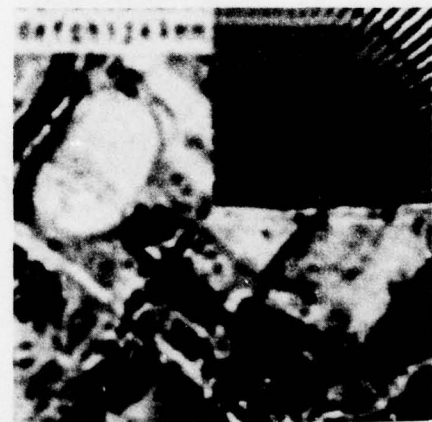
(D) 4:1 D/I Round
31x31 β=1.0 ρ=0.25

Figure 4.1.6.2
4:1 Decimation/Interpolation Computer Simulation Results

175
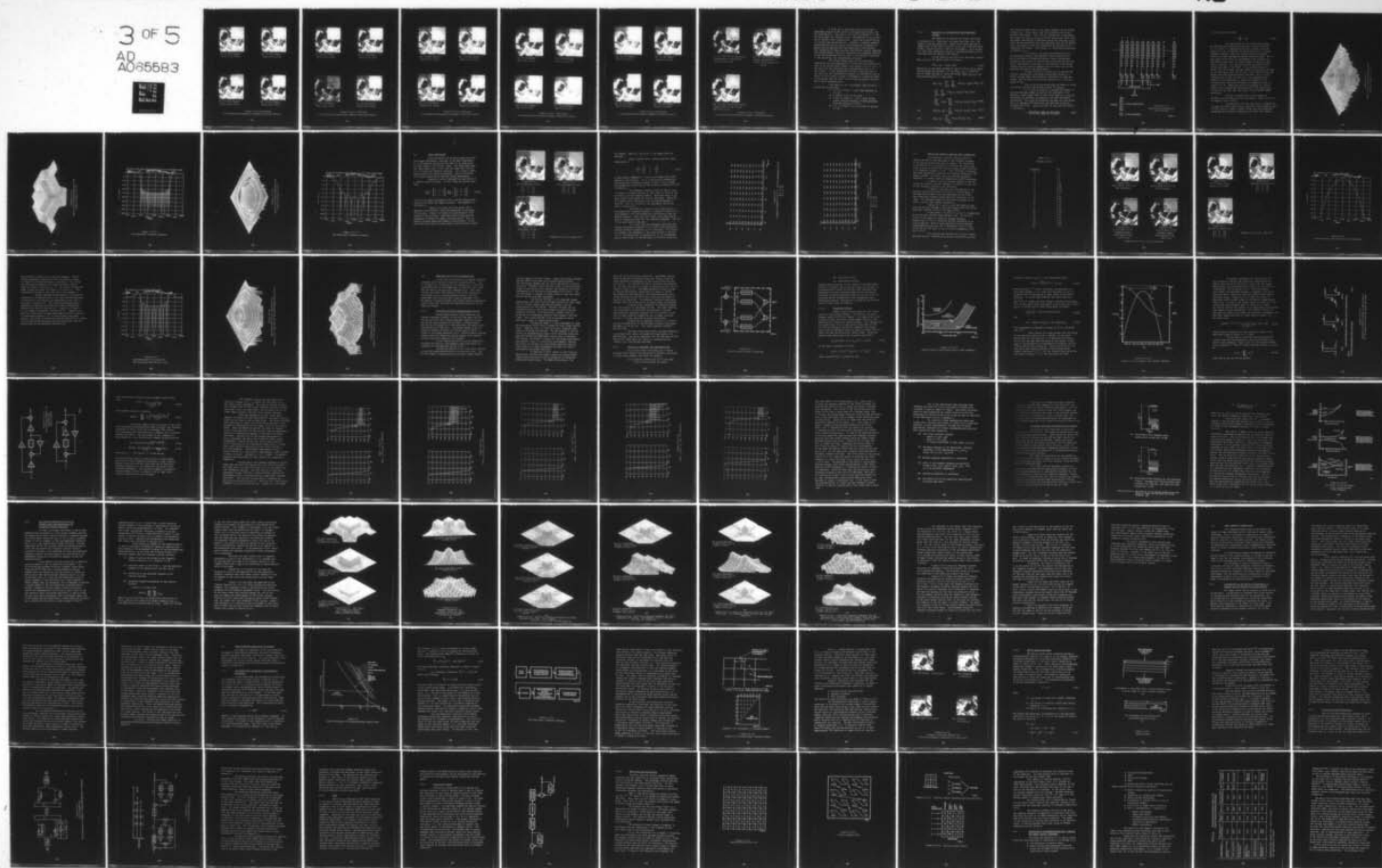
(E) 4:1 D/I Square
31x31 β=1.0 ρ=0.25

(F) 4:1 D/I Round
31x31 β=3.0 ρ=0.25
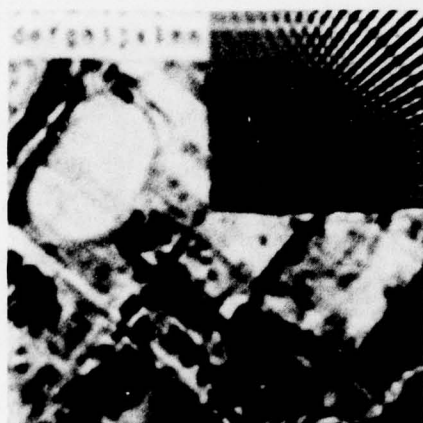
(G) 4:1 D/I Square
31x31 β=3.0 ρ=0.25

(H) 4:1 D/I Round
31x31 β=0.0 ρ=0.25

Figure 4.1.6.2 (continued)
4:1 Decimation/Interpolation Computer Simulation Results

(I) 4:1 D/I Round
31x31 β=1.0 ρ=0.21

(J) 4:1 D/I Round
31x31 β=3.0 ρ=0.17
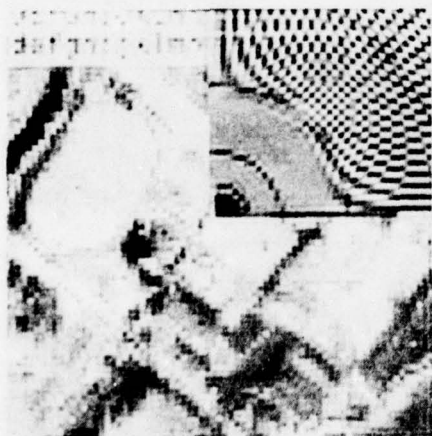
(K) 4:1 D/I Round
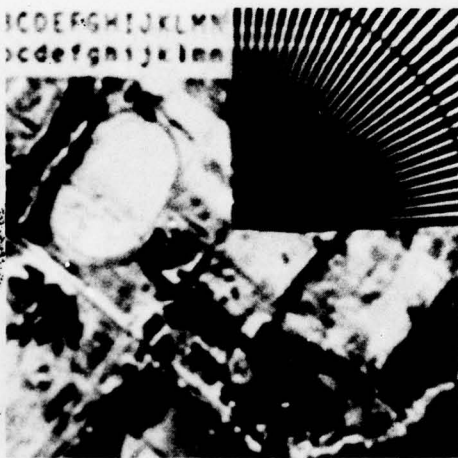31x31 β=3.0 ρ=0.42

(L) 4:1 D/I Round
15x15 β=1.0 ρ=0.25

Figure 4.1.6.2 (continued)
4:1 Decimation/Interpolation Computer Simulation Results
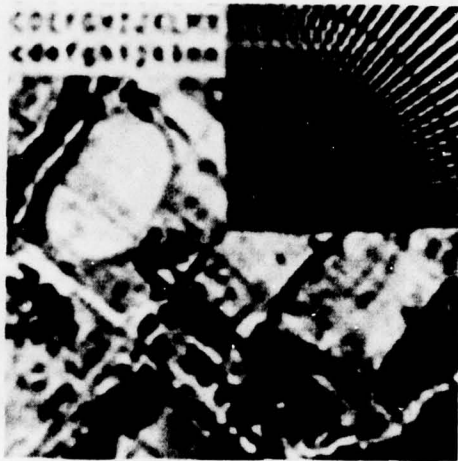
(M) 4:1 D/I Square
15x15 $\beta=1.0$ $\rho=0.25$
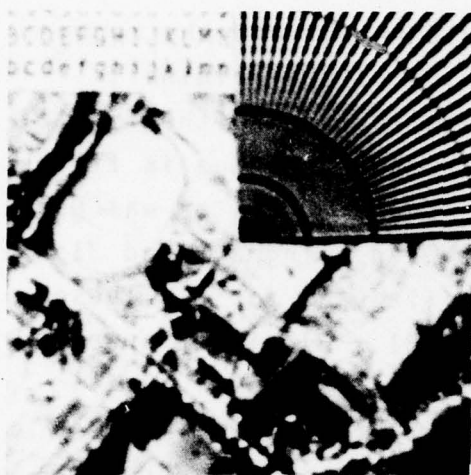
(N) 4:1 D/I Square
15x15 $\beta=3.0$ $\rho=0.25$
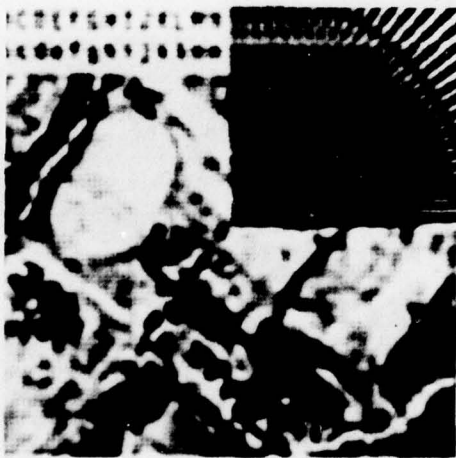
(O) 4:1 D/I Round
15x15 $\beta=0.0$ $\rho=0.25$

(P) 4:1 D/I Round
15x15 $\beta=1.0$ $\rho=0.14$

Figure 4.1.6.2 (continued)
4:1 Decimation/Interpolation Computer Simulation Results

(Q) 4:1 D/I Round
9x9 β=3.0 ρ=0.01
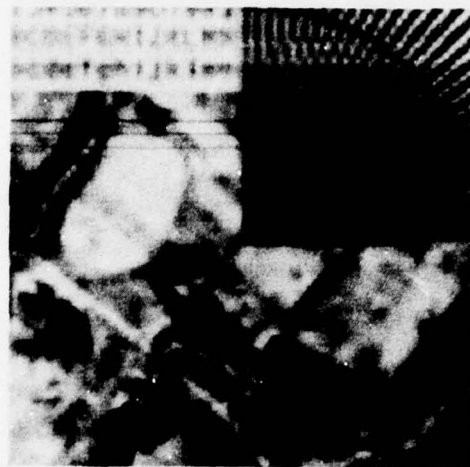
(R) 4:1 D/I Round
9x9 β=3.0 ρ=0.25

(S) 4:1 D/I Square
9x9 β=3.0 ρ=0.25

(T) 4:1 D/I Round
9x9 β=1.0 ρ=0.25

Figure 4.1.6.2   (continued)
4:1 Decimation/Interpolation Computer Simulation Results

179

(U) 4:1 D/I Square
9x9 β=1.0 ρ=0.25

(V) 4:1 D/I Round
9x9 β=0.0 ρ=0.25

(W) 4:1 D/I Round
9x9 β=1.0 ρ=0.05

(X) 4:1 D/I Square
9x9 β=1.0 ρ=0.05

Figure 4.1.6.2 (continued)
4:1 Decimation/Interpolation Computer Simulation Results
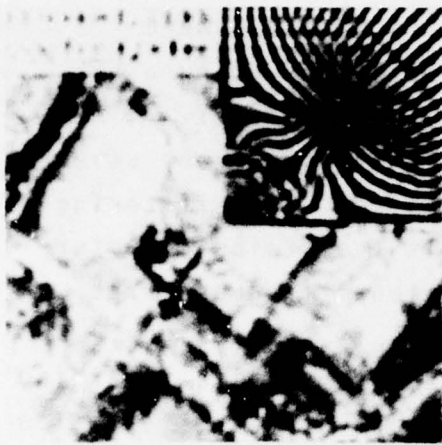
(Y) 4:1 D/I Trivial Decimation
Interpolation Filter Round
31x31 β=1.0 ρ=0.25
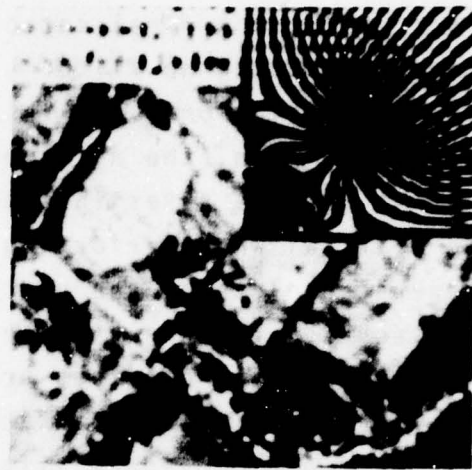
(Z) 4:1 D/I Trivial Deci-
mation Interpolation
Filter Round 15x15 β=1.0
ρ=0.25
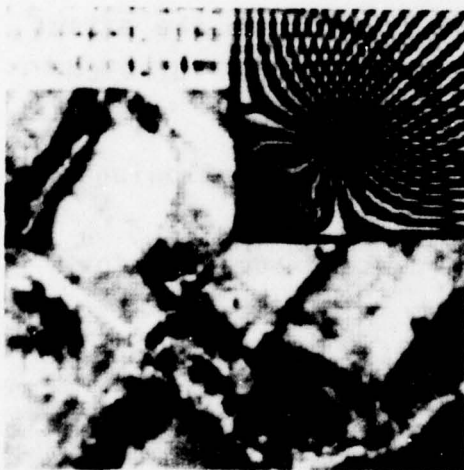
(AA) 4:1 D/I Trivial Decimation
Interpolation Filter Square
9x9 β=1.0 ρ=0.25

Figure 4.1.6.2 (continued)
4:1 Decimation/Interpolation Computer Simulation Results

181

A final set of experiments for 4:1 D/I were performed using no filter prior to decimation but using a LPF for interpolation. The results are shown in Figures Y, Z, AA. As can be seen, the aliasing error from sampling is very severe and it remains after interpolating. Hence the LP prefiltering is critical when performing D/I. Appendix I contains computer-generated plots of the various one-dimensional frequency responses used to generate the two-dimensional filter designs. This collection of plots provides quantitative results regarding the in-band ripple, transition bandwidth, and stopband rejection of the two-dimensional filters used in the computer simulation of the decimation and interpolation processes.

One unanticipated result of the simulation experiments was the appearance of a fine grid-like structure in some of the reconstructed images (see Figure 4.1.6.2 V, W, X, Z, AA) which had been decimated and interpolated using 9 x 9 FIR filters. It was determined that this effect was due to the nature of the interpolation process; an explanation and analysis of this effect is given in Appendix J. Since the effect is noticeable only for small filter sizes it poses no problem for an ASITS implementation.

From these 4:1 D/I experiments, the following conclusions can be drawn:

a) A 31 x 31 filter is more than adequate for 4:1 D/I

b) A square filter can be used

c) A 15 x 15 square $\beta = 1.0$ $\rho = 0.25$ filter yields good performance, slightly degraded from the optimum LP filter.

d) A 9 x 9 filter is not sufficient to perform 4:1 D/I.

4.1.7   Separable vs. Nonseparable Two-Dimensional Filters

The design of 2D digital FIR filters was given in Section 4.1.5. There were two types discussed, viz., the round LPF and the square LPF. These filters were applied to imagery and, as was seen in Section 4.1.6, the round and square filters yielded virtually identical performance. This section will show that substantial savings in hardware/software can be realized using the square filter design.

As was shown in section 4.1.5, the space response $\bar{h}(n_1, n_2)$ of a 2D square filter is given as

$$\bar{h}(n_1, n_2) = h(n_1)\, h(n_2) \tag{4-25}$$

where $h(n)$ is the space response of the 1D filter used to generate the square 2D response. If this $\bar{h}(n_1, n_2)$ is convolved with an image $x(p_1, p_2)$ to yield the output image $y(m_1, m_2)$, the convolution equation is applicable:

$$y(m_1, m_2) = \sum_{p_1=0}^{N-1} \sum_{p_2=0}^{N-1} x(m_1-p_1, m_2-p_2)\, \bar{h}(p_1, p_2)$$

$$= \sum_{p_1=0}^{N-1} \sum_{p_2=0}^{N-1} x(m_1-p_1, m_2-p_2)\, h(p_1)\, h(p_2)$$

$$= \sum_{p_1=0}^{N-1} h(p_1) \sum_{p_2=0}^{N-1} x(m_1-p_1, m_2-p_2)\, h(p_2) \tag{4-26}$$

Let

$$q(m_1-p_1, m_2) = \sum_{p_2=0}^{N-1} x(m_1-p_1, m_2-p_2)\, h(p_2) \tag{4-27}$$

Then

$$y(m_1, m_2) = \sum_{p_1=0}^{N-1} h(p_1)\, q(m_1-p_1, m_2). \tag{4-28}$$

183

This equation states that if the space response can be written as $\bar{h}(n_1, n_2) = h(n_1) h(n_2)$, then 2D convolution can be performed in two steps: first vertical convolution is performed with $h(p_2)$ and $x(m_1-p_1, m_2-p_2)$ to yield $q(m_1-p_1, m_2)$ after which horizontal convolution is performed using $h(p_1$ and $q(m_1-p_1, m_2)$. Since the 2D convolution has been separated into two 1D convolutions, the square filter will henceforth be referred to as a "separable" 2D filter. This process is illustrated graphically in Figure 4.1.7-1.

It is easy to see that each output point of a 2D convolution using a NxN separable filter requires an N point correlation followed by another N point correlation. (Actually, this result is not strictly true since $(N-1)/2$ vertical convolutions on the ends of the data must first be performed, but this will be ignored since it occurs only at the beginning and end of the convolution.)

If one utilizes a 1D array scan to perform the vertical convolution, with these convolutions stored in a buffer storage where the horizontal convolution is then performed, then an array of size N can perform an N x N 2D separable filter.

This is to be contrasted with the method of using a 2D array scan which would have to have N^2 elements.

It is also instructive to compare the number of multiply-and-adds needed to perform a 2D separable filter function. Each output point of the filter requires a vertical correlation of N points, followed by an N point horizontal correlation. This give 2N multiplies and adds for each output point as opposed to N^2 multiplies and adds when using non-separable 2D filter. Hence the ratio of required calculations r, defined as

$$r = \frac{\text{multiplies, adds for 2D square}}{\text{multiplies, adds for 2D round}} \qquad (4\text{-}29)$$

Figure 4.1.7-1
Separable Two-Dimensional
FIR Filtering
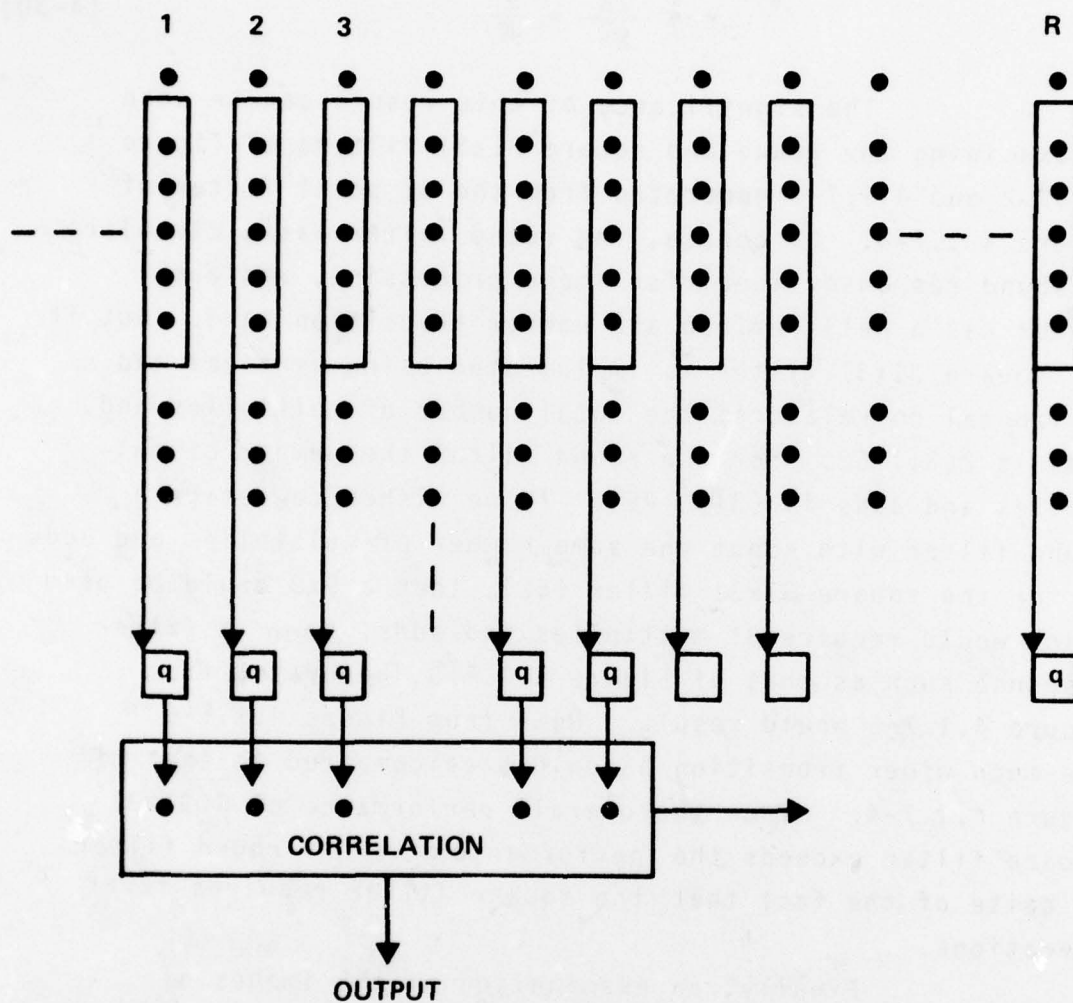
LEGEND:
5 POINT CORRELATION

q STORAGE REGISTER

1 2 3 ... R

CORRELATION

OUTPUT

10320-13

185

is, as we have just shown

$$r = \frac{2N}{N^2} = \frac{2}{N} \;.$$ (4-30)

The significance of this result can be seen
by examining the round and square 31x31 filters of Figure
4.1.7-2 and 4.1.7-3 generated from the 31 point filter of
Figure 4.1.7-4. Of course, the round filter has a circular
passband response, ideal for image processing, and each
filter has a well defined and narrow transition band. But if
the square 31x31 filter is implemented using vertical and
horizontal correlators, the total number of multiplies and
adds is 2(31)=62. For the round filter the number of mul-
tiplies and adds is $(31)^2$=961. If we wished to design a
round filter with about the same number of multiplies and adds
as for the square 31x31 filter (62), then a 9x9 could be used
which would require 81 multiplies and adds. Then a filter
response such as that of Figure 4.1.7-5, generated from
Figure 4.1.7-6 would result. Note from Figure 4.1.7-6
the much wider transition bandwidth as compared to that of
Figure 4.1.7-4. Hence the overall performance of a 31x31
square filter exceeds the performance of a 9x9 round filter
in spite of the fact that the square filter requires fewer
operations.

Finally, an examination of the images of
Section 4.1.6 will bear out this conclusion : Figure 4.1.6.2-E
is superior to 4.1.6.2-Q.

In conclusion, for the same level of complexity,
a square 2D filter rather than a round 2D filter should be used
for D/I since it yields a better filter when the transition
bandwidth and stop-band attenuation are taken into account.

186
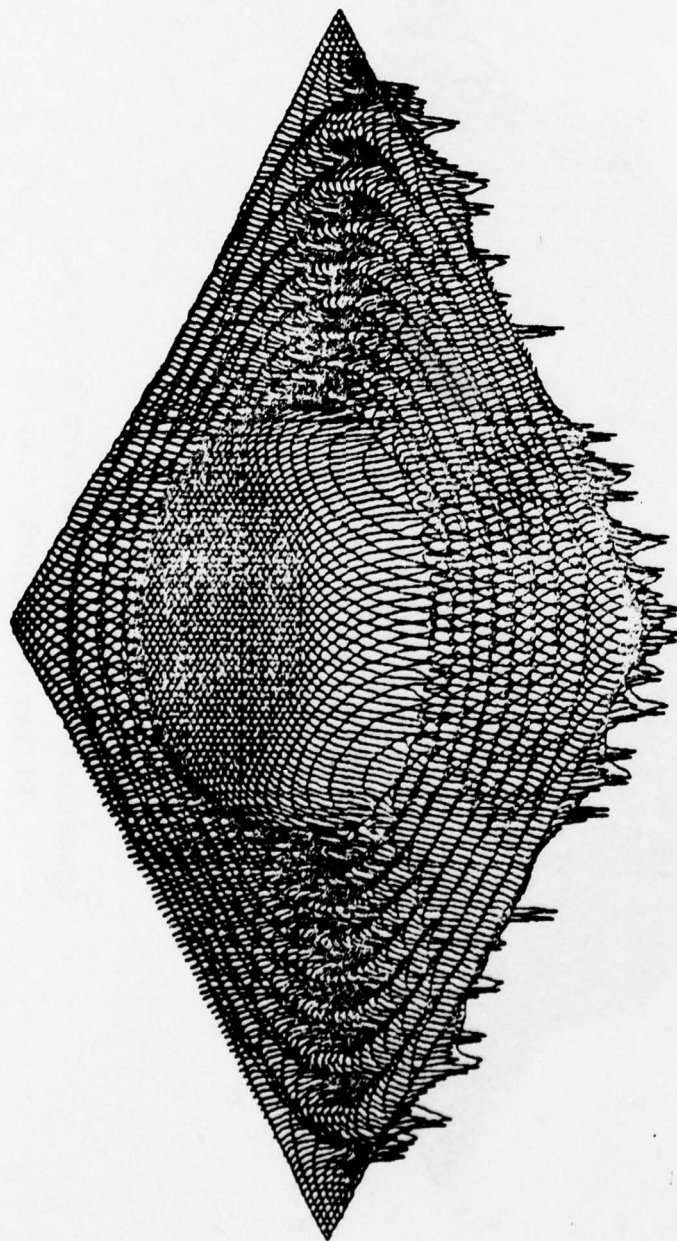
Figure 4.1.7-2
Round Filter (31x31) Generated From
Filter of Figure 4.1.7-4

187
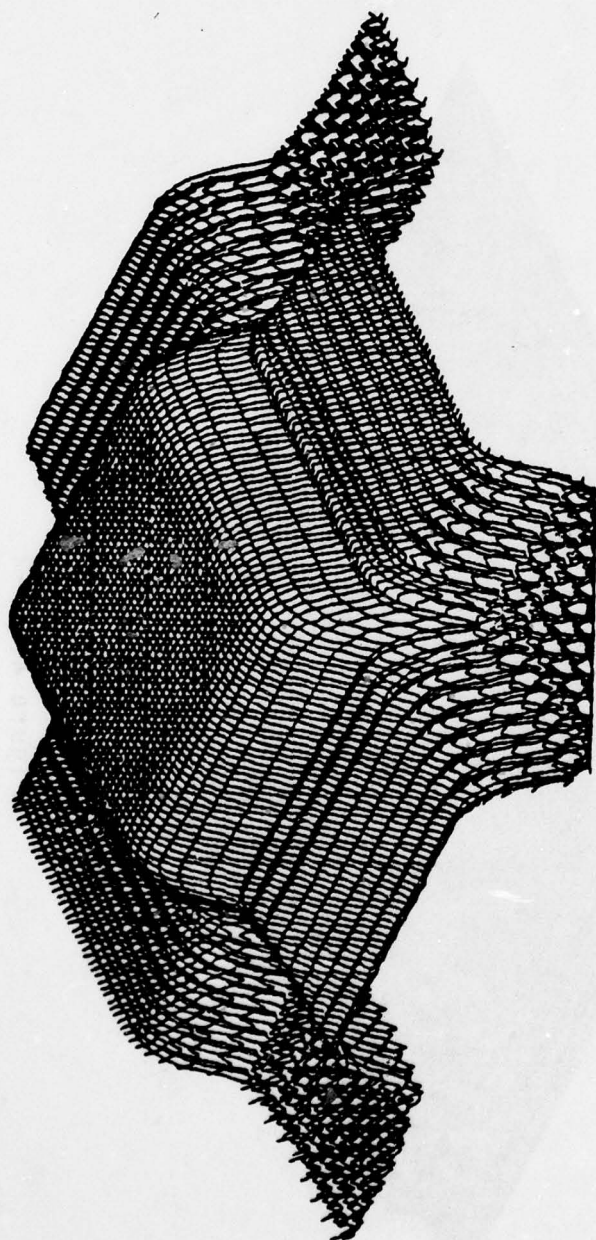
Figure 4.1.7-3

Square Filter (31x31) Generated From

Filter of Figure 4.1.7-4

188
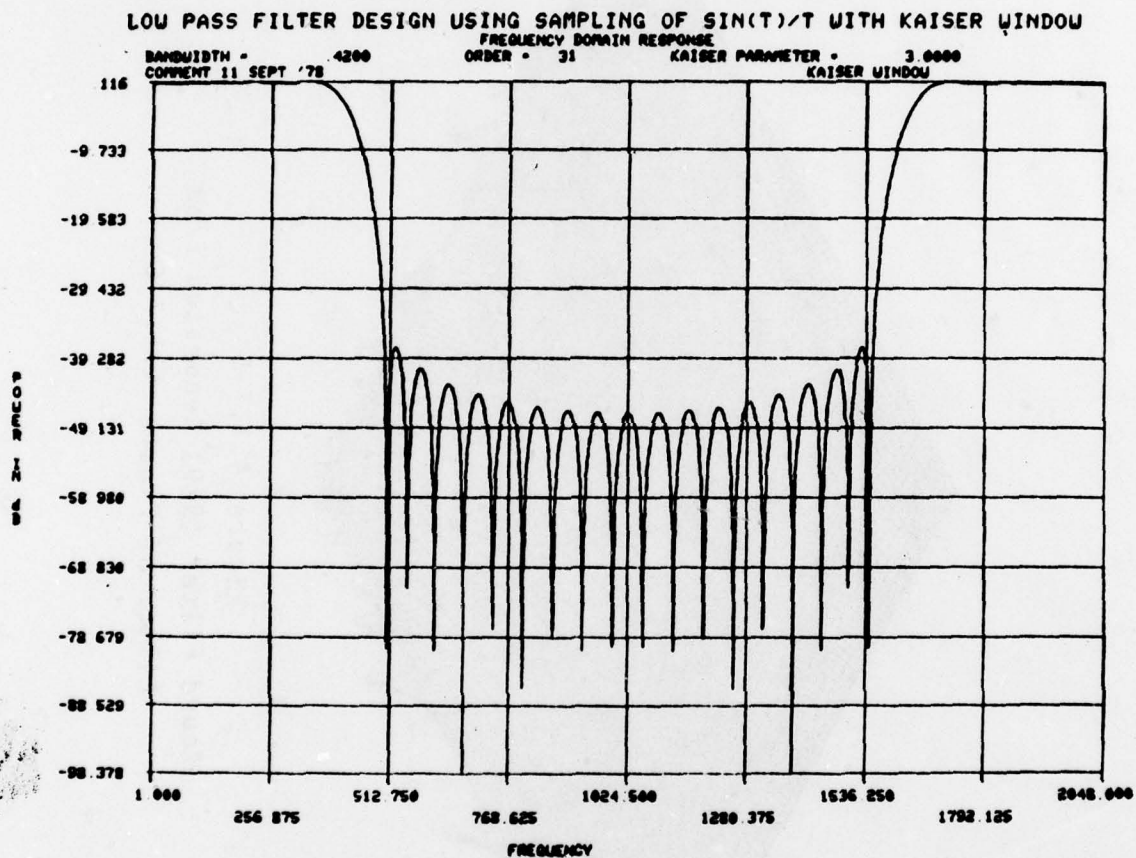
Figure 4.1.7-4

One-Dimensional Frequency Response
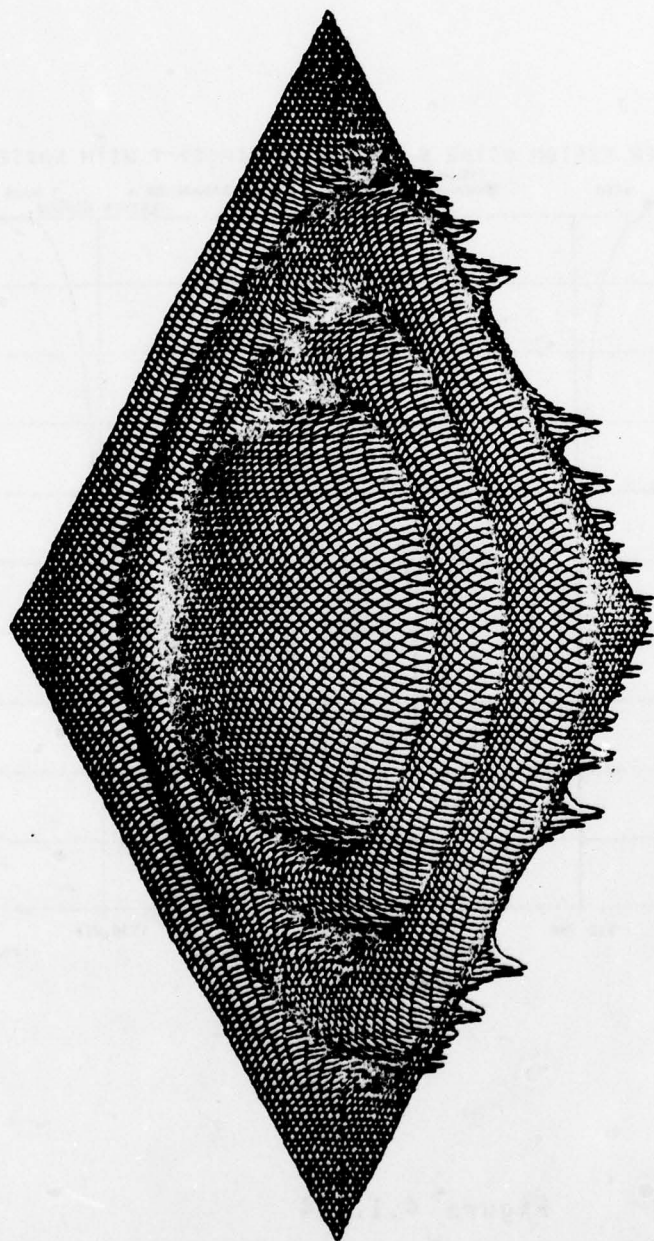
Figure 4.1.7-5
Round Filter (9x9) Generated From
Filter of Figure 4.1.7-6

LOW PASS FILTER DESIGN USING SAMPLING OF SIN(T)/T WITH KAISER WINDOW

FREQUENCY DOMAIN RESPONSE

BANDWIDTH = 2100   ORDER = 9   KAISER PARAMETER = 3.0000

COMMENT 11 SEPT '78   KAISER WINDOW
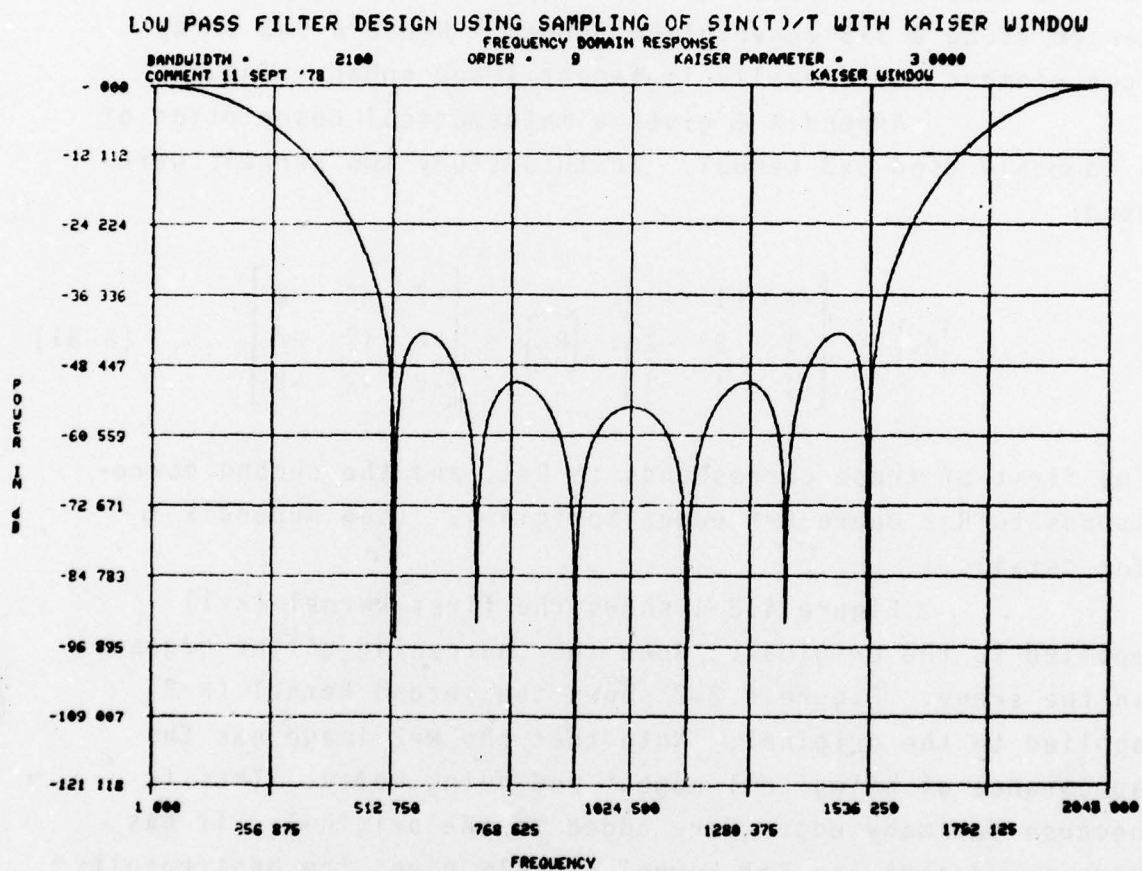
Figure 4.1.7-6
One-Dimensional Frequency Response

191

4.2 IMAGE ENHANCEMENT

Array processing can be easily applied to perform image enhancement, sometimes called edge enhancement. It is performed by generating the edges of an image which are then added to the original image. The added edges make the image appear more "crisp" with the edges more visible. It is a simple but powerful technique. It is usually implemented using a 3x3 convolution kernel. Hence a 3x3 array scan element could easily implement image enhancement.

Appendix G gives a mathematical description of a commonly used 3x3 kernel. In this study two kernels were used:

$$\begin{bmatrix} R_1 \end{bmatrix} = \begin{bmatrix} -1 & -1 & -1 \\ -1 & 9 & -1 \\ -1 & -1 & -1 \end{bmatrix}, \begin{bmatrix} R_2 \end{bmatrix} = \begin{bmatrix} -2 & -2 & -2 \\ -2 & 17 & -2 \\ -2 & -2 & -2 \end{bmatrix} . \quad (4\text{-}31)$$

The first of these corresponds to R=1, and the second corresponds to R=2 where R=% edges/%original. (See Appendix G for details.)

Figure 4.2-1 shows the first kernel (R=1) applied to the original. Note the sharpening of the edges in the scene. Figure 4.2-2 shows the second kernel (R=2) applied to the original. Note that the R=2 image has the appearance of being "all edges" and being noisy. This is because too many edges were added to the original. It has been found that the R=1 kernel usually gives the best results

192

Figure 4.2-1
R=1 Enhancement Filter

$$\begin{bmatrix} -1 & -1 & -1 \\ -1 & 9 & -1 \\ -1 & -1 & -1 \end{bmatrix}$$

Figure 4.2-2
R=2 Enhancement Filter

$$\begin{bmatrix} -2 & -2 & -2 \\ -2 & 17 & -2 \\ -2 & -2 & -2 \end{bmatrix}$$
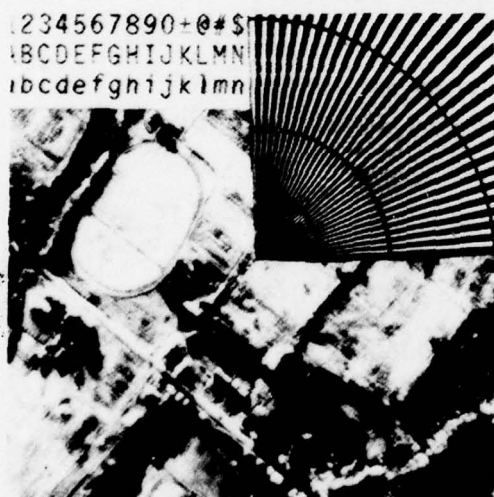
Figure 4.2-3
Enhancement Filter

$$\begin{bmatrix} 1 & -2 & 1 \\ -2 & 5 & -2 \\ 1 & -2 & 1 \end{bmatrix}$$

Figures 4.2-1, 4.2-2 and 4.2-3

193

for imagery. When R>1, the noise in the image starts to dominate.

Another kernel which could be used for image enhancement is

$$[S] = \begin{bmatrix} 1 & -2 & 1 \\ -2 & 5 & -2 \\ 1 & -2 & 1 \end{bmatrix} \qquad (4-32)$$

as described in Appendix H. Figure 4.2-3 shows this kernel applied to the original. It is instructive to examine the two-dimensional frequency response of $[S]$ as well as $[R_1]$. The mathematical derivation of the frequency response is given in Appendix H.

The frequency response in dB for $[S]$ is given in Figure 4.2-4 where the gain of the filter is given at the grid points of the frequency domain. Note that there is no gain along the horizontal or vertical direction. Hence $[S]$ will enhance only frequencies that are not horizontal or vertical. This is, of course, not desirable, and can be seen in Figure 4.2-3.

The kernel R_1, however, has a more circular two-dimensional frequency response, as shown in Figure 4.2-5. (See Appendix H for the mathematical derivation of the frequency response.) Note that this kernel gives about 20 dB gain at frequencies near half the sampling frequency. The R=2 filter gives about 25 dB gain.

It is seen from the frequency plots that the kernels described in Appendix G will yield good performance and will enhance frequencies in all directions. This kernel is, however, not separable in the sense defined in Section 4.1.7. The kernel $[S]$ is separable but is not recommended due to lack of gain in the horizontal or vertical direction.
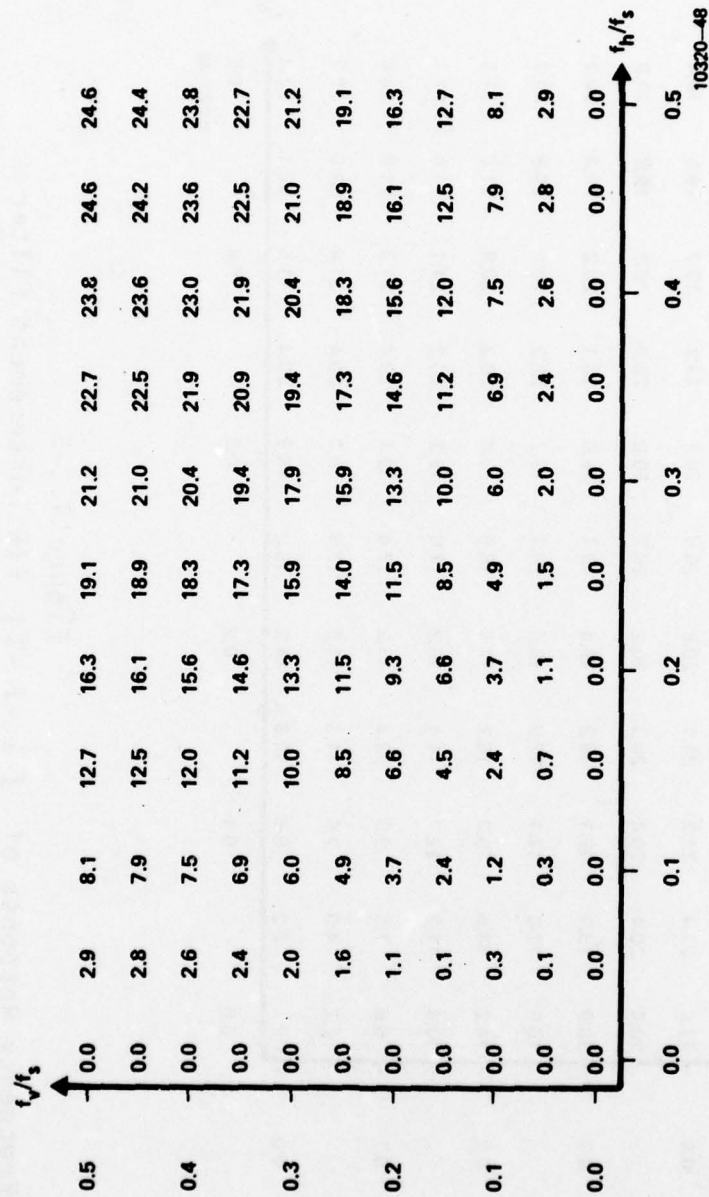
Figure 4.2-4

Frequency Response of $\begin{bmatrix} 1 & -2 & 1 \\ -2 & 5 & -2 \\ 1 & -2 & 1 \end{bmatrix}$ FIR Enhancement Filter

f_v/f_s \ f_h/f_s	0.0	0.1	0.2	0.3	0.4	0.5
0.5	0.0	2.9	8.1	12.7	16.3	19.1	21.2	22.7	23.8	24.6	24.6
0.4	0.0	2.8	7.9	12.5	16.1	18.9	21.0	22.5	23.6	24.2	24.4
	0.0	2.6	7.5	12.0	15.6	18.3	20.4	21.9	23.0	23.6	23.8
0.3	0.0	2.4	6.9	11.2	14.6	17.3	19.4	20.9	21.9	22.5	22.7
	0.0	2.0	6.0	10.0	13.3	15.9	17.9	19.4	20.4	21.0	21.2
0.2	0.0	1.6	4.9	8.5	11.5	14.0	15.9	17.3	18.3	18.9	19.1
	0.0	1.1	3.7	6.6	9.3	11.5	13.3	14.6	15.6	16.1	16.3
0.1	0.0	0.1	2.4	4.5	6.6	8.5	10.0	11.2	12.0	12.5	12.7
	0.0	0.3	1.2	2.4	3.7	4.9	6.0	6.9	7.5	7.9	8.1
0.0	0.0	0.1	0.3	0.7	1.1	1.5	2.0	2.4	2.6	2.8	2.9
	0.0	0.0	0.0	0.0	0.0	0.0	0.0	0.0	0.0	0.0	0.0

10320—48

195

Figure 4.2-5. FIR Enhancement Filter

Frequency Response of
$$\begin{bmatrix} -1 & -1 & -1 \\ -1 & 9 & -1 \\ -1 & -1 & -1 \end{bmatrix}$$

Frequency response (in dB) as a function of f_v/f_s (vertical axis) and f_h/f_s (horizontal axis):

f_v/f_s \ f_h/f_s	0.0	0.05	0.1	0.15	0.2	0.25	0.3	0.35	0.4	0.45	0.5
0.5	22.3	22.2	22.0	21.7	21.3	20.8	20.3	19.8	19.4	19.2	19.1
0.45	22.1	22.0	21.8	21.6	21.2	20.8	20.3	19.9	19.5	19.3	19.2
0.4	21.5	21.4	21.3	21.1	20.8	20.5	20.2	19.9	19.7	19.5	19.4
0.35	20.4	20.4	20.4	20.3	20.2	20.2	20.1	20.0	19.9	19.9	19.8
0.3	18.9	19.0	19.1	19.2	19.4	19.7	19.9	20.1	20.2	20.3	20.3
0.25	16.9	17.0	17.4	17.9	18.5	19.1	19.7	20.2	20.5	20.8	20.8
0.2	14.2	14.5	15.2	16.2	17.4	18.5	19.4	20.2	20.8	21.2	21.3
0.15	10.8	11.3	12.7	14.4	16.2	17.9	19.2	20.3	21.1	21.6	21.7
0.1	6.6	7.6	9.9	12.7	15.2	17.4	19.1	20.4	21.3	21.8	22.0
0.05	2.2	4.0	7.6	11.3	14.5	17.0	19.0	20.4	21.4	22.0	22.2
0.0	0	2.2	6.6	10.8	14.2	16.9	18.9	20.4	21.5	22.1	22.3

10320—49

196

4.3   <u>MODULATION TRANSFER FUNCTION (MTF) CORRECTION</u>

The modulation transfer function (MTF) is loosely defined as the magnitude of the frequency response of an imaging system from input to output. MTF correction is defined here as the process of filtering the input range prior to passing through the imaging system so that the effective frequency response is flat. This, in effect, eliminates the image degradation caused by the frequency response of the imagery system. Of course, noise can not be too great; otherwise, its effects will be enhanced by the MTF correction.

In order to give a concrete example of how MTF correction performs, the MTF response of Table 4.3.1 was used as the frequency response to be corrected.

A computer subroutine was incorporated in the computer program described in Section 4.1.5 which reads in the magnitude response, and then generates an FIR filter whose magnitude response approximates the reciprocal of the input. This program allows for the Kaiser parameter to be used to control the stopband attenuation.

Figures 4.3.1 and 4.3.2 are the result of passing the original through a round and square 15x15 FIR filter, generated from the 1D filter of Figure 4.3.8.

As was shown in Section 4.1.3, D/I is accomplished by passing the original image through a LPF: for 2:1 D/I, $\rho = 1/2$ for the ideal LPF needed to prevent aliasing. Suppose that 2:1 D/I is required, and MTF correction is to also be applied. Both of these operations can be applied simultaneously using just the LP decimation filter if this filter has the MTF boost up to its cut-off frequency ($\rho \cong 1/2$ for 2:1 D/I).

This approach was applied for a 2:1 D/I experiment and boosted frequencies up to the $\rho = 1/2$ point by using

197

TABLE 4.3.1.

RESPONSE FOR MTF

Frequency	MTF
0	1.0
1	1.0
2	1.0
3	1.0
4	0.95
5	0.80
6	0.68
7	0.575
8	0.5
9	0.42
10	0.40
11	0.37
12	0.33
13	0.32
14	0.30
15	0.28
16	0.27
17	0.26
18	0.25
19	0.24
20	0.23

Figure 4.3.1
Round 15x15 β=0.0 ρ=1.0
MTF Correction
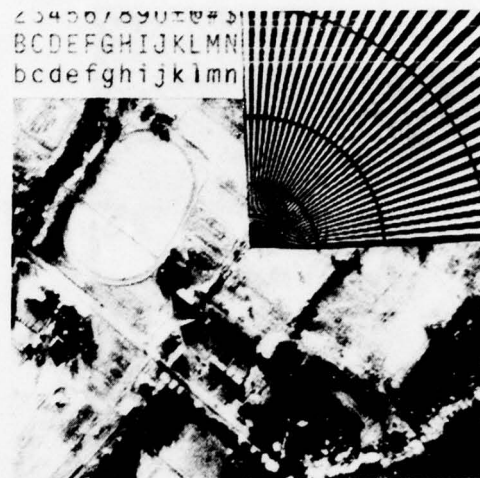
Figure 4.3.2
Square 15x15 β=0.0 ρ=1.0
MTF Correction
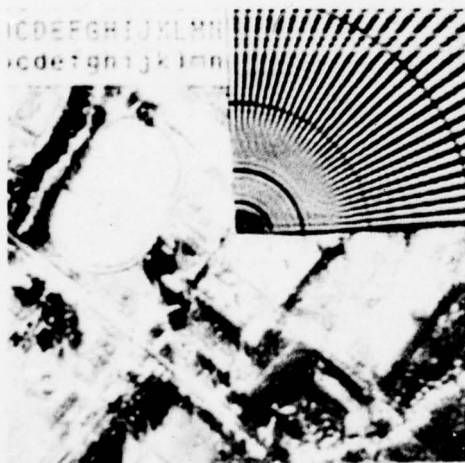
Figure 4.3.3
2:1 D/I With 6.5 dB
Frequency Boost.
15x15 Round Filter
β=0.0 ρ=0.5
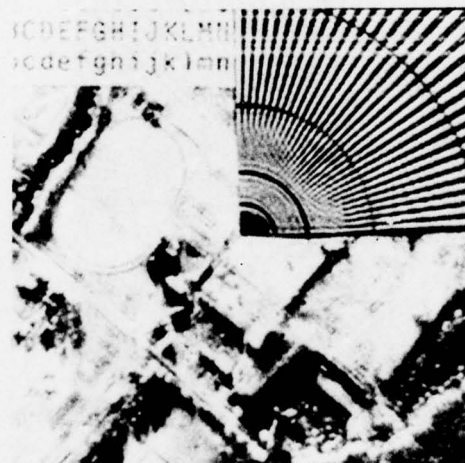
Figure 4.3.4
2:1 D/I With 6.5 dB
Frequency Boost.
15x15 Square Filter
β=0.0 ρ=0.5

Figures 4.3.1, 4.3.2, 4.3.3, and 4.3.4

199
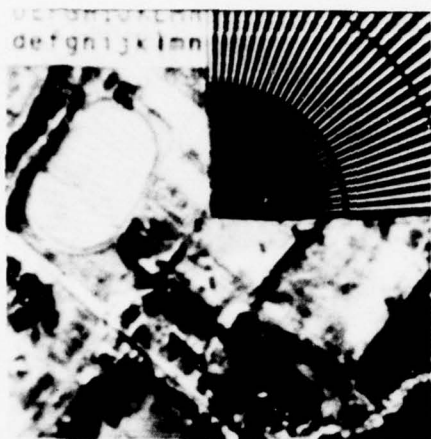
Figure 4.3.5
2:1 D/I Only 31x31,
Round β=1.0 ρ=0.46

Figure 4.3.6
Applied to Figure 4.3.5

$$\begin{bmatrix} -1 & -1 & -1 \\ -1 & 9 & -1 \\ -1 & -1 & -1 \end{bmatrix}$$

Figure 4.3.7
Applied to Figure 4.3.5

$$\begin{bmatrix} -2 & -2 & -2 \\ -2 & 17 & -1 \\ -1 & -1 & -1 \end{bmatrix}$$

Figures 4.3.5, 4.3.6 and 4.3.7

MTF CORRELATION LP FILTER WITH KAISER FILTER

FREQUENCY DOMAIN RESPONSE

| BANDWIDTH - | 1 0000 | ORDER - 15 | KAISER PARAMETER - | 0 0000 |
| COMMENT | | | | KAISER WINDOW |
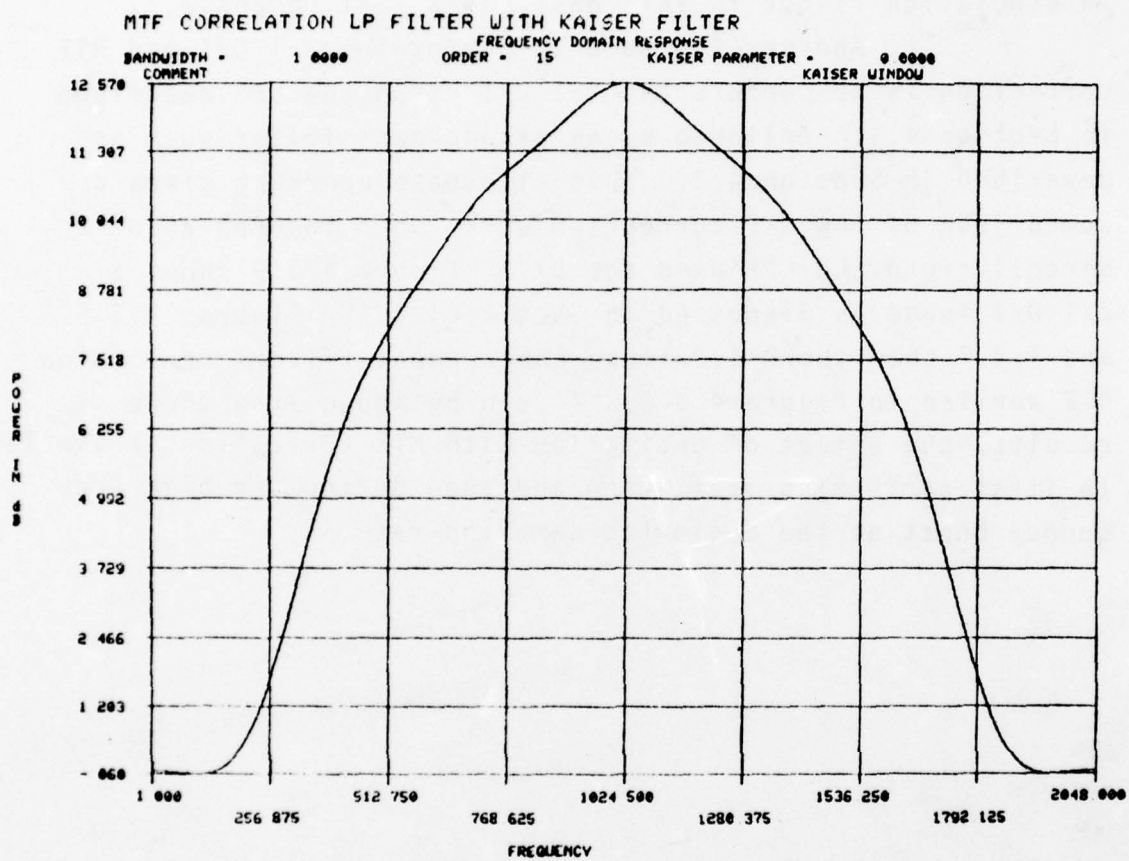
Figure 4.3.8

One-Dimensional MTF Filter for Full Resolution

the top half of Table 4.3.1 as the MTF response. The 1D
filter generated to perform this MTF correction is shown
in Figure 4.3.9 and gives about 6.5 dB boost. This filter
was then used to generate a 2D round and square filter,
shown in Figures 4.3.10 and 4.3.11. The results of applying
these filters are shown in Figures 4.3.3 and 4.3.4. (The
interpolation filter in this case has a flat response.)

Another approach to performing 2:1 D/I and MTF
correction is to perform the 2:1 D/I using the LPF described
in Section 4.1.6 followed by an enhancement filter such as
described in Section 4.2. This alternate approach gives a
comparison of how MTF correction works when incorporated
directly into the LPF used for D/I. Figure 4.3.5 shows a
2:1 D/I image as discussed in Section 4.1.6. Figures 4.3.6
and 4.3.7 show the R=1,2 image enhancement filters of Section
4.2 applied to Figure 4.3.5. As can be shown from these
results, the effect of decimation with MTF correction is similar
to first performing decimation and then performing high fre-
quency boost at the decimated sampling rate.
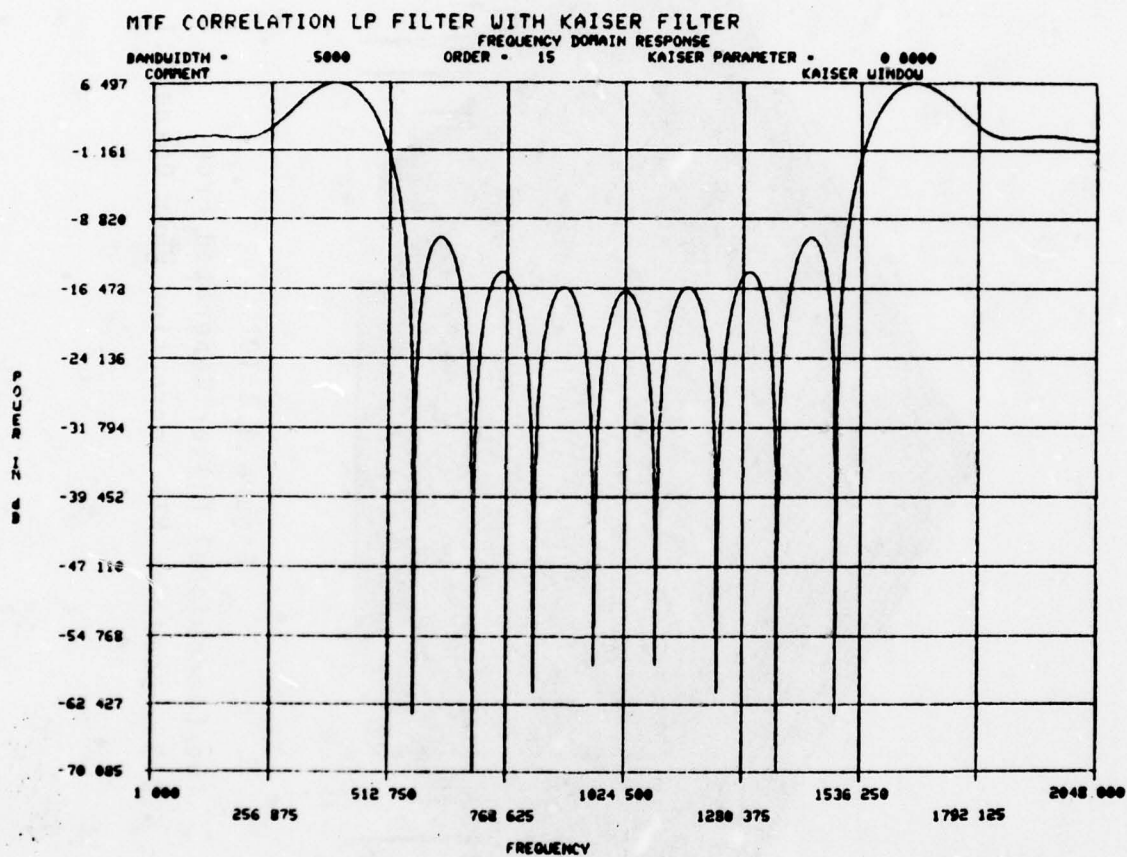
Figure 4.3.9
One-Dimensional Filter Used for
MTF Correction When Doing 2:1 D/I.

203
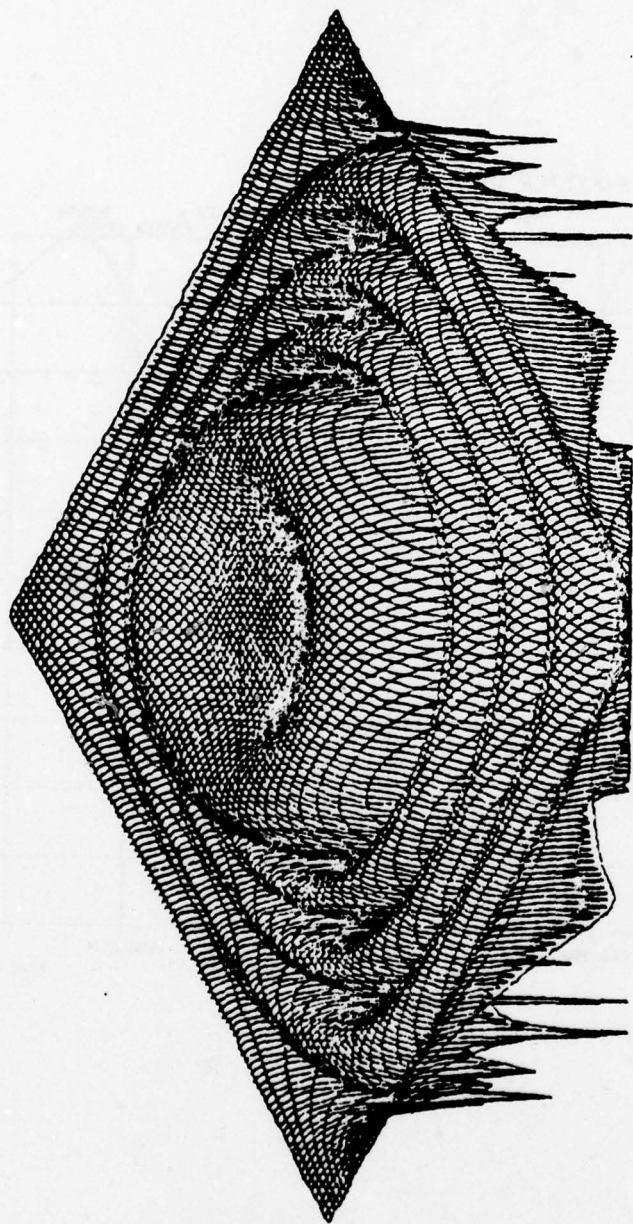
Figure 4.3.10

Two-Dimensional Filter Generated From

Figure 4.3.9-- Used for MTF Correction When Doing 2:1 D/I.
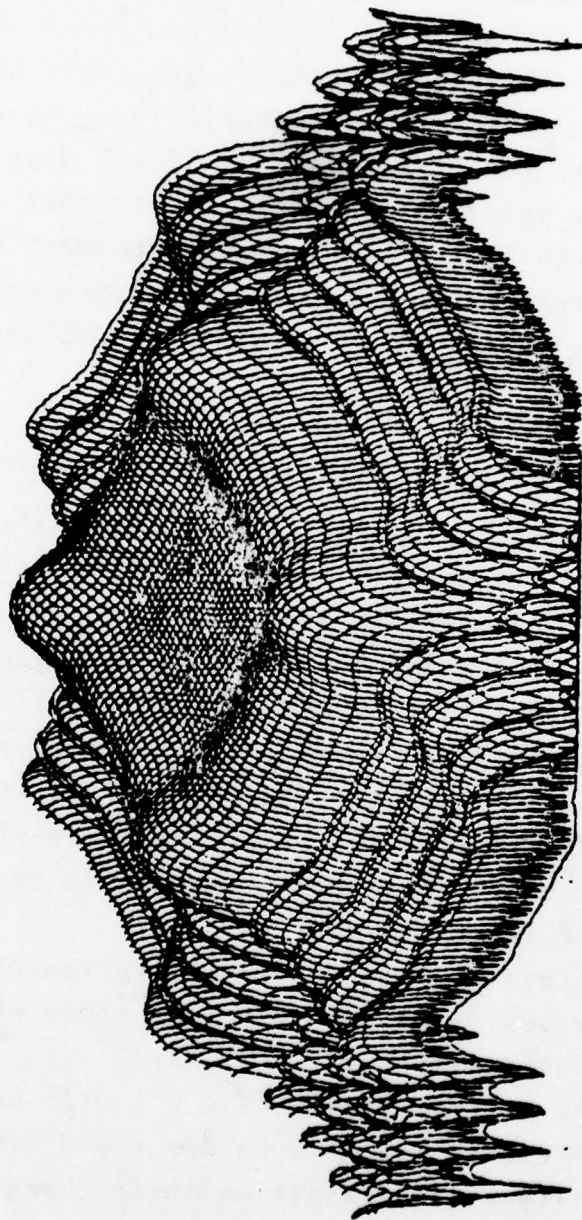
Figure 4.3.11
Two-Dimensional Filter Generated From
Figure 4.3.9-- Used for MTF Correction When Doing 2:1 D/I.

4.4   PRACTICAL FIR FILTER IMPLEMENTATIONS

In this section we begin by surveying currently
available CCD's and their operating characteristics. This
is followed by a discussion of the degradation of FIR filter
performance due to the nonidealness of available CCD's that
must be used in any practical implementation. More speci-
fically, we discuss the effects of the signal dispersion,
tap weight errors, and quantization accuracy that are
associated with practical CCD's used to implement FIR's.
We develop a dispersion model and present computed theoretical
results that show the effect of capacitive coupling and CTI
among CCD stages.

4.4.1   Currently Available Charge-Coupled Devices

Charge coupled device (CCD) technology has
enjoyed tremendous progress in the last ten years and CCD's
are now available that perform important imaging, storage,
and analog signal processing functions. Charge-coupled
devices may be thought of as discrete-time, continuous ampli-
tude analog shift registers. The analog sample values are
stored as packets of electrical charge, each of which is
stored in individual potential wells. Multiple-phase clocking
signals cause the electrical charge packets to be shifted
serially along the length of the register.

In this section we briefly survey commercially
available CCD devices, with emphasis upon those which are
suitable for implementation of FIR filters.

The Reticon family of CCD's will be of interest
in the ASITS application and will be described first. The
Reticon product literature classifies their charge transfer

device products into two classes: those using bucket brigade.
devices (BBD's) and those using charge coupled devices.
The differences between the two lie in the details of device
structure. The BBD's allow external access to the individual
stages of the analog shift register and therefore facilitate
implementation of externally programmable FIR filters. The
CCD technology is capable of higher sampling rates and higher
density devices then BBD technology.

The Reticon TAD-32A is a 32 stage BBD tapped
analog delay line with source follower buffers for each stage.
The "A" version reduces the odd-even pattern that was
characteristic of the TAD-32. External resistors may be
attached to each of the buffer outputs to perform the tap
weighting function. This device has a dynamic range of
60 dB and can accommodate sampling rates between 1 kHz and
5 MHz. Two or more TAD-32A's may be cascaded to obtain
additional stages of tapped analog delay.

The Reticon R5602 is a mask programmed 64 stage
BBD transversal (FIR) filter intended for high volume applica-
tions. Sampling rates of 1 MHz and typical stopband rejec-
tions of 50 dB can be obtained. The tap weights of the FIR
filter are implemented by using a split electrode structure.
Both the TAD-32A and R5602 BBD's can be used to implement
FIR filters; the former is useful for low-volume experimental
applications since it is externally programmable, whereas
the latter is suitable for high volume production applica-
tions since it is mask programmable and does not require
the external tap weight resistors.

In addition to CTD's useful in FIR filtering
applications, Reticon also makes a much more sophisticated
signal processing device that has potential for bandwidth
compression applications. The R5601 CCD performs a 512

point DFT using the Chirp-z algorithm. Each R5601 contains
four 512-tap split electrode tranversal filters, with tap
weight patterns corresponding to two cosine chirps and two
sine chirps. Two external multiplier functions are required
for use with this device in order to perform the DFT; this is
shown in Figure 4.4.1. The R5601 operates at rates as high
as 100 kHz and exhibits output SNR's in excess of 70 dB.
The commercial availability of the R5601 demonstrates that
custom designed 512 tap FIR filters could be fabricated if
required for the ASITS. The computer simulation experiments
indicate that FIR filters with far fewer stages are adequate.

A CCD of great usefulness in bandwidth compres-
sion applications is the Hughes CRC 101. This dual function
chip is mounted in a 40 pin DIP and performs a 16-point
one-dimensional Hadamard transform (or its inverse) in real
time at input sampling frequencies up to 10 MHz, and also
contains a 16 input parallel-to-serial multiplexer.

Another CCD of potential interest in a digital
storage oriented ASITS is the TMS 3064 65,536-bit CCD memory
packaged in a 16-pin DIP. This device operates between 1
MHz and 5 MHz.

The above discussion briefly surveyed commercial-
ly available CTD's which are potentially applicable to an
ASITS design. The two of importance for the remainder of this
section are those which are useful in implementing FIR
filters, i.e., the TAD-32A and R5602.

4.4.2   Analyses of Nonideal FIR Implementations

This section deals with three ways in which
practical CCD's depart from analog shift registers consisting
of ideal delay elements with ideal tap weights:

                (1)   dispersion effects due to CTI and capa-
                      citive coupling among CCD stages

208
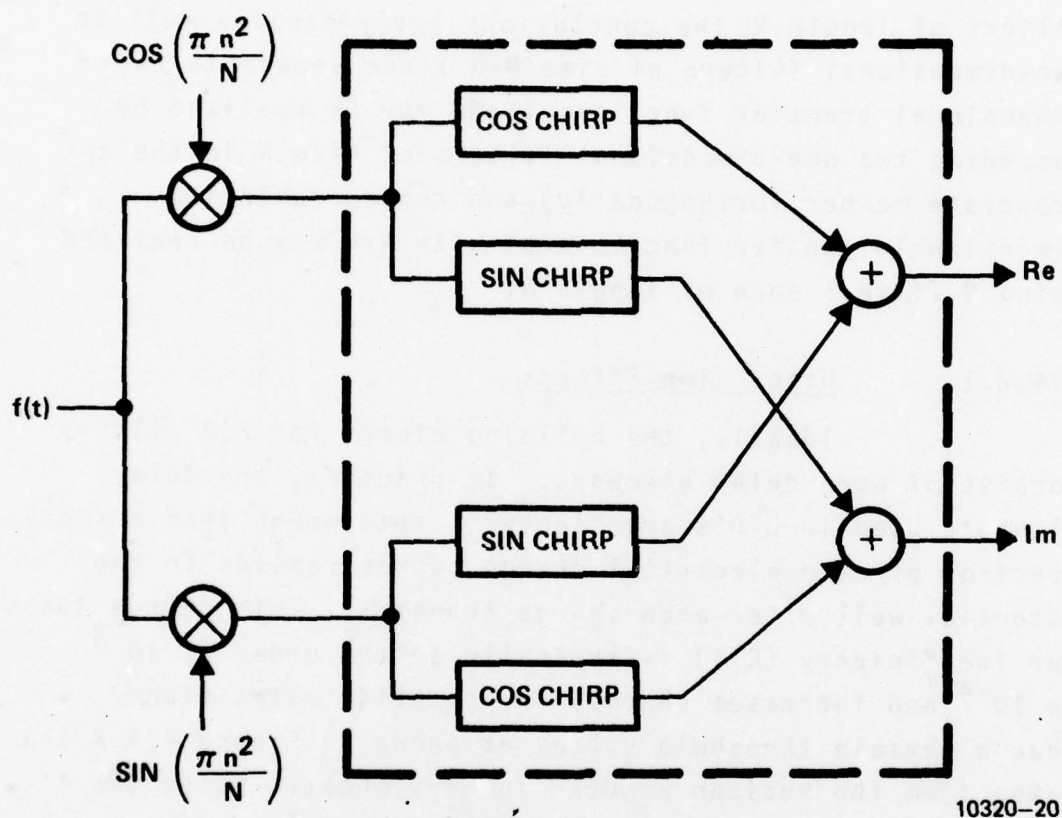
Figure 4.4.1
Block Diagram of Chirp Z Algorithm

209

(2) tap weight errors

(3) quantization effects

Although the discussion is with regard to one-dimensional
filters of length N the conclusions apply equally well to
two-dimensional filters of size NxN since separable two-
dimensional transfer functions (NxN) may be realized by
cascading two one-dimensional filters of size N in the ap-
propriate manner (orthogonally) and nonseparable two-
dimensional transfer functions of size NxN may be realized
using N filters each of length N.

4.4.2.1 Dispersion Effects

Ideally, the building blocks for FIR filters
consist of pure delay elements. In practice, the delay
elements used in CTD's are "leaky" - this means that a small
fraction of each electrical charge packet remains in the
potential well after each charge transfer. This charge trans-
fer inefficiency (CTI) is typically on the order of 10^{-3}
to 10^{-4} and increases sharply for sampling rates higher
than a certain threshold value, as shown in Figure 4.4.2.1-1
taken from the Reticon product summary sheet. Using the
equation describing the charge transfer process [9]

$$V_k \left[(n+1)T \right] = (1-\epsilon) V_{k-1}(nT) + \epsilon V_k(nT) \qquad (4-33)$$

we can take z transforms to obtain

$$V_k(z) = (1-\epsilon)z^{-1} V_{k-1}(z) + \epsilon z^{-1} V_k(z) \qquad (4-34)$$

where $z=\exp(i2\pi f/f_s)$, f_s=sampling rate.
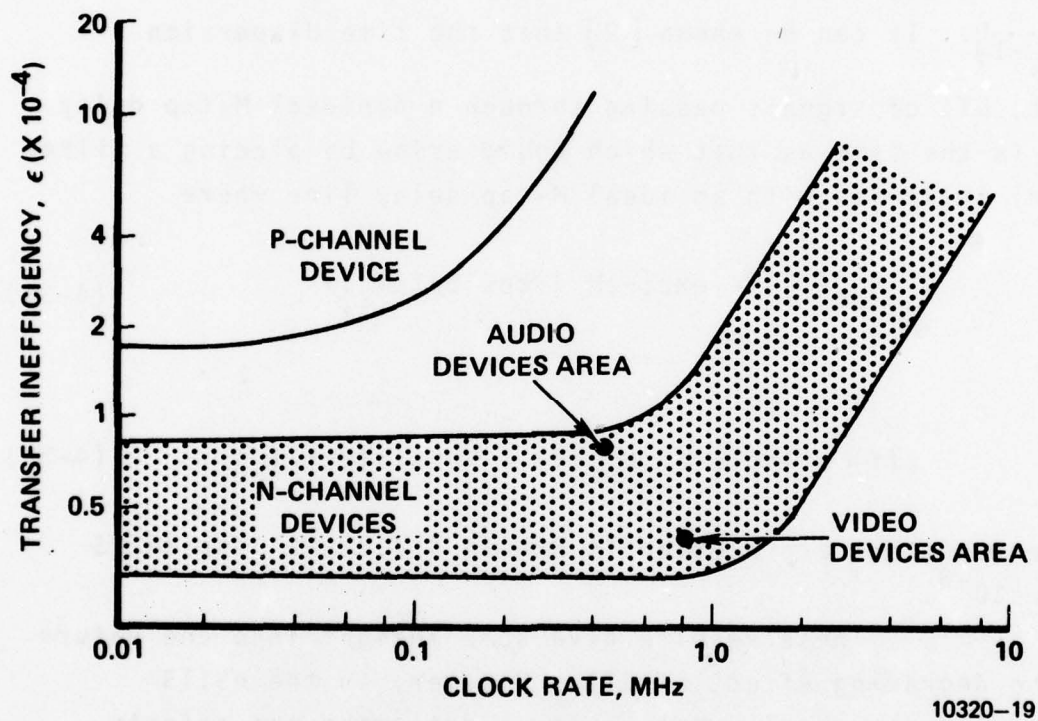
Figure 4.4.2.1-1

Charge Transfer Inefficiency Versus Clock Frequency

Collecting terms on $V_k(z)$ in this expression yields

$$V_k(z) = \left(\frac{1-\varepsilon}{1-\varepsilon z^{-1}}\right) z^{-1} V_{k-1}(z) \qquad (4-35)$$

Recalling that z^{-1} is the z transform corresponding to a pure delay element, it is clear that the effect of CTI is to modify the z transform of an ideal delay by the factor $\left(\frac{1-\varepsilon}{1-\varepsilon z^{-1}}\right)$. It can be shown [9] that the time dispersion due to CTI of signals passing through a nonideal M-tap delay line is the same as that which would arise by placing a filter $H_{DL}(z)$ in series with an ideal M-tap delay line where

$$\left|H_{DL}(f)\right| = \exp\{-\varepsilon M \ 1-\cos(2\pi f/f_s)\} \qquad (4-36)$$

and

$$\phi(f) = \text{Angle of } H_{DL}(f) = M\varepsilon \ \sin(2\pi f/f_s). \qquad (4-37)$$

These functions are plotted in Figure 4.4.2.1-2 for M=225 and $\varepsilon = 10^{-3}$.

These results give some insight into the nature of the degrading effect of CTI. However, in the ASITS application the real question is to determine the effects of CTI upon the magnitude and phase of the lowpass filters used in the decimation and interpolation processes, and the filters used for MTF correction. One way to do this is to substitute the transfer function of the nonideal delay element, denoted by $(z^{-1})'$, for the transfer function of the ideal delay element, z^{-1}, in the expression for H(z).
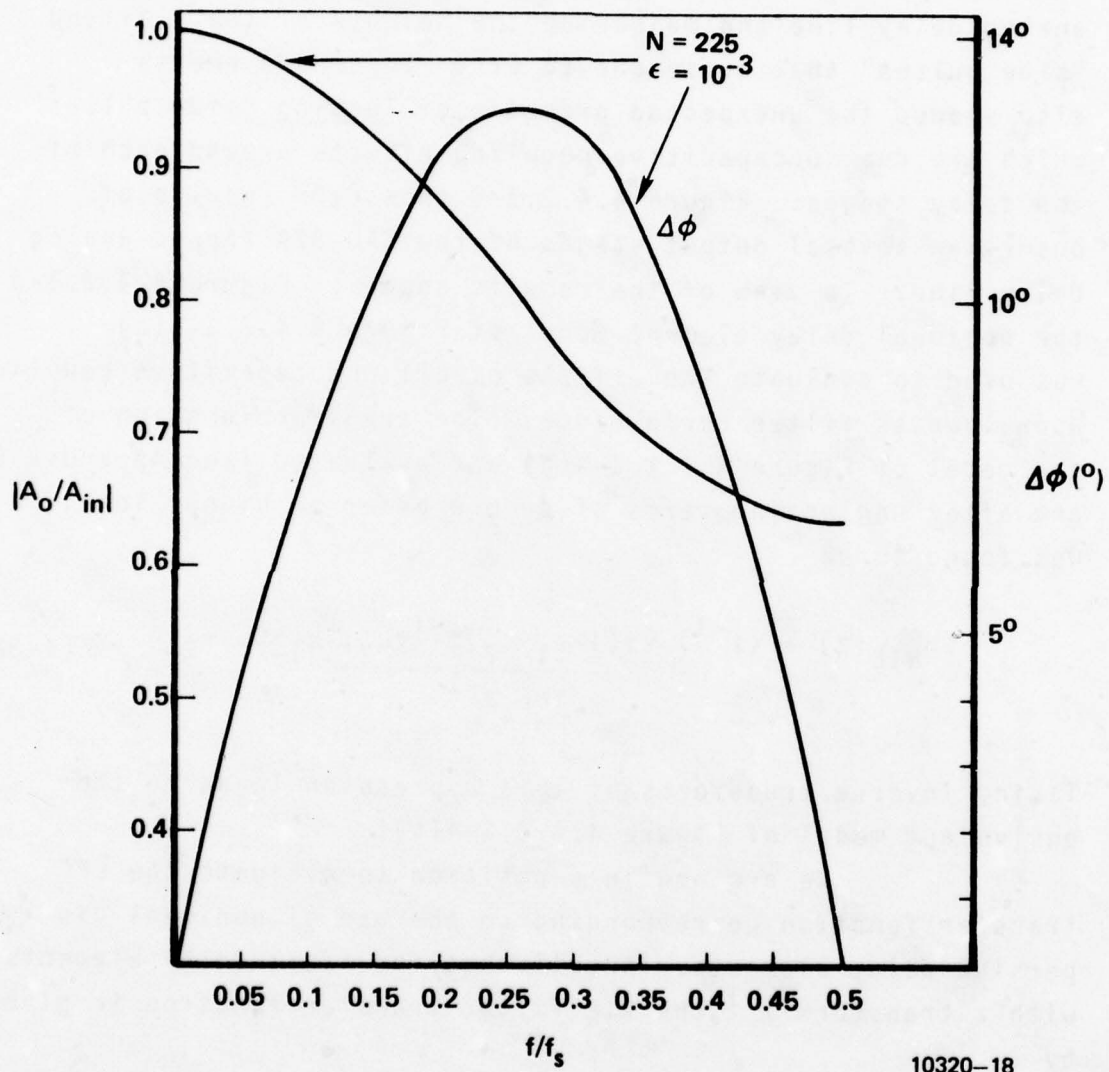
Figure 4.4.2.1-2
Effects of CTI on Delay Line Transfer Function

In order to determine the value of the CTI for the Reticon TAD-32A some laboratory measurements were made on this device by injecting a signal into the tapped analog delay line and measuring the heights of the trailing "side pulses" that arose due to CTI. The measurements also showed the unexpected presence of leading "side pulses" which are due to capacitive coupling effects around each of the delay stages. Figure 4.4.2.1-3 shows the results of observing several output stages of the TAD-32A tapped analog delay line. In view of the results shown in Figure 4.4.2.1-3 the nonideal delay element model of Figure 4.4.2.1-4(a) was used to evaluate the effects of CTI and capacitive coupling upon lowpass filter performance. The transfer function of the model of Figure 4.4.2.1-4(a) was evaluated (see Appendix B) and after neglecting terms of second order or higher in ε, was found to be

$$H_{NIE}(z) = (z^{-1})' = \frac{(1-\varepsilon_1-\varepsilon_2)z^{-1}+\varepsilon_2}{1-\varepsilon_1 z^{-1}}, \quad \varepsilon_1 \geq 0, \quad \varepsilon_2 \leq 0 \qquad (4-38)$$

Taking inverse transforms of this expression leads to the equivalent model of Figure 4.4.2.1-4(b).

We are now in a position to evaluate the LPF transfer function corresponding to the use of nonideal dispersive delay elements. Recall that for ideal delay elements with z-transform z^{-1} the FIR filter transfer function is given by

$$H_I(z) = \sum_{k=0}^{N-1} h_k z^{-k} \qquad (4-39)$$

where the h_k are the FIR tap weights.

214

2150 mV

75

−425

TAP 31

650

100

2350 mV

−200

TAP 17

350
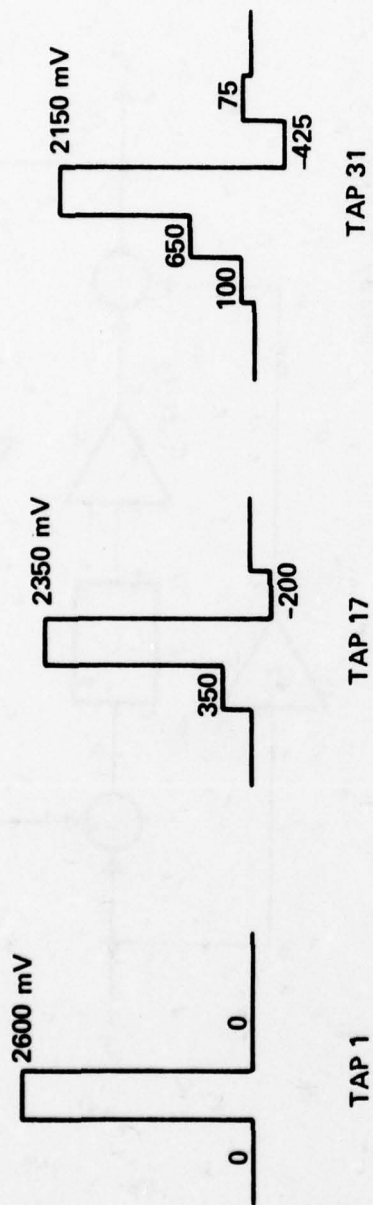
(EVEN TAPS IDENTICAL STRUCTURE, SLIGHTLY HIGHER LEVELS)

NOTE:

2.3V BIAS, UNBALANCED CLOCK VOLTAGES

2600 mV

0

0

TAP 1

10320−17

Figure 4.4.2.1-3

Dispersive Effects Present in TAD-32 Due to
CTI and Capacitive Coupling Among CCD Stages
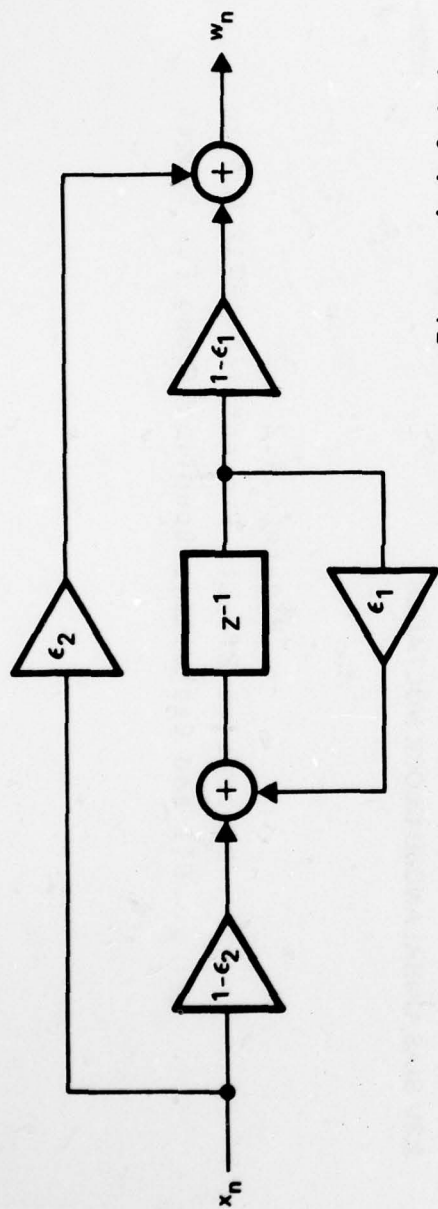
Figure 4.4.2.1-4
Two Equivalent Models for
Nonideal CCD
Delay Elements
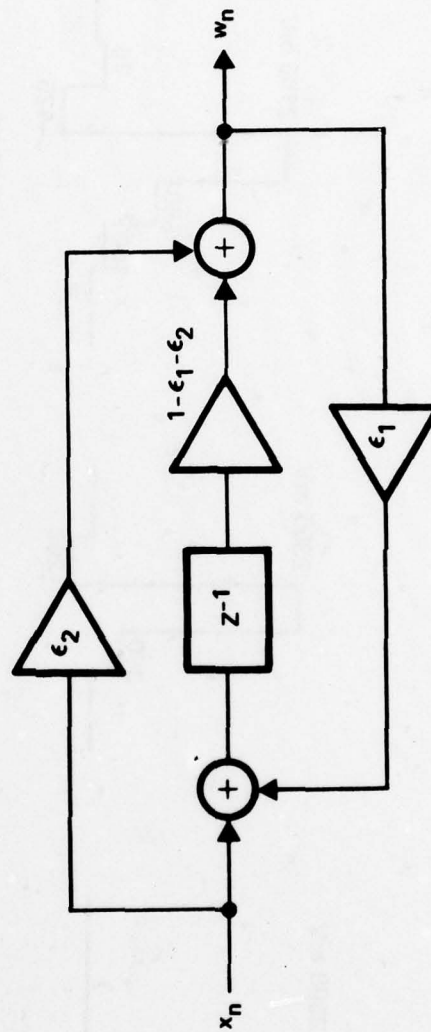
10320—16

216

Then for nonideal dispersive delay elements with z-trans-
form

$$(z^{-1})' = \frac{(1-\epsilon_1-\epsilon_2)z^{-1}+\epsilon_2}{1-\epsilon_1 z^{-1}} \quad . \tag{4-40}$$

the transfer function is given by

$$H_{NI}(z) = \sum_{k=0}^{N-1} h_k \left[\frac{(1-\epsilon_1-\epsilon_2)z^{-1}+\epsilon_2}{1-\epsilon_1 z^{-1}} \right]^k \tag{4-41}$$

Since there appear to be no results in the liter-
ature regarding simultaneously present "forward" and "backward"
dispersion in delay lines used to implement FIR filters,
this expression was evaluated using a computer with a graphics
display capability. The tap weights h_k were computed as
the product of a sinc function and a Hamming window function:

$$h_k = \left[0.54+0.46 \cos\left(\frac{2\pi}{N}\left(k+1-\frac{N+1}{2}\right)\right) \right] \quad x \tag{4-42}$$

$$\left[\sin\left(\pi \left(k+1-\frac{N+1}{2}\right)\right) \Big/ \left(\pi \ k+1-\frac{N+1}{2}\right) \right] (fc/\pi) \tag{4-43}$$

for k=0,1,2,..... N-1 where N is an odd number

The sinc function impulse response using a unity window
gives only 13 dB of stopband attenuation; using a Hamming
window on the sinc function gives aobut 40 dB additional
stopband attenuation at the expense of increased filter
transition bandwidth. The resulting stopband attenuation
of approximately 53 dB is evident in all of the filter
transfer functions that were obtained.

217

This computer program was exercised using a variety of values for ε_1, ε_2, and N for two values of f_c, the filter cutoff frequency. The graphics display for each run includes plots of the filter frequency transfer function using both linear and logarithmic (dB) ordinate scales, the filter phase response, and the filter impulse response.

Since the degradation of the linear phase response in these plots was imperceptible, the phase response plots are not shown in the figures below. The impulse response plots were used to verify the filter design portion of the program and consequently are not shown in all of the figures below. Some representative results are shown in Figures 4.4.2.1-5 through 4.4.2.1-9 for the N=31 case and additional results are contained in Appendix C for N=9, N=15, N=63, and N=225. Choosing 0.01 as the maximum magnitude of ε_1 and ε_2 represents the worst case situation likely to be encountered. Typical values for ε_1(CTI) range from 10^{-4} to 10^{-3} according to the literature; Figure 4.4.2.1-1 shows that a well-defined knee exists in the curve relating ε_1 to clock frequency. Experimental measurements using a Reticon TAD-32 at a clock rate of approximately 1 MHz yielded a value a value of ε_1=0.0092 and $|\varepsilon_2|$ = 0.0057. The details regarding the derivation of these results are contained in Appendix B.

Turning now to the computed theoretical results based upon the model of Figure 4.4.2.1-4, we first display the ideal case (ε_1=ε_2=0) in Figure 4.4.2.1-5 for comparison with subsequent results. The "(a)" portion of this and subsequent figures utilizes a linear ordinate, whereas the corresponding "(b)" portions utilize a logarithmic ordinate (dB scale). The abscissa in each case is frequency normalized by the sampling rate f_s. Note that the filter cutoff frequency f_c is normalized by $f_s/2$. Figure 4.4.2.1-6 shows

218
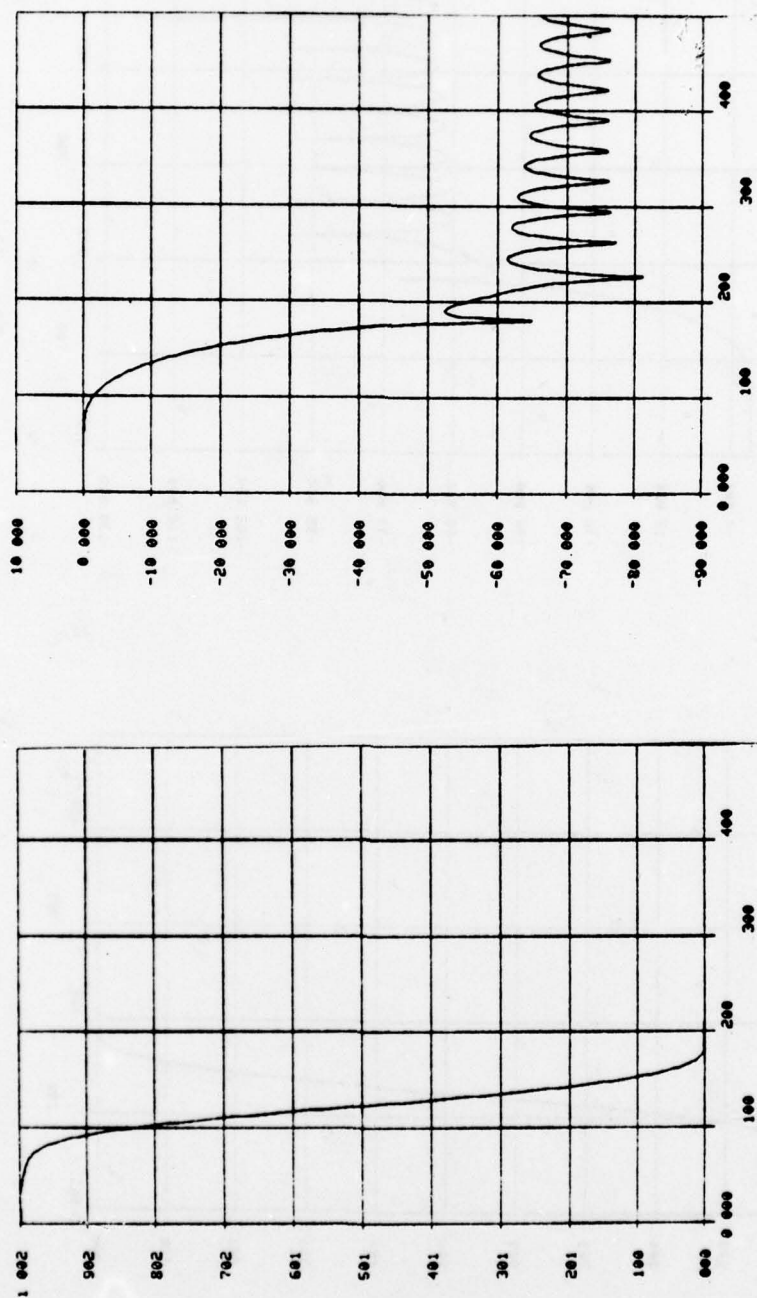
Figure 4.4.2.1-5
$N=31$, $\epsilon_1=0$, $\epsilon_2=0$, $fc=.25(fs/2)$
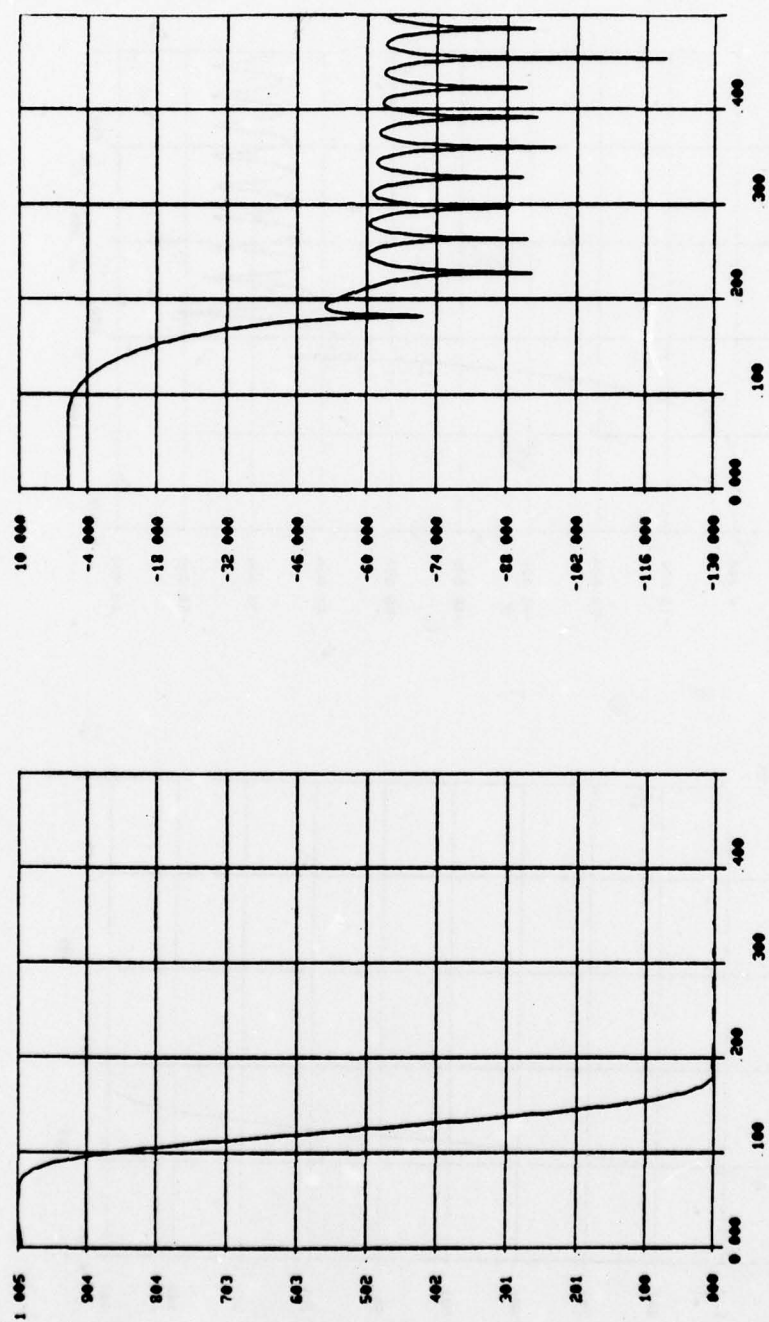
Figure 4.4.2.1-6

$N=31$, $\varepsilon_1=.01$, $\varepsilon_2=0$, $f_c=0.25(f_s/2)$

220
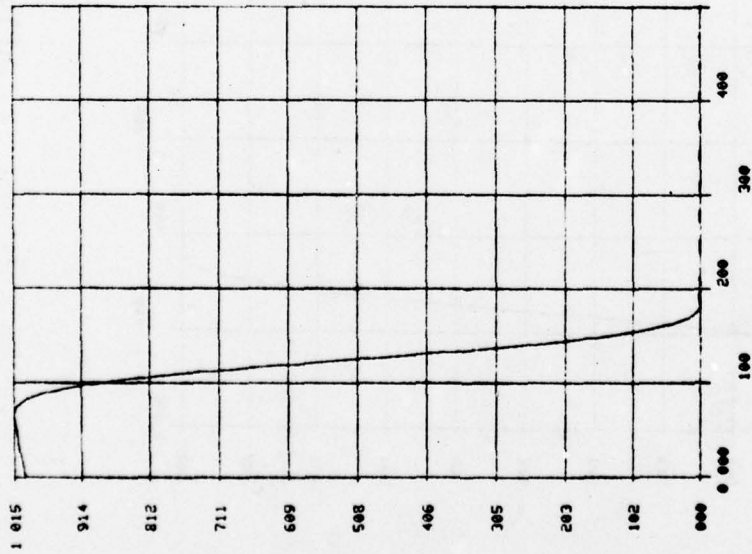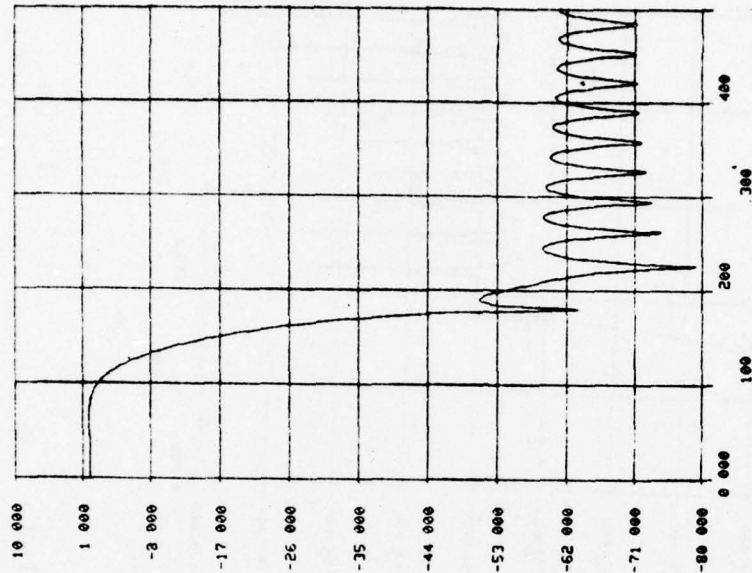
Figure 4.4.2.1-7

N=31, $\epsilon_1=0$, $\epsilon_2=-.01$, $fc=0.25$ $(fs/2)$
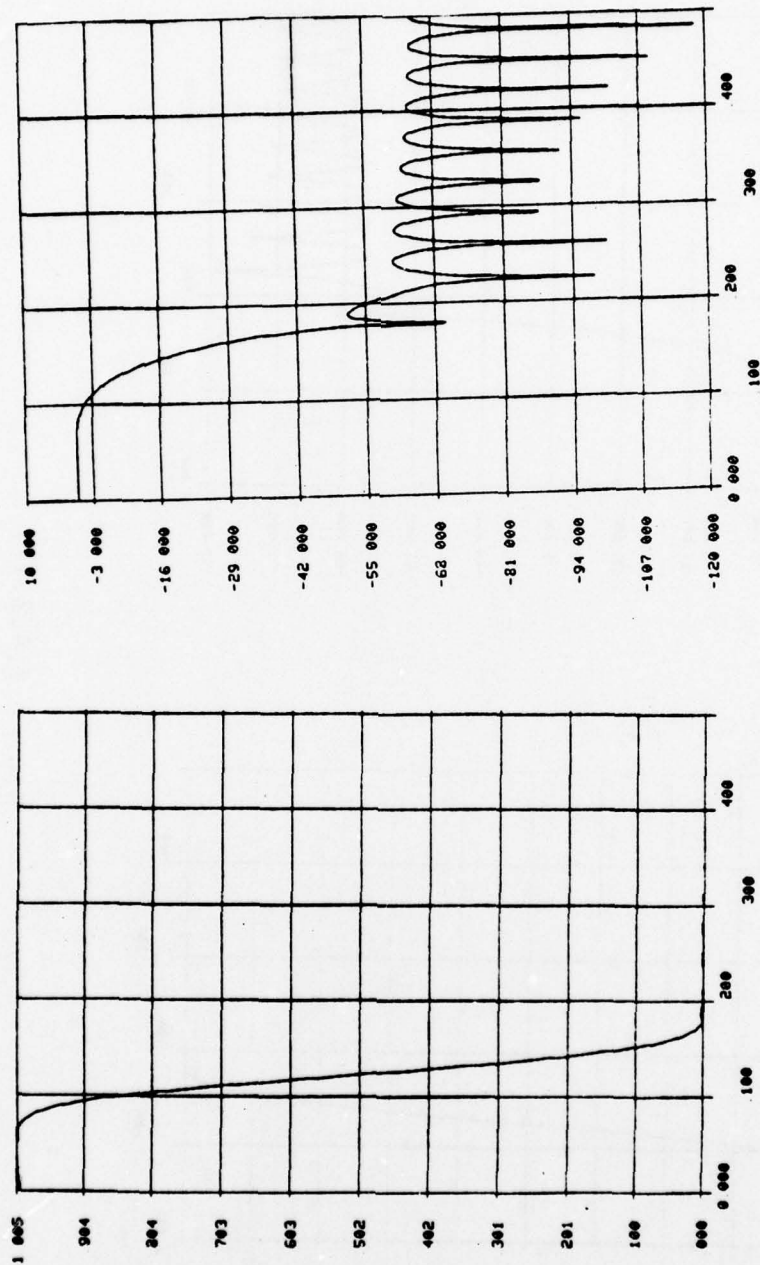
Figure 4.4.2.1-8

$N=31$, $\varepsilon_1=.01$, $\varepsilon_2=-.01$, $f_c=0.25(f_s/2)$

222
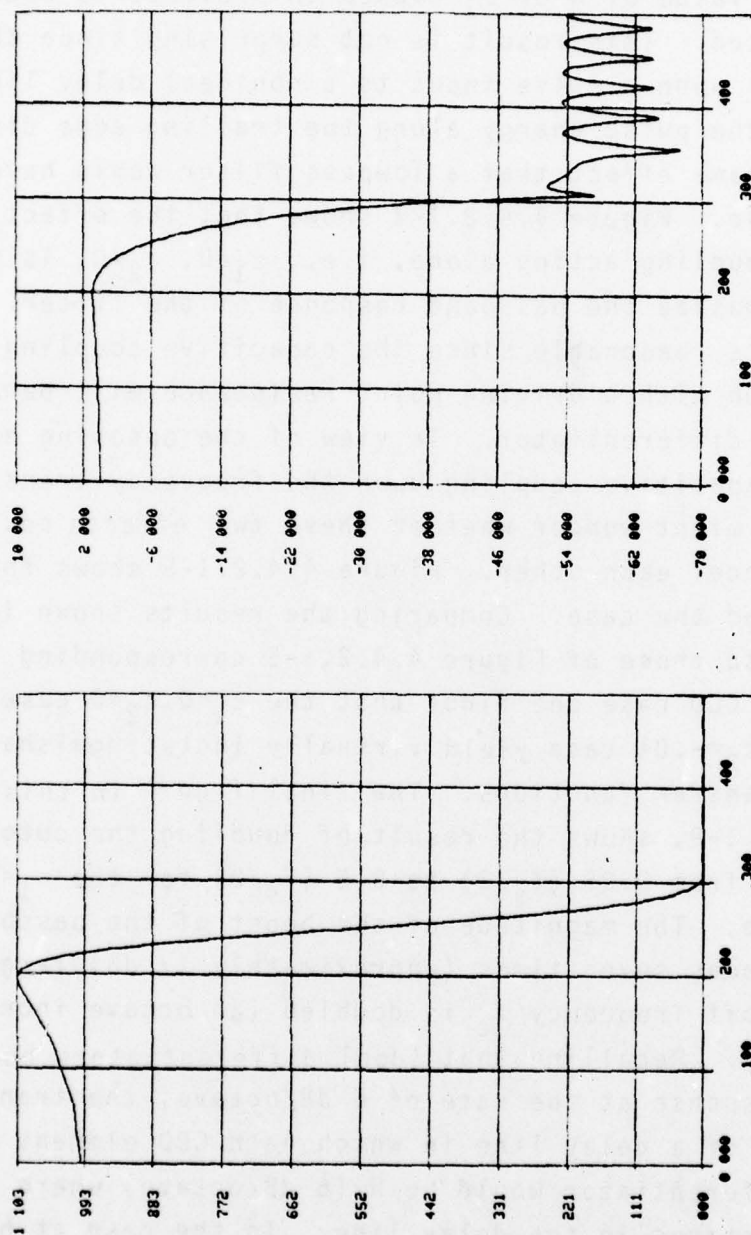
Figure 4.4.2.1-9

$N=31$, $\varepsilon_1=0$, $\varepsilon_2=-.01$, $fc=0.5$ $(fs/2)$

that the effect of CTI acting above, i.e., $\varepsilon_1 \neq 0$, $\varepsilon_2 = 0$, is
to cause the passband response of the filter to droop; in-
creasing the value of N or ε_1 causes this effect to become
more pronounced. This result is not surprising since the
effect of CTI upon a pulse input to a nonideal delay line
is to smear the pulse energy along the trailing edge direction--
this is the same effect that a lowpass filter would have upon
an input pulse. Figure 4.4.2.1-7 shows that the effect of
capacitive coupling acting alone, i.e., $\varepsilon_1 = 0$, $\varepsilon_2 \neq 0$, is to
boost or emphasize the passband response of the filter.
Again, this is reasonable since the capacitive coupling
in conjunction with a driving point resistance will behave
like a leaky differentiator. In view of the opposing effects
of CTI and capacitive coupling upon the frequency transfer
function one might wonder whether these two effects could
partially cancel each other. Figure 4.4.2.1-8 shows that
this is indeed the case. Comparing the results shown in
this figure to those of Figure 4.4.2.1-5 corresponding
to the ideal CCD case one finds that the $\varepsilon_1 = 0$, $\varepsilon_2 = 0$ case and
the $\varepsilon_1 = .01$, $\varepsilon_2 = -.01$ case yield virtually indistinguishable
frequency transfer functions. The final figure in this series,
Figure 4.4.2.1-9, shows the result of doubling the cutoff
frequency f_c from C.25 ($f_s/2$) to 0.5 ($f_s/2$) for the $\varepsilon_1 = 0$,
$\varepsilon_2 = -0.01$ case. The magnitude of the boost of the passband
response becomes seven times (approximately 17 dB) larger
when the cutoff frequency f_c is doubled (an octave increase
in frequency). Recalling that ideal differentiators boost
frequency response at the rate of 6 dB/octave, the trans-
fer function of a delay line in which each CCD element was
an ideal differentiator would be Nx(6 dB/octave) where
N=number of stages in the delay line. In the case at hand
the differentiation is "leaky" and the frequency transfer
function is that of a generalized filter rather than a delay
line.

All of the observations that have been made
regarding the N=31 FIR filters also apply to filters with
a greater or smaller number of stages. The effects discussed
above are more pronounced for larger values of N and less
pronounced for smaller values of N, as may be seen by referring
to the additional results in Appendix C.

As a result of these computations based upon
a model which includes the effects of either CTI or capacitive
coupling, or both simultaneously, we make the following
observations regarding FIR filters implemented with practical
CCD's exhibiting time dispersion.

(1) the filter passband response:
  - droops if $\varepsilon_1 \neq 0$, $\varepsilon_2 = 0$
  - peaks if $\varepsilon_1 = 0$, $\varepsilon_2 \neq 0$
  - is largely unaffected if $\varepsilon_1 \neq 0$, $\varepsilon_2 \neq 0$, $|\varepsilon_1| = |\varepsilon_2|$

(2) the phase response is not appreciably affected
   regardless of the combination of ε_1 and ε_2
   values for $\varepsilon_1 < 0.01$, $|\varepsilon_2| < 0.01$

(3) Minimum stopband attenuation is unaffected

(4) nulls in the stopband response are partially
   filled in for $\varepsilon_1 = 0$, $\varepsilon_2 \neq 0$ or $\varepsilon_1 \neq 0$, $\varepsilon_2 = 0$. This
   is of no practical consequence.

(5) transition bandwidth is unaffected

(6) the effects of CTI and capacitive coupling tend
   to offset each other

225

On the basis of these worst case simulation
results we conclude that commercially available CCD's are
adequate to meet the ASITS filtering requirements. For FIR
filters with a large number of taps the filter weights can
be modified to counteract the droop in the passband response
by designing a "pre-emphasis" filter assuming ideal CCD
elements with just enough passband boost to compensate for
the passband droop due to CTI dispersion along the delay line.

4.4.2.2   Tap Weight Tolerance and Quantization Effects

Two issues of some importance in practical
realizations of FIR filters are random tap weight errors and
tap weight quantization errors. These issues and others have
been studied by Baertsch et al [10] and their results are
applicable to the ASITS application. Random tap weight
errors are due to CCD process variations such as nonuniform
etching whereas quantization errors arise as a result of
computerized photolithographic maskmaking processes in which
the tap weights must be rounded off to integral multiples of
a minimum coordinate spacing.

The effect of quantization of tap weights to
one part in 600 is shown in Figure 4.4.2.2-1 (taken from [10])
for an optimum equiripple FIR filter designed using the Parks-
McClellan algorithm [11].

It is clear that the passband response and
transition bandwidth are not appreciably affected, but that
the stopband attenuation is substantially degraded by 3 dB
to 9 dB depending upon relative sampling frequency. Figure
4.4.2.2-1 also demonstrates the value of choosing the sampling
rate to be as low as possible when designing FIR filters,
since this decreases the required filter order by virtue of the
empirical relationship due to Rabiner et. al. [13]
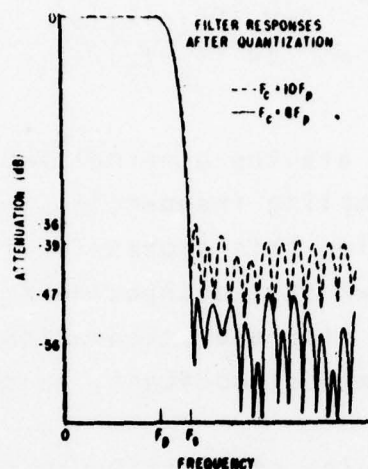
(a) Calculated Filter Response After
Quantization to One Part in 600
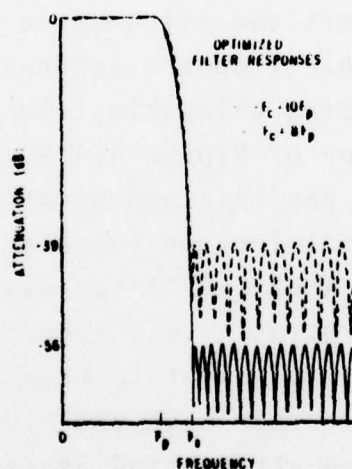
(b) Calculated Filter Response for Two Optimized
Filters. Passband and Transition Band Speci-
fications are Identical, But Ratio of Clock
Frequencies is 5/4

Figure 4.4.2.2-1. The Effects of Tap Weight Quantization and
Relative Sampling Rate Upon FIR Filter
Response 227

$$N = \frac{-10 \log_{10}(\delta_i \delta_2) - 15}{14 \ (f_s - f_p)/f_{cl}} \qquad (4\text{-}44)$$

where f_s, f_p, and f_{cl} are the unnormalized stopband, pass-band, and clock or sampling frequencies, respectively.

By solving this expression for δ_2 (stopband ripple) it can be shown that decreasing f_{cl} allows δ_2 to be decreased (increasing stopband attenuation) while maintaining all other filter parameters constant, as shown in Figure 4.4.2.2-1.

The results of Monte Carlo tap weight tolerance calculations performed by Baertsch et. al. [10] are shown in Figure 4.4.2.2-2. The (a) portion of this figure shows that increasing the number of taps in a FIR filter decreases the permissable tap weight tolerance if degradation of stopband attenuation is to be avoided; the N=31 FIR filters discussed elsewhere in this report can allow up to 1% tap weight toler-ance without appreciable stopband attenuation degradation, whereas the corresponding allowable tolerance for N=63 is only 0.01%. The (b) portion of Figure 4.4.2.2-2 shows how the average value of peak positive and negative passband ripples varies with tap weight tolerance (with and without tap weight quantization) for the N=63 FIR filter case; if passband ripple were the only consideration (i.e., ignoring stopband attenua-tion degradation) the tap weight tolerance could be chosen as high as 0.5 to 1%, rather than the 0.01% value required for negligible stopband attenuation degradation. The (c) portion of Figure 4.4.2.2-2 displays the mean and variance of stopband attenuation versus tap weight tolerance for both the quantized and unquantized tap weight case. This result shows that a reasonable choice for tap weight tolerance is in the 0.1% to 0.3% range.
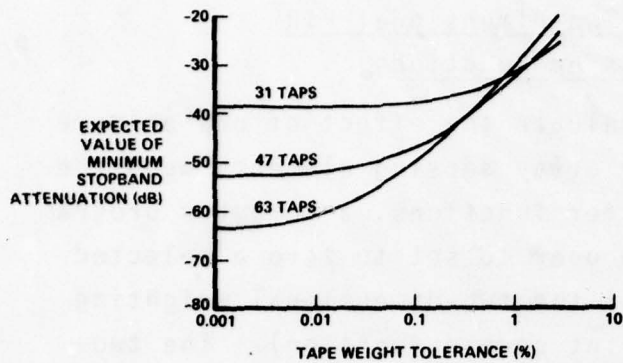
a. MONTE CARLO CALCULATION OF
EXPECTED VALUE OF MINIMUM STOP-
BAND ATTENUATION VERSUS TAP
WEIGHT TOLERANCE FOR THREE
OPTIMIZED LOW-PASS FILTER DESIGNS
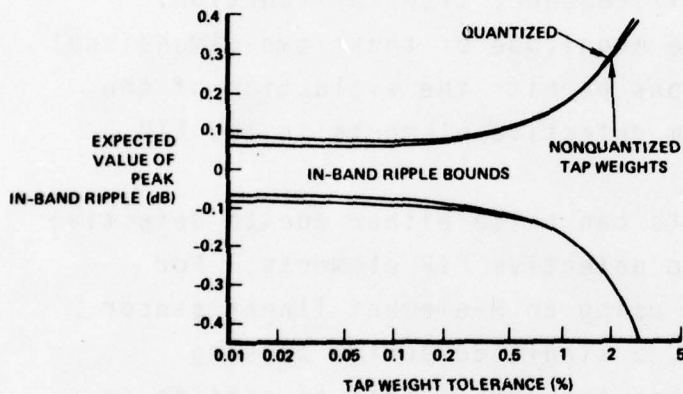
b. MONTE CARLO CALCULATION OF
EXPECTED VALUE OF PEAK IN-BAND
RIPPLE VERSUS TAP WEIGHT TOLER-
ANCE FOR 63-TAP LOW-PASS FILTER
OF a. IN ONE CASE, TAP WEIGHTS
WERE QUANTIZED TO 1 PART IN 600
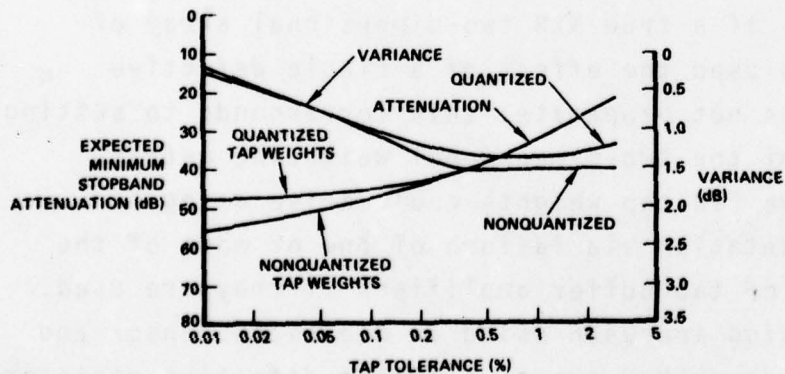
c. MONTE CARLO CALCULATION OF
EXPECTED VALUE AND VARIANCE OF
MINIMUM STOPBAND ATTENUATION
VERSUS TAP WEIGHT TOLERANCE
FOR 63-TAP LOW-PASS FILTER OF a.
QUANTIZATION WAS TO 1 PART IN 600

10320—15

Figure 4.2.2.2-2
The Effect of FIR Tap Weight
Error Tolerance Upon
Filter Response

229

4.4.3 The Effect of Defective FIR Filter Elements Upon Two-Dimensional FIR Frequency Transfer Functions

In order to evaluate the effect of one or more defective FIR tap weights or array sensing elements upon the two-dimensional filter transfer functions, a computer program was written which allows the user to set to zero a selected element or row of elements of the two-dimensional weighting matrix (i.e., the sampled point spread function). The two-dimensional DFT of the resulting defective weighting matrix yields the two-dimensional frequency transfer function. Perspective display of the magnitude of these two-dimensional frequency transfer functions permits the evaluation of the degradation resulting from defective elements in the FIR weighting matrix.

Array defects can arise either due to defective sensing elements or due to defective FIR elements. For an array sensing approach using an N-element linear sensor array and an N^2-stage TAD, a single defective sensing element with zero output has the same effect as setting an entire row of the two-dimensional weighting matrix to zero. On the other hand, if a true NxN two-dimensional array of sensor elements is used the effect of a single defective sensor element does not propagate; this corresponds to setting a single element of the two-dimensional weighting matrix to zero. Defective FIR tap weights could arise using a TAD-32 FIR implementation via failure of one or more of the tap resistors and/or tap buffer amplifiers if they are used. For the array sensing approach using an N-element sensor and an N^2 element TAD described above, a single defective resistor now is equivalent to setting a single element of the N^2

230

weighting matrix to zero; recall that a single defective sensing element in this approach is equivalent to setting an entire row of the weighting matrix to zero. For separable FIR filter realizations utilizing a cascade of two one-dimensional FIR filters a single defective resistor is equivalent to setting an entire row or column of the weighting matrix to zero. Separable and nonseparable two-dimensional FIR filters were discussed in Section 4.1.5.

Since setting an element of the weighting matrix to zero is equivalent to adding an impulse of opposite sign and strength at the appropriate location of the two-dimensional weighting matrix, we can infer the following effects of a defective element upon the frequency transfer function:

(1) change in gain at the origin of the frequency transfer function, i.e., $|H(0,0)| \neq 0$ dB

(2) nonlinear phase of the filter (unless the defective element is the center one of the PSF, odd N)

(3) distortion of the magnitude response of the transfer function

(4) decreased stopband attenuation of the transfer function

Effect (1) arises since

$$H(0,0) = \sum_{k=1}^{N=1} \sum_{j=1}^{N-1} h_{jk=1}$$

(where h_{jk} are the filter tap weights) and setting one of the h_{jk} to zero will prevent the double summation over h_{jk} from attaining its desired value of unity. Effect (2) is due

231

to the fact that linear phase FIR filters require tap weight
symmetry with respect to the midpoint of the sampled point
spread function. This symmetry is destroyed if any tap weight
element other than the center one (for odd N) is changed.
Effect (3) is an obvious result of modifying an element of
the tap weight matrix; the extent of the distortion depends
upon the magnitude and location of the defective element.
The decreased stopband attenuation, effect (4), may be re-
garded as the result of adding an impulse to the tap weight
matrix; superposition applies and the DFT of an impulse is
two-dimensional white noise. If the magnitude of this "white
noise" exceeds the stopband attenuation, filter performance
will be degraded.

Note that the term "white noise" is somewhat
misleading as used in this explanation; it is intended only
to help describe the shape of the transfer function in the
stopband region and is not to be interpreted as being additive
noise in any sense.

Figures 4.4.3-1 through 4.4.3-6 show the
perspective plots of the magnitude of the two-dimensional
transfer functions that result when various elements or rows
of elements of the filter tap weight matrix are set equal
to zero.

Figure 4.4.3-1(a) shows the magnitude of the
transfer function for a 31 x 31 filter without any defective
elements; this separable filter is characterized by Kaiser
parameter $\beta=3$ and bandwidth parameter $\rho=0.42$. The (b) portion
of the figure shows that setting element (15, 18) to zero
does not hamper the effectiveness of the filter, whereas
Figure 4.4.3-1(c) shows that losing the center filter element
(16, 16) renders this half bandwidth filter useless. Recall
that deleting (i.e., setting to zero) an element of the filter
matrix lowers the gain and raises the stopband; both of these
effects are evident in Figure 4.4.3-1.

232
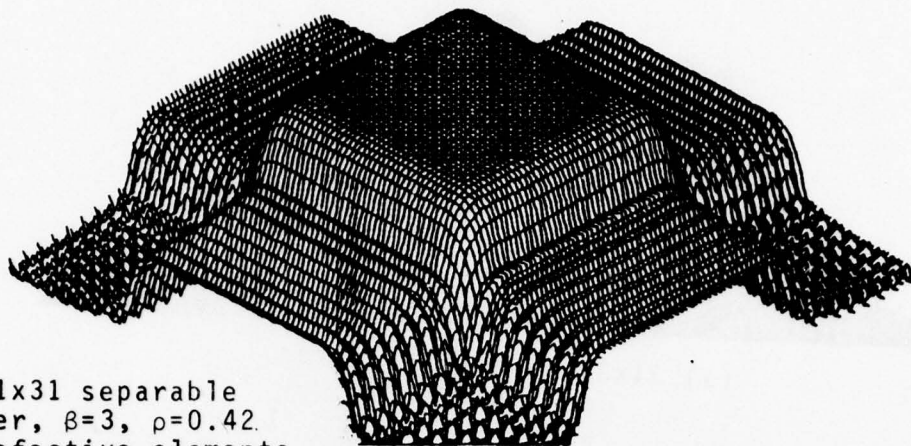
(a) 31x31 separable
filter, β=3, ρ=0.42
no defective elements
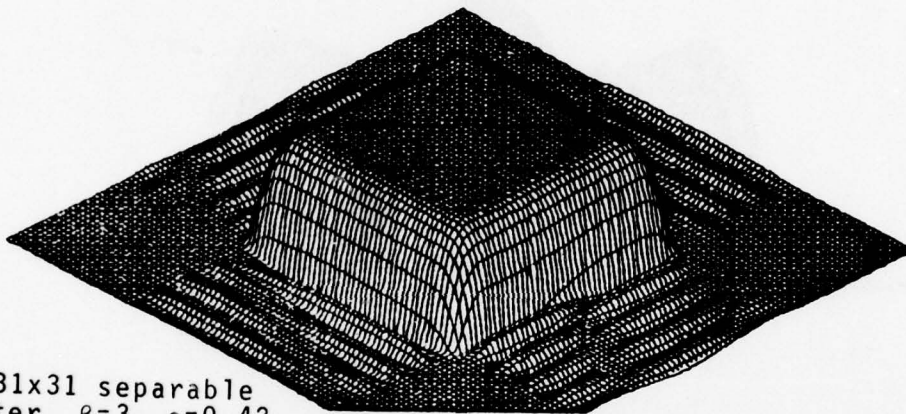
(b) 31x31 separable
filter, β=3, ρ=0.42
element (15,18)
defective
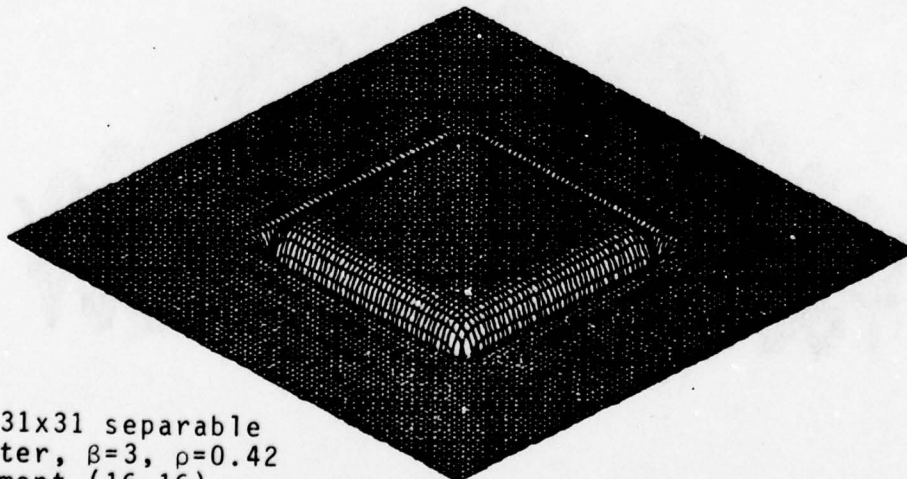
(c) 31x31 separable
filter, β=3, ρ=0.42
element (16,16)
defective

Figure 4.4.3-1. The Effect
of a Defective Element
Upon a Separable 31x31,
β=3.0, ρ=0.42 FIR Filter

233
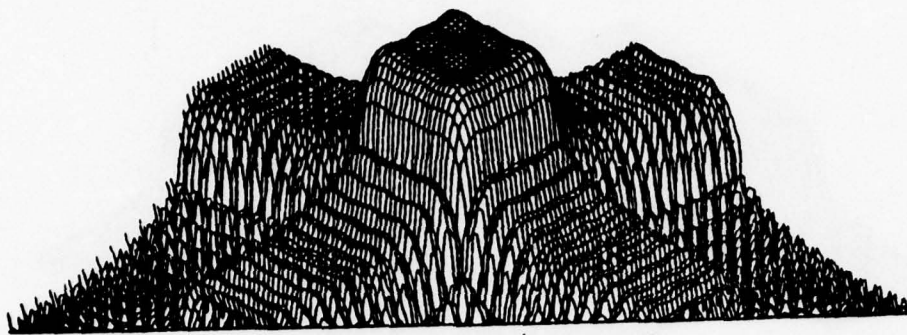
(a) 31x31 separable filter
$\beta=1.0$, $\rho=0.21$
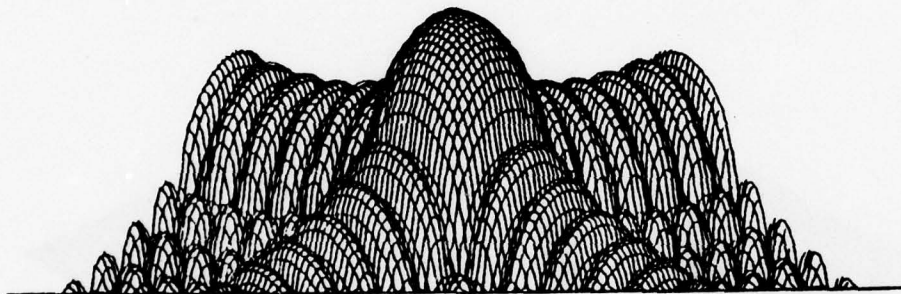
(b) 15x15 separable filter
$\beta=1.0$, $\rho=0.14$
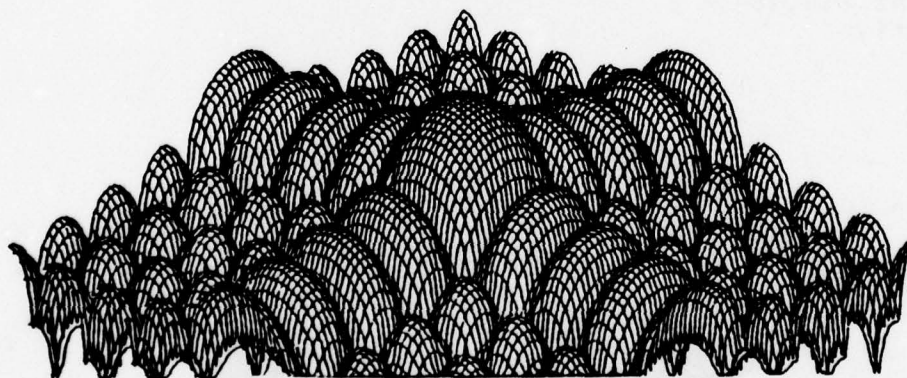
(c) 9x9 separable filter
$\beta=1.0$, $\rho=0.05$

Figure 4.4.3-2
Frequency Responses for
N=31x31, 15x15, and 9x9
Separable FIR Filters Having
No Defective Elements

234
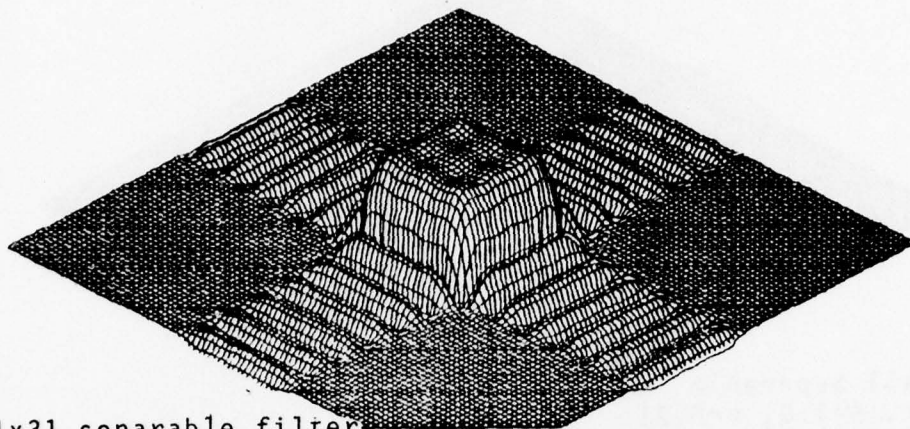
(a) 31x31 separable filter
$\beta=1.0$, $\rho=0.21$, element
(16,16) = 0
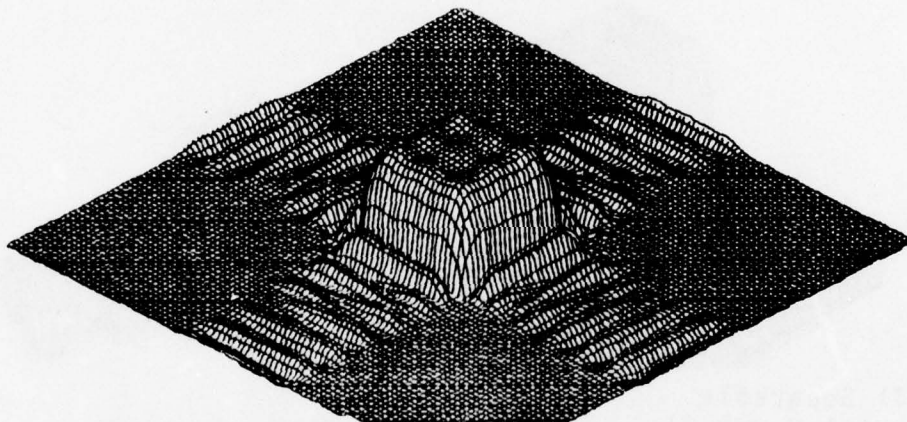
(b) 31x31 separable filter
$\beta=1.0$, $\rho=0.21$, element
(17,17) = 0
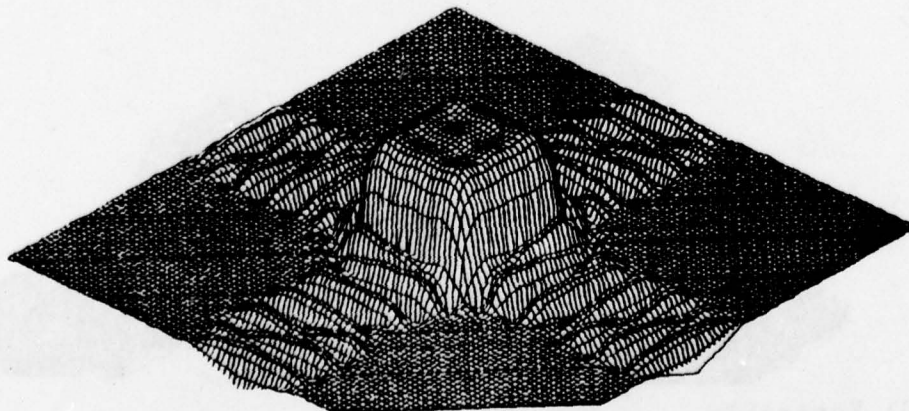
(c) 31x31 separable filter
$\beta=1.0$, $\rho=0.21$, element
(18,18) = 0

235

Figure 4.4.3-3. Defective Frequency Responses for 31x31,
Separable FIR Filter: PSF Elements
(16,16), (17,17), and (18,18) Defective
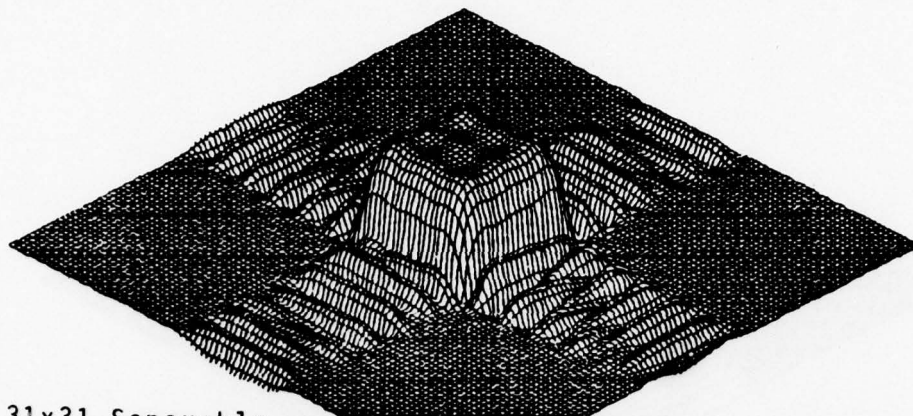
(a) 31x31 Separable
Filter, β=1.0, ρ=0.21
Element (15,18) = 0
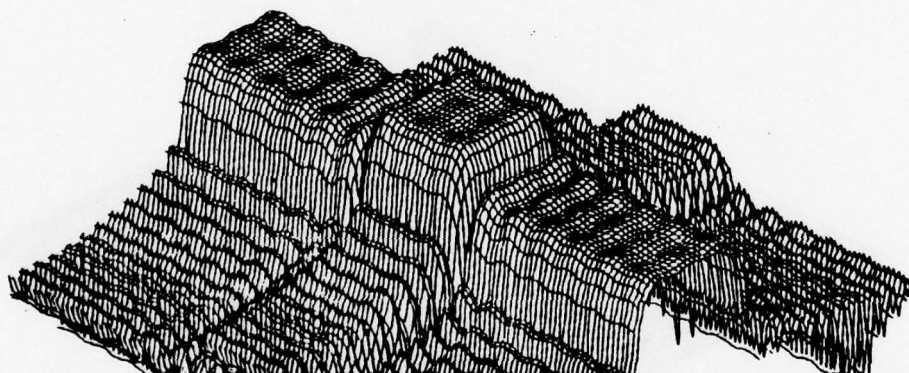
(b) 31x31 Separable
Filter, β=1.0,ρ=0.21
Elements (16,all) = 0
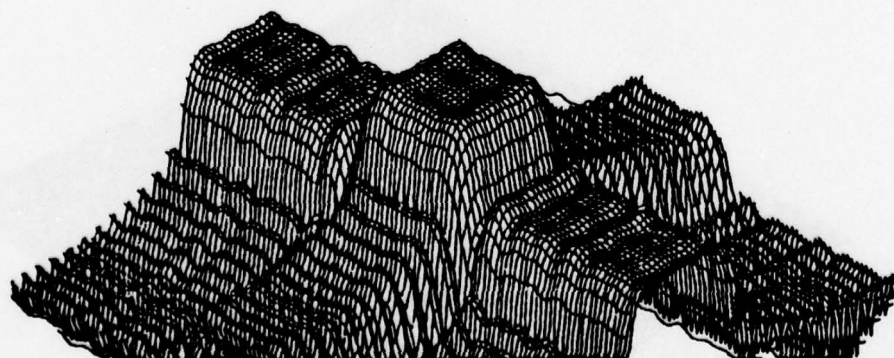
(c) 31x31 Separable
Filter, β=1.0, ρ=0.21,
Elements (19, all)=0

236

Figure 4.4.3-4. Defective Frequency Responses for 31x31
Separable FIR Filter: PSF Elements (15,18), (16,all),
and (19, all) Defective
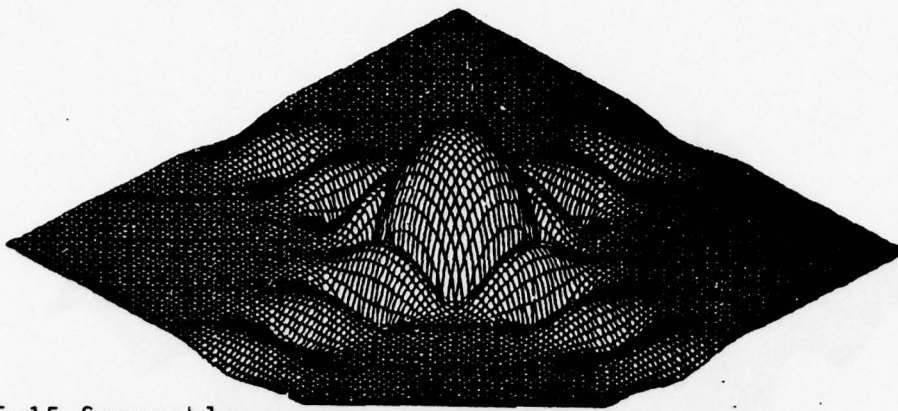
(a) 15x15 Separable
Filter β=1.0, ρ=0.14,
Element (8,8)=0
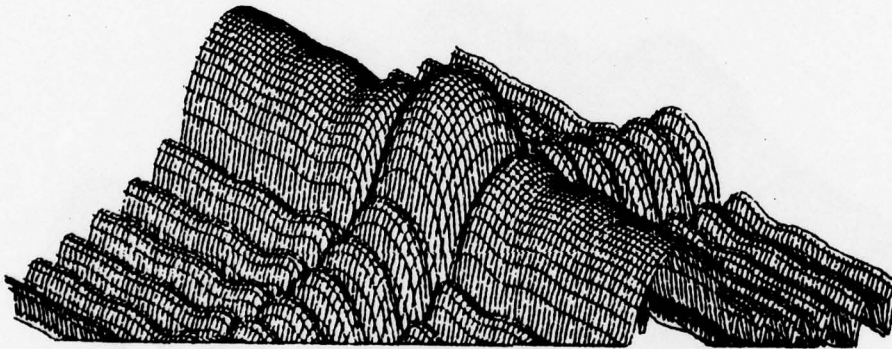
(b) 15x15 Separable
Filter β=1.0, ρ=0.14,
Element (8,all)=0

(c) 15x15 Separable
Filter β=1.0, ρ=0.14,
Element (10,10)=0

237

Figure 4.4.3-5. Defective Frequency Responses for 15x15
FIR Filter: PSF Elements (8,8), (8,all), and (10,10)
Defective
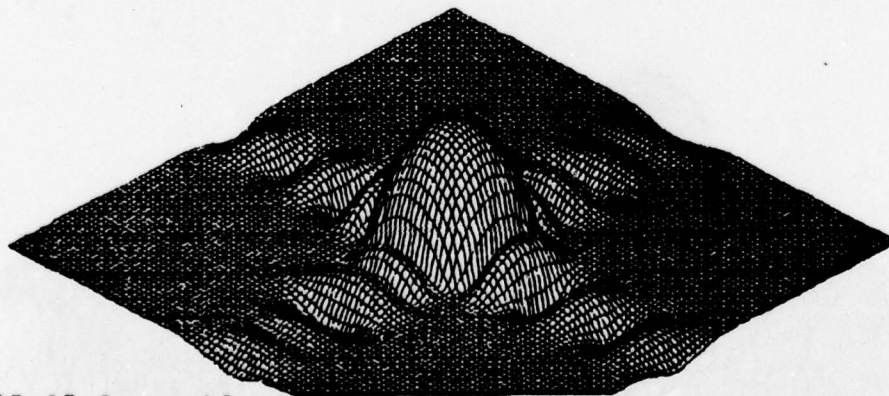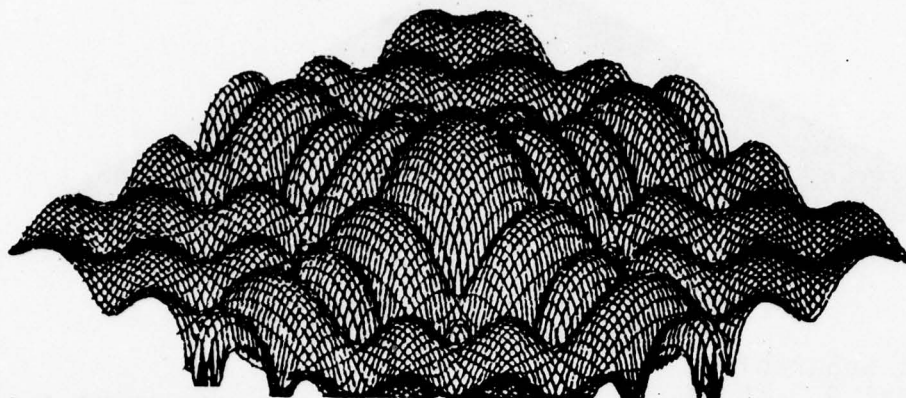
(a) 9x9 Separable
Filter $\rho=0.05$, E
Element (5,5)=0
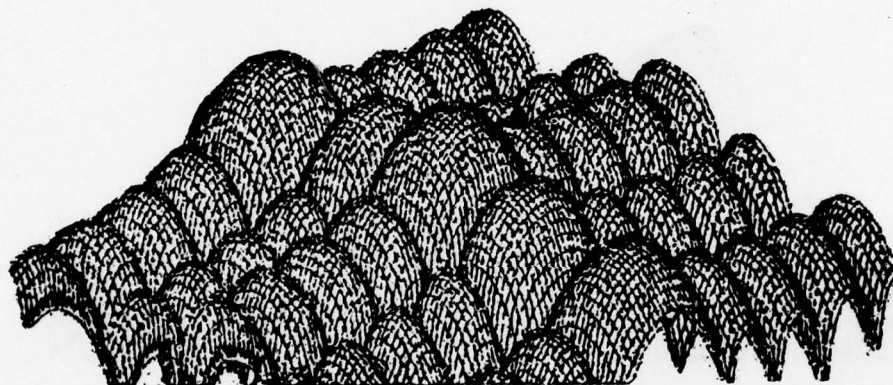
(b) 9x9 Separable
Filter $\rho=0.05$,
Element (5,all)=0
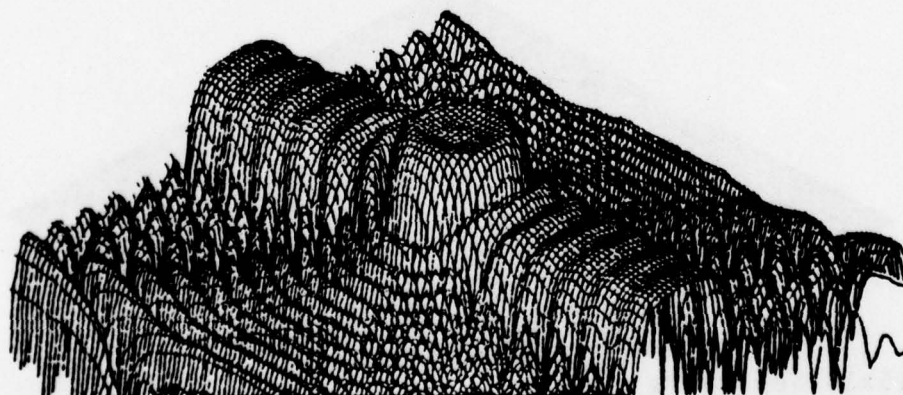
(c) 31x31 Nonseparable
Filter, $\rho=0.21$, $\beta=1.0$,
Element (16,all)=0

238

Figure 4.4.3-6   Defective Frequency Responses for 9x9
FIR Separable Filters With PSF Elements (5,5) and (5,all)
Defective and for 31x31 FIR Nonseparable Filter with
PSF Element (16,all) Defective

The remainder of the figures deal with separable filters (with one exception) having Kaiser parameter β=1.0 and dimensions 31 x 31, 15 x 15, and 9 x 9. These filters were designed so that their first stopband null fell at the quarter-bandwidth point. The fact that lower order filters have wider transition band for all other parameters constant means that the value of ρ will decrease for smaller values of N. For the filters shown in the following figures, the value of ρ is 0.21, 0.14, and 0.05 for N=31, 15, and 9, respectively. Although subjective evaluation of the decimated/interpolated images showed that larger values of ρ are appropriate for a decimation/interpolation factor of four, results shown in these figures indicate the general nature of the effects of defective filter (or sensor) elements upon filter transfer functions.

Figure 4.4.3-2 shows the frequency transfer functions for separable filters having N=31, 15, and 9 and no defective elements. These results serve as the basis for comparison of the defective transfer functions.

Figure 4.4.3-3 shows the defective frequency responses corresponding to defective elements located at positions (16,16), (17,17), and (18,18) for the 31 x 31 FIR filter. In all three cases the stopband attenuation in the diagonal frequency direction (halfway between the horizontal and vertical frequency axial directions) is degraded but does not decrease to less than the along-axis value. For the element (16,16)=0 case the symmetry of the frequency response is preserved; setting the center element (16,16) of the point spread function (PSF) to zero does not disturb the symmetry of the PSF about its center element. The defective response of the FIR filter having element (16,16)=0 therefore still has linear phase. The misshapen along-axis stopband sidelobes evident in Figure 4.4.3-3(b) and 4.4.3-3(c)

are a result of the destruction of the symmetry of the PSF
that occurs whenever an element other than the center one
is set to zero.

Figure 4.4.3-4(a) shows the response for the
case in which element (15,18) is defective; this response
is not radically different from the previous ones which had
defective elements along the diagonal of the PSF, viz.,
(16,16), (17,17), and (18,18). The (b) and (c) portions
of Figure 4.4.3-4 show the frequency responses for the cases
in which elements (15, all) and (19, all) are defective,
respectively. The "all" notation indicates that the element
values of an entire row or column of the PSF matrix are
zero. As might be expected, setting an entire row of elements
to zero has a profound effect upon the frequency response.

Furthermore, the closer the defective row
is to the center of the PSF the greater the degradation of
the frequency response. The remarkable fact is that the
frequency response degradation resulting from a defective
PSF row more than two rows away from the center row is ap-
parently not devastating, judging from Figure 4.4.3-2(a)
and Figure 4.4.3-4(b) and (c).

Figure 4.4.3-5 shows the effect upon the fre-
quency response of a 15 x 15 FIR filter having one element
or one row of the PSF equal to zero. As in the 31 x 31
case, losing a single FIR element, even the center one, is not
catastropic, whereas losing the center row of the PSF degrades
filter performance significantly along one frequency axis.
Note the slight change in stopband ripple structure between
the (8,8) case and the (10,10) case, (a) and (c) of Figure
4.4.3-5, respectively.

The 9 x 9 separable FIR filter frequency re-
sponses corresponding to defective PSF elements (5,5) and
(5, all) are shown in the (a) and (b) portions of Figure
4.4.3-6, respectively. Figure 4.4.3-6(c) shows that the

previously observed behavior regarding defective rows in separable PSF's is also characteristic of nonseparable filter PSF's as well. Again, losing a single PSF element does not significantly impair filter response, whereas losing the center row of the PSF causes significant degradation in the frequency response along one axis.

The results presented in this section have indicated that, generally speaking, losing one element of the $\rho=.25$ two-dimensional PSF weighting matrix does not significantly degrade FIR filter performance for 31 x 31, 15 x 15, and 9 x 9 filters. However, if the center row of the PSF weighting matrix is lost, filter performance is degraded to such an extent that it is probably unacceptable. For the $\rho=.5$ half-bandwidth filter, losing the center element of a 31x31 filter rendered the filter response useless.

5.0   IMAGE BANDWIDTH COMPRESSION

        This paragraph begins with an overview of the
nature of image redundancy and its relation to source coding
techniques. This is followed by a description of image re-
duction (resolution reduction) via decimation and interpolation
which is the basis of the REARCS concept. The theory of op-
eration of the several candidate image compression techniques
is explained and a performance versus implementation complexity
matrix is given, assuming conventional single element raster
scanning.

        The relationship between implementation complexity
and the nature of the scanning process is alluded to and the
stage is set for the further investigation of this relation-
ship in the following Section 6.0, Candidate Systems.

        This paragraph is mainly intended to serve as
a tutorial overview of image bandwidth compression techniques.
The critical issues concerning bandwidth compression imple-
mentation complexity tradeoffs, the system impact of the REARCS
requirement, and the concomitant two-dimensional filtering
requirement assuming array scanning are addressed in more
depth in paragraph 6.0, Candidate Systems.

5.1   Introduction to the Nature of Redundancy in
            Imagery and Its Relation to Source Coding

        All image signals may be regarded as being the sum
of two parts: a predictable or redundant part which contains
no information and therefore need not be transmitted, and
an unpredictable or nonredundant part called the innovation
which contains all the information regarding the image. In
general, the redundancy of the image is of two kinds. The
first kind of redundancy is evidenced by correlation among
spatially adjacent picture elements (pixels), or, in the

two-dimensional spatial frequency domain, by nonuniform power spectral density. The adjacent pixels of an image characterized by a uniform power spectral density are uncorrelated, as may be easily shown using the Nyquist Sampling Theorem. The second kind of redundancy is evidenced by the nonuniform probability density function of the image pixel values. This simply means that for signals which have been quantized in amplitude, some amplitude levels occur more frequently than others. This kind of redundancy can be reduced by assigning shorter channel code words to the more frequently occurring amplitude levels via a statistical coding procedure.

Source coding techniques fall into two broad categories: entropy preserving and nonentropy preserving. Entropy preserving techniques are those for which the reconstructed (decoded) image is exactly the same as the original source image, i.e., there is no degradation of image quality. The average number of bits/pixel at the output of an entropy preserving coder can approach the entropy of the source for sufficiently complex coding techniques; note that the entropy of the source is a measure of the information content of the innovation signal and that the predictable or redundant signal has zero entropy. The average bandwidth compression ratio for such coders is image source dependent, and, moreover, varies within an image depending upon the activity of the local part of the image that is being coded; this implies that a channel buffer is required if the channel is to be fully utilized. Nonentropy preserving techniques can obtain large bandwidth compression ratios at the expense of the quality of the reconstructed image. For these techniques, a replica of the innovation signal is not available at the receiver since the channel bit rate is insufficient to match the entropy of the source. Shannon's rate distortion theory mathematically

243

describes the bound for the trade-off between the fidelity
(mean squared error criterion) of the reconstructed image and
the image bandwidth compression ratio for any nonentropy
preserving source coding technique. This permits the per-
formance of any source coding technique to be evaluated in
terms of how closely its rate distortion characteristic ap-
proaches the Shannon rate distortion bound.

For nonadaptive, nonentropy preserving source
coders, the bandwidth compression ratio is constant regardless
of the activity of the image area being encoded; this implies
that the quality of the reconstructed image is degraded more
in the high activity regions of the image. For the adaptive
source coder this is not necessarily the case.

One method of reducing the number of bits that
are used to represent a source image is to reduce the number
of pixels in the source image via decimation and interpolation.
This is a nonentropy preserving technique. The penalty for
reducing the required image transmission bandwidth in this
way is reduced resolution in the reconstructed image and the
possible introduction of spurious detail (called aliasing)
into the reconstructed image. The degree of degradation due
to aliasing depends upon the sophistication of the two-dim-
ensional decimation and interpolation filters. This aspect
of bandwidth reduction via decimation/interpolation was dis-
cussed in detail in Section 4.0.

The decimation/interpolation technique can be
very profitably combined with conventional source coding tech-
niques in order to obtain very large image bandwidth compres-
sion ratios. This approach to image bandwidth compression,
called the Redundant Area Coding System (REARCS), was develop-
ed by RADC and Harris under contract to RADC in connection
with the Experimental Image Compression System (EICS). The
primary feature of this philosophy of image bandwidth

244

compression is that it takes full advantage of the fact that
for typical military imagery certain areas of the image
(called nonredundant areas) are more important than the
remainder of the image (called redundant area). Typically,
the nonredundant areas of an image contain objects that are
of high military interest, whereas the redundant areas may
include rivers, fields, or other geographical features which
are used primarily for orientation of the image. Imagery
transmission systems utilizing the REARCS concept require
that the nonredundant areas be designated by the operator
prior to transmission of the image. This is accomplished
by dividing the source image into 1-inch squares using a
transparent grid template and identifying all 1-inch square
blocks which are considered nonredundant areas (refer to
Figure 4.1.1). Once the nonredundant areas have been iden-
tified, a desired resolution and source coding technique
is selected for both the nonredundant and redundant areas
of the image. Typically, moderate or high resolution and
entropy preserving source coding is required for the non-
redundant areas (implying moderate bandwidth compression)
whereas low resolution and nonentropy preserving source coding
is permissible in the redundant areas (implying very high
bandwidth compression). Thus, the REARCS technique permits
the interesting portions of an image to be transmitted with
high quality while transmitting the remainder of the image
at a lower quality. The result is that the objectives of a
military image transmission system are met while substantially
decreasing the required transmission time per image.

The issues involved with image reduction via
decimation/interpolation were discussed in detail in para-
graph 4.0.

5.2   Image Bandwidth Compression Techniques

The theory of operation of the two-dimensional
orthogonal transformation technique, the hybrid technique,
multiple tap Delta modulation, statistical coding, DPCM, and
MAPS is presented in this section. The rate-distortion coding
performance for various source coding algorithms [20] is
compared to the Shannon rate distortion bound for bandlimited
signals in Figure 5.2.

5.2.1   Two Dimensional Orthogonal Transformation
                      Techniques

A gray-shade image can be modelled by specifying
its brightness $u(x,y)$ at each spatial coordinate (x,y). If
the resulting signal is band-limited, it may be represented
by a matrix P of n x n discrete picture elements or pixels.
In standard pulse code modulation, each of these pixels is
quantized into one of 2^m different levels and each level may
then be represented by an m-bit number. It has been shown
[14, 15] that if this matrix P is transformed by certain
linear reversible transformations before quantization, fewer
bits are needed to represent the image for a given fidelity
than with pulse code modulation. This transformation opera-
tion is usually represented by

$$F = APA^T \tag{5-1}$$

where A is the transform matrix and T denotes transpose. In
this equation A operates on the columns of P and A^T operates
on its rows. All terms in this equation are n x n matrices;
F is the transformed image. The final step in the coding
procedure is to quantize the elements in F to form F_q.
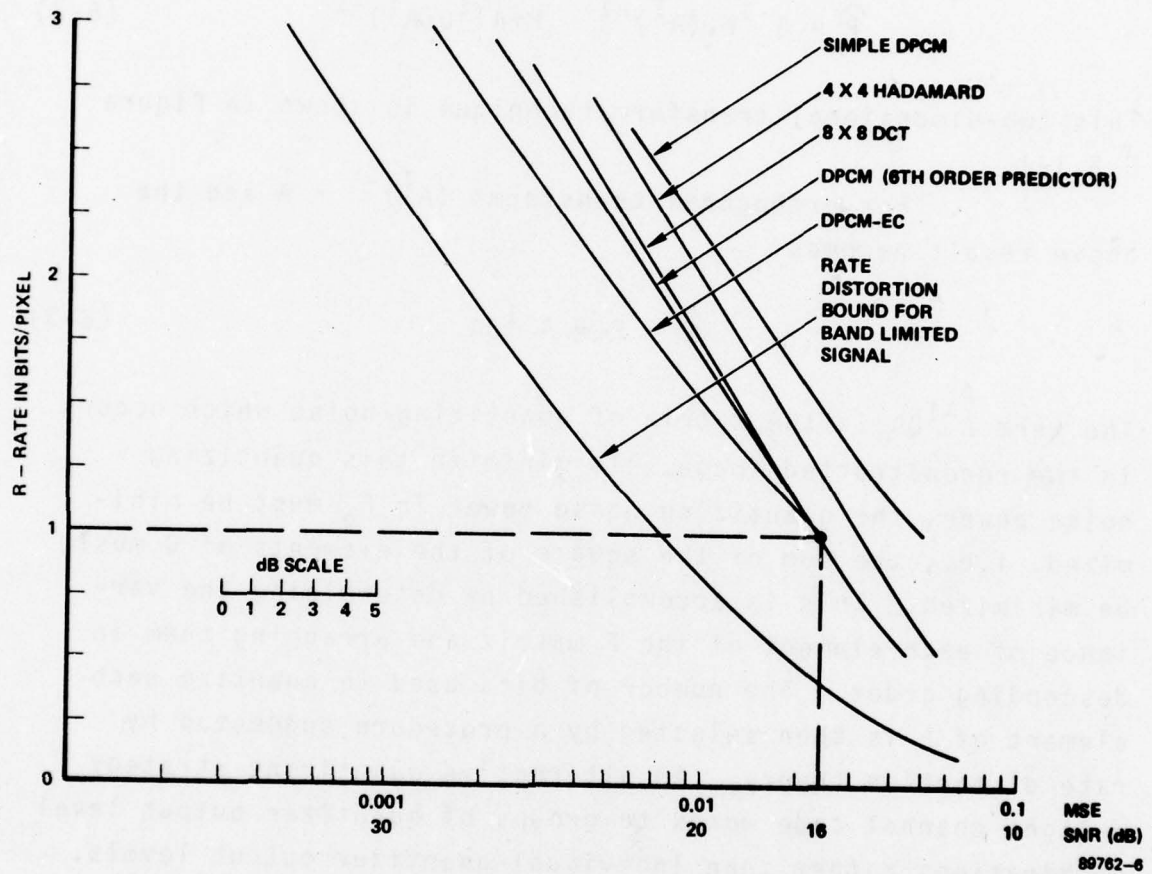
Figure 5.2

Coder Performance for Unweighted Mean Square Error

Each element in F_q is then represented by a binary number and $F_q = F + Q$ where Q is an n x n matrix of the quantizing noise. The reconstructed image $\widehat{P}$ is formed by a linear inverse transformation of F_q:

$$\widehat{P} = A^{-1}F_1(A^T)^{-1} = P + A^{-1}Q(A^T)^{-1} \qquad (5-2)$$

This two-dimensional transform technique is shown in Figure 5.2.1-1.

For orthogonal transforms $(A^T)^{-1} = A$ and the above result becomes

$$\widehat{P} = P + A^{-1}QA \qquad (5-3)$$

The term $A^{-1}QA$ is the matrix of quantizing noise which occurs in the reconstructed image. To minimize this quantizing noise power, the quantizing noise power in F_q must be minimized, i.e., the sum of the square of the elements of Q must be minimized. This is accomplished by determining the variance of each element of the F matrix and arranging them in descending order. The number of bits used to quantize each element of F is then selected by a procedure suggested by rate distortion theory. An alternative quantizing strategy assigns channel code words to groups of quantizer output level combinations rather than individual quantizer output levels.

The two-dimensional transform source coding technique accomplishes bandwidth compression by virtue of two properties of orthogonal transformations. The first property is that the image energy is highly compacted into one corner of the transform domain, i.e., low order transform coefficients have large values and high order transform coefficients have small values. In contrast to this, the

248
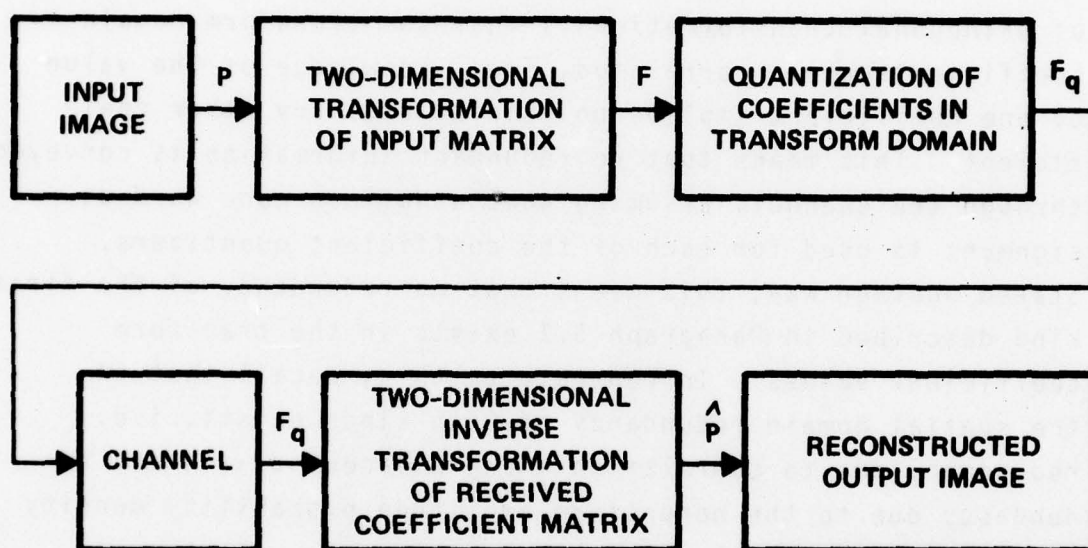
89762–28

Figure 5.2.1-1
Two-Dimensional Transform Technique

image energy (the square of the pixel values) is more uniformly
distributed in the spatial domain. This energy compaction
property implies that the high order, negligibly small co-
efficients need not be transmitted at all and that the
resulting increase in the number of available bits can
then be used to better specify (i.e., more precisely quantize)
the remaining low order coefficients. The second property
of orthogonal transformation is that the transform domain
coefficients are uncorrelated, i.e., knowledge of the value
of one coefficient implies no knowledge of any other coef-
ficient. This means that no redundant information is conveyed
through the channel, assuming that a Huffman code word as-
signment is used for each of the coefficient quantizers.
Stated another way, this means that no redundancy of the first
kind described in Paragraph 5.1 exists in the transform
coefficient values. In contrast to this, recall that in
the spatial domain redundancy of both kinds exists, i.e.,
redundancy due to correlation among adjacent pixels and re-
dundancy due to the nonuniform amplitude probability density
function of the pixel values.

In any practical two-dimensional transform
bandwidth compression technique, the dimension of the input
matrix of pixels (subimages or image subblocks) must be
limited to a fairly small value such as 4, 8, 16, or possibly
32 in order to maintain reasonable memory requirements
(note that input pixel values, transform coefficient values,
and transformation matrix values must be stored). Fortunately,
statistical influences in typical images only extend over
a relatively small number of pixels. This assertion is
supported by the fact that the output image SNR increases by
a negligible amount in going from 8 x 8 transform size
to 16 x 16 transform size [16] . The relationship between
image subblocks of size n x n and the input image pixel matrix
is shown in Figure 5.2.1-2(a).

MATRIX P OF PIXELS
CORRESPONDING
TO AN IMAGE

n

n
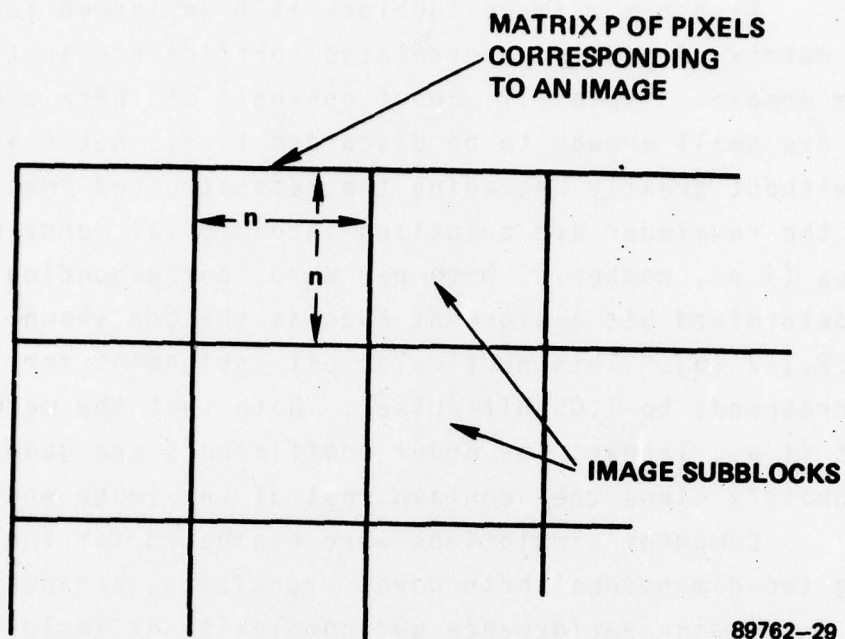
IMAGE SUBBLOCKS

89762—29

(a) Relationship of Image Subblocks to the
Matrix P of Pixels Representing the Image

	1	2	3	4	5	6	7	8
1	6	4	3	2	2	2	2	
2	4	3	2	2	2	2		
3	3	2	2	2	2			
4	2	2	2	2				
5	2	2	2					
6	2	2						
7	2							
8								

NOT
TRANSMITTED

89762—30

(b) Typical Bit Assignment in Transform Domain

Figure 5.2.1-2

Aspects of Two-Dimensional Transform Coding

251

Each n x n image subblock is transformed into an n x n matrix of nearly uncorrelated coefficients in the transform domain. Typically, about one-half of these coefficients are small enough to be discarded (i.e., not transmitted) without greatly degrading the reconstructed image quality; the remainder are quantized into digital words with accuracies (i.e., number of bits per word) corresponding to a predetermined bit assignment such as the one shown in Figure 5.2.1-2 (b). This particular bit assignment for n = 8 corresponds to 1.05 bits/pixel. Note that the more important (i.e., larger) low order coefficients are quantized more accurately since they contain most of the image energy.

Computer simulations were evaluated for the following two-dimensional orthogonal transforms, arranged in order of decreasing performance and complexity of implementation.

- Discrete Cosine Transform (DCT)
- Hadamard Transform
- Haar Transform

The results of these simulations are shown in Figure 5.2.1-3.

The implementation complexity of each of these techniques is dictated by the average number of multiplications and additions required per pixel, where multiplications are much more time consuming than additions or subtractions. The DCT matrix of transformation contains (n^2-n) irrational numbers implying (n^2-n) multiplications and n^2 additions (ignoring normalization), whereas the Hadamard transformation matrix contains only ±1's, implying that n^2 additions or subtractions are required. The Haar transformation matrix is sparsely populated, i.e., it contains slightly fewer than $n^2/2$ zeros, and the non-zero entries are ±1, so that approximately $n^2/2$ additions or subtractions are required.

(a) 8x8 Cosine, 2 bits/pixel

(b) 8x8 Hadamard, 2 bits/pixel

(c) 8x8 Haar 2 bits/pixel

(d) Original 4 bits/pixel

Figure 5.2.1-3
Computer Simulation Results for
Three 8x8 Orthogonal Transforms at 2 bits/pixel.

253

5.2.2   Hybrid Coding Technique

The hybrid source coding technique utilizes a one-dimensional transform of length n in one spatial dimension, followed by Differential Pulse Code Modulation (DPCM) of the transform coefficients in the other spatial dimension as shown in Figure 5.2.2-1 (a). These sequential one-dimensional operations attempt to decorrelate the image data in both spatial dimensions. The one-dimensional transform compacts the image energy into the low-order coefficients and de-correlates the coefficients. The bandwidth compression implications of these two properties of transformation were discussed in Paragraph 5.2.1. The mathematical formulation of the one-dimensional transform is

$$\bar{y} = \bar{x} A \qquad (5\text{-}4)$$

where

$\bar{x}$ = row vector of input pixel values; dimension 1 x n

$\bar{y}$ = row vector of transform coefficient values; dimension 1 x n

A = matrix of transformation; dimension n x n

The inverse one-dimensional transformation of the quantized coefficient row vector $\bar{y}_q = \bar{y} + \bar{q}$ ($\bar{q}$ is the vector of quantizing noise) is given by

$$\hat{\bar{x}} = \bar{y}_q A^{-1}$$

$$= (\bar{y} + \bar{q})A^{-1} = \bar{y}A^{-1} + \bar{q}A^{-1}$$

$$= \bar{x}AA^{-1} + \bar{q}A^{-1} = \bar{x} + \bar{q}A^{-1} \qquad (5\text{-}5)$$

ONE-DIMENSIONAL
TRANSFORM OF
LENGTH n

IMAGE

DPCM TRANSMISSION
OF TRANSFORM
COEFFICIENTS

89762—31
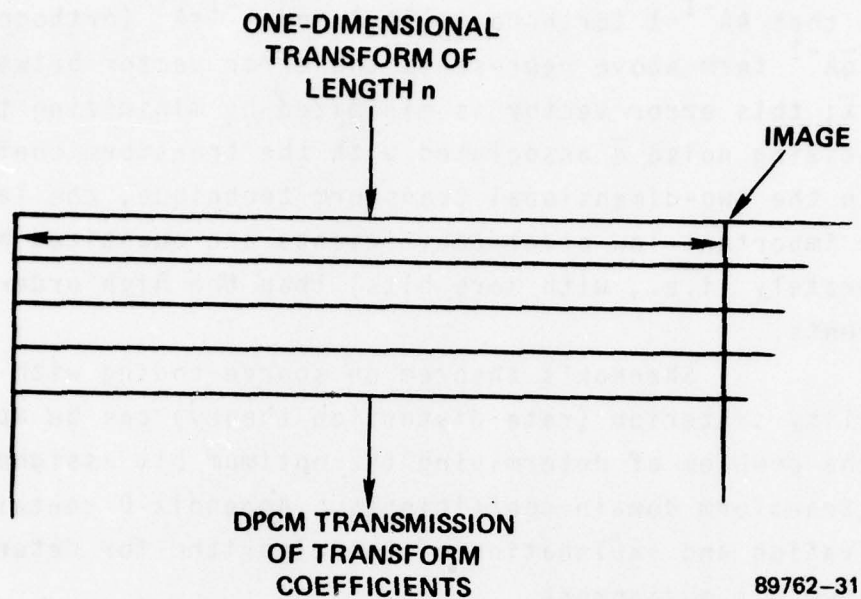
Arrangement of One-Dimensional Transform Blocks Within
A Source Image for Hybrid Coding Technique
(a)

n = 16

| 4 | 3 | 2 | 2 | 2 | 1 | 1 | 1 | 1 | NOT TRANSMITTED |

89762—32
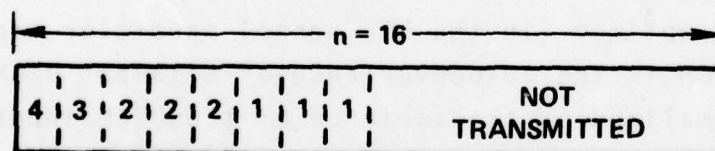
Bit Assignment for One-Dimensional
Transform/DPCM Hybrid Coder
(b)

Figure 5.2.2-1
Hybrid Coding

255

Note that $AA^{-1} = 1$ (orthonormality) and $A^{-1} = A^T$ (orthogonality). The $\bar{q}A^{-1}$ term above represents the error vector between $\hat{\bar{x}}$ and $\bar{x}$; this error vector is minimized by minimizing the quantizing noise $\bar{q}$ associated with the transform coefficients. As in the two-dimensional transform technique, the larger, more important low order coefficients are quantized more accurately (i.e., with more bits) than the high order coefficients.

Shannon's theorem on source coding with a MSE fidelity criterion (rate distortion theory) can be applied to the problem of determining the optimum bit assignment for the transform domain coefficients. Appendix D contains a derivation and explanation of the algorithm for determining the optimum bit assignment.

A particular bit assignment that corresponds to 1.0 bit/pixel for n = 16 is shown in Figure 5.2.2-1 (b).

For the special case in which the DPCM predictor tap value is equal to unity, the DPCM operation may be thought of as quantizing and transmitting the difference of coefficient values in adjacent rows. It is shown in Appendix E that the optimum (in the MSE sense) predictor tap value for one-tap DPCM is the autocovariance of adjacent DPCM input values normalized by the variance of the DPCM input values. In the presence of channel errors, the predictor tap values should be decreased somewhat in order to combat the effects of channel errors. Smaller predictor tap values cause the effects of channel errors to die out more quickly. The relationship between predictor tap value and channel noise effects and quantizing noise is derived in Appendix E. Fortunately, the MSE performance of DPCM systems is a rather weak function of the predictor tap value.

Further insight into the operation of DPCM may be obtained by referring to Figure 5.2.2-2. The ith quantizer quantizes the difference between the present value a_i of the ith coefficient and the predicted value $\hat{a}_i$. Note that except for a unit delay and a scaling factor, the predictor output a_i at the encoder is the output of a recursive digital low-pass filter whose input is the quantized version of the error sequence e_i. The low-pass filter cutoff frequency is determined by the value of α_i, the predictor tap value. The decoder is simply a digital low-pass filter, or "leaky integrator," which may be thought of as integrating the error sequence (plus quantizing noise sequence) that is transmitted over the channel. This point of view explains why the effects of channel errors decay exponentially: the output of a leaky integrator is an exponentially weighted past (EWP) average of its input values. If one of the input values is erroneous (due to a channel error), this error will be weighted less heavily at each sucessive output instant. The tradeoff between the MSE in the decoder output due to channel errors and the MSE in the decoder output due to DPCM source coding is explained and quantified in Appendix E.

5.2.3 Multiple Tap Delta Modulation

Multiple Tap Delta Modulation operates by quantizing the difference between the input sample value and an estimate of its value obtained from a predictor network. The predicted value, or estimate, of the present sample value is obtained in the predictor network as a linear weighted sum of selected previous values; this is illustrated in Figure 5.2.3 for a six-tap delta system. The optimum values for the predictor taps a_i, $i=1,2,...n$, for an n-tap delta modulation

257
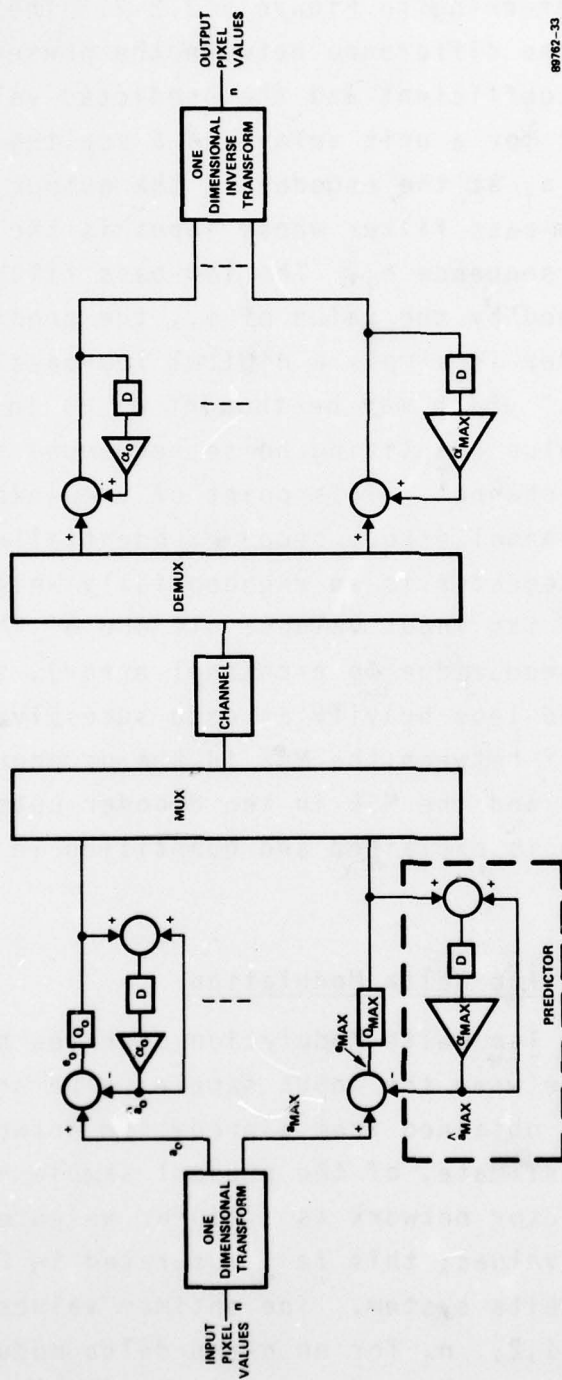
Figure 5.2.2-2

Block Diagram for

One-Dimensional Orthogonal Transform/DPCM Hybrid Technique

258
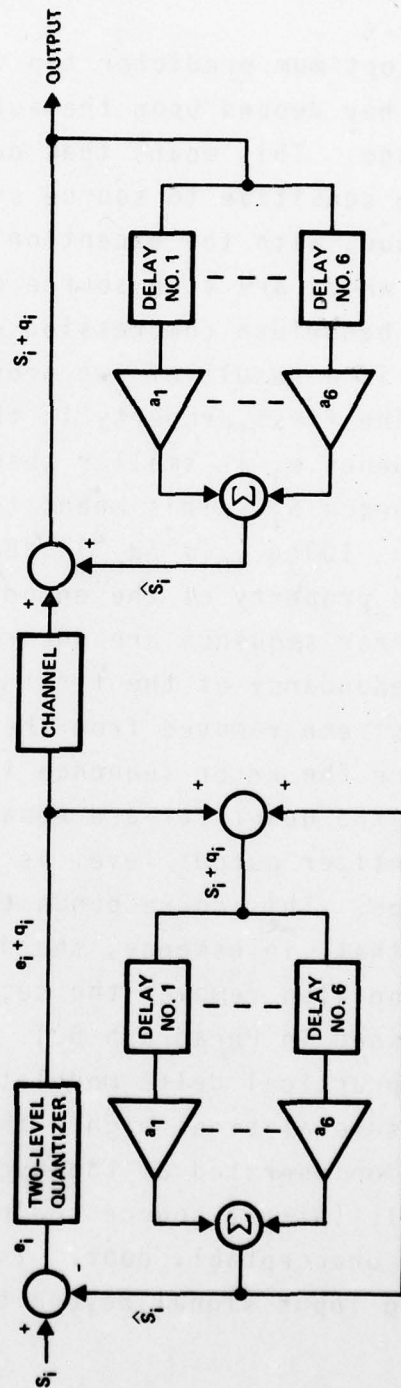
Figure 5.2.3
Six-Tap Delta Modulation

89762-24

259

system with linear prediction are the solutions of a system of n equations in n unknowns; this result is derived in Appendix E.

The optimum predictor tap values are input data dependent since they depend upon the autocovariance matrix of the source image. This means that delta modulation encoders are more sensitive to source statistics than the transform technique, with the exception of Karhunen-Loeve transformations, which are also source dependent.

The bandwidth compression obtainable using delta modulation is a result of two properties of the source encoding loop. The first property is that the variance σ_e^2 of the error sequence e_i is smaller than the variance σ^2 of the input sequence S_i. This means that the same SNR can be obtained using $10\log_{10}(\sigma^2/\sigma_e^2)$ dB/(6dB/bit) fewer bits. The second property of the encoding loop is that the samples of the error sequence are uncorrelated. This means that the image redundancy of the first kind discussed in Paragraph 5.1 has been removed from the input sequence. In addition, since the error sequence is zero-mean the two output levels of the quantizer are equally likely and (trivially) each quantizer output level is represented by a code word of length one. This corresponds to the simplest possible Huffman code so that, in essence, the delta modulation encoding operation also removes the second kind of image redundancy discussed in Paragraph 5.1.

In practical delta modulation systems the sampling rate is usually several times higher than the Nyquist rate. If delta modulation operated at the Nyquist rate the one bit per Nyquist sample (pixel) source coding performance that results is often unacceptably poor. Increasing the sampling rate of an analog input signal beyond the Nyquist rate

260

increases the correlation between adjacent samples and, therefore, increases the efficiency of the linear prediction portion of the coder. The penalty for this improved performance is that there are now several channel bits per Nyquist sample since there are several coder samples per Nyquist interval. This is a favorable tradeoff of complexity and performance for some situations, and, in fact, delta modulation out performs DPCM for RC-type signal spectra at low bit/(Nyquist sample) rates [17].

5.2.4 DPCM

Multiple-tap Differential PCM (DPCM) operation is the same as that of multiple-tap delta modulation shown in Figure 5.2.3 except that the simple two level quantizer (comparator with ±k volt output) is replaced with a more complex n-bit or N-level quantizer [19], where usually $N=2^n$ in order to fully utilize the bits of the quantizer output codewords. Quantizers of more than two levels are much more complex than comparators and there are performance/complexity tradeoffs among these. For example, nonuniformly spaced quantizing levels yield improved performance for signals having nonuniform probability density functions, but are more complex and expensive to implement than quantizers with uniformly spaced output levels. Optimum nonuniform Laplace quantizers give the best performance in DPCM systems, but optimum uniform Laplace quantizers are easier to implement [27, 28]. In practice, DPCM encoders usually operate at or near the Nyquist sampling rate, whereas delta modulation systems almost invariably operate with a sampling frequency several times higher than the Nyquist rate for reasons explained in Section 5.2.3. DPCM encoding followed by

Huffman coding of the DPCM quantizer outputs gives improved
rate-distortion performance, but at the expense of the addition-
al complexity associated with channel buffers and Huffman
coders.

5.2.5   Statistical Coding

          Statistical coding refers to an entropy pre-
serving technique in which a Huffman code is used to transmit
the difference in gray shade of adjacent pixels in the along-
scan direction of the digitized image. The block diagram
of this coding technique is shown in Figure 5.2.5. The band-
width compression of statistical coding is a result of the
high degree of spatial correlation between adjacent pixels
in typical imagery. The amplitude probability density function
of the difference of adjacent pixels is very sharply peaked
(about zero) as a result, which implies that Huffman coding
of the adjacent pixel differences can yield useful bandwidth
compression ratios on the order of 2:1 to 3:1, depending
upon the image source statistics. The primary advantage of
statistical coding is that it is an entropy preserving
technique, i.e., the reconstructed image is exactly like
the source image, in the absence of channel errors. The
disadvantages are three-fold: the Huffman code is source-
dependent,the nonconstant encoder output bit rate requires
channel buffers at the encoder and decoder, and the effect
of channel errors propagates indefinitely in the reconstructed
image. The propagation of the effects of channel errors can
be controlled by periodic reinitialization with an acceptably
small penalty in overhead rate but at the cost of increased
complexity.

89762—50

S_i

UNIT
DELAY

HUFFMAN
DECODER

CHANNEL

HUFFMAN
CODER

UNIT
DELAY

S_{i-1}

S_i
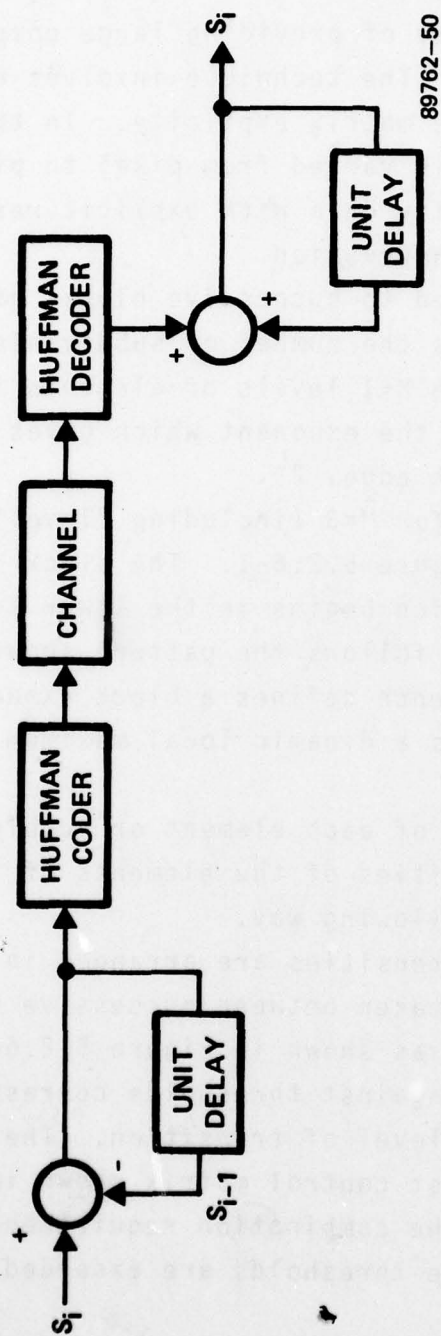
Figure 5.2.5

Statistical Coding Technique

5.2.6 MAPS Algorithm Description

The Micro Adaptive Picture Sequencing (MAPS) technique has the capability of providing large compression ratios in digital imagery. The technique involves defining the resolution of the image matrix explicity. In this process, the element size is varied from pixel to pixel. Replacing redundant intensity data with explicit resolution information provides the compression.

MAPS is applied to successive blocks of pixels of size $2^M \times 2^M$ where M is the number of subdivisions within the block. Thus, there are M+1 levels of elements in each block. This level is just the exponent which gives the number of pixels along the element edge, 2^L.

The elements for M=3 (including "level" as a subscript) are shown in Figure 5.2.6-1. The block sequence used is an "inverted z" which begins in the lower left corner of each element and follows the pattern shown in Figure 5.2.6-2. This sequence defines a block exhaustion configuration which imposes a dynamic local maximum block size constraint.

The intensity of each element or subblock is calculated from the intensities of the elements of the next lower level in the following way.

First, the intensities are arranged in increasing order and differences are taken between successive values and between extreme values as shown in Figure 5.2.6-3. These contrasts are then tested against thresholds correspondong to both contrast type and level of transition. The contrast thresholds form the contrast control matrix shown in Figure 5.2.6-4, which specifies the combination requirements for each level. If none of the thresholds are exceeded, the

Figure 5.2.6-1
Subframe Partition For M=3
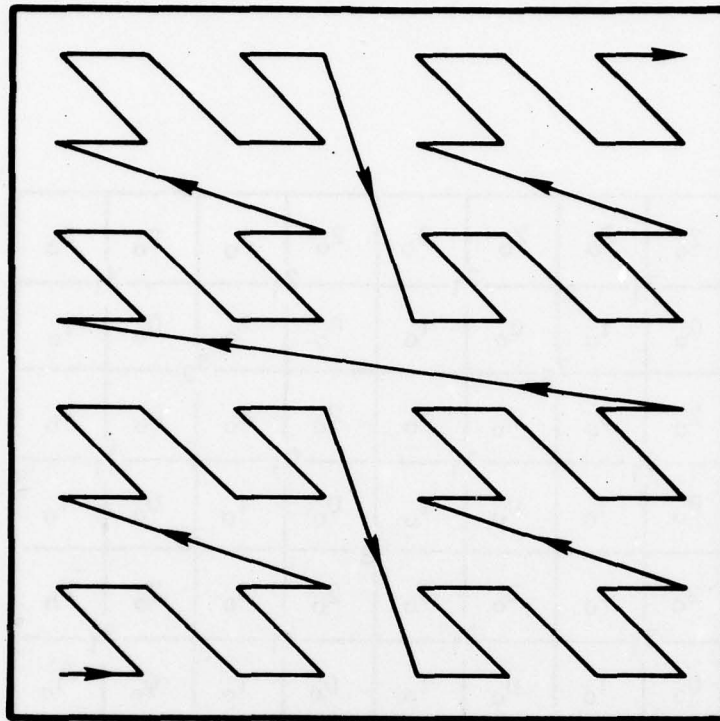
10293—7

Figure 5.2.6-2

"Block" Sequence Path

266

SUCH THAT

$$I_2 < I_1 < I_0 < I_3$$

4 ELEMENT BLOCK

10293–8
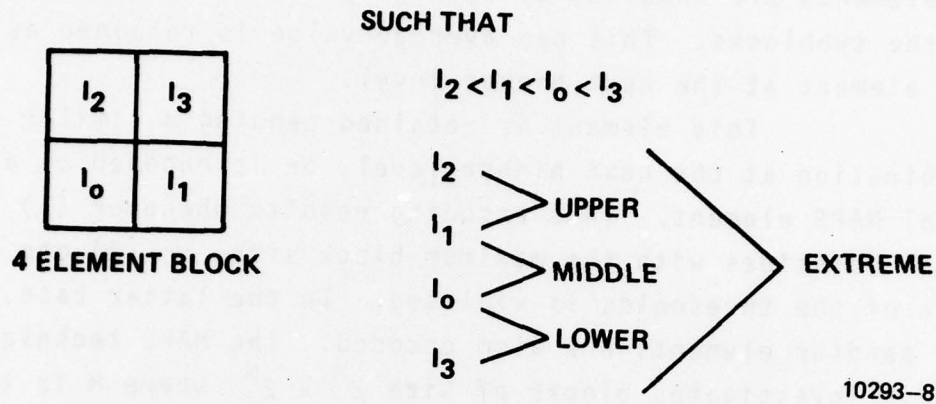
Figure 5.2.6-3. Fidelity Control Intensity/Contrast Definition

CONTRASTS

10293–6

Figure 5.2.6-4. Contrast Control Matrix

267

subelements are combined by averaging the intensity value of the subblocks. This new average value is retained as a new element at the next higher level.

This element is retained pending a similar combination at the next higher level, or is encoded as a final MAPS element. This encoding results whenever (1) the level coincides with the maximum block size, or (2) one or more of the thresholds is violated. In the latter case, all pending elements are also encoded. The MAPS technique always investigates blocks of size $2^M \times 2^M$ where M is the maximum number of subdivisions within the block.

The maximum block size is determined by trading off the buffer memory required for temporary storage of the elements and the advantage acquired in achievable compression ratio.

The encoding procedure consists of two parts. The compound codeword is composed of a resolution code which describes the level of the MAPS combination, and an intensity code which defines the local block intensity. The number of bits necessary to describe the resolution is an important factor in choosing maximum block size, since it affects compression ratios directly.

5.3   <u>EVALUATION OF PERFORMANCE/COMPLEXITY TRADEOFF FOR SOURCE CODING TECHNIQUES</u>

The theory and operation of six source coding algorithms were described in subsections 5.2.1 through 5.2.6.

- Two-dimensional transform coding
- Hybrid coding (one-dimensional transform along rows followed by DPCM transmission of coefficients along columns)

- Six-tap Delta Modulation
- DPCM
- Statistical coding
- MAPS

In evaluating source coding algorithms the following characteristics should be considered:

- Overall subjective quality of reconstructed imagery
- Resolution of reconstructed imagery
- Normalized MSE performance
- Propagation of channel errors in the reconstructed imagery
- Sensitivity to image source statistics
- Ease of implementation -- impacted by

  - Memory requirements
  - Speed requirements
  - Arithmetic precision requirements
  - Synchronization/interface requirements
  - Flexibility requirements
  - REARCS requirements

The results of the computer simulations for some of the candidate coding techniques were used to help construct the trade-off matrix shown in Table 5.3.

Based upon the simulation results and considering the results contained in the wealth of literature regarding image bandwidth compression [16-26] the hybrid coding technique utilizing a one-dimensional Discrete Cosine Transform (DCT) appears to be an appropriate choice to meet the bandwidth compression requirement. It is claimed in references [16, 21, 22 and 23] that the performance of hybrid

TABLE 5.3   Performance/Complexity Matrix for
Several Source Coding Techniques

CHARACTERISTIC	Two-Dimensional Transform	One-Tap DPCM	Hybrid	Six-Tap Delta Modulation	MAPS	Statistical Coding
Subjective Image Quality	FAIR	FAIR	GOOD	FAIR	GOOD	EXCELLENT
Image Resolution	GOOD	FAIR	GOOD	FAIR	FAIR	EXCELLENT
Normalized MSE Performance	FAIR	FAIR	GOOD	POOR	-	-
Immunity to Channel Error Effects	FAIR	FAIR	FAIR	FAIR	-	*POOR TO MODERATE
Insensitivity to Source Statistics	GOOD	POOR	GOOD	POOR	GOOD	POOR
Implementation Complexity	VERY HIGH	LOW	HIGH	LOW	HIGH	*MODERATE TO HIGH

*Depending upon channel error control strategy

-Not applicable or unknown

270

coding with DCT is superior to that of two-dimensional transform coders, and, further, that hybrid coders perform nearly as well as optimal Karhunen-Loeve transform coders.

The performance of the hybrid technique at 1.0 bit/pixel is very good even in channels characterized by BER=10^{-3} (worst-case); typical channels should exhibit a nominal BER=10^{-5}. A reconstructed hybrid-coded image is shown in Figure 5.3 for BER=10^{-3}; the unprocessed original is also shown there for comparison. The performance versus complexity tradeoff remains to be evaluated under the array scanning assumptions.

The basic source coding algorithms that have been described in this section, with the exception of the two-dimensional transform, hybrid and MAPS techniques, all accept pixel values sequentially, one at a time. The two-dimensional transform, MAPS, and hybrid bandwidth compression algorithms operate on two-dimensional or one-dimensional arrays of image data; for scanning systems which output pixel values sequentially, some storage medium is required in order to accumulate the one or two-dimensional image data blocks required for these three algorithms. For single point scanning systems the storage requirement is such that digital storage must be used; the associated control functions and digital arithmetic functions, combined with the sheer quantity of digital storage required, lead to implementations of high complexity. For array scanning systems, the one- or two-dimensional nature of the sensing and recording techniques is better suited to the block data structure required for hybrid and two-dimensional transformation bandwidth compression algorithms.

In this section we have discussed the concepts involved in image bandwidth compression and described the operation of six source coding algorithms. The performance and

271

(a)   Reconstructed Image
1.0 bit/pixel, BER = 10^{-3}

(b)   Original Source Image
6 bit/pixel

Figure 5.3

Original Source Image and Reconstructed Image Using
the Hybrid Technique, 1.0 bit/pixel BER=10^{-3}

complexity for each of these techniques were ranked and the
hybrid technique was judged as giving the best overall
performance. It is perhaps not surprising that sophisticated
algorithms give better performance than simple ones; it is
the purpose of the next paragraph, Candidate Systems, to
propose and evaluate the cost effectiveness of a variety
of ASITS architectures for several of the bandwidth compression
techniques discussed in this section. This task is made
all the more difficult because of the REARCS requirement,
but the REARCS capability is so absolutely vital to achieving
the desired overall bandwidth compression ratios that it
can hardly be abandoned. It will be shown in the next
section that the implementation complexity of the high
performance bandwidth compression schemes, viz., the hybrid,
MAPS, and two-dimensional transform coding algorithms, is
greatly reduced when full advantage is taken of array scanning
techniques.

6.0   CANDIDATE SYSTEM ARCHITECTURES FOR ASITS

In this section we present and evaluate a number of ASITS architectures which are capable of implementing various combinations of desirable ASITS functions, including:

- selectable image bandwidth compression ratios
- selectable resolution
- REARCS, which implies selectable image bandwidth compression ratios and selectable resolution for designated portions of the source image
- two-dimensional filtering in conjunction with REARCS
- image enhancement
- image MTF correction

Architectures which do not implement all of these desirable ASITS functions are presented here for several reasons. First, presenting architectures of varying capabilities shows the tradeoff between system capability and implementation complexity in a way that is easy to understand. Second, this method of presenting system architectures facilitates an easier grasp of the various aspects of the ASITS functions. Finally, this approach provides a shopping list for applications which have less sophisticated or less comprehensive system requirements than those we have arbitrarily imposed for the purposes of providing some structure for the study effort.

Recall from Section 5.0 that the hybrid algorithm was considered to be the most desirable high performance bandwidth compression technique for single point scanning systems when one considers performance versus implementation complexity. We now re-evaluate the implementation complexity

274

of this and the other bandwidth compression techniques
discussed in Section 5.0 assuming an array scanning technique
rather than a single-point scanning technique. This
re-evaluation of bandwidth compression implementation com-
plexity is integrated with an evaluation of the overall
system complexity assuming that array scanning is used for
the sensing and recording tasks. The approaches to system
implementation presented in this section include various
degrees of digital signal processing versus sampled-data
analog signal processing. Also, since it was shown in
Sections 2.0 and 3.0 that one-dimensional scanning techniaues
are far easier to implement than two-dimensional scanning
techniques, all of the candidate systems presented in this
section use one-dimensional scanning in conjunction with
analog or digital storage in order to synthesize two-dimen-
sional scanning.

In this section we present candidate systems
that may be described as follows:

- nonseparable two-dimensional filtering,
  one-tap DPCM, single spot recording
- separable two-dimensional filtering, one-
  tap DPCM, REARCS, single spot recording
- separable two-dimensional filtering, one-
  tap DPCM, REARCS, single spot recording,
  MTF correction, REARCS
- separable two-dimensional filtering,
  one-tap DPCM, multiple-spot recording,
  MTF correction
- two-dimensional DCT transform/PCM with
  REARCS, MTF correction, multiple-element
  recording
- hybrid (1 dimensional DCT/DPCM) with
  REARCS, MTF-correction, multiple-element
  recording

275

- All digital implementation of hybrid
  DCT/DPCM, no REARCS, no filtering
- MAPS BWC, multiple-element recording
- Entropy-coded multitap DPCM and statistical
  coding

6.1   NONSEPARABLE TWO-DIMENSIONAL FILTERING, ONE-TAP
DPCM, MTF CORRECTION, SINGLE-ELEMENT RECORDING

The system architecture to be presented below
is relatively simple and performs only two image processing
functions: two-dimensional nonseparable filtering and band-
width compression via one-tap DPCM, an unsophisticated source
coding technique when compared to some of the others. This
simple system does serve to illustrate the level of imple-
mentation complexity of one of the simpler ASITS schemes,
and, in addition, is a convenient vehicle for explaining
the implementation of two-dimensional FIR filters using a
one-dimensional array sensing technique.

Figure 6.1-1 shows how this system would be
implemented using a tapped analog delay line of length N^2
in conjunction with N^2 tap weights where N is the length of
the one-dimensional sensing array. The one-tap DPCM source
encoding shown here is one-dimensional in nature and does
not take advantage of the vertical redundancy existing within
the image; more sophisticated techniques are two-dimensional
in nature and will be discussed in later sections. Note
that the output of the transmitter portion of the system of
Figure 6.1-1 corresponds to a single scan line of the re-
constructed image and therefore requires only a single-
element recording technique.

Figure 6.1-2 is a graphical representation of
a two-dimensional nonseparable transversal (FIR) filter
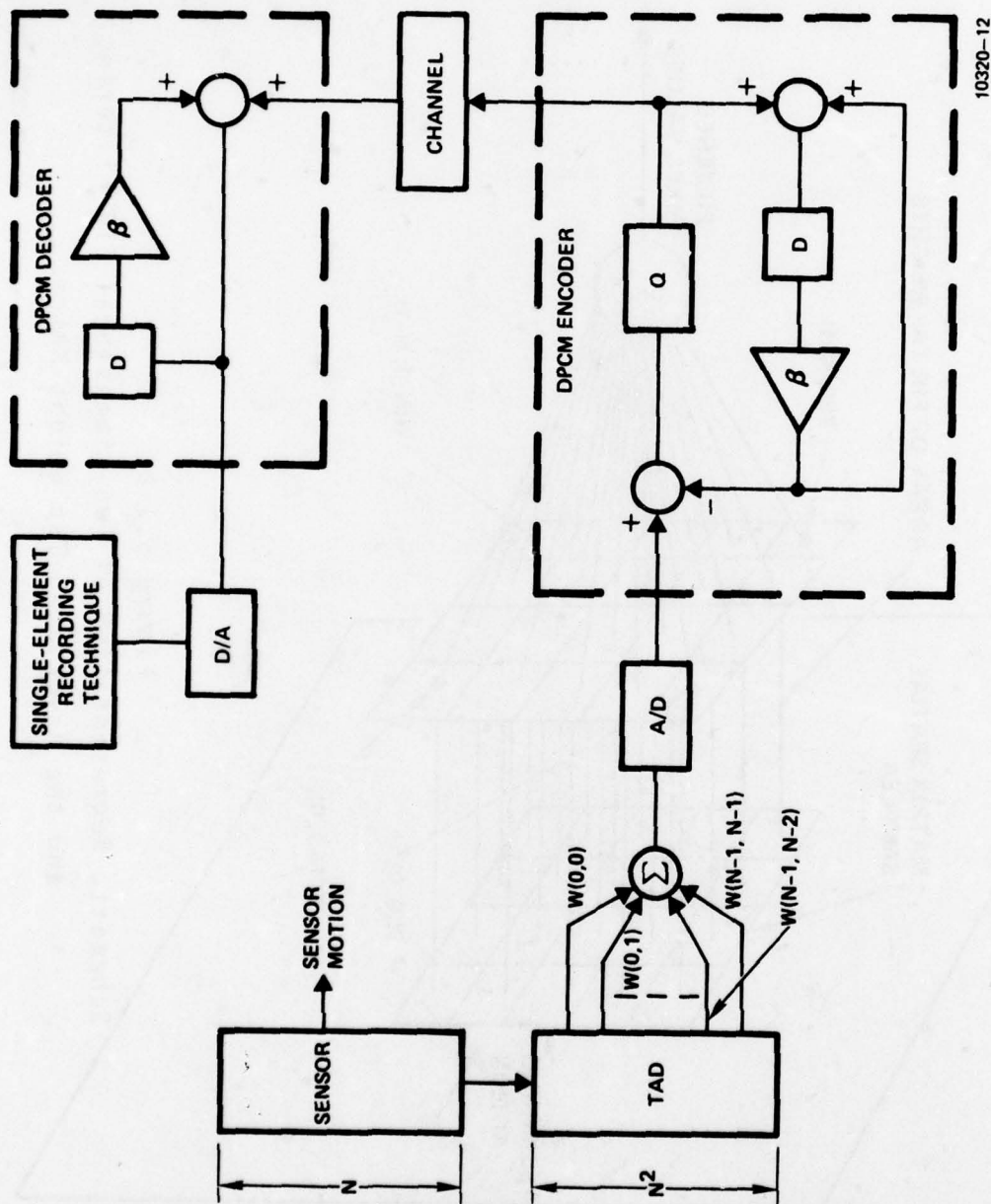
Figure 6.1-1
Nonseparable Two-Dimensional Filtering, MTF Correction,
One-Tap DPCM, Single Element Recording

277
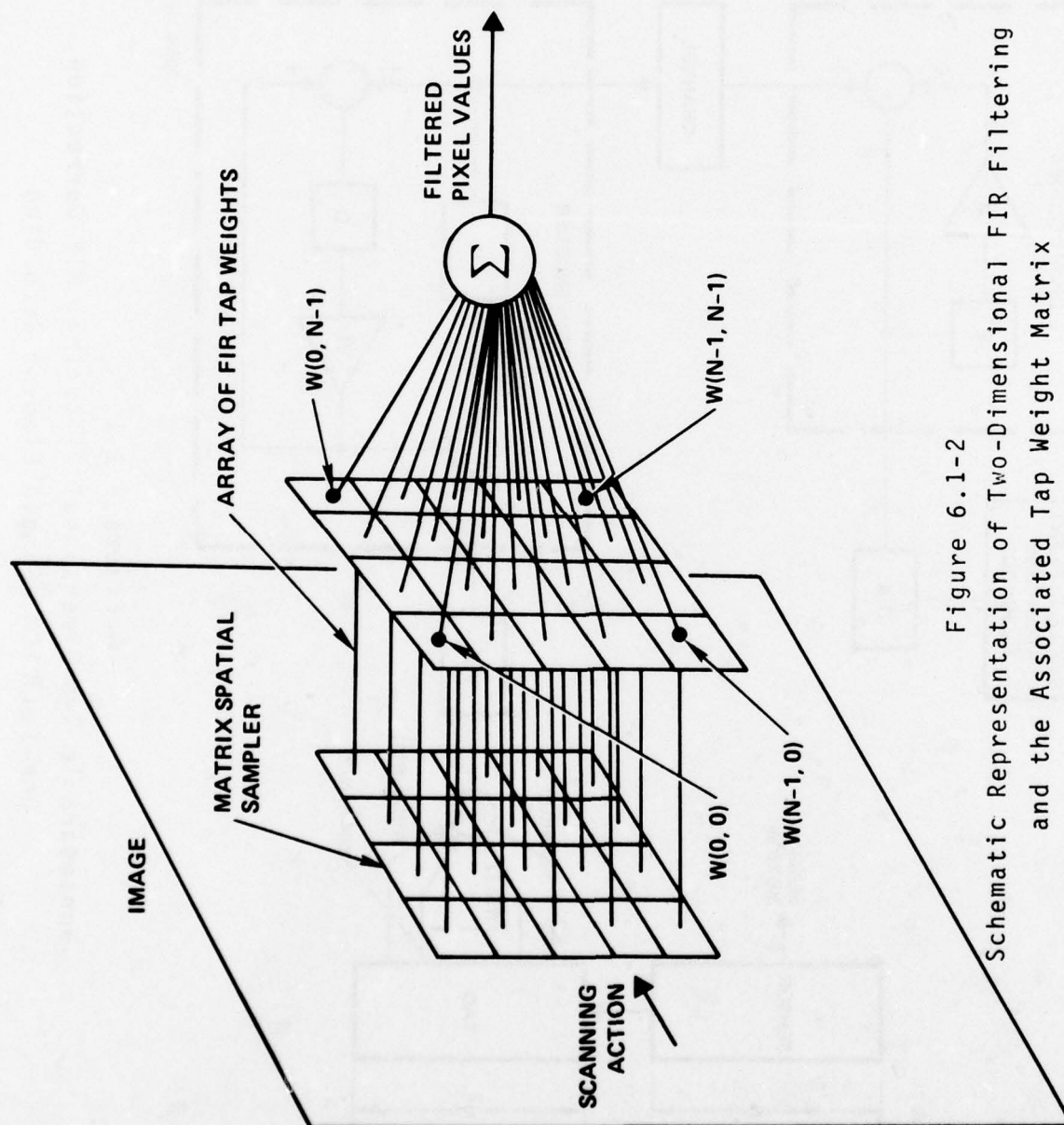
Figure 6.1-2

Schematic Representation of Two-Dimensional FIR Filtering
and the Associated Tap Weight Matrix

10320—34

that is driven by a two-dimensional sensor array of the appropriate size. In order to understand how the one-dimensional sensor array of Figure 6.1-1 is used to implement nonseparable filtering, refer to Figure 6.1-3. Figure 6.1-3 shows how a column array of sensors is used to sequentially read out the pixel values of a square matrix of pixels, one column at a time. As the N-element sensor array advances to the next column of pixels, each block of N pixels stored in the N^2-length TAD is replaced by the block of pixels that had been previously stored just above it in the TAD. While the N x N nonseparable filters discussed above have better performance than the corresponding N x N separable filters, the lower implementation complexity of separable filters makes them attractive. The next section discusses an ASITS utilizing separable filters instead of nonseparable filters.

6.2   SEPARABLE TWO-DIMENSIONAL FILTERING, ONE-TAP
        DPCM, MTF CORRECTION, SINGLE ELEMENT RECORDING

        The system architecture shown in Figure 6.2-1 performs the same functions as that of the previous section, 6.1. The lower implementation complexity has been achieved at the price of symmetry in the two-dimensional frequency response.

        The two-dimensional filtering function in Figure 6.2-1 is implemented as two sequential one-dimensional filtering operations. The class of filters that can be implemented in this fashion is restricted to those which have separable frequency transfer functions. Recall from paragraph 4.0 that separability implies that

$$H(f_h, f_v) = H_1(f_h) H_2(f_v) \tag{6-1}$$
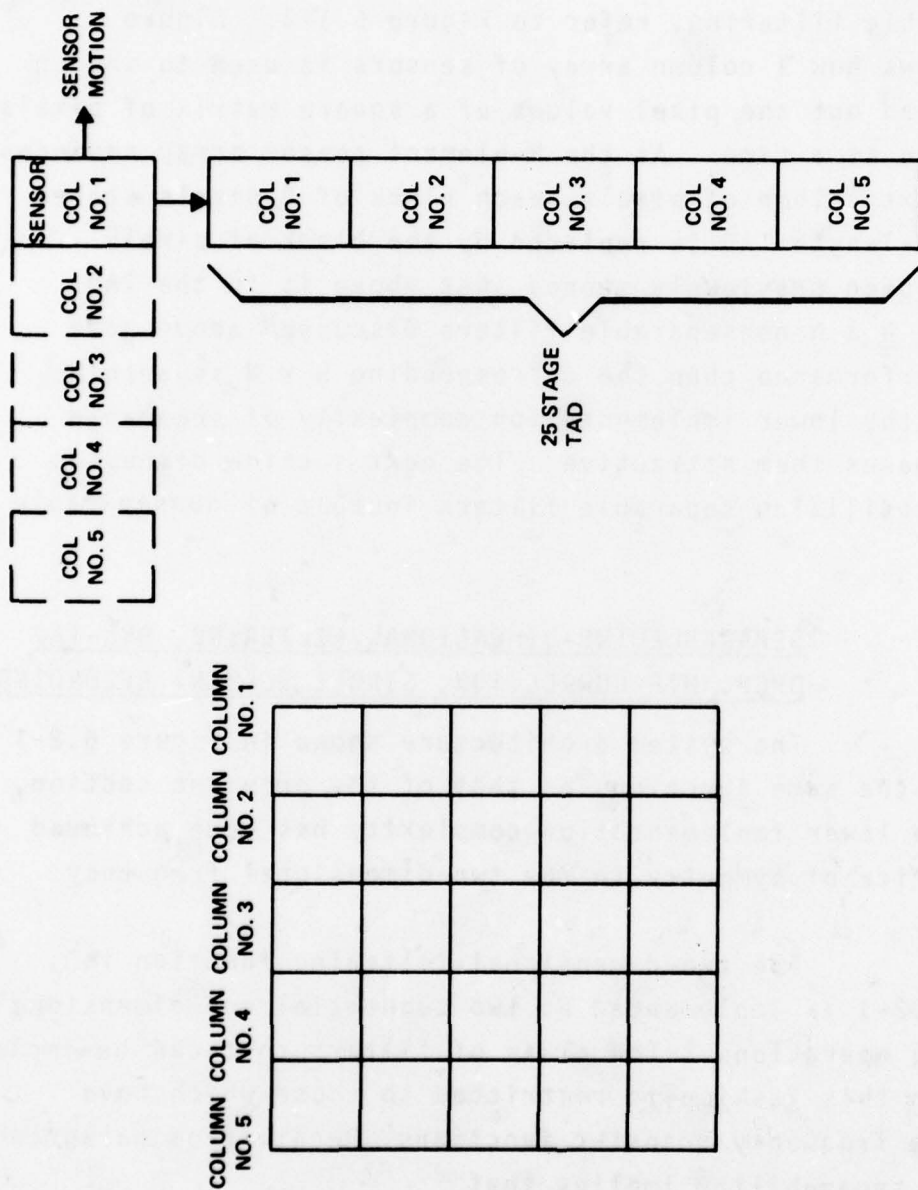
Figure 6.1-3. Implementation of Nonseparable Two-Dimensional Filters Using One-Dimensional Sensor
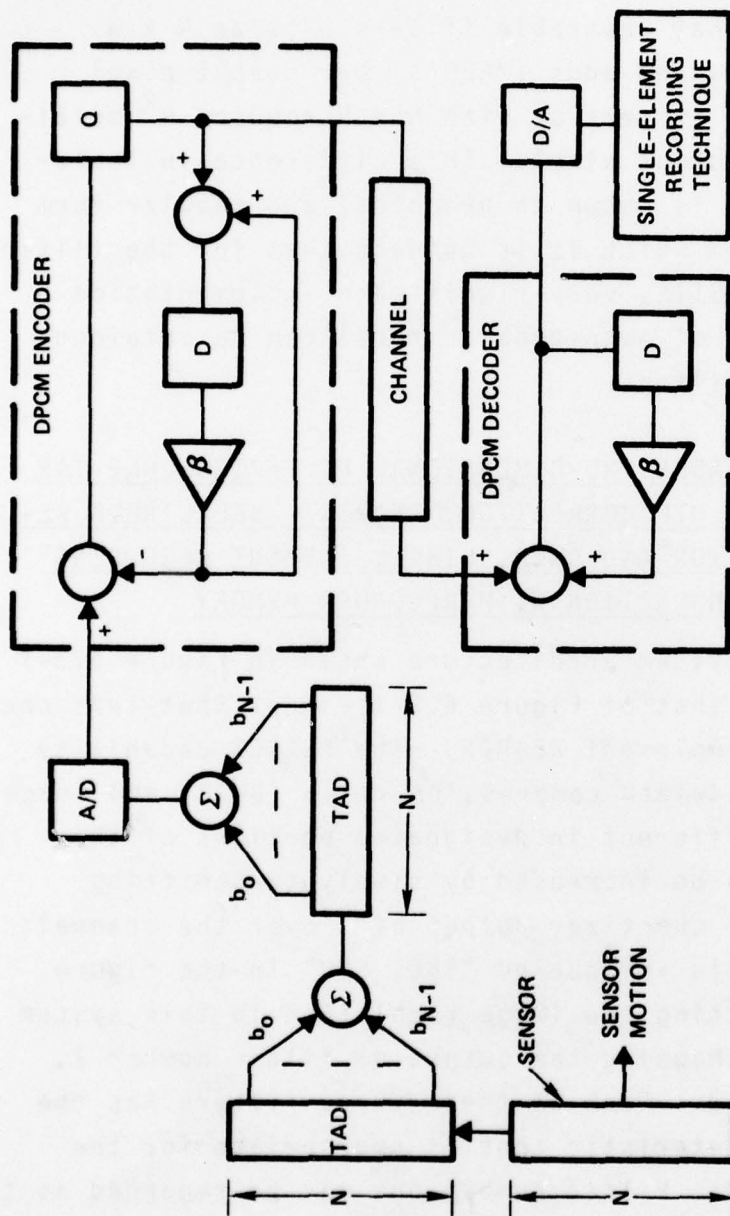
10320—14

Figure 6.2-1
Separable Two-Dimensional Filtering, MTF Correction, One-Tap DPCM,
Single Element Recording

281

where f_h and f_v refer to horizontal spatial frequency and
vertical spatial frequency, respectively. The difference in
implementation complexity between separable and nonseparable
filters increases rapidly with the filter dimension N. This
is due to the fact that separable filters of size N x N
require 2N multiplies and adds (MADD's) per output pixel
whereas nonseparable filters of size N x N require N^2 multi-
plies and adds per output pixel. This difference in imple-
mentation complexity is shown in graphical and tabular form
in Figure 6.2-2, from which it is evident that for the filter
sizes required for ASITS, very significatn implementation
advantages (an order of magnitude or more) can be obtained
by using separable filters.

6.3 SEPARABLE TWO-DIMENSIONAL FILTERING, ONE-TAP
DPCM, MTF CORRECTION, REARCS - SELECTABLE RE-
SOLUTION AND BWCR, SINGLE ELEMENT RECORDING
IN CONJUNCTION WITH RECORDER MEMORY

The system architecture shown in Figure 6.3-1
is quite similar to that of Figure 6.2-1 except that this one
has the ability to implement REARCS. The REARCS capability
implies that the bandwidth compression ratio (BWCR) and image
resolution may be different in designated portions of the
image. The BWCR can be increased by simply transmitting
fewer of the encoder quantizer output bits over the channel;
the command to do this is labeled "BWCR CMD" in the figure.

Selecting the image resolution in this system
is accomplished by choosing the output of filter number 1,
number 2, or number 3. Each of these three filters has the
MTF correction characteristic that is appropriate for the
selected resolutions. Filter number one may be regarded as the
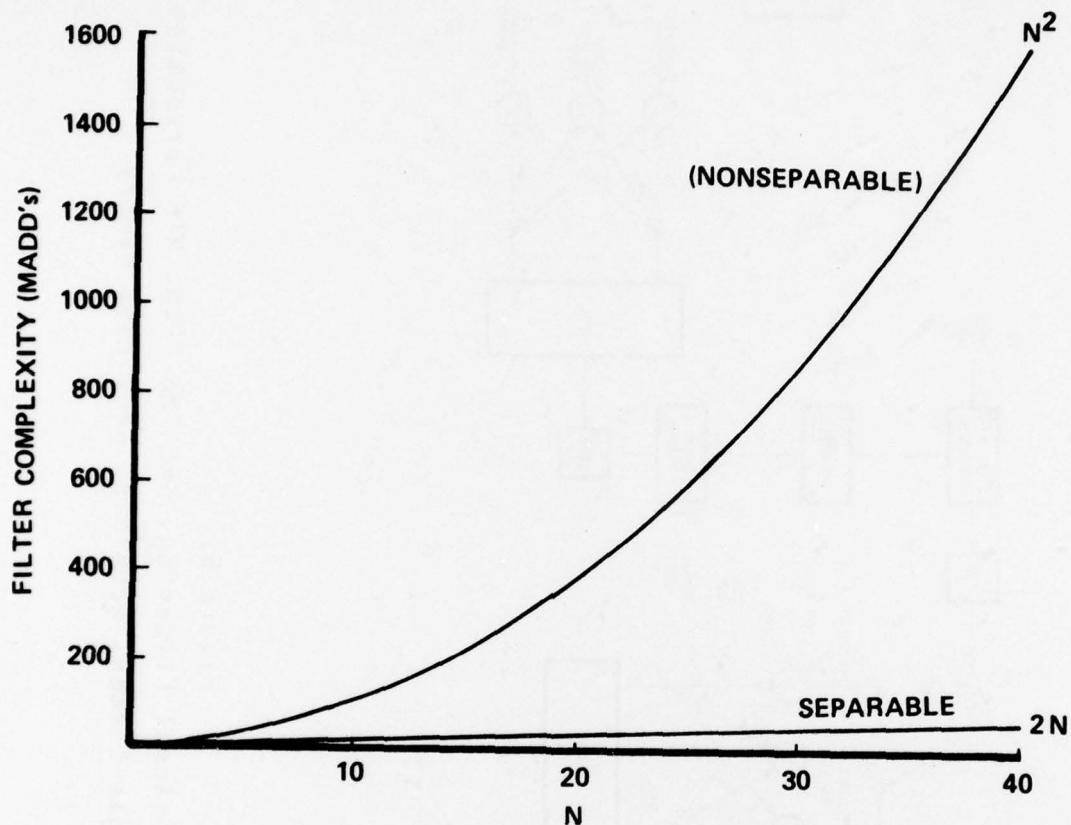
N	2N (SEPARABLE FILTER)	N² (NONSEPARABLE FILTER)
5	10	25
9	18	81
15	30	225
21	42	441
31	62	961
63	126	3,969

10320—10

Figure 6.2-2
Filter Complexity of Separable Versus
Nonseparable Filters
283
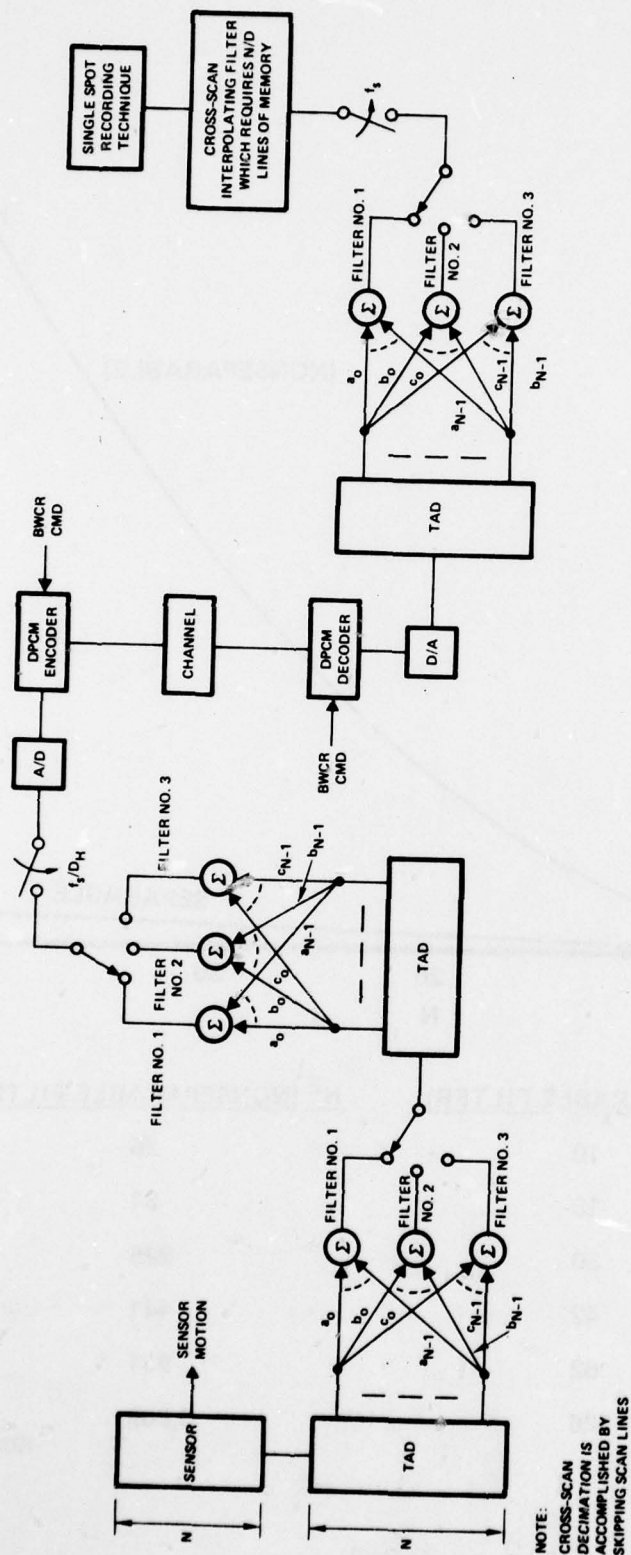
Figure 6.3-1

Separable Two-Dimensional Filtering, One-Tap DPCM, MTF Correction, REARCS, Single-Element Recording Requiring Memory

full resolution MTF correction filter, whereas filters two
and three perform the MTF correction and lowpass filtering
appropriate for the half-resolution and quarter-resolution
situations, respectively.

The most efficient use is made of the channel
when the samples of the filter output are taken at the Nyquist
rate, i.e., at twice the highest frequency present in the
filter output. Designating the sampling rate at full re-
solution as f_s, it is then clear that at half resolution and
quarter resolution, the Nyquist sampling rate required is
only $f_s/2$ and $f_s/4$, respectively. Since the image is sampled
in two spatial dimensions, this corresponds to a reduction
in information rate over the channel by a factor of $2^2 = 4$
or $4^2 = 16$ for decimation factors of two and four, respec-
tively. Since the recording medium is always exposed at the
number of samples per inch corresponding to the highest
system resolution, the decimated sample sequence must be
interpolated up to this rate. Decimation and interpolation
were discussed in detail in Section 4.1.3. The decimation
ratio is designated by D in Figure 6.3-1 and the horizontal
decimation/interpolation process is explicitly shown in
the figure. The vertical decimation is accomplished by
merely skipping the appropriate number of scan lines. The
implementation of the vertical (cross-scan) interpolation
process is more involved and is shown in more detail in
Figure 6.3-2 for the case of interpolating by a factor of
two with a FIR filter of length seven. Note that several of
the tap weights (a_1, a_3, a_5) are associated with zero-valued
pixels in the figure. All of the tap weights are necessary
since when reconstructing the following line, tap weights
a_0, a_2, a_4, and a_6 will then be associated with zero-valued
pixels.

STORED PIXEL VALUES AT RECORDER WHICH
HAVE BEEN HORIZONTALLY INTERPOLATED
BUT NOT VERTICALLY INTERPOLATED

kTH ROW OF
OUTPUT IMAGE WHICH
HAS BEEN INTERPOLATED
BOTH VERTICALLY AND
HORIZONTALLY

a_0
a_1
a_2
a_3
a_4
a_5
a_6
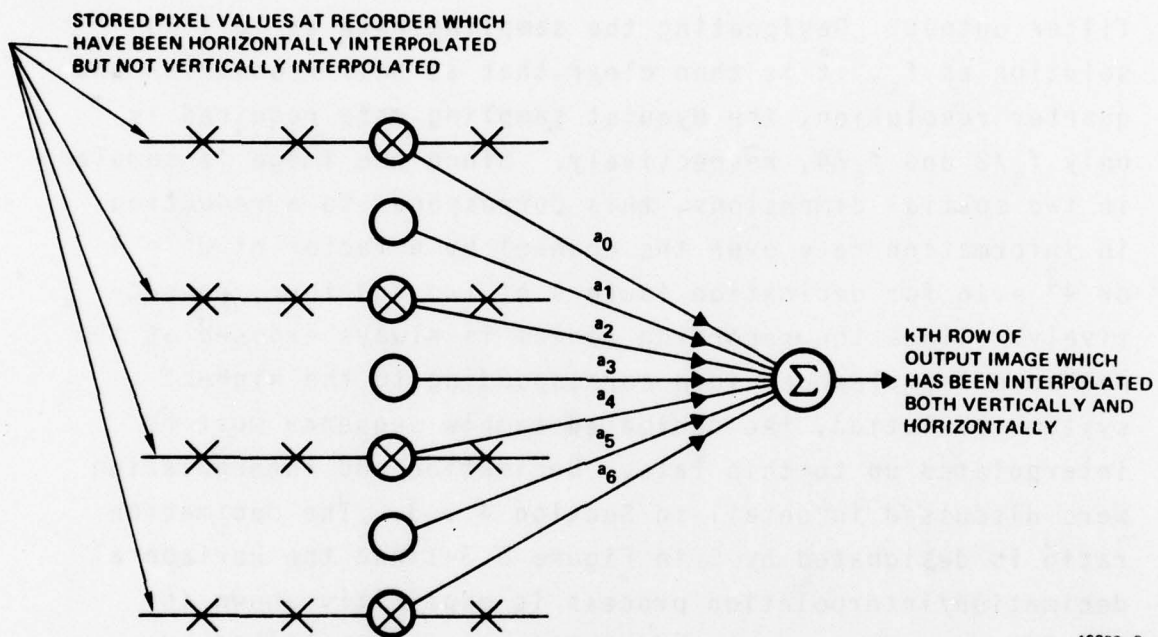
10320-8

Figure 6.3-2
Detailed Description of
Vertical Interpolation Process at the
Recorder for an Interpolation Factor of Two

286

Notice that for this simple example that alternate lines are reconstructed using odd and even numbers of nonzero-valued tap weights into the summing junction of the interpolating filter. Since these nonzero-valued pixels at the interpolating filter input have the same statistics, i.e., mean and variance, regardless of line location, the effect of using a different number of effective tap weights on alternate lines is to modulate the filter gain from line to line. Since this same effect is present in the interpolation process in the orthogonal dimension, the result is that the reconstructed image will appear to have a grid-like structure superimposed on it. For filters having a large value of N, the difference between $(\frac{N+1}{2})$ and $(\frac{N+1}{2} - 1)$ is small and the corresponding modulation of filter gain is negligible, i.e., the grid-like pattern is not visible. This effect is much more pronounced when interpolating by a factor of four and is evident in some of the N=9 filtered images discussed in paragraph 4.0. This effect is ameliorated by using a zero-mean pixel value representation system. See Appendix J for a detailed explanation of this effect.

The memory requirement for the cross-scan interpolating scheme of Figure 6.3-2 may be computed as follows. The number of pixels per line to be stored is (384 pixels/in)(9 in) = 3456 pixels/line and the maximum number of lines required to be stored is (N+1)/2 as may be seen from the example of Figure 6.3-2. For the filter sizes used in the simulations N=9, 15, and 31, this implies 17,280 words, 27,648 words, and 55,296 words of storage respectively, and at 4 bits/pixel this translates into a recorder memory requirement of 69.1 Kbits, 110.6 Kbits, or 2.2 Mbits for N=9, 15, or 31, respectively. These memory requirements add substantially to the implementation complexity of this approach. The candidate system to be presented in the next section retains the REARCS capability of the system of Figure 6.3-2 while eliminating the massive memory requirement.

6.4   <u>SEPARABLE TWO-DIMENSIONAL FILTERING, ONE-TAP</u>
                     <u>DPCM, MTF CORRECTION, REARCS- SELECTABLE RESOLU-</u>
                     <u>TION AND BWCR, MULTIPLE-ELEMENT RECORDING</u>

           In this section we present the logical extension
of the candidate system presented in Section 6.3. The trans-
mitting and receiving architectures of this multiple-element
recording approach are shown in Figures 6.4-1 and 6.4-2,
respectively. In both these figures only one set of tap
weights is shown with each TAD, when in fact, three sets
of tap weights are required for the three different resolutions.
The alternate sets of tap weights were left out of the figures
for clarity, but are required for actual implementation.
In the transmitter architecture of Figure 6.4-1 the vertical
portion of the separable filtering is performed for M scan
lines simultaneously rather than for only one scan line.
The number of tap weights per summing junction is designated
by K and N is the length of the linear array sensor. The
value of K in Figure 6.4-1 was chosen as K=5 for clarity;
in an operational system K must be larger, perhaps K > 15,
in order to achieve acceptable results. The horizontal
portion of the separable filtering is performed using M
separate TAD's, each of length K; the output of each of these
FIR filters is then decimated by the horizontal decimation
factor D_h prior to being stored in a P/S converter of length
M. The contents of the P/S converter are clocked out se-
quentially, explicitly decimated by the vertical decimation
factor D_v, A/D converted and encoded for transmission over
the channel by a multiplexed DPCM encoder. Note that the
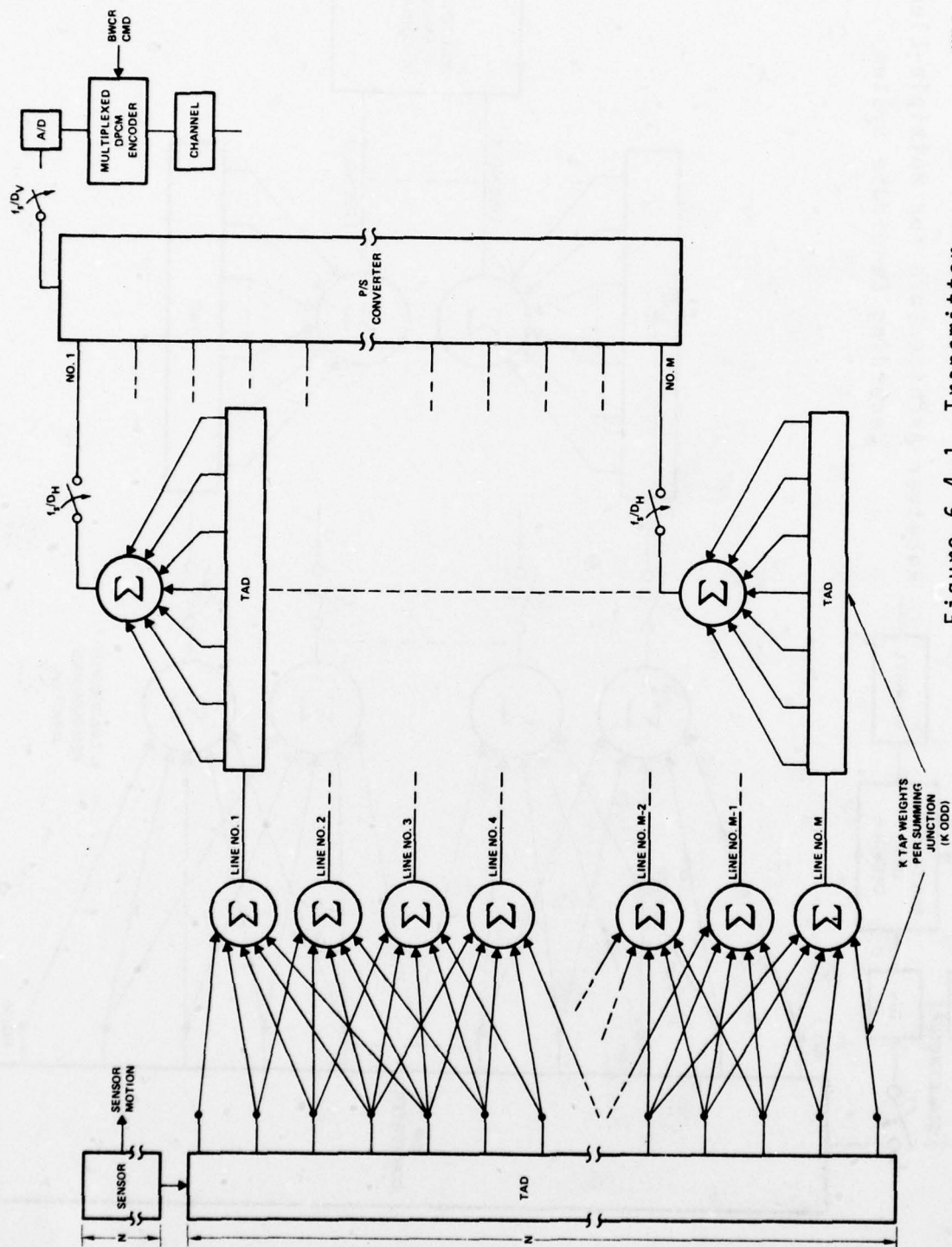
Figure 6.4-1. Transmitter
Architecture for Multiple-Element
Recording Candidate System

10320—7

Figure 6.4-2   Receiver Architecture for Multiple-Element
Recording Candidate System

10320-6

290
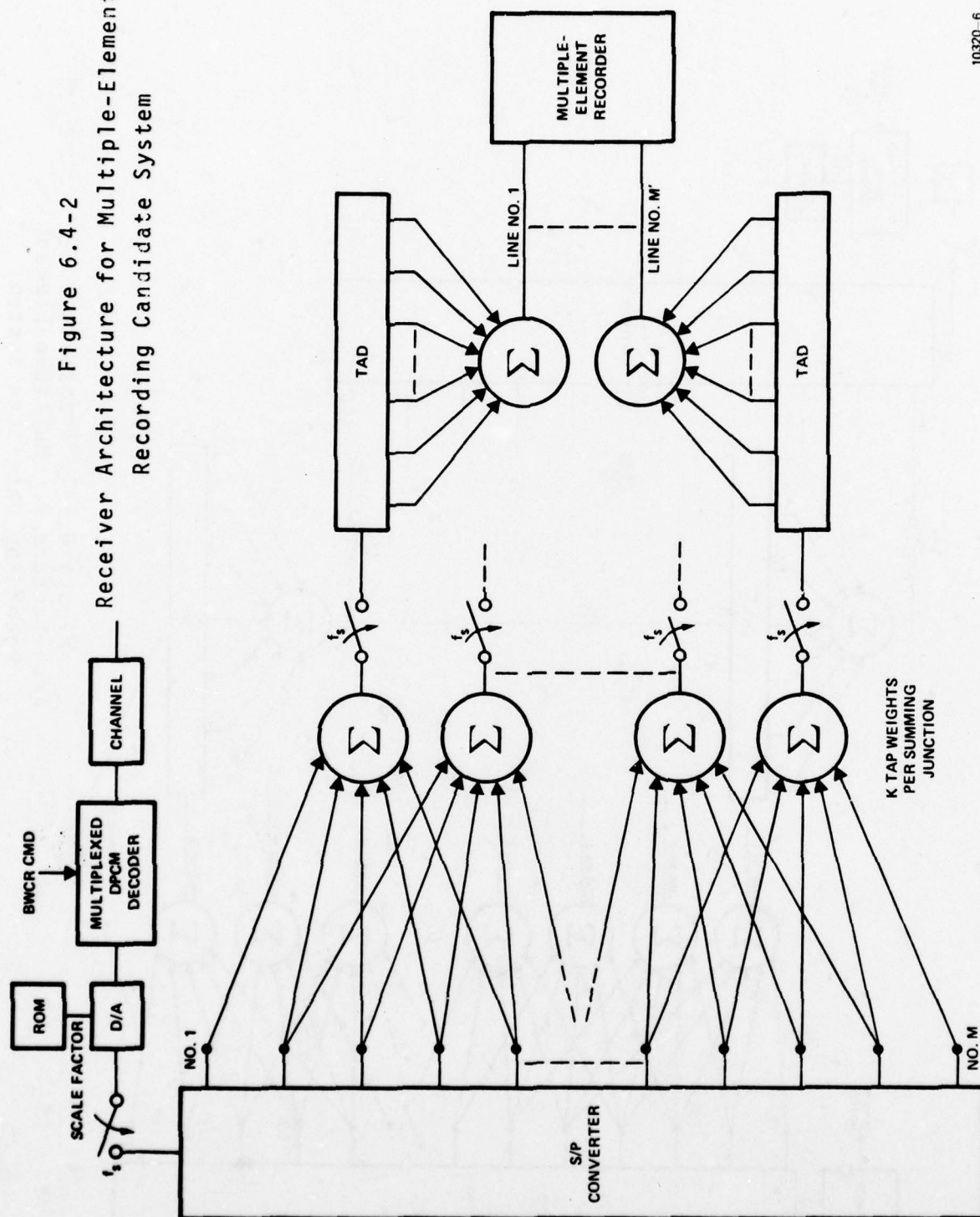
vertical and horizontal decimation factors D_h and D_v are identical for the REARCS technique; the subscripts are used here only for added clarity. Also, note that K, M, and N are related by

$$N = M + 2\left(\frac{K+1}{2} - 1\right) = M + K-1 \qquad (6-2)$$

At the receiver the sequence of operations is the reverse of those at the transmitter. This is shown in Figure 6.4-2, where the received digital data is decoded using a multiplexed DPCM decoder prior to being D/A converted. The output samples of the D/A converter are interleaved with zero-valued samples in such a way that the vertical sampling rate at the input to the S/P converter is again f_s. For $D_v = 2$ or $D_v = 4$ this implies inserting one or three zero-valued samples, respectively, between each pair of D/A output samples. This process is symbolically represented in Figure 6.4-1 by a switch at the output of the D/A closing at the vertical sampling rate f_s, even through the D/A output samples occur at the rate f_s/D_v. This symbolic notation will be used throughout the remainder of this report to represent the process of inserting zero-valued samples between nonzero-valued samples. Note that the vertical and horizontal sampling rates are identical and that both are designated by f_s throughout this report.

The contents of the S/P converter, including the zero-valued samples inserted at the output of the D/A process, are used in conjunction with the M' summing junctions to perform the vertical interpolation process. The output pixels of each of these M' vertical interpolation filters are then interspersed with the appropriate number of zero-valued samples prior to the horizontal interpolation process.

The horizontal interpolation process is performed by M'
distinct FIR filters using TAD's, and the M' filter outputs
then drive a multiple element recorder to complete the re-
construction of the image. The values of M, M', and K are
related by

$$M = M' + K - 1. \qquad (6-3)$$

Note that, unlike the candidate system of
Section 6.3, the recording structure of this candidate system
can take advantage of the fact that some pixels are zero-
valued by deleting the tap weights that are always associated
with zero-valued pixels. Recall that in the previous candi-
date system the same set of tap weights in effect, moved
vertically across pixel values, and each tap weight therefore
was not associated exclusively with either zero-valued a
nonzero-valued pixels. For the present candidate system,
this is not the case and approximately one-half or one
quarter of the tap weights can be deleted from the vertical
interpolating filters according to whether the interpolating
factor is two or four.

The DPCM encoder and decoder must operate in a
multiplexed fashion since they must process pixel values
corresponding to M rows over a channel that is serial in
nature. A block diagram of the multiplexed DPCM encoder and
decoder is shown in Figure 6.4-3. In this figure the blocks
labeled D_1, D_2, ... represent the one-sample delays required
in one-tap DPCM. For this multiplexed one-tap DPCM system
each delay element would be realized as one word of a digital
memory.

292

a. ENCODER

b. DECODER

10320–5
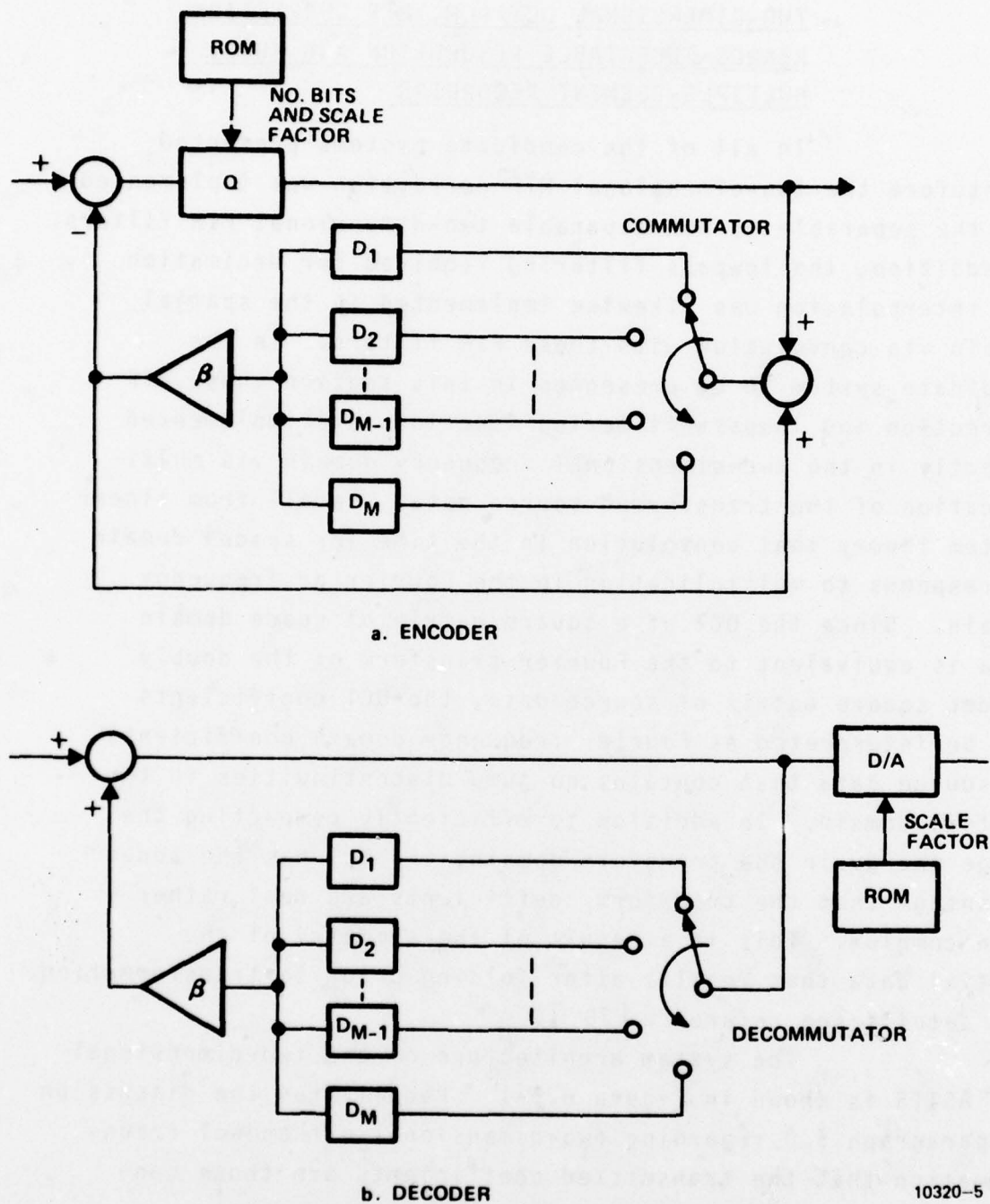
Figure 6.4-3

Multiplexed DPCM Encoder/Decoder

6.5   TWO-DIMENSIONAL DCT/PCM, MTF CORRECTION,
       REARCS-SELECTABLE RESOLUTION AND BWCR,
       MULTIPLE-ELEMENT RECORDING

In all of the candidate systems presented
heretofore the two-dimensional MTF correction was implemented
via the separable or non-separable two-dimensional FIR filters.
In addition, the lowpass filtering required for decimation
and interpolation was likewise implemented in the spatial
domain via convolution with these FIR filters. In the
candidate system to be presented in this section these MTF
correction and lowpass filtering functions are implemented
directly in the two-dimensional frequency domain via multi-
plication of the transformed source data. Recall from linear
system theory that convolution in the time (or space) domain
corresponds to multiplication in the Fourier or frequency
domain. Since the DCT of a square matrix of space domain
data is equivalent to the Fourier transform of the doubly
folded square matrix of source data, the DCT coefficients
may be interpreted as Fourier frequency domain coefficients
of source data that contains no jump discontinuities in the
spatial domain. In addition to efficiently compacting the
image energy in the transform domain, the DCT has the added
advantage that the transform coefficients are real rather
than complex. This is a result of the symmetry of the
spatial data that results after folding prior to transformation.
For details see reference [30].

The system architecture of the two-dimensional
DCT ASITS is shown in Figure 6.5-1. Recall from the discussion
of paragraph 5.0 regarding two-dimensional orthogonal trans-
formation that the transmitted coefficients are those con-
tained within certain zones defined by their manhattan
distance from the origin. These coefficients differ in
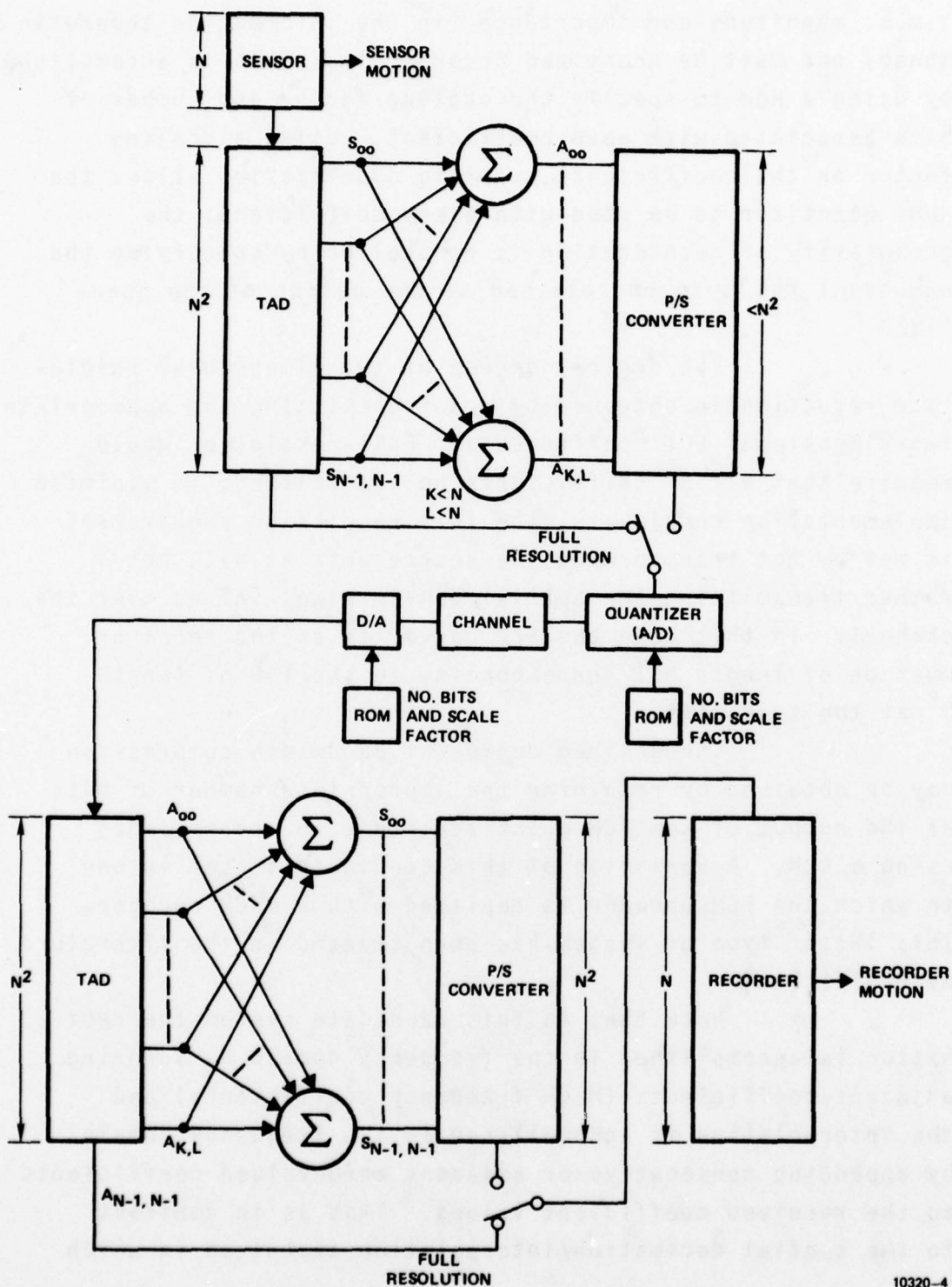
294

Figure 6.5-1. Two-Dimensional DCT/PCM With Multielement Recorder

295

r.m.s. magnitude and importance (in the information theoretic sense) and must be quantized accordingly. This is accomplished by using a ROM to specify the scaling factor and number of bits associated with each coefficient. Using a scaling factor on the coefficients prior to quantization allows the same quantizer to be used with every coefficient; the granularity of quantization is controlled by specifying the number of MSB's to be retained at the output of the quantizer.

The desired degree of two-dimensional resolution reduction is obtained by not transmitting the appropriate two-dimensional DCT coefficients. Full resolution would require that all N^2 coefficients be transmitted; to minimize implementation complexity, the full resolution requirement is met by not transforming the source data at all, but rather transmitting the spatial domain pixel values over the channel. In this case the S/P converter at the receiver must be of length N^2, corresponding to the TAD of length N^2 at the transmitter.

The desired degree of bandwidth compression may be obtained by retaining the appropriate number of bits at the output of the PCM quantizer; this is accomplished using a ROM. A variation of this candidate system is one in which the PCM encoder is replaced with a DPCM encoder. This latter type of system has been treated in the literature by Habibi [16].

Note that in this candidate system the decimation is accomplished in the frequency domain by ignoring adjacent coefficients (high frequency coefficients) and the interpolation is accomplished in the frequency domain by appending consecutive or adjacent zero-valued coefficients to the received coefficient values. This is in contrast to the spatial decimation/interpolation technique in which

the zero-valued pixels were _alternated_ with nonzero-valued
pixels.

Before presenting an alternative realization
of the two-dimensional DCT/PCM technique, refer once more
to Figure 6.5-1. If the TAD device shown there is assumed
to be the Reticon TAD-32, the size of the transform is limited
to 5 x 5. By cascading two such Reticon TAD-32 devices
for an overall length of 64, one can implement the commonly
used 8 x 8 DCT in order to obtain better BWC performance
and higher flexibility regarding BWCR and image resolution.
Whether one or two TAD-32's is used, it is necessary to include
buffer amplifiers (not shown) at each stage of the TAD in
order to properly drive the input resistors of the operational
amplifiers that perform the weighting and summing operations
indicated in Figure 6.5-1. An alternative to using one
(or two) TAD-32's and associated buffer amplifiers at each
tap to drive the various weighting-and-summing operational
amplifiers is to utilize a number of mask-programmable BBD's
such as the Reticon R5602, as shown in Figure 6.5-2. Each
of the R5602's is mask programmed with a different two-
dimensional DCT basis function, with each adjacent column
of the basis function occupying consecutive blocks of the
N^2-length mask. Choosing N=8 gives good BWC performance
and also utilizes all 64 stages of the R5602 BBD. Since
the DCT is its own inverse within a scale factor, the same
DCT architecture shown in Figure 6.5-2 for the transmitter
could also be utilized at the receiver.

297
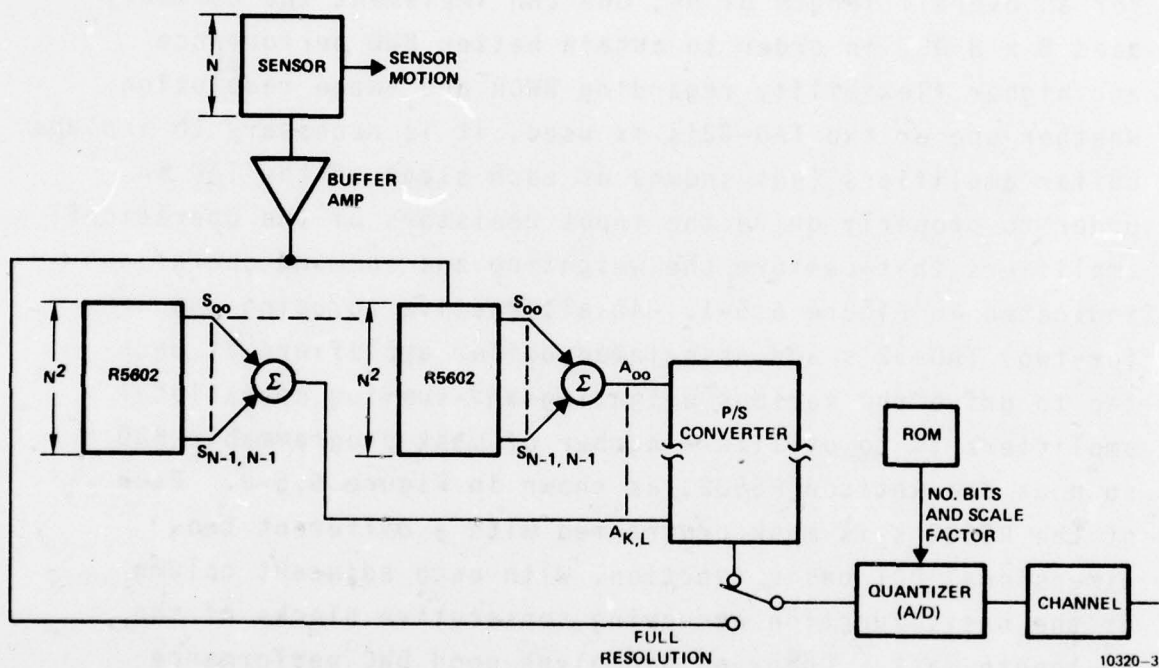
Figure 6.5-2
Alternate Architecture for Realization of
Two-Dimensional DCT Using R5602's for $N \leq 8$

298

6.6   <u>HYBRID DCT/DPCM, MTF CORRECTION, REARCS-</u>
            <u>SELECTABLE RESOLUTION AND BWCR, MULTIPLE-</u>
            <u>ELEMENT RECORDING</u>

            Recall from the discussion in paragraph 5.0
of the hybrid BWC technique that it consists of performing
successive one-dimensional DCT transformations of columns
(or rows) of pixels and then transmitting the resulting
coefficients via DPCM. An ASITS architecture using Reticon
TAD-32 devices for implementing the hybrid technique is
shown in Figure 6.6-1. This implementation uses a TAD to
store the analog samples from the sensor. These stored
pixel values are then scaled and summed using resistors and
operational amplifiers to obtain the various transform
coefficients. The implementation shown could be used to
implement any real transform such as the Haar, Hadamard or
discrete cosine transform (DCT); of these, the DCT yields
the best BWC performance. For full resolution all N trans-
form coefficients shown in Figure 6.6-1 (K=N-1) must be
computed and transmitted. A more efficient implementation
for the full resolution case would be to simply transmit the
pixel values stored in the TAD without transforming them
at all, although this is not shown in Figure 6.6-1.

            An alternate realization of the hybrid encoder
is shown in Figure 6.6-2. Rather than using one TAD-32
to store and buffer the pixel values from the sensor and one
to perform each of the lowpass filtering operations, this
approach uses K(K<N-1) mask-programmable Reticon R5602 devices
as correlators to obtain the K DCT coefficients and uses K
additional R5602 devices to perform the convolutions associated
with the along-scan lowpass filters required for decimation.
This alternate realization using R5602 devices has lower

299
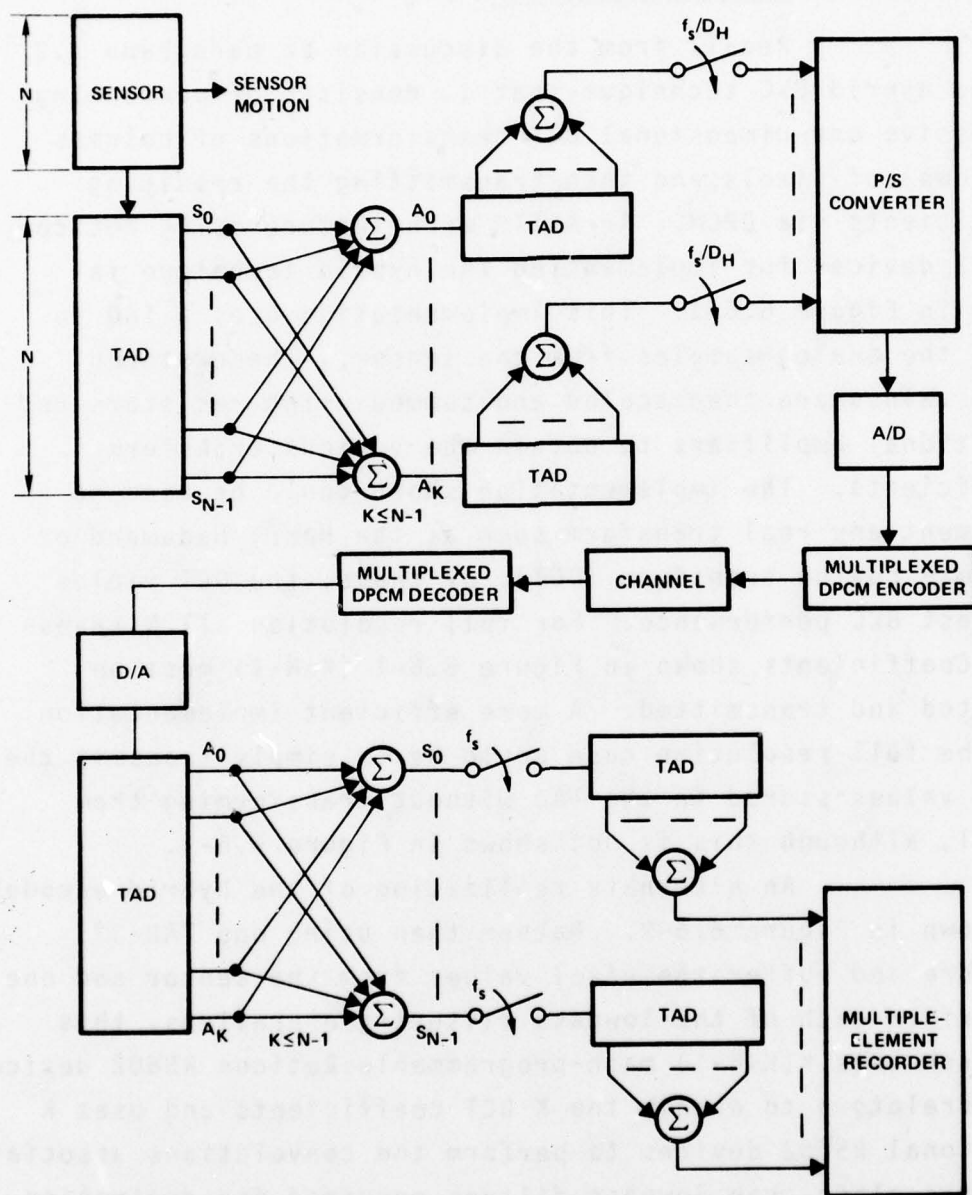
Figure 6.6-1

ASITS Architecture for Hybrid BWC Technique
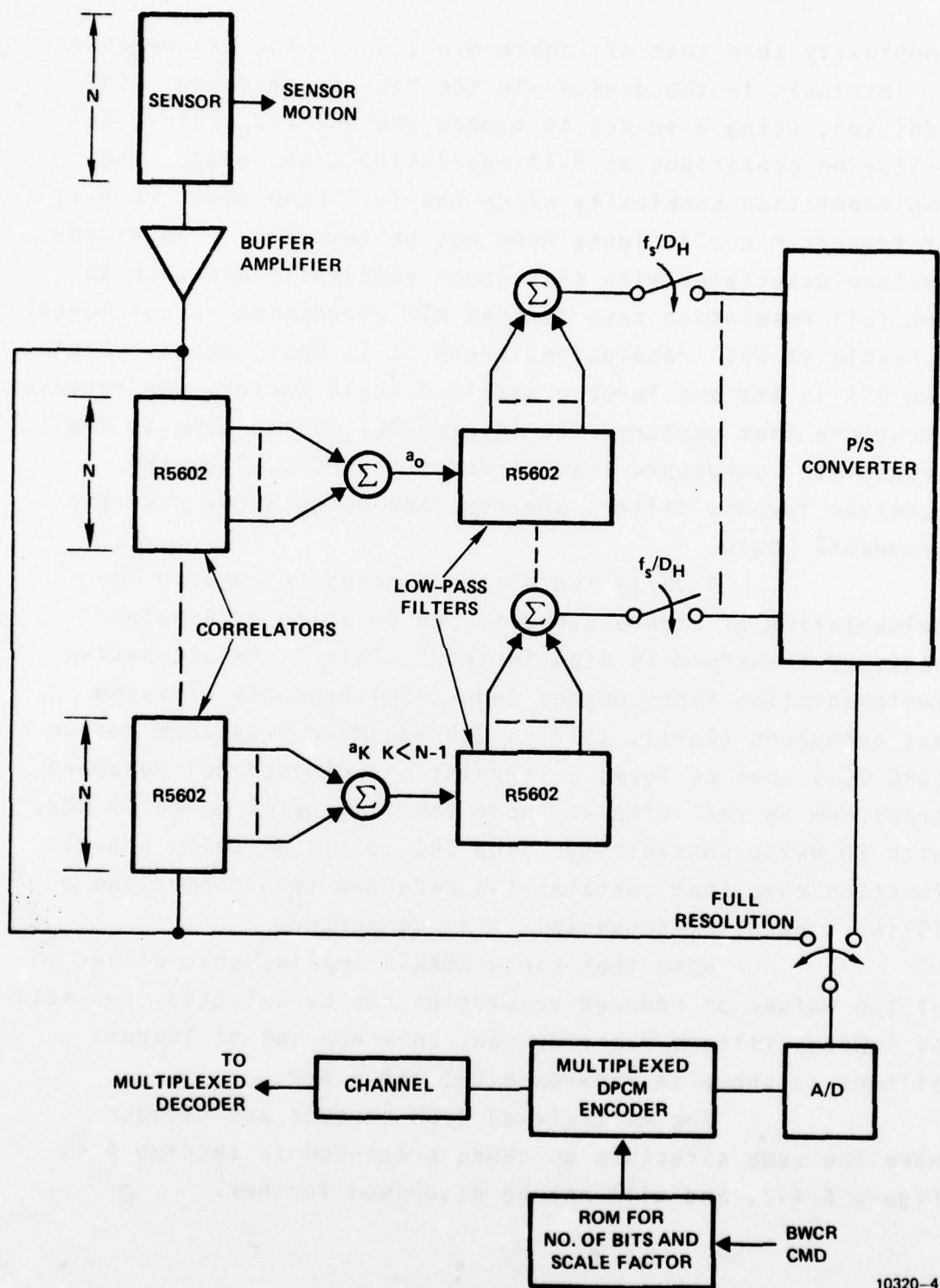
Figure 6.6-2 Alternate Realization of Hybrid Encoder

301

complexity than that of Figure 6.6-1 since the tap weighting
is intrinsic to the device via the mask programming. In
addition, using a switch to bypass the DCT and transversal
filtering operations at full resolution also reduces the
implementation complexity since the full complement (K=N-1)
of transform coefficients need not be computed. The disad-
vantage associated with this lower complexity approach to
the full resolution case is that MTF correction is not longer
possible at full resolution, where it is most needed. Since
the DCT is its own inverse within a scale factor, the receiver
structure that performs the inverse DCT is the same as the
transmitter structure that performs the DCT; also, the
receiver lowpass filters are realized using R5602 mask pro-
grammable CCD's.

A variation of the N-point DCT hybrid im-
pelmentation of Figure 6.6-2 is one in which a 16-point
Hadamard transform is used instead. This is an attractive
implementation since Hughes Industrial Products Division
has announced (April, 1977) a CCD Hadamard Transform device
(CRC 101) that performs a 16-point one-dimensional Hadamard
transform in real time at input sampling rates up to 10 MHz,
with 20 MHz a possibility. The CRC 101 is actually a dual
function chip that contains the Hadamard transformer and a
16-input parallel-to-serial (P/S) converter.

Note that since REARCS implies that either
of two values of reduced resolution can be selected, two sets
of lowpass filters are required; only one set of lowpass
filters is shown in Figures 6.6-1 and 6.6-2.

The multiplexed DPCM encoder and decoder
have the same structure as those presented in Section 6.4,
Figure 6.4-3, and will not be discussed further.

As was pointed out in Section 6.5 for two-dimensional transform techniques, the resolution can be selected or controlled in the frequency domain as well as in the spatial domain. In the hybrid BWC approach shown in Figures 6.6-1 and 6.6-2 the spatial resolution in the vertical spatial dimension is controlled by the number of transform coefficients a_i that are transmitted over the channel; discarding more of the high order coefficients in the frequency domain decreases the spatial resolution within the image after inverse transformation. Unlike the two-dimensional transform technique, however, the horizontal spatial resolution is controlled by FIR transversal filters whose inputs are the along-scan spatial sequence of transform coefficients and whose outputs are decimated by the appropriate decimation factor. It is clear that in this hybrid ASITS the vertical spatial resolution is controlled in the frequency domain by eliminating transform coefficients while the horizontal spatial resolution is controlled in the spatial domain via lowpass filtering using transversal filters. This approach is appropriate in view of the mixed-domain nature of the two-dimensional number sequence that is transmitted over the channel.

6.7   ALL-DIGITAL IMPLEMENTATION OF HYBRID
          DCT/DPCM BWC TECHNIQUE

In all of the candidate systems presented heretofore the implementations have been largely sampled-data analog in nature, with very little digital processing. This partitioning of the processing between analog and digital implementations is generally advantageous in that the highly computation-intensive two-dimensional filtering tasks at the transmitter and receiver can be accomplished using sophisticated, commercially available CCD's that can be either externally programmed (TAD-32) or mask-programmed

303

(R5602). In order to help evaluate the relative merits of
these predominantly analog (sampled-data) ASITS imple-
mentations that have been presented we present several al-
ternative all-digital implementations of the basic hybrid
DCT/DPCM BWC technique without the REARCS capability for
specifying two-dimensional resolution. Recall from
the earlier discussion of Section 6.6 that for the hybrid
technique the vertical resolution is determined by the
number of DCT coefficients that are retained for transmission
over the channel, while the horizontal resolution is reduced
by lowpass filtering each of the retained DCT coefficient
sequences. Thus, the all-digital hybrid algorithm imple-
mentation of this section has implicit control capability
for vertical resolution but no control capability for
horizontal resolution.

Several different digital implementations of
a hybrid DCT/DPCM bandwidth compression system are discussed
in this section. The options presented are intended to
provide a broad overview of the range of digital implemen-
tations which are possible.

Figure 6.7-1 shows the functional processing
steps involved in the hybrid DCT/DPCM bandwidth compression
approach. The DCT itself is defined to be

$$A_k = \sum_{N=0}^{N-1} f(n) \cos \frac{(2n+1)K\pi}{2n} , \qquad (6-4)$$

for

$$k = 0, 1, 2, \ldots, N-1, \qquad (6-5)$$

304
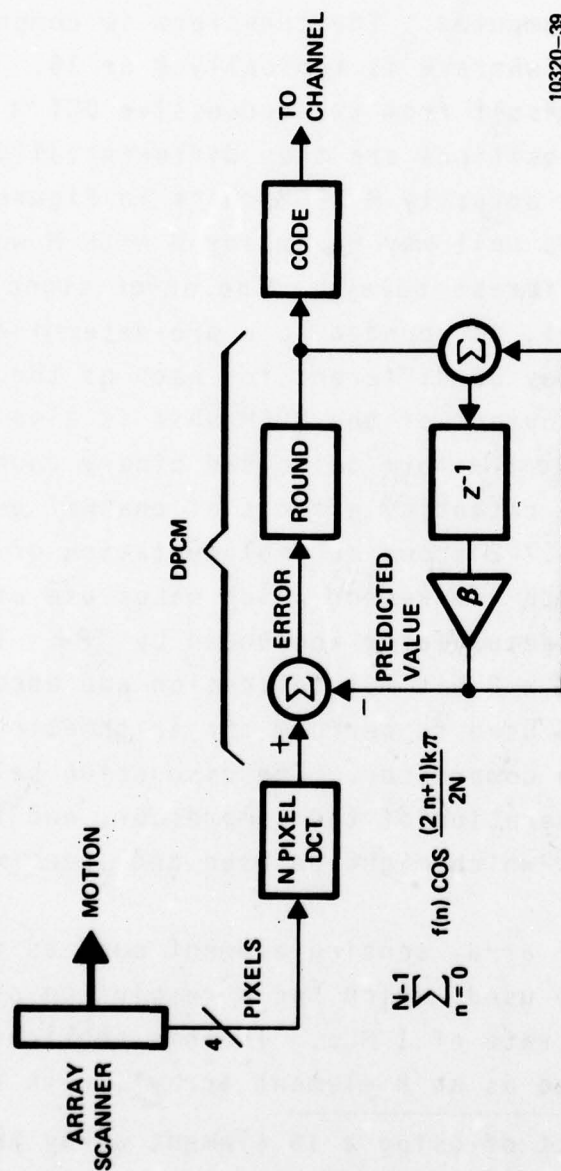
Figure 6.7-1

Functional Block Diagram of the Hybrid BWC Approach

where f(n) is the pixel value, and N is the number of points
in the transform. The transform is defined for N values of
k, but typically only the lower indexed coefficients need
be computed. In the following it is assumed that M<N coef-
ficients are actually computed. The transform is computed
on a block of N pixels, where N is typically 8 or 16. The
2M coefficients which result from two successive DCT's computed
at successive scanner positions are then differentially en-
coded. Hence there are actually M DPCM units in Figure 6.7-1,
although one time-shared unit may be employed with M words
of memory for the M different delays. The error signal,
which is already digital, is rounded to a pre-determined
number of bits, which may be different for each of the M
DCT coefficients. The output of the DPCM unit is also typically
re-coded from 2's complement form to folded binary codeword
form [30] to reduce the potential effects of channel errors.

Figure 6.7-2 shows an implementation of the
hybrid DCT/DPCM bandwidth compressor which makes use of the
single chip multiplier/accumulator announced by TRW. The
TDC 1008J can perform 8 x 8 bit multiplication and accumula-
tion in 70 nsec, and is used to perform the arithmetic re-
quired in the bandwidth compressor. The discussion below
explains the overall operation of the compressor, and identi-
fies typical components which might be used and speed/memory
requirements.

A linear array sensing element such as the
Reticon RL-64P could be used, which has a resolution of 500
lpi and a maximum data rate of 1 MHz. In this application
the RL-64P would be used as an 8 element array*, with a pixel

---

* In general, the effect of using a 16 element array and trans-
form is to double the memory requirements given subsequently.
The speed of the devices used in most of the approaches dis-
cussed below is quite adequate to handle the higher through-
put required by the 16 point DCT.
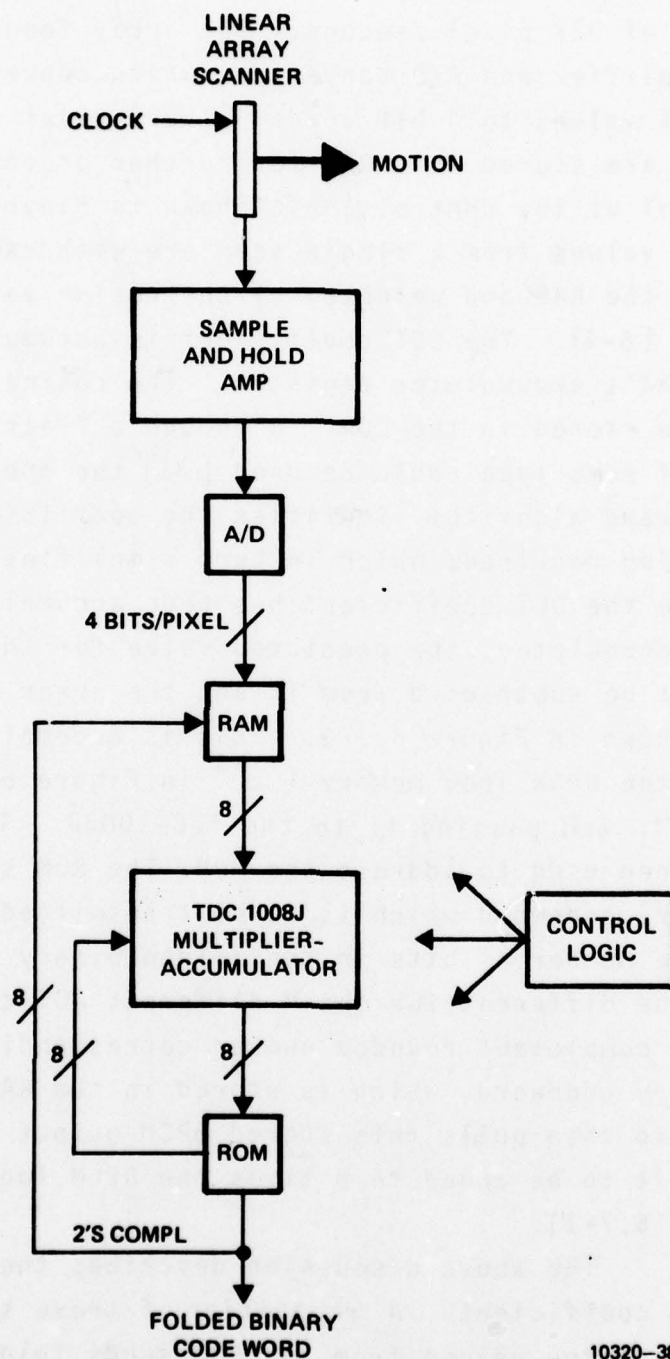
Figure 6.7-2

Hardware Implementation Using TDC 100BJ

Multiplier/Accumulator

output rate of 32K pixels/second. The array feeds a sample-
and-hold amplifier and A/D converter, which converts the
analog pixel values to 4 bit words. The 8 pixel values
from a scan are stored in a RAM for further processing.
Under control of the control logic shown in Figure 6.7-2,
the 8 pixel values from a single scan are withdrawn sequen-
tially from the RAM and weighted by the cosine values as
in equation (6-4). The DCT coefficient is accumulated in
the TDC-1008J's accumulator register. The cosine values
required are stored in the ROM. Although a "fast" DCT
algorithm of some type could be used [31] the speed of the
straightforward algorithm simplifies the coefficient and
pixel indexing required, which in turn simplifies the control
logic. Once the DCT coefficient has been accumulated in the
TDC 1008J accumulator, the predicted value for the coef-
ficient must be subtracted from it and the error rounded and
coded, as shown in Figure 6.7-1. This is accomplished by
retrieving the DPCM loop memory (z^{-1} in Figure 6.7-1)
from the RAM, and passing it to the TDC-1008J. The accumulator
output is then used to address the ROM. The ROM supplies the
folded binary codeword which is to be transmitted over the
channel, the number of bits in the folded binary codeword
(which may be different for the M different DCT coefficients),
and the 2's complement rounded number corresponding to the
folded binary codeword, which is stored in the RAM. The
control logic then pulls this stored DPCM output from RAM
and causes it to be added to β times the DPCM loop memory
(see Figure 6.7-1).

The above discussion describes the processing
for one DCT coefficient. A repetition of these steps with
appropriate cosine values from the ROM sends folded binary
codewords over the channel for the remaining (M-1) DCT coef-
ficients.

The TDC-1008J must compute M DCT coefficients
per 8 new pixels accepted from the scanner. At 32K pixels/
second, this is a rate of M DCT coefficients per 250 micro-
seconds. If it were necessary to compute all 8 coefficients
(M=8), this is 31 microseconds per coefficient worst-case.
Since each coefficient requires 8 multiply-adds using a "non-
fast" algorithm, the required worst-case multiply-add time is
31/8=3.9 microseconds, which is well within the capabilities
of the TDC-1008J (70 nsec).

The RAM must be able to hold the 8 pixel
values which are currently being processed, plus the 8 new
pixel values which are being placed in memory while the
current pixels are processed. It must also hold the M DPCM
loop memories, which is at most 8 words for M=8. Allowing
for a small scratch-pad area, a RAM of 32 words x 8 bits
should suffice.

The ROM must hold the 8M cosine values (to
make the control logic as simple as possible no symmetry is
used), which for M=8 is a maximum of 64 cosine values. The
ROM must also hold the folded binary codewords, the 2's
complement rounded values, and the number of bits in the
folded binary codeword for each DCT coefficient. If we
assume that M=6, and that 16 bits are required to retain
the above information, then the number of 8 bit words of
storage required is

$$2^8 \times 6 \times 2 + 64 = 3136 \qquad (6\text{-}6)$$

The 2^8 factor results from the 8 bit accumulator output used
to address the ROM, the factor of 6 results from the 6 dif-
ferent DCT coefficients, the factor of 2 results from the
2 words (16 bits) of storage required for each access, and

309

the 64 is the number of cosine values which must be stored.
The required storage can be realized in a single chip such
as Texas Instruments' TMS 4732, which has a 4096 word x 8
bit organization.

Careful consideration of the implementation
described above reveals that the hard-wired control logic
must be fairly complex in order to properly sequence the
compressor operation, provide ROM memory addresses, etc.
An alternative approach is to use a microprocessor for control,
such as the AMD 2901. Figure 6.7-3 shows a block diagram of
a micro-processor-based bandwidth compressor. Due to the
programmability of the micro-processor, the processor
shown in Figure 6.7-3 could also be used to perform other
image processing algorithms. The architecture is general
purpose with special features added to enhance its signal
processing capability. The processor is built around a central
array of four 4-bit AM2901A processing elements. Emanating
from the central array are two unidirectional data busses,
each 16 bits wide.

Between these two busses are positioned:
- Data Memory (autoincrementing)
- High Speed Multiplier (16 x 16 in 200 ns)
- Saturation Circuitry
- Sign Extension Circuitry
- Bit Reversal Circuitry
- Bidirectional I/O Buss

The microprogram sequencer used to control
fetches from a separate instruction memory is a single chip
AMD 2901 device that provides a variety of conditional
branching, looping and subroutine calls along with an internal
loop counter. One level of pipelining is used in the 56-bit
wide instruction stream and one level of program controlled
interrupt is provided.

310
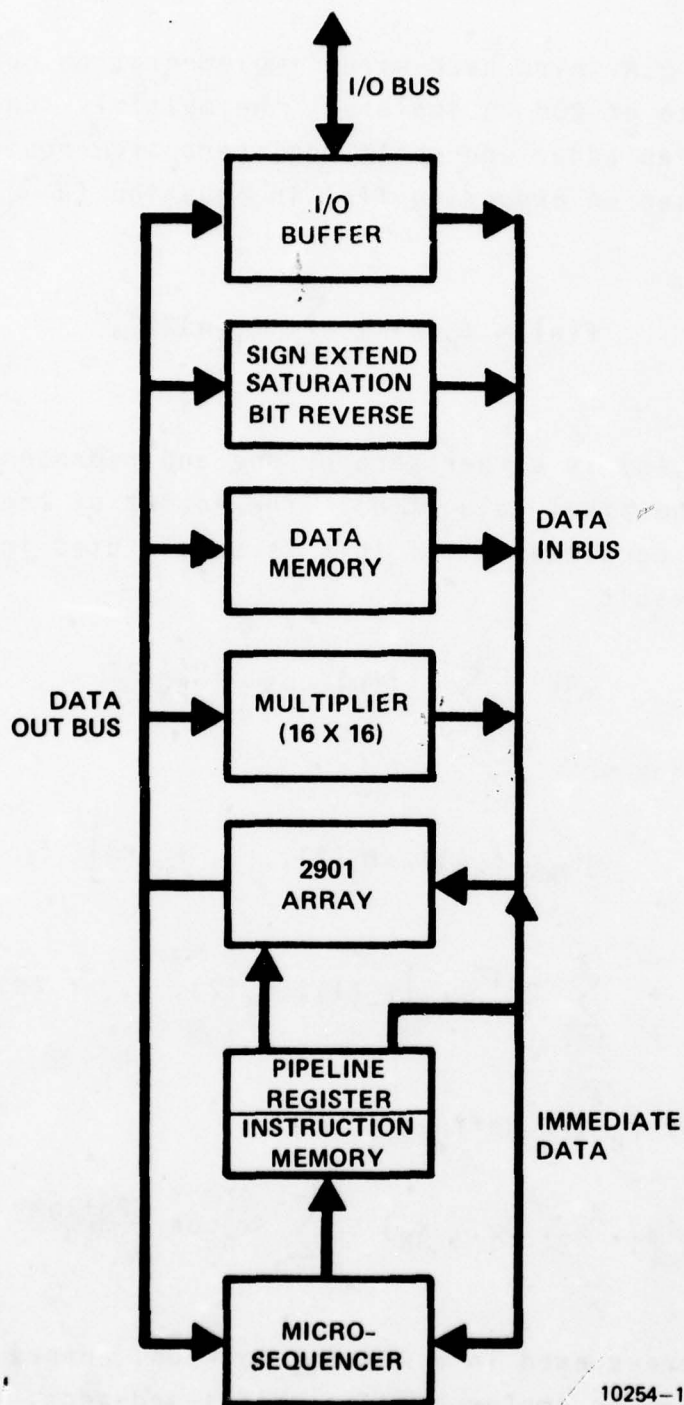
Figure 6.7-3.
Block Diagram of a Micro-Processor-Based
Bandwidth Compressor

311

A third hard-wired implementation option involves the use of ROM to implement the multiply function [32] so that only an adder and shift registers are required. The method is based on expanding $f(n)$ in equation (6-4) in the form

$$f(n) = f_o(n) + \sum_{i=1}^{3} f_i(n)2^{-i},$$ (6-7)

where each $f_i(n)$ is either zero or one and represents the ith bit in the pixel value $f(n)$. The format of the pixel value is 2's complement. If this is substituted in equation (6-4), the result

$$Ak = \sum_{n=0}^{N-1} f(n) \cos \frac{(2n+1)k\pi}{2N} =$$

$$\phi_k \left[f_o(1), f_o(2), \ldots, f_o(N) \right]$$

$$+ \sum_{i=1}^{3} 2^{-i} \phi_k \left[f_i(1), f_i(2), \ldots, f_i(N) \right]$$ (6-8)

The functions ϕ_k are defined to be

$$\phi_k(x_1, x_2, \ldots, x_N) \equiv \sum_{n=0}^{N-1} x_n \cos \frac{(2n+1)k\pi}{2N}$$ (6-9)

and can be pre-stored in a ROM for look-up. Hence all operations can be implemented as shifts-and-adds, as is

312

apparent from (6-8). One of the disadvantages of this approach is the need to have the ith bit of all N pixels available in parallel, which requires the use of tapped shift registers. The other approaches lend themselves more naturally to use word-organized memories which currently have a higher level of integration.

A fourth approach would employ ROM for table look-up of multiplications, thereby eliminating the need for a hardware multiplier such as the TDC-1008J. The ROM must be present in any event to provide the table look-up for the folded binary codewords, etc. If the pixel values and the DCT coefficient values are each 4 bits long, then 2^8=256 words of ROM memory are sufficient to provide a table of all possible multipliers and multiplicands and their resulting products. When added to the 3136 words of ROM required for the folded binary codewords, cosine values, etc., the total ROM required is 3392 words. This would fit within a single 4096 x 8 bit chip, such as Texas Instruments' TMS 4732. Note, however, that an adder, an accumulator, and various registers are required to utilize the ROM in the processing required for bandwidth compression. Hence the parts count may not be significantly less than that for some of the other approaches.

Considering the options presented above from an overall point-of-view, it would appear that the first two options are the best choices. The microprocessor-based option has the added feature of programmability, if the application requires it. The microprocessor approach may even have a lower overall parts count than the hardwired approach, depending primarily on the comparison which exists between the hard-wired control logic parts count and the software-based microprocessor parts count.

313

6.8   MAPS BWC, MULTIPLE-ELEMENT RECORDING

The Micro-Adaptive Picture Sequencing BWC
technique was invented in 1977, and the relative effectiveness
of this algorithm is the subject of current research. An
array scanning implementation of the MAPS technique is presented
here for the sake of completeness, although it does not
exhibit many of the desirable features of an ASITS such as
explicit control of resolution reduction or MTF control.

Figure 6.8 shows an array scanning implemen-
tation of the MAPS algorithm. Note that the implementation
is all-digital with the A/D and D/A interfaces located dir-
ectly at the array sensor output and array recorder input,
respectively. The only advantage, other than higher image
throughput rate, of this array scanning implementation over
a conventional single-point scanning implementation is
that the quantity of required data storage memory is much
smaller. A simple example is illustrative. Consider a
MAPS system for which the maximum data block size is con-
strained to be 8 pixels by 8 pixels. For the conventional
single-point scanning approach this would require

$$384 \text{ pixels/in} \times 9 \text{ in} \times 8 \text{ lines} \times 4 \text{ bits/pixel} = 110.6K \text{ bits} \tag{6-10}$$

of storage both at the transmitter and at the receiver. For
an array scanning approach, on the other hand, the required
amount of data memory is only

$$8 \times 8 \times 4 = 256 \text{ bits} \tag{6-11}$$

which is smaller by a factor of 432. Aside from the difference
in required data storage the remainder of the digital im-
plementation is the same regardless of whether single-point

314

10320-36
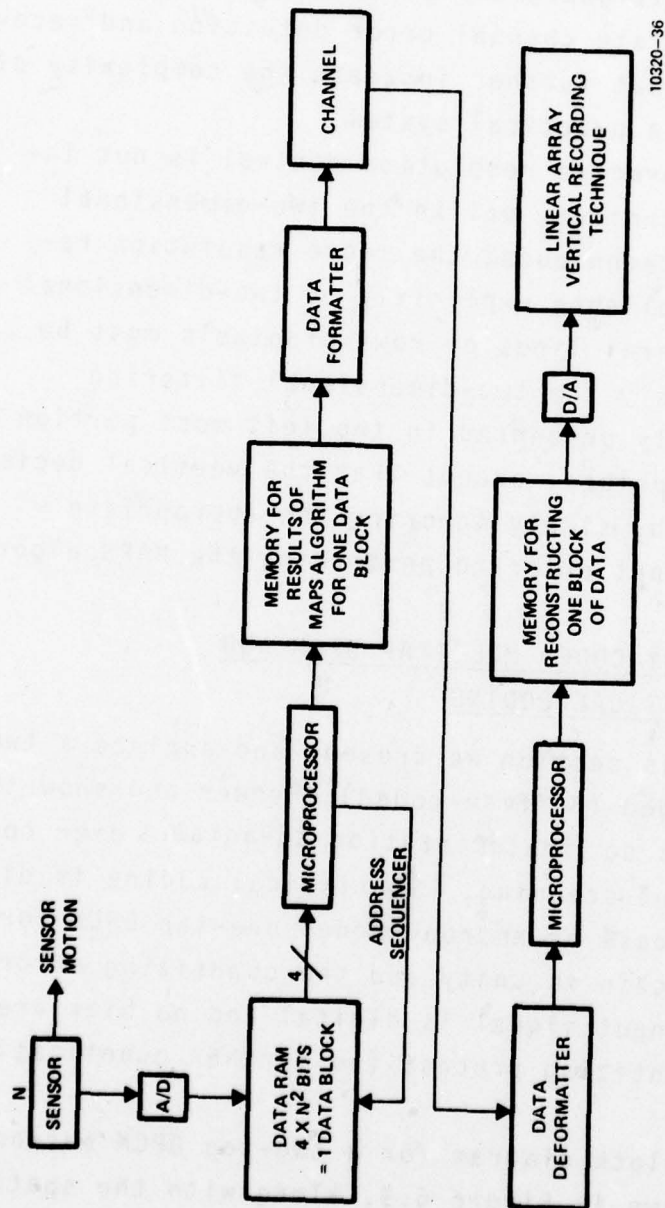
Figure 6.8

All-Digital Architecture for Implementing MAPS Algorithm

scanning or array scanning is used.

One disadvantage of using the MAPS technique is
that a channel buffer is required on both ends of the channel
due to the nonconstant data rate of encoded output data;
in addition to the additional memory associated with the
channel buffers, elaborate channel error detection and recovery
schemes are required that further increase the complexity of
the implementation of a practical system.

Since precise resolution control is not in-
herent in the MAPS technique, unlike the two-dimensional
transform and hybrid techniques, the image resolution re-
duction must be accomplished explicitly by two-dimensional
filtering. Since several lines or rows of pixels must be
processed simultaneously the two-dimensional filtering
architecture previously presented in the left most portion of
Figure 6.4-1 is appropriate, except that the vertical decima-
tion is accomplished by simply ignoring the appropriate
horizontal filter output prior to performing the MAPS algorithm.

6.9   ENTROPY-CODED MULTITAP DPCM AND
           STATISTICAL CODING

In this section we present and analyze a two-
tap DPCM, entropy-coded (Huffman-coded) encoder and show that
array scanning offers no implementation advantages over con-
ventional single-point scanning. Statistical coding is dis-
cussed as a special case of entropy coded one-tap DPCM for
which the predictor gain is unity and the quantizing error
is zero, i.e., the input signal is digital and no bits are
discarded in the quantizing process (no further quantization
occurs).

The block diagram for a two-tap DPCM entropy
coded encoder is shown in Figure 6.9, along with the spatial

COLUMN (j-1)   COLUMN j

ROW (i-1)   X   X $\boxed{X}$ $S_{i-1, j}$ β = COV $(S_{i-1, j}, S_{i, j})$

β

S_{ij}

ROW i   X $\boxed{X}$ $\xrightarrow{\alpha}$ $\bigotimes$ α = COV $(S_{i, j-1}, S_{i, j})$

$S_{i, j-1}$

a.
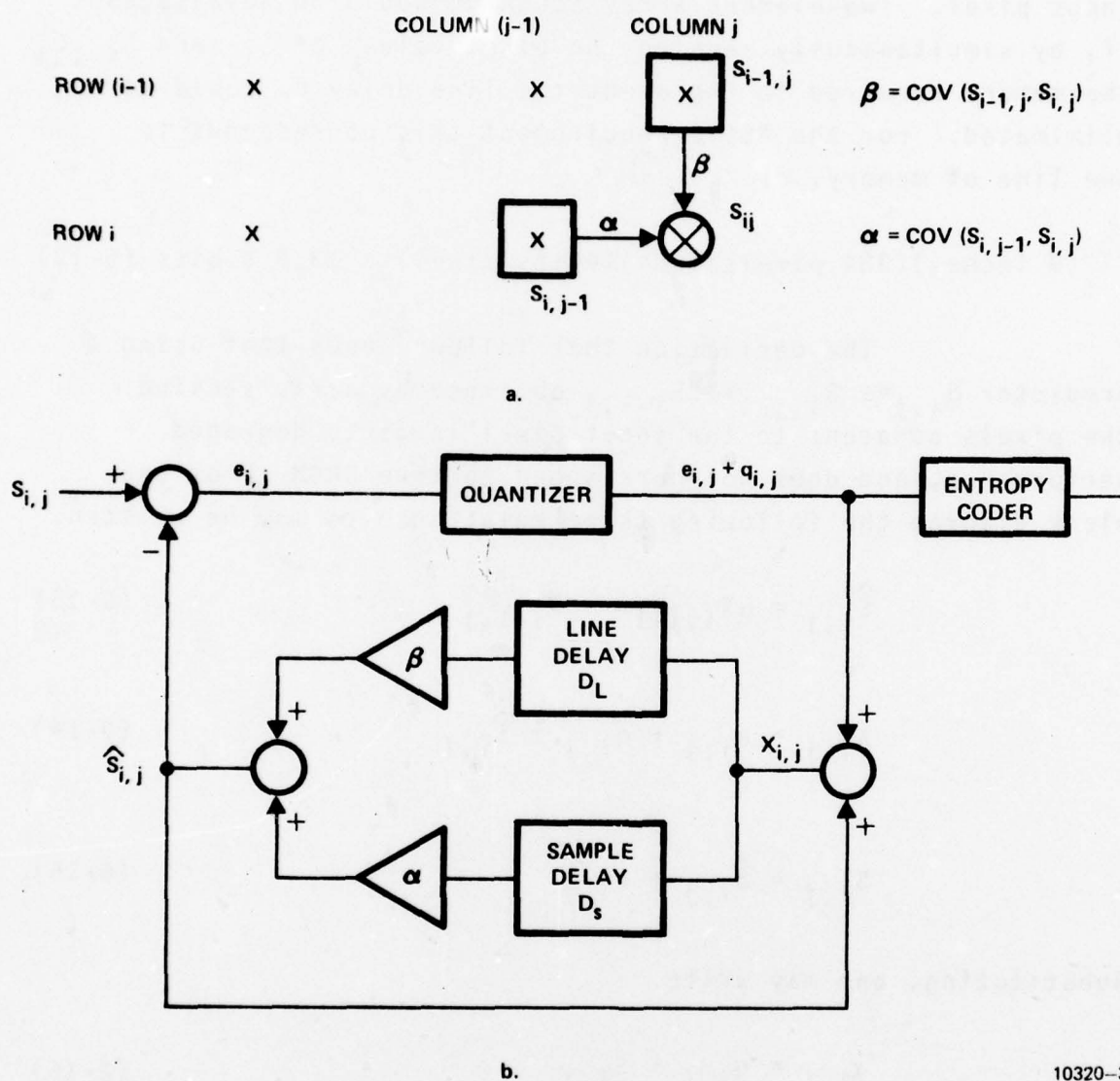
Figure 6.9
Two-Tap Entropy-Coded DPCM

10320—35

317

relationships among the input pixel or sample $S_{i,j}$ and the two samples, $S_{i-1,j}$ and $S_{i,j-1}$, used to predict the value of the input pixel. Two-element array scanning would be advantageous if, by simultaneously sensing the pixel values of $S_{i,j}$ and $S_{i-1,j}$ the memory required to implement the line delay D_L could be eliminated. For the ASITS requirement this corresponds to one line of memory, or

$$(9 \text{ inches})(384 \text{ pixels/inch})(4\text{bits/pixel}) = 13.8 \text{ K bits} \quad (6\text{-}12)$$

The derivation that follows shows that using a predictor $S_{i,j} = \alpha S_{i,j-1} + \beta S_{i-1,j}$ obtained by array sensing the pixels adjacent to the input pixel leads to degraded performance, and does not correspond to true DPCM. From the block diagram the following three relationships may be written.

$$\widehat{S}_{i,j} = \alpha X_{i,j-1} + \beta X_{i-1,j} \quad (6\text{-}13)$$

$$X_{i,j} = e_{i,j} + q_{i,j} + \widehat{S}_{i,j} \quad (6\text{-}14)$$

$$S_{i,j} = \widehat{S}_{i,j} + e_{i,j} \quad (6\text{-}15)$$

Substituting, one may write

$$X_{i,j} = q_{i,j} + S_{i,j} \quad (6\text{-}16)$$

and then

$$\widehat{S}_{i,j} = \alpha \left[q_{i,j-1} + S_{i,j-1} \right] + \beta \left[q_{i-1,j} + S_{i-1,j} \right] \quad (6\text{-}17)$$

$$\widehat{S}_{i,j} = \alpha S_{i,j-1} + \beta S_{i-1,j} + \{ \alpha q_{i,j-1} + \beta q_{i-1,j} \}$$

318

It is clear from the last expression that the "two-dimensional" quantizing noise terms within the brackets must be included in the estimate, in addition to the scaled values of the adjacent pixels, in order to obtain true two-tap DPCM operation. Recall that the proposed predictor based upon two-element array scanning was

$$S_{i,j} = \alpha \, S_{i,j-1} + \beta \, S_{i-1,j} \qquad (6\text{-}18)$$

This predictor differs from that required for true DPCM operation by the quantity $\{\alpha q_{i,j-1} + \beta q_{i-1,j}\}$ and the SNR performance is degraded accordingly. Since the SNR performance improvement associated with going from one-tap DPCM to two-tap DPCM is slight to begin with, on the order of 1.9 dB according to theoretical calculations by O'Neal [19], the performance degradation that results from using the array scanning predictor discussed above probably negates this marginal increase in SNR performance due to going to a two-tap DPCM system. For this reason, the array scanning approach is not well suited for multitap DPCM systems.

Statistical coding is a special case of entropy-coded DPCM; for the entropy-coded two-tap DPCM system of Figure 6.9, setting $\beta=0$, $\alpha=1$ and eliminating the quantizer yields a statistical coder. Since statistical coding is a one-dimensional process array scanning offers no implementation advantages over conventional single-point scanning. In addition, statistical coding requires the additional implementation complexity associated with channel buffers and channel error recovery procedures. The channel buffers are required to accomodate the varying data rate at the output of the Huffman coder. One popular channel error recovery strategy replaces a line or line segment containing

319

the effects of a channel error with the previously decoded
vertically adjacent line or line segment; this requires one
line of storage plus the associated error detection and control
circuitry. In view of all of the above considerations, it is
clear that statistical coding is not appropriate for array
scanning systems.

7.0 CONCEPTUAL DESIGN OF AN ARRAY SCANNING
IMAGE TRANSMISSION SYSTEM

In this section the basis for selecting the
hybrid DCT/DPCM candidate ASITS system for detailed design
is discussed. The validity of the hybrid mixed-domain filter-
ing approach used to control vertical and horizontal spatial
resolution is illustrated with a simple example using a four-
element DCT and this is followed by a mathematical proof
for the general case of transforms of length N. A conceptual
design is presented and explained with the aid of a detailed
block diagram and some of the implementation and system aspects
of this hybrid candidate system are discussed.

7.1 SELECTION OF A CANDIDATE SYSTEM
FOR DETAILED CONCEPTUAL DESIGN

The criteria for selecting one of the candidate
systems presented in paragraph 6.0 for detailed conceptual
design include

- cost/implementation complexity
- flexibility
- processing capability
    - MTF correction or image enhancement
    - BWC
    - Decimation/Interpolation
    - REARCS
    - throughput rate
- reliability
- performance

From the discussion and tradeoff matrix of para-
graph 5.0 it was concluded that both the hybrid DCT/DPCM

321

technique and the two-dimensional DCT technique give superior
BWC performance but at the expense of relatively high com-
plexity when conventional single-point scanning is used.
It was demonstrated in paragraph 6.0 that hybrid DCT/DPCM and
two-dimensional DCT implementations are considerably simplified
when array scanning is used in conjunction with CCD's.

The two-dimensional FIR filtering computer
simulation experiments reported in paragraph 4.0 showed that
fairly large FIR filters, e.g., at least larger than 15 x 15
and perhaps as large as 31 x 31, are required in order to obtain
suitable decimation/interpolation filtering performance. While
this requires very large digital memories and very fast
digital arithmetic capabilities for single-point scanning
systems, the use of array scanning allows both the storage
and computation required for two-dimensional (or one-dimensional)
filtering to be performed using CCD's operating upon analog
sampled-data pixel values.

By comparing the complexity of the various
ASITS implementations presented in paragraph 6.0 it is clear
that using CCD technology is the key to implementing a high
performance, low complexity, high speed, flexible image trans-
mission system. While both the two-dimensional DCT and the
hybrid DCT/DPCM candidate systems are attractive in terms of
the selection criteria the superior subjective and objective
image quality of the hybrid technique and its potential for
higher image throughput rate make it the logical choice for the
detailed conceptual design.

7.2   THE HYBRID MIXED-DOMAIN APPROACH TO SPATIAL
          RESOLUTION CONTROL

Recall from the discussion of Section 6.6 that
for the hybrid BWC technique the vertical spatial resolution
is controlled in the frequency domain by eliminating coef-
ficients of the vertical DCT while the horizontal spatial

322

resolution is controlled in the spatial domain via transversal lowpass filtering. The numbers that result from the hybrid encoding and that are transmitted over the channel are not in either the spatial domain or the frequency (transform) domain, but, rather, are in a sort of mixed domain with the vertical dimension having units of frequency and the horizontal dimension having units of space.

Figure 7.2-1 illustrates with an example why FIR filtering in the along-scan direction is appropriate for horizontal resolution control in the hybrid encoder. The (a) portion of the figure shows a DCT of a column of pixels of length N=4 followed by the corresponding inverse DCT, the result of which is, of course, the original four pixel values. The sequence of horizontal pixel values at the points labeled S_0, S_1, S_2, and S_3 is then lowpass filtered with transversal filters whose outputs S_0', S_1', S_2', and S_3' exhibit reduced resolution. Now consider the (b) portion of Figure 7.2-1. This configuration resulted from "pushing" the transversal filters of Figure 7.2-1(a) through the summing points (operational amplifiers) and then through the weights of the inverse DCT implementation. Since this system is a linear system and all the transversal filters are assumed to be identical the resulting system of Figure 7.2-1(b) is equivalent to that of Figure 7.2-1(a). By then inserting four channels (or one TDM channel) and four DPCM encoders and decoders between the transversal filter outputs and the inverse DCT inputs one constructs the conventional hybrid BWC system--here we have shown all transform coefficients being transmitted for clarity in the above explanation.

The mathematical validity of the two-dimensional hybrid filtering concept presented above may be demonstrated as follows. (The DPCM encoding/decoding process will be considered to be transparent and is therefore ignored in the following). The notation to be used in the derivation is

323

Figure 7.2-1. Illustration of Mixed Domain Resolution Control

324
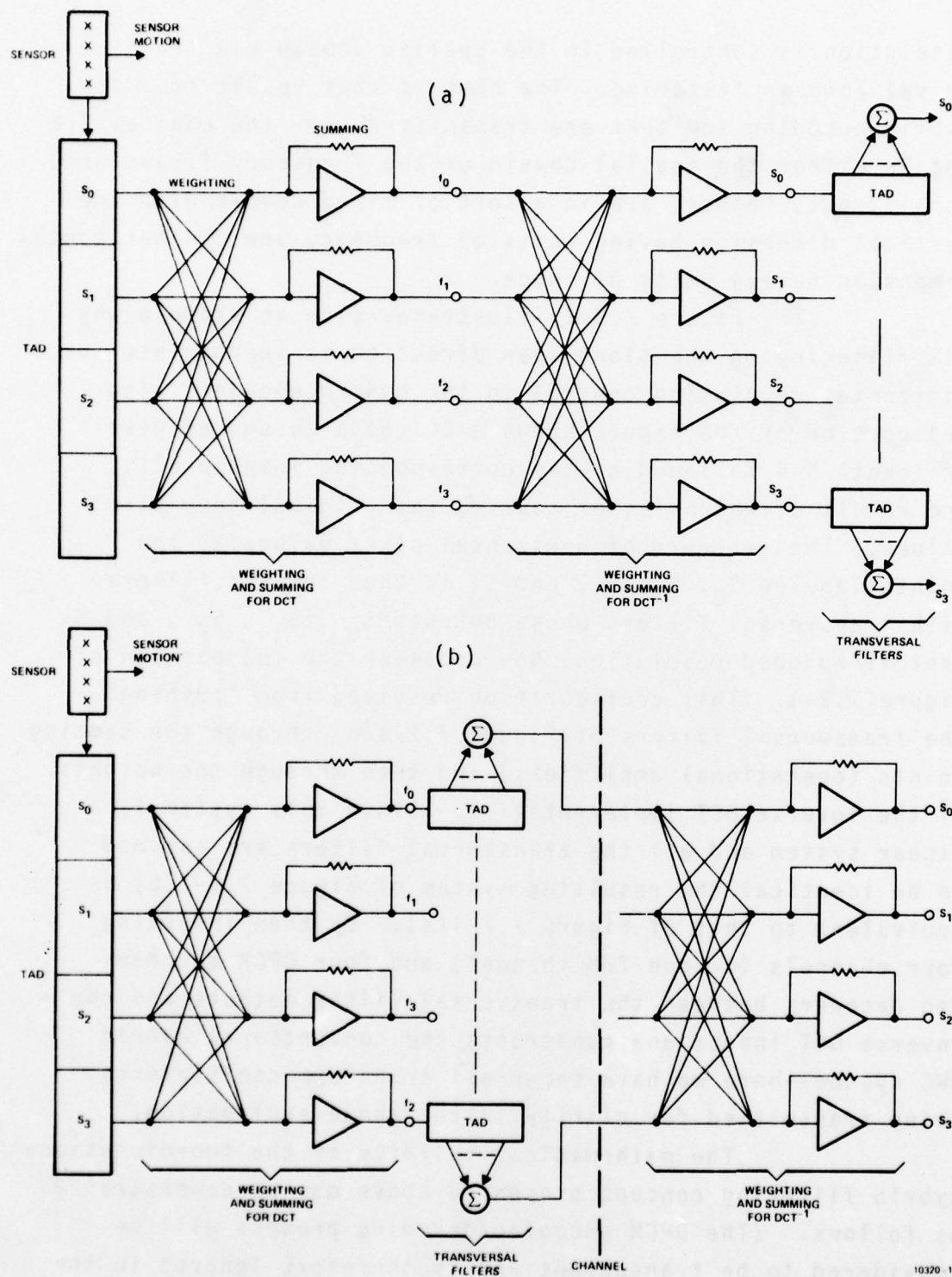
defined in Figure 7.2-2. This derivation is for the case in which the one-dimensional transformation is the Discrete Fourier Transform (DFT), although the conclusion is equally valid for the DCT. Using the DFT in this derivation facilitates the interpretation of the transform coefficients as being conventional spatial frequency components.

The sequence $\{X(m.n)\}$ represents the image pixel values whose spatial location is indexed by row m and column n. Performing the DFT vertically (along columns) yields the transform coefficients

$$\bar{X}_k(n) = \sum_{m=0}^{N-1} X(m,n) \exp(j2\pi mk/N) \qquad (7-1)$$

Filtering the resulting two-dimensional (mixed domain) sequence in the <u>vertical</u> direction is accomplished by merely scaling the vertical transform coefficients by the constants a_k, whereas filtering the sequence in the horizontal direction is accomplished by using a FIR transversal filter to perform the following convolution:

$$Y_k(1) = \sum_n a_k \bar{X}_k(n) \, h_1(1-n) \qquad (7-2)$$

where

$$h_1(1-n) = \text{filter impulse response (tap weights) reversed in space (or time).}$$

Substituting the expression for $\bar{X}_k(n)$ into this expression one obtains:

$$Y_k(1) = a_k \sum_n h_1(1-n) \sum_{m=0}^{N-1} X(m,n) \exp(j2\pi mk/N) \qquad (7-3)$$

325

HORIZONTAL SPACE INDEX

n=0 n=1 n=2
m=0 X   X   X ---
m=1 X   X   X   ← SCAN DIRECTION
m=2 X   X   X ← x (m, n) = PIXEL VALUES

VERTICAL
SPACE
INDEX

(AFTER ONE-DIMENSIONAL TRANSFORMATION IN VERTICAL DIRECTION)

⟹

HORIZONTAL SPACE INDEX
AT FILTER INPUT

n=0 n=1 n=2
k=0 X   X   X ---
k=1 X   X   X
k=2 X   X   X

VERTICAL
SPATIAL
FREQUENCY
INDEX

$X_k (n)$ = MIXED-DOMAIN VALUE AFTER VERTICAL ONE-DIMENSIONAL TRANSFORMATION

TAD

Σ

$y_k (\ell)$
ℓ = HORIZONTAL SPACE INDEX AT FILTER OUTPUT

10320—40

Figure 7.2-2

Definition of Notation to be Used in Hybrid Filtering Derivation

326

We now take the inverse vertical DFT in order to return
to the fully spatial domain from the mixed domain; this
corresponds to the function performed by the receiver in the
hybrid BWC technique. From the definition of the inverse
DFT

$$Z_s(1) = \frac{1}{N} \sum_{k=0}^{N-1} Y_k(1)\exp(-j2\pi sk/N) \qquad (7-4)$$

where 1 is the horizontal space index, s is the vertical space
index at the receiver, and $z_s(1)$ is the two-dimensional
sequence of the reconstructed image pixel values. Substituting
for $Y_k(1)$ in the above definition yields

$$Z_s(1) = \frac{1}{N} \sum_{k=0}^{N-1} \exp(-j2\pi sk/N) \sum_{n} A_k\overline{X}_k(n)h_1(1-n) \qquad (7-5)$$

and substituting for $\overline{X}_k(n)$ gives

$$Z_s(1) = \sum_{k=0}^{N-1} A_k\exp(-j2\pi sk/N \sum_{n} h_1(1-n) \sum_{m=0}^{N-1} X(m,n)$$

$$\cdot \exp(+j2\pi mk/N) \qquad (7-6)$$

$$Z_s(1) = \sum_{n} h_1(1-n) \sum_{m=0}^{N-1} X(m,n)\left[\frac{1}{N} \sum_{k=0}^{N-1} A_k\exp(j2\pi k(m-s)/N)\right] \qquad (7-7)$$

Recognizing that the bracketed term is a function of (s-m),
which function we will designate as $h_2(s-m)$, the reconstructed
two-dimensional pixel sequence may be written as

$$Z_s(1) = \sum_{n} \sum_{m=0}^{N-1} X(m,n) \, h_2(s-m)h_1(1-n) \qquad (7-8)$$

327

But this last expression is simply the convolution of the original two-dimensional image pixel sequence with a separable FIR filter impulse response

$$h_{TOT}(s,1) = h_1(1)h_2(s) \qquad (7-9)$$

This result demonstrates that the reconstructed image at the output of the hybrid decoder has been two-dimensionally filtered by a separable frequency transfer function.

Recall from paragraph 4.0 that using separable two-dimensional FIR filters to effect MTF correction (or image enhancement) suffers from the disadvantage that the two-dimensional MTF correction filter frequency response exhibits cusps or peaks at the corners of the transfer function. This is a result of the fact that for separable filters the two-dimensional frequency transfer function is the product of a one-dimensional vertical filter and a one-dimensional horizontal filter. Thus, for example, if a one-dimensional MTF correction filter with 10 dB gain at f_c is used for both the vertical and horizontal filtering, then the resulting separable two-dimensional MTF correction filter has 20 dB gain at ($f_h = f_c$, $f_v = f_c$) and only 10 dB gain at ($f_h = 0$, $f_v = f_c$) and ($f_h = f_c$, $f_v = 0$). This is an undesirable result since some frequencies are emphasized more than others. Since the proposed hybrid technique implements separable rather than nonseparable FIR filters, the ASITS MTF correction will not be uniform within the passband of the system two-dimensional transfer function. The separable MTF correction computer simulation experiments reported in paragraph 4.0 indicate that this is an acceptable price to pay for the much lower implementation complexity of separable filters compared to nonseparable filters.

7.3   DETAILED BLOCK DIAGRAM FOR CONCEPTUAL DESIGN

Figure 7.3-1 shows a detailed block diagram
presenting the hybrid technique proposed for the ASITS. The
ASITS pictured in Figure 7.3-1 is capable of

- MTF correction/image enhancement

- REARCS operation

- BWCR at 4:1, 2:1, or 1:1 using the hybrid
  technique

- Resolution reduction of 4:1, 2:1, or 1:1

- Decimation and interpolation by factors
  of 2 and 4, in conjunction with two-
  dimensional separable lowpass filtering

These ASITS capabilities are discussed below in the explanation
of the block diagram of Figure 7.3-1.

The hybrid ASITS block diagram of Figure 7.3-1
shows a conceptual design that makes liberal use of Reticon
R5602 CCD's (designated by dashed line enclosures in the
figure). These 64-tap mask programmable CCD's are used to
perform three distinct functions in this implementation:
DCT basis function correlation, separable horizontal lowpass
filtering at intermediate and low resolution with integrated
MTF correction or image enhancement, and image enhancement or
MTF correction at maximum resolution where no lowpass filtering
is required.

The linear array sensing technique selected
for this conceptual design is the AOBD, dithered raster,
galvanometer-based approach discussed in detail in Paragraph
2.0. This approach is based upon well-developed technologies
and is regarded as low-risk. Extensive trade-off analyses

329

330
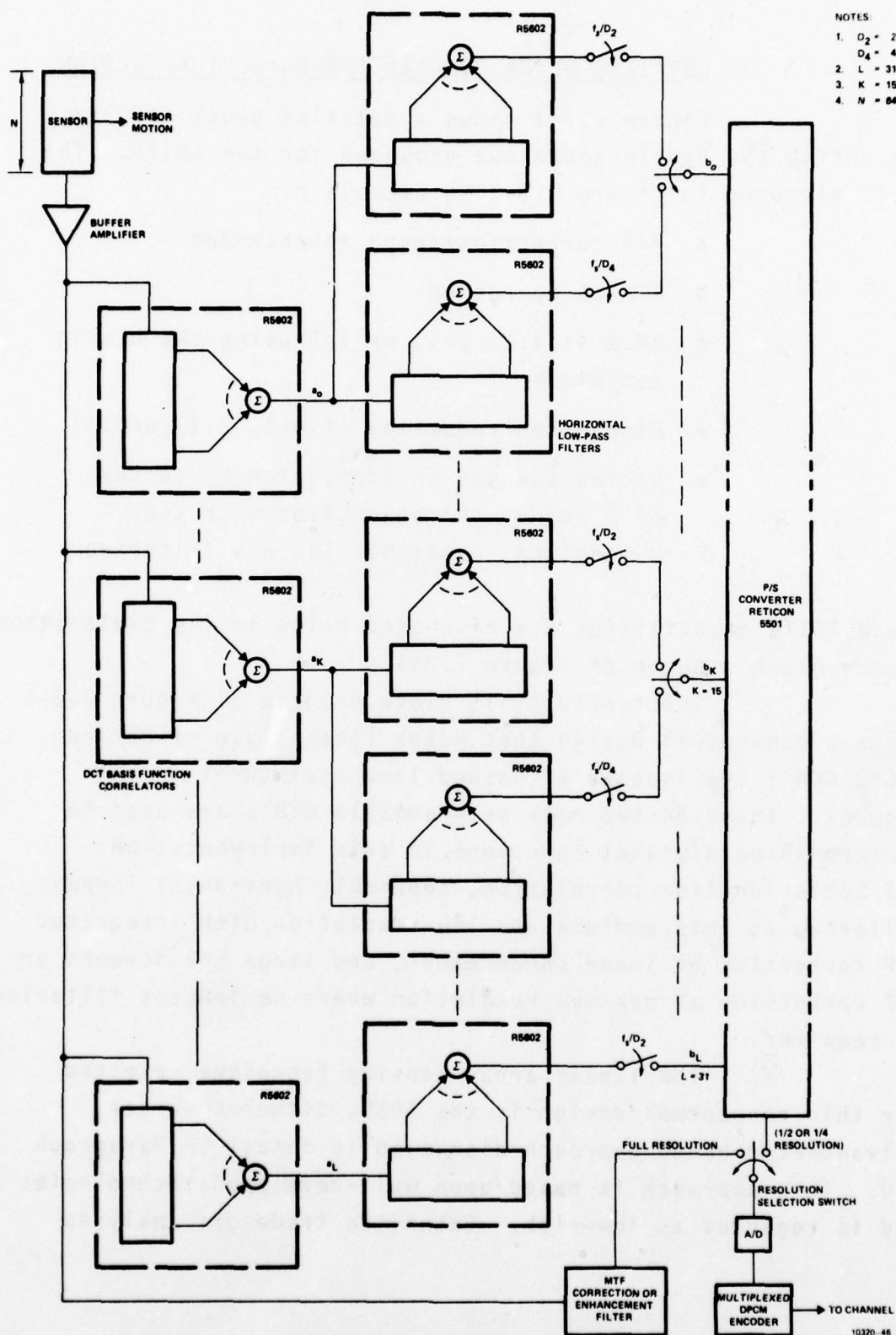
Figure 7.3-1. ASITS Hybrid Transformer Block Diagram

for this approach were presented in paragraph 2.0. A 64
element sensor is required in order to fully utilize the pro-
cessing capability of the Reticon R5602 CCD's used to per-
form the hybrid transform.

The ASITS operation is as follows. The sensor
array serially outputs 64 pixel values corresponding to a ver-
tical column within the image being scanned; the vertical
spacing between pixels is 1/384 ppi = 0.002604 inches. These
64 pixel values are buffered and shifted simultaneously into
32 (L=31) R5602 CCD's. Each of these R5602 CCD's is mask
programmed with one of the first 32 DCT basis functions of
the 64-point DCT. These basis functions are correlated with
the 64 pixel values that are stored in the R5602 CCD's so that
the CCD outputs are the DCT coefficients A_o through A_{31}.
These thirty-two DCT coefficients are required in order to
obtain one-half the full vertical resolution, since the DCT
is of length 64. For the one-quarter resolution case, only
16 of the 64 DCT coefficients need be computed (K=15 in
Figure 7.3-1). A new set of DCT coefficients A_o through A_{31}
is computed corresponding to each new set of 64 pixel values
output by the sensor array; the sensor array outputs these
64 pixel values by horizontally advancing a distance equal to
the pixel separation, 1/384ppi=.002604 inches. Each of the coef-
ficient sequences is convolved with a sampled filter impulse
response in order to provide horizontal lowpass filtering
and MTF correction prior to along-scan decimation. Since
both intermediate (192 ppi) and low resolution (96 ppi) modes
must be provided, two sets of horizontal lowpass filters
are required for the first 16 DCT coefficients with cutoff
frequencies of fs/4 and fs/8, respectively. The appropriate
filter outputs are selected for parallel-to-serial conversion,
depending upon whether 192 ppi or 96 ppi resolution is desired.

The parallel-to-serial converter shown in
Figure 7.3-1 is a 32-stage Reticon R5501, which is a recently
introduced Reticon product. If full resolution (384 lpi)
is required then both the vertical DCT and the horizontal
lowpass filtering operations are bypassed and the resolution
selection switch of Figure 7.3-1 is switched to the full re-
solution position. In this situation the sensor data passes
through the MTF correction or image enhancement filters
indicated in Figure 7.3-1. The implementation of these filters
is shown in Figure 7.3-2. The 7x7 nonseparable MTF correction
filter utilizes a R5602 CCD with (64-49)=15 tap weights pro-
grammed to zero. Recall that nonseparable MTF correction
filters are more desirable (i.e., more flexible) than separable
filters. Since at full resolution no stopband is required,
low order filters should be adequate for MTF correction.
Note that with 64 pixel values per column and a 7x7 FIR filter
implemented in one linear CCD shift register, a clock enable
(CE) signal is required so that only 7 of the pixel values
comprising each column are actually shifted into the CCD.
Although any 7 of the 64 pixel values could be selected, we
will choose to read the 7 "topmost" pixel values of the 64
pixel column into the filter CCD's. This requires that the CE
signal be inhibited during the time that the first 57 pixel
values of each column are being read out of the sensor.
Similarly, the CE signal must be inhibited during the first
61 sample times if image enhancement rather than MTF cor-
rection is desired. Note from Figure 7.3-2 that a switch
controls the selection of image enhancement or MTF correction.
Recall from Section 4.2 that any desired degree of image
enhancement can be obtained using a 3x3 FIR filter with
appropriate tap weights. The 3x3 enhancement filter can
utilize either a R5602 or a TAD-32A; the latter choice allows
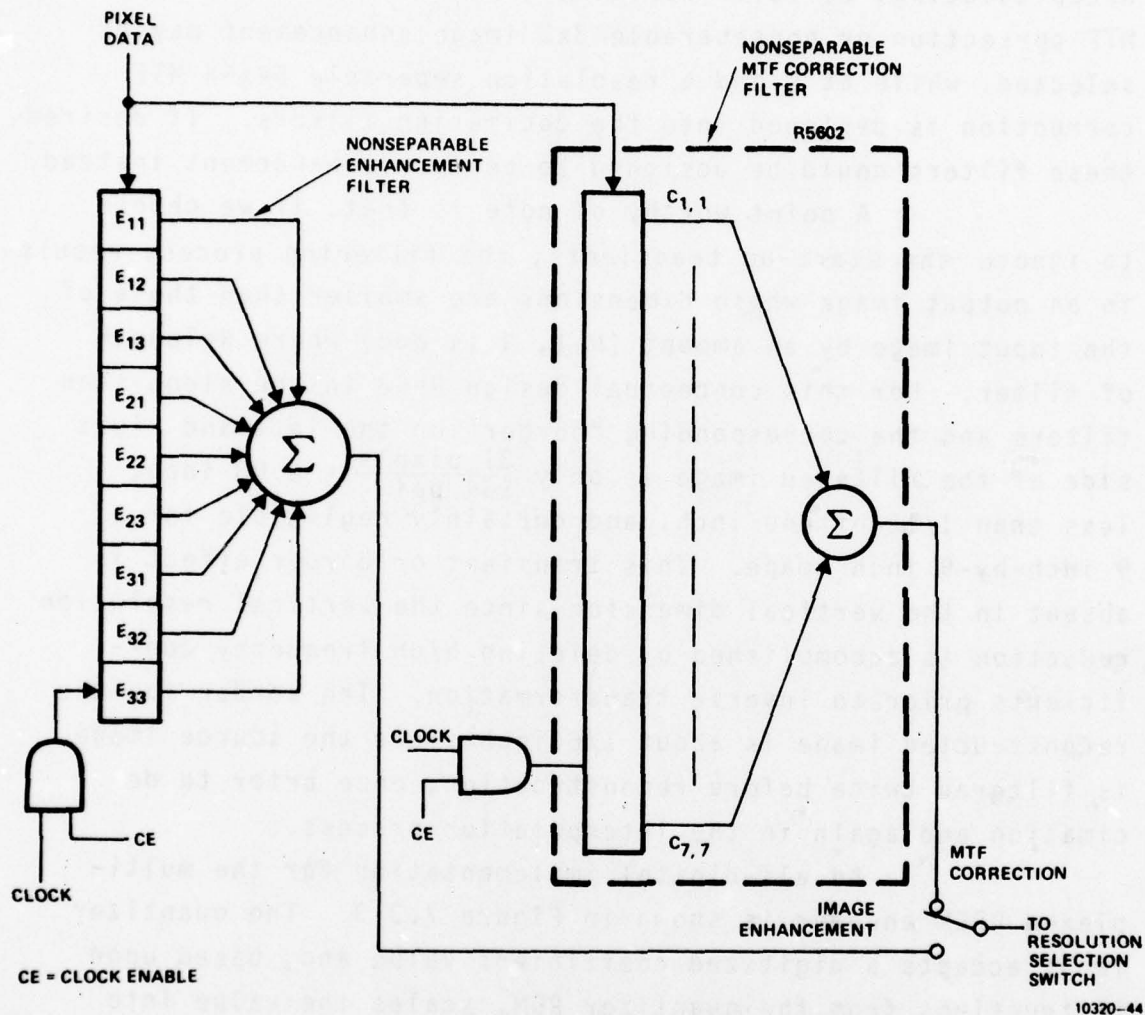
Figure 7.3-2
Selectable Nonseparable MTF Correction
and Image Enhancement Filters

the degree of image enhancement to be changed by simply adjusting 9 resistor values which set the FIR tap weights. Recapitulating, at full resolution, either nonseparable 7x7 MTF correction or nonseparable 3x3 image enhancement may be selected, while at ½ and ¼ resolution separable 64x64 MTF correction is designed into the decimating filters. If desired, these filters could be designed to perform enhancement instead.

A point worthy of note is that, if we choose to ignore the start-up transients, the filtering process results in an output image whose dimensions are smaller than those of the input image by an amount (N-1, N is odd) where N=length of filter. For this conceptual design N=63 in the along-scan filters and the corresponding "border" on the left and right side of the filtered image is only $\frac{31 \text{ pixels}}{384 \text{ ppi}}$ = 0.08 inch, less than 1/12 of one inch, and certainly negligible for a 9 inch-by-9 inch image. This transient or border effect is absent in the vertical dimension since the vertical resolution reduction is accomplished by deleting high frequency coefficients prior to inverse transformation. The border for the reconstructed image is about 1/6 inch since the source image is filtered twice before reconstruction, once prior to decimation and again in the interpolation process.

An all-digital implementation for the multiplexed DPCM encoder is shown in Figure 7.3-3. The quantizer input accepts a digitized coefficient value and, based upon instructions from the quantizer ROM, scales the value into the proper quantizer range via the appropriate number of shifts and sets the correct number of LSB's to zero; the forced-zero LSB's out of the quantizer are necessary for the predictor arithmetic, but are not transmitted over the channel. The proper scaling factor and quantizer accuracy are accessed in the quantizer ROM by forming an address using the BWCR CMD
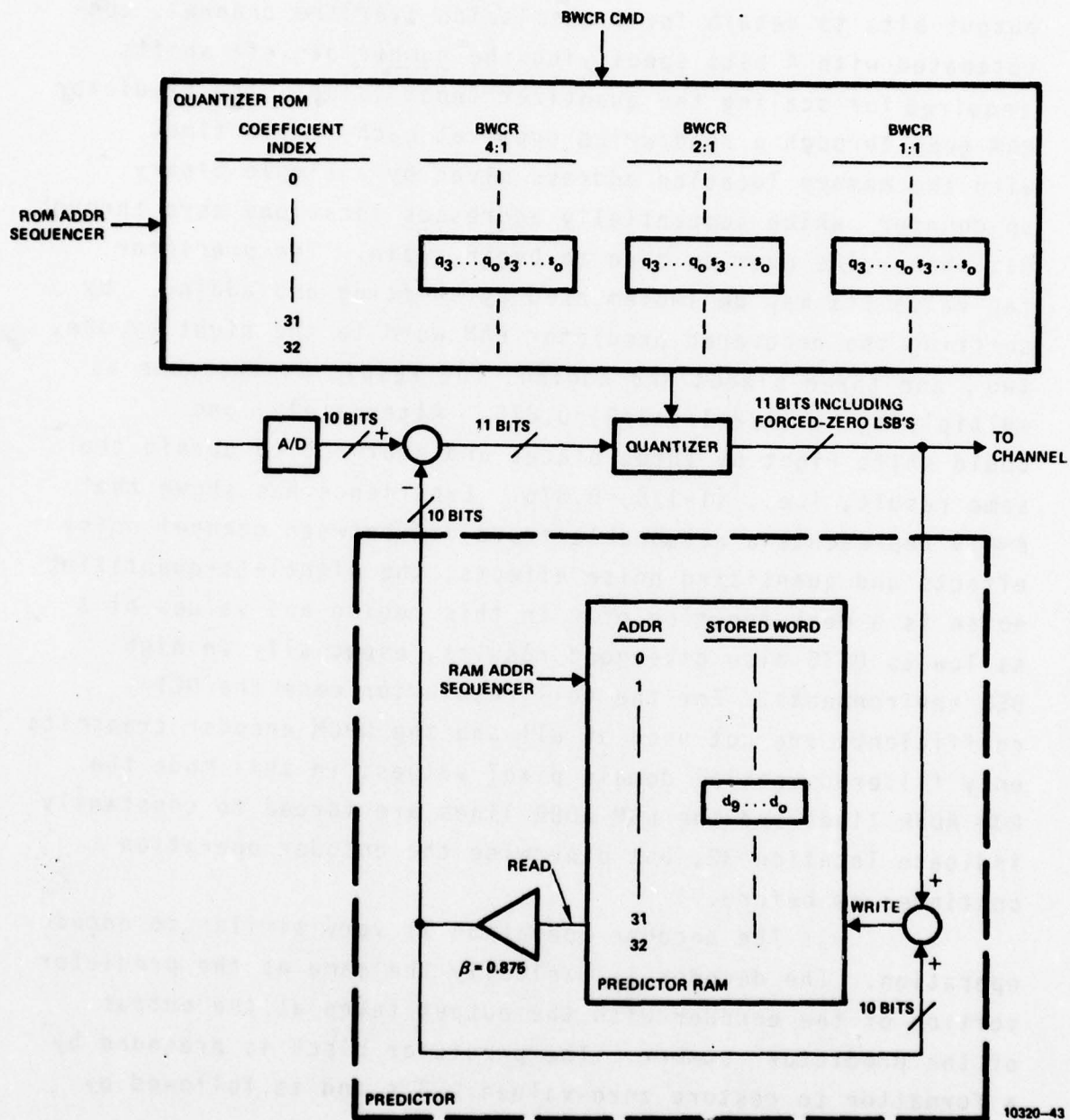
Figure 7.3-3
All-Digital Implementation of Multiplexed DPCM Encoder

and the coefficient index (zero through 31). The ROM quantizer
word consists of 4 bits designating the number of quantizer
output bits to retain for transmission over the channel, con-
cotenated with 4 bits specifying the _number_ of left shifts
required for scaling the quantizer input value. The predictor
RAM goes through a read/write cycle at each sample time,
with the memory location address given by a simple binary
up-counter which sequentially addresses locations zero through
31, then rolls over to zero to begin again. The predictor
tap value $\beta < 1$ may be implemented by shifting and adding. By
shifting the recovered predictor RAM word to the right by one,
two , and three places and adding, the result is the same as
multiplying by $(1/2+1/4+1/8)=0.875$. Alternately, one
could shift right by three places and subtract to obtain the
same result, i.e., $(1-1/8)=0.875$. Experience has shown that
$\beta \approx 0.9$ represents a reasonable trade-off between channel noise
effects and quantizing noise effects; the signal-to-quantizing
noise is a weak function of β in this region and values of β
as low as 0.75 also give good results, especially in high
BER environments. For the full resolution case the DCT
coefficients are not used at all and the DPCM encoder transmits
only filtered spatial domain pixel values; in this mode the
ROM ADDR lines and the RAM ADDR lines are forced to constantly
indicate location 32, but otherwise the encoder operation
continues as before.

The decoder operation is very similar to encoder
operation. The decoder is basically the same as the predictor
portion of the encoder with the output taken at the output
of the predictor summer. The predictor block is preceded by
a formatter to restore zero-valued LSB's and is followed by
an inverse scaler.

The hybrid ASITS receiver is shown in Figure
7.3-4. The sequence of operations is the reverse of those
at the hybrid transmitter. If full resolution mode is not
selected the DCT coefficients from the output of the multi-
plexed DPCM decoder are inverse transformed to obtain 64
vertical pixel values. The horizontal sequence of pixel
values that results from successive inverse transformations
is then interpolated by a factor of two or four. The inter-
polated pixel values are stored in two Reticon 5501 CCD's
P/S converters, whose serial outputs are alternately connected
to the linear array recorder. This arrangement is necessary
in order to synthesize a 64-stage P/S converter from two
32-stage P/S converters. If the full resolution mode is
selected, then the buffered DPCM decoder output is read directly
into the linear array recorder.

As in the hybrid transmitter implementation,
liberal use is made of the mask-programmable 64-stage Reticon
5602 CCD. As mentioned earlier, the multiplexed DPCM decoder
implementation is similar to that of the encoder shown in Figure
7.3-3 and is not discussed further. The hybrid ASITS receiver
is of higher complexity than the hybrid ASITS transmitter in
that twice as many R5602 CCD's are required for the inverse
DCT. This is because only 32 of the 64 DCT coefficients need
be computed at the transmitter (corresponding to one-half
resolution) whereas all 64 spatial domain pixels must be
computed via the inverse DCT at the hybrid receiver. Each
of the 64-stage $(DCT)^{-1}$ basis function correlators shown in
Figure 7.3-4 is loaded with 32 DCT coefficients and 32 zeros
for the one-half resolution case (or 16 coefficients and 48
zeros for the one-quarter resolution case) in order to perform
the inverse DCT. The receiver complexity is further increased
by virtue of the fact that two interpolating filters are
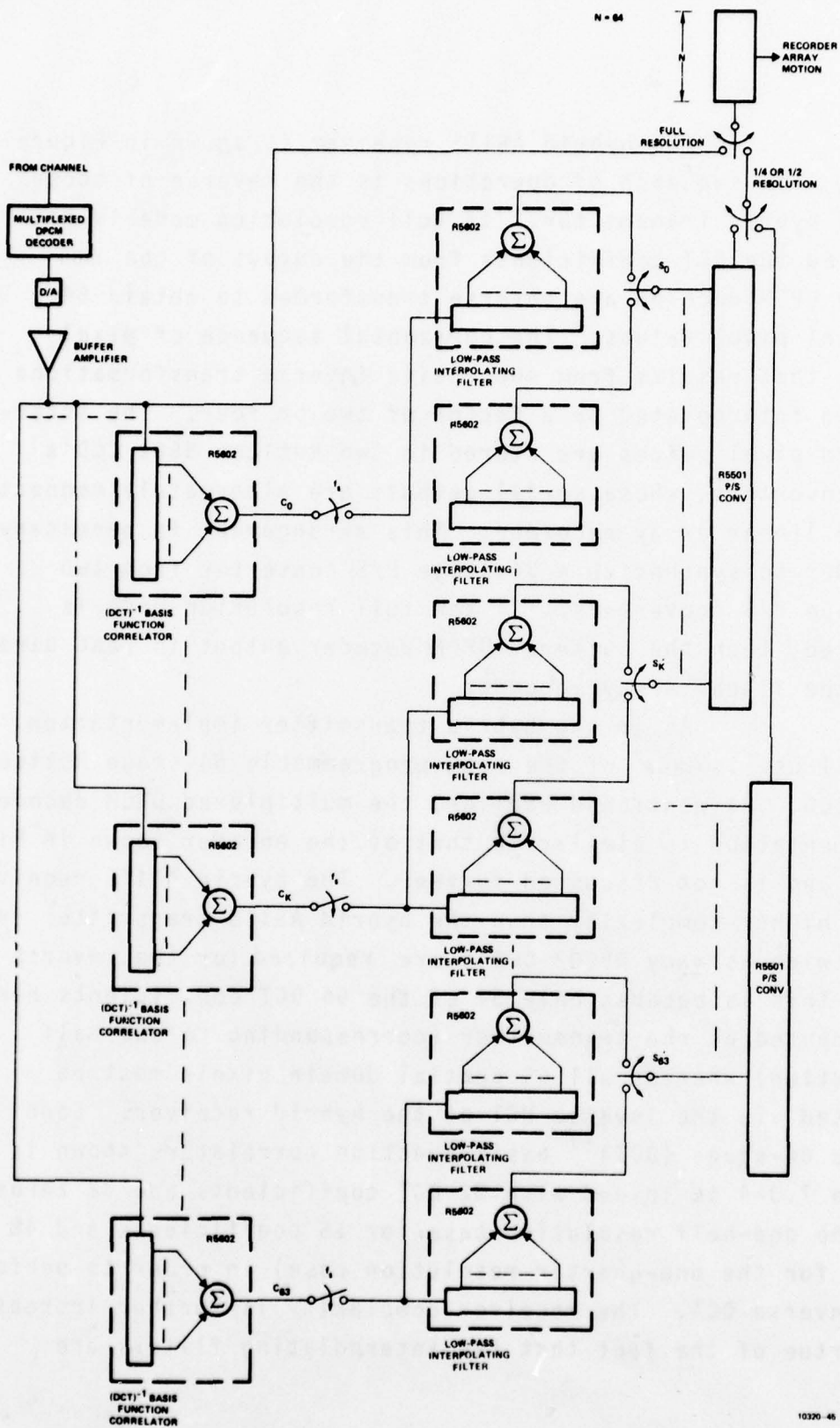
Figure 7.3-4. ASITS Hybrid Receiver Block Diagram

338

required for each of the 64 inverse DCT basis function cor-
relators. Since the DCT is its own inverse, the first 32
$(DCT)^{-1}$ basis function correlators are identical to the 32
DCT basis function correlators used in the hybrid trans-
mitter. In addition, all the quarter-bandwidth decimating
and interpolating filters in the system are identical, as
are all the half-bandwidth decimating and interpolating filters.

The linear array recording technique selected
for this conceptual design is the AOBD scanned recording
approach discussed in some detail in paragraph 3.0. Of the
several array recording approaches evaluated in paragraph
3.0, the AOBD approach is the lowest in cost, and its $N \leq 1500$
element, 75 M pixels/sec capability insures that it can easily
meet the ASITS requirements we have specified. However, it
was pointed out in paragraph 3.0 that it is difficult to change
scanning speeds with this technique; this is a factor of impor-
tance discussed in Section 7.4, System Considerations and
Trade-offs, which follows.

7.4 SYSTEM CONSIDERATIONS AND TRADE-OFFS

Briefly stated, the ASITS system parameters
are determined by the requirement to transmit a 9 inch-by-9 inch
image quantized to four bits per pixel within ten minutes over a
4.8 Kbps channel. For the purpose of defining maximum pixel
rates, it will be assumed that this image will have 12 square
inches transmitted at a resolution of 384 ppi with the re-
maining 69 square inches transmitted at a resolution of 96
ppi. Simple calculations show that a bandwidth compression
ratio of four-to-one throughout the image is adequate to meet
the above requirement.

339

It is also desirable to be able to select a
resolution of 192 ppi and a BWCR of 2:1 or 1:1 wherever desired
within the image; of course, the 10 minute transmission time
requirement will not be met under these circumstances. It
should be pointed out that specifying a 4:1 BWCR for both
the target region and the background region would probably not
be typical of ASITS operation since 4:1 BWCR in the target
region is equivalent to 1-tap delta modulation and would not
yield the image quality desired for the target region; the
specification of 4:1 BWCR in both regions in the example above
simply serves to determine the pixel rate required.

Before computing the required pixel rates at
the sensor, recorder, and CCD processors, we present several
possible bit assignments for the hybrid technique. In dis-
cussing the bit assignments and their relationships to the
BWCR we will treat resolution reduction and BWCR as separate
processes in keeping with the spirit of the REARCS definitions
of these terms. Since we assume a 64-point DCT, this means
that 32 coefficients will be retained for half resolution and
16 coefficients will be retained for quarter-resolution.
The horizontal resolution is controlled by decimation filters
in each case. The bit assignment over the retained coefficients
then determines the BWCR as we have defined it in this report.
For example, if we retain only 16 of the 64 coefficients, we
call this the quarter resolution case. Furthermore, if we
then choose a bit assignment for these 16 retained coefficients
that has a total of, say, 32 bits, then this corresponds to
a BWCR of 32 bits/16 coefficients = 2 bits/pixel at one quarter
resolution, where these pixels are low resolution pixels
prior to interpolation. This definition of BWCR is in contrast
to the one commonly found in the literature which includes
the unretained coefficients in the BWCR computation; however,

our definition is consistent with the REARCS definitions of
BWC and image resolution. The BWCR is defined in terms of
the pixels that remain after resolution reduction has taken
place. In Table 7.4-1 we present for illustration purposes some
bit assignments associated with BWCR's of 4:1, 2:1, and 1:1
for both the half-resolution and quarter resolution cases.
These bit assignments are estimates based upon some prior
experience with the hybrid technique and have not been optimized
for this application. However, they do serve to illustrate
the general nature of hybrid transform bit assignments. Note
that for the 1 bit/pixel case some of the higher coefficients
are set to zero, which further decreases the real available
resolution below one-quarter or one half; this is unavoidable
since assigning one bit to each coefficients is clearly sub-
optimum. Assigning more bits to the lower coefficients
results in better image quality, and for the 1 bit/pixel case
this necessitates assigning zero bits to some of the higher
"retained" coefficients.

We now examine the required swath scanning rate
(inches/second) and the associated pixel scanning rate (pixels/
second) at the sensor output. This will allow us to determine
whether the pixel rate capabilities of the sensor, recorder,
and CCD processors are exceeded when the system throughput
requirement stated earlier is imposed. Figure 7.4-1 depicts
the scanning action at either the sensor or the recorder and
shows that each sweep of the 64-element sensor (or recorder)
across the image covers an area 1/6 inch by 9 inches, hereafter
called a swath. In the background (low resolution) region
of the image the sensor advances 64 lines at a time in non-
overlapping swaths. However, in the target (full-resolution)
region the sensor advances only one line at a time in order
to accomplish the two-dimensional MTF correction filtering--
the DCT is not performed. In those portions of the image

TABLE 7.4-1
HYBRID TRANSFORM BIT ASSIGNMENT VERSUS
BWCR AND RESOLUTION SELECTION

	Quarter Resolution Case BWCR			Half Resolution Case BWCR		
Coefficient	4:1	2:1	1:1	4:1	2:1	1:1
C_0	4	7	9	3	8	10
C_1	2	5	8	2	6	9
C_2	1	4	7	2	5	9
C_3		3	7	1	4	9
C_4		2	7		3	8
C_5		1	6		3	8
C_6			5		3	7
C_7			3		2	6
C_8			2		2	6
C_9			2		2	5
C_{10}			2		2	5
C_{11}	1		2		2	4
C_{12}	0		1		2	4
C_{13}			1		2	4
C_{14}			1		1	4
C_{15}			1			3
C_{16}			0			3
C_{17}						3
C_{18}						3
C_{19}						2
C_{20}						2
C_{21}						2
C_{22}						2
C_{23}				1	1	2
C_{24}				0		
C_{31}						1
C_{32}						0
C_{63}						

342

Figure 7.4-1
The Nature of the
Linear Array Scanning Action

in which a scan line intersects both the target region and the background region, the operation may be described as follows. Consider swath #43 of Figure 7.4-1: the first line of the 64 lines comprising this swath is the uppermost line of the target region. After completing swath #43 the sensor must move upward 32 lines and begin the line-at-a-time scanning necessary in the target region; the sensor output is ignored when passing over the background region during the next (32+64)=96 line advances. When the sensor has advanced 97 lines and is positioned directly over the 64 lines comprising swath #45, the hybrid DCT operation is performed on the sensor output while the sensor is moving across the background region and the two-dimensional MTF correction filtering (only) is performed while the sensor is moving across the target region. After one line advance the sensor output is again ignored when passing over the target region but utilized when passing over the target region; this process continues for the next 62 lines. After 62 more lines the sensor is positioned directly over swath #44 and the above operation sequence repeats until the sensor is positioned directly over swath #49. At this point no hybrid DCT is required since the sensor is wholly within the target region; the line-by-line scanning action then continues for the remainder of the image.

Now that the scanning operation has been described, the required swath scanning rate and associated pixel rate at the sensor output and in the channel can be computed for the image of Figure 7.4-1 as follows. The number of seconds T_B required to scan the full width of 42 swaths at a constant swath scanning rate SR is

$$T_B = (9(\text{in/swath})/SR(\tfrac{\text{in}}{\text{sec}})) \times 42 \text{ swaths} = \frac{378}{SR} \text{ sec}$$

$$(7-10)$$

344

In the target region the sensor array advances only one scan line at a time rather than 64 scan lines at a time. The number of seconds T_T required to scan the 2 in x 384 lpi = 768 lines passing through the target region is:

$$T_T = 9(in/line)/SR(in/sec) = 768 \text{ lines} = \frac{6912}{SR} \text{ sec} \quad (7-11)$$

Note that the 32 lines of swath #42 that must be rescanned exactly compensate the last 32 lines of the bottom swath that are not scanned due to border effects. Now since $T_T + T_B = 10$ min (600 sec) the required swath scanning rate may be computed as follows:

$$T_B + T_T = 600 \text{ sec} = (378/SR + 6912/SR) \text{ sec.} \quad (7-12)$$

Then SR=12.15 (inches/sec) and the time required to scan one swath is 9 inches/12.15 inches/sec=0.74074 sec. The corresponding pixel rate PR_S at the sensor output is given by

$$PR_S = (64 \text{ pixels/column}) \times (384 \text{ columns/inch}) \times (SR \frac{\text{inches}}{\text{sec}})$$
$$= 18,186 \text{ pixels/sec} \quad (7-13)$$

This sensor pixel rate is well within the capability of the sensor array, recording array, and CCD image processing devices proposed for this conceptual design implementation.

There is a disadvantage to using a constant swath scanning rate, as was assumed for the above calculations: the pixel rate (and therefore the bit rate) in the channel is four times faster when scanning the background region than when scanning the target region, which implies the need for a

345

channel buffer if a constant channel data rate is desired
or required. This may be demonstrated as follows. Recall
that 4:1 BWCR implies 1 bit/pixel in both target and background
regions. In the target region the channel pixel (bit) rate
may be computed as

$$PR_T = (384 \text{ pixels/in})(9 \text{ in})/(0.74074 \text{ sec})$$

$$= 4,666 \text{ pixels/sec} = 4,666 \text{ bits/sec} \qquad (7-14)$$

In the background the along-scan pixels are decimated by four,
but 16 of the 64 vertical DCT coefficients are retained
and transmitted at an average rate of one bit/pixel for 4:1
BWCR; the channel bit rate in the background region is thus
given by

$$PR_B = \frac{(9\frac{\text{in}}{\text{scan}})(16\frac{\text{coefficients}}{\text{pixel column}})(384 \frac{\text{pixels}}{\text{in}} \div 4 \text{ decimation})}{0.74074 \text{ sec/scan}}$$

$$= 4 \times 4.666 = 18,662 \text{ bits/sec} \qquad (7-15)$$

If the swath scan rate SR is to be held constant the size of
the required channel buffer is then bounded by B=(differential
bit rate)x(total scan time for 42 contiguous background region
swaths) = (18,662-4800) bits/sec x (378/12.15)sec
    B = 575,796 bits.

        The requirement for channel buffers could be
eliminated by decreasing the swath scanning rate by a factor
of four in the background regions so as to obtain a constant
channel data rate. However, if the swath scanning rate is not
speeded up (from 4.666 Kbps to 4.8 Kbps) in order to compensate,
the 10 minute transmission time requirement will be exceeded.

346

Accounting for the fact that one swath may intersect both target and background regions, and allowing SR to change within a swath after crossing a region boundary we may compute the two new swath scanning rates required for both kinds of regions in order to keep the link full as follows.
Using

$$T_B = \frac{(9 \text{ in/swath}) \times (42+(7/9)6) \text{ swaths}}{SR_B} \qquad (7\text{-}16)$$

and

$$T_T = \frac{(9 \text{ in/line}) \times (384 + 2/9(384)) \text{lines}}{SR_T} \qquad (7\text{-}17)$$

and

$$600 \text{ sec} = T_B + T_T = (\frac{382.7}{SR_B} + \frac{4224}{SR_T}) \text{sec} \qquad (7\text{-}18)$$

we obtain one equation in two unknowns. Recall that with nonconstant SR (and thus constant channel data rate),

$$SR_B = 1/4 \ SR_T. \qquad (7\text{-}19)$$

We may then write $600 \text{ sec} = \frac{382.7}{SR_B} + \frac{4227}{4(SR_B)}$ and solve for

$$SR_B = 2.397 \text{ inches/sec}$$

$$SR_T = 4SR_B = 9.588 \text{ inches/sec}$$

347

The corresponding sensor pixel rates are then:

background region: PR = (64 pixels/column)(384 columns/inch) x
                    (2.397 inches/sec)
                    = 58,909 pixels/sec

target region: PR = (64 pixels/column)(384 columns/inch) x
                    (9.588 inches/sec)
                    = 235,634 pixels/sec

      All of the computations thus far have assumed
a 4.8 kbps link. Since sensor pixel rates are linearly related
to SR we can easily tabulate the corresponding results for
other data rates of interest. Table 7.4-2 shows these results
for the first case we considered, in which the swath rate
was held fixed throughout the image and channel buffers were
required to accomodate the resulting nonconstant channel
data rate. Note that required buffer size is independent
of channel data rate. This is because the differential data
rate Δd increases linearly with data rate d whereas total
scan time decreases as 1/d, and the required buffer size is
the product of these two terms. Table 7.4-3 shows the corres-
ponding results for the latter case we considered in which
the SR is four times slower in the background region than
in the target region in order to eliminate the channel buffer
requirement.

348

TABLE 7.4-2
SCANNER PIXEL RATES
FOR THE CONSTANT SR SCANNER IMPLEMENTATION

Available Channel Data Rate (kbps)	PR_s Scanner Pixel Rate (kilopixels/sec)
2.4	149.299
4.8	298.598
8.0	497.663
9.6	597.196
16	995.327
32	1,990.653

Note: required buffer size is 575,796 bits, independent of data rate

TABLE 7.4-3
SCANNER PIXEL RATES FOR THE
NONCONSTANT SR SCANNER IMPLEMENTATION

Available Channel Data Rate (kbps)	Scanner Pixel Rates (kilopixels/sec)	
	PR_B	PR_T
2.4	29.455	117.817
4.8	58.909	235.634
8.0	98.182	392.723
9.6	117.818	471.268
16	196.363	785.447
32	392.727	1,570.893

In order to determine the capabilities of the selected array sensing technique when applied to this conceptual hybrid design for the ASITS, we must modify the results presented in Section 2.0, which were based on the assumption of a scan period T_{SS}=13.5 milliseconds. We have shown that the scan periods required for the conceptual design presented here (N=64) are as follows.

Constant SR approach: T_{SS}=0.74074 seconds

Nonconstant SR approach:

background region: T_{SS}=9 inches/2.397 inches/sec=3.7547 sec

target region: T_{SS}=9 inches/9.588 inches/sec=0.9387 sec

Since N is directly proportional to T_{SS}, the scale for the vertical axis for N in the tradeoff summary curves of Figure 2.3.3.4 should be multiplied by the following scale factors in order to determine the maximum value of N applicable to the hybrid ASITS approach presented here:

Multiplicative Scale Factor

Constant SR approach: 0.74074/.0135 = 54.9

Nonconstant SR approach:

background: 3.7547/.0135 = 278.1

target: 0.9387/.0135 = 69.5

Choosing the worst case photodetector bandwidth of BW=1.0 MHz for which N=10 if T_{SS}=13.5 msec implies that the maximum value of N for the 4.8 kbps channel data rate is

Constant SR approach: N=10x54.9=549

Nonconstant SR approach:

background: N=10x278.1=2781

target: N=10x69.5=695

351

Several notes are appropriate here about the
feasibility of the very large array sizes just computed.
The tradeoff being made is clearly a valid one, since it is
simply a consideration of the transition between vertical-
raster and horizontal-raster scanning; thus, ultimately, as
many pixels as are scanned horizontally in a conventional
system may be scanned vertically using a dithered raster tech-
nique, provided the relationship of the scan times can be
adjusted accordingly. However, some caution must be used in
applying these results to a specific scanner implementation.
For the current case, with the system design as described
in Paragraph 2.3.3, an additional constraint on array column
height is posed by the detector size. In the absence of
a more sophisticated system design, the long narrow detector
can readily intercept light from only about 1/3 of an inch
of document area. Thus the light budget (and hence SNR)
tradeoffs would limit array size to about 128 pixels (at
384 pixels/inch). If we accept this limitation to a specific
scanner design, then we may take the above SR calculations
as evidence that there are no bandwidth problems anticipated
for $N \leq 128$.

For the case at hand, i.e., for the N=64
case corresponding to the proposed conceptual design, we are
interested in determining whether the sensor pixel rates
required at the various channel data rates can be supported
by the selected scanning approach. Since the sensor pixel
rate increases directly with N and inversely with swath scan
period we may write

$$PR = (N/T_{SS})(9 \text{ in})(384 \text{ pixels/in}) \qquad (7\text{-}20)$$

Referring to Figure 2.3.3.4 and choosing the (worstcase)
photodector bandwidth curve labeled BW=1.0 MHz for which N = 10
we may compute the maximum pixel rate

$$PR = \frac{10 \text{ pixels/column } 3456 \text{ columns/swath}}{13.5 \times 10^{-3} \text{ sec/swath}}$$

$$= 2.56 \times 10^6 \text{ pixels/sec}$$

The corresponding result for the BW = 2.6 MHz (best case) photodetector curve for which N=25 is 2½ times larger or PR = 6.4×10^6 pixels/sec. Both of these sensor pixel rate capabilities exceed the sensor pixel rates required for the 32 Kbps link whether a constant SR approach or nonconstant SR is selected. Recall from Tables 7.4-2 and 7.4-3 that the 32 Kbps link requires maximum sensor pixel rates of 1.990653×10^6 pixels/sec and 1.570893×10^6 pixels/sec for the constant SR and nonconstant SR approaches, respectively. Thus, the sensor pixel rates dictated by the system parameters, viz., N=64 and 32 Kbps channel data rate, are well within the capability of the state of the art for the proposed array sensing technique. The array recording rate capability (75 Megapixels/sec) of the proposed array recording technique is more than an order of magnitude greater than the rate dictated by system requirements. In this section we have demonstrated that holding swath scanning rate SR constant implies a nonconstant channel data rate, and conversely, maintaining constant channel data rate implies a nonconstant swath scanning rate; the ratio of the two rates is 4:1 in either case. Conceptually at least, either of these approaches could be implemented without undue complexity. Since the source image target regions are designated and this information transmitted to the receiver prior to image transmission, the receiver knows when to expect data rate changes or when to change its swath scanning rate SR, depending upon whether channel data rate or swath scanning rate is held fixed.

An attractive alternative to the conceptual
design just presented in this section is one in which the hybrid
transform is performed for all three resolutions and BWCR's,
not just for the quarter and half resolution cases. Such an
approach would require that 64 DCT coefficients be computed
at the transmitter rather than the 32 required for the approach
presented in Figure 7.3-1. This alternative approach requires
32 additional Reticon R5602 CCD's for computing 32 additional
DCT coefficients and one additional Reticon R5501 P/S converter
and associated switch; however, the two Reticon R5602's
associated with the image enhancement or MTF correction filters
are no longer required. Thus, 30 additional R5602's and one
R5501 are required for this alternative approach. This increased
cost and implementation complexity must be evaluated in light
of the higher image quality that results at high BWCR's when
the hybrid BWC technique is used at full resolution. Since
image quality is very subjective, this evaluation can only
be accomplished by computer simulating this alternative system
and comparing the reconstructed imagery to that of the system
of Figure 7.3-1. Using the alternative approach also simplifies
the scanning procedure in that no line ever need be scanned
more than once, i.e., swaths do not overlap in the target
region. The corresponding hybrid receiver for the alternative
hybrid transmitter described above performs the inverse of the
transmitter operations; its block diagram is not shown since
it is a straightforward extension of the hybrid portion of
the receiver of the conceptual design presented earlier.

Note that all of the tradeoff results have
been based upon one particular geometry and ratio of image
target area and background area; different geometries and area
ratios will give different results. However, this choice is
perhaps representative and does provide some insight into how
the various system parameters are related.

It should be mentioned that, depending upon the power levels required, dangerous levels of coherent laser light may be present in the sensing or recording portions of the ASITS and due precautions should be taken when operating or servicing such equipment.

7.5   IMPLEMENTATION COST CONSIDERATIONS

The ASITS conceptual design presented in Section 7.4 makes liberal use of CCD technology at both the transmitter and the receiver to perform the two-dimensional filtering and BWC functions. The total number of Reticon R5602 64-stage transversal filters used at the transmitter is (3x16+2x16+2)=82, while the number used at the receiver is 3x64=192, for a total of 274 per ASITS. Three Reticon R5501 P/S converters are required per ASITS, one at the transmitter and two at the receiver. Recall that the alternative ASITS that was briefly mentioned at the end of Section 7.4 required 30 additional R5602's and one additional R5501. The current prices for various quantities of these two Reticon CCD's are given in Table 7.5-1 below. The price structure of the Reticon TAD-32A is identical to that of the Reticon R5501.

The cost of the signal processing CCD's per complete ASITS may be easily computed and is given below in Table 7.5-2.

The support circuitry required to implement one R5602 filter is quite modest and consists of eight resistors, four $10 \mu f$ electroytic capacitors, two 0.1 μf capacitors, 3 diodes, one zener diode, one 50K potentiometer, and one LF356 operational amplifier.

The Reticon R5602 is packaged in a standard 16-pin dual-inline-package (DIP) and requires only +15 volts for power and a single trigger input to control the internal

355

TABLE 7.5-1

RETICON CCD PRICE STRUCTURE

RETICON DEVICE	1-9	10-49	50-99	100-499	500-999	1000-2499	2500-4999	5000-9999	>10,000
R5602	$50	$40	$30	$25	$17	$14.50	$12	$10	$8.5
R5501 or TAD-32A	$48	$35	$25						

TABLE 7.5-2

TOTAL COST OF R5602's AND R5501's

PER ASITS VERSUS NUMBER OF ASITS FABRICATED

# of ASITS FABRICATED	1	5	10	20	50
Conceptual Design	$6994	$4117	$3393	$2845	$2404
Alternative Design	$7792	$4600	$3788	$3180	$2724

357

sampling. Since the R5602 requires very little support cir-
cuitry, the required number of R5602's could be mounted on a
relatively small number of printed circuit cards.

There are three basic approaches to implementing
the hybrid ASITS processing functions:

(1) utilize the architecture of Figure 7.3-1
     and sampled-data analog hardware based
     upon CCD technology

(2) utilize the architecture of Figure 7.3-1
     but perform all of the storage and arith-
     metic functions using dedicated digital
     hardware

(3) utilize a general purpose mini-computer
     and write the appropriate software to
     perform the hybrid algorithm

The capabilities of an ASITS implemented using either approach
(1) or (2) are limited by the fixed architecture of the hard-
ware, while the approach of (3) is completely general in
that the software can be rewritten to perform any desired
function. In general, system flexibility may be traded for
system speed (image throughput rate). In comparing approaches
(1) and (2), we find that the CCD implementation is conducive
to relatively high image processing rates, whereas an all digital
implementation requires more internal control and housekeeping
functions, and is more constrained by inherent speed limitations.

For a relatively complex system such as the
ASITS, the amount of software/firmware required for a micro-
processor-based digital implementation can become an important
contributor toward the overall system cost. For example, an
all-digital, microprocessor-based, single-spot scanning hybrid

system requires several thousand lines of software of the
industry-wide estimate for the cost of generaging, debugging,
and documenting software is on the order of $25 per line.

In conclusion, it is clear that the CCD-
oriented implementation of an ASITS is a cost effective low-
risk approach that allows high image throughput rates while
simultaneously performing sophisticated, computation-
intensive image processing.

8.0 STUDY SUMMARY, CONCLUSIONS AND RECOMMENDATIONS

The conclusions of the various aspects of this study effort are documented throughout this final report. In this section we briefly review some of the major activities of the study and mention the corresponding conclusions. There is much useful data throughout the body of the report regarding pertinent tradeoffs, alternative architectures, and performance limits and degradations. Analysis, computer simulation, and some experimental work played major roles in the performance of this study. This section concludes with recommendations for further work that should be conducive to the ultimate realization of an ASITS making extensive use of CCD technology and novel applications of electro-optical technology.

8.1 STUDY SUMMARY AND CONCLUSIONS

This study has shown that an array scanning image transmission system is both feasible and advantageous when compared to conventional single-point scanned image transmission systems.

One major focus of the study was the evaluation of the risk and performance parameters of various array sensing and recording techniques. It was found that the current state of electro-optics technology does not support two-dimensional (matrix) array sensing or recording. However, the technology does support one-dimensional sensing and recording arrays capable of operating at useful pixel rates in image transmission systems. A one-dimensional linear sensing array N elements long can be used in conjunction with N^2 memory locations to synthesize a two-dimensional sensing array. At the receiver, one-dimensional linear recording arrays are sufficient to satisfy the gray shade imagery array recording

requirements. If two-dimensional recording arrays were
feasible, the image recording rate could be increased by
virtue of the "hopping" scanning action appropriate for a
two-dimensional recorder. However, the system image through-
put rate is limited by the pixel rate of the array sensor
rather than by that of the array recorder; in part, this is
because the array sensor has to scan and process many source
pixels in order to generate one processed pixel ready for
recording.

    Another major focus of the study effort was
the exploitation of the nature of the array scanning technique
in order to accomplish sophisticated signal processing func-
tions with low implementation complexity. The nature of
the array scanning process lends itself quite naturally to
analog sampled-data processing via CCD's. A set of realis-
tic and meaningful systems requirements was adopted in order
to define the system and subsystem tradeoffs. It was found
that a relatively simple ASITS implementation relying almost
entirely upon two types of CCDs manufactured by Reticon cor-
portation is capable of performing all of the desired sophis-
ticated signal processing functions. The ASITS conceptual
design presented in Section 7.0 is capable of three BWCR's,
three resolutions, image decimation and interpolation by
factors of two or four, selection of either image enhancement
or MTF correction at full resolution, fixed image enhance-
ment or MTF correction (not selectable) at one-half or one-
quarter resolution, and REARCS operation. Computer-assisted
evaluation of the effects of CCD time dispersion showed
that this property of practical CCD's will not be a limiting
factor on system performance. Likewise, computer experiments
regarding defective sensor or TAD elements showed that losing
an element or row of elements is not catastrophic for the

two-dimensional filter sizes likely to be used in any ASITS im-
plementation. Very extensive computer simulations and subjec-
tive evaluation of the resulting imagery showed that two-
dimensional nonseparable FIR filters of size 31x31 gave very
good performance in conjunction with decimation and interpola-
tion. It was found that values of the Kaiser filter window
parameter β that give the best performance depend upon the D/I
factor. The very considerable reduction in implementation
complexity that occurs when separable filters are used provided
the impetus for examining the performance of these filters. In
all except the most demanding situations, it is felt that sep-
arable filters of size 31x31 or larger give quite adequate
performance. In fact the only region of the source image where
a difference between separable and nonseparable filter per-
formance could be discerned was within the region of the
frequency wedge corresponding to "diagonal", i.e., off-axis
two-dimensional frequencies. The separable filters actually
pass more frequencies than the nonseparable filters, and with-
out any additional aliasing degradation. To see why this is
so, refer to Figure 8.1 (a), which shows both the two-dimen-
sionally sampled source spectrum (cross hatched) and the sampled
data lowpass filter prior to decimating the lowpass filter
output. Figure 8.1 (b) shows the spectrum at the filter
output after decimation. Note that whether "round" (non-
separable) or "square" (separable) lowpass filters are used,
no aliasing occurs. This situation is improved still more by
virtue of the fact that spectral energy of images that have
been rectilinearly sampled tends to "cling" to the two fre-
quency axes. We verified this fact by plotting a three
dimensional perspective of the spectrum of a small portion
of the source image.
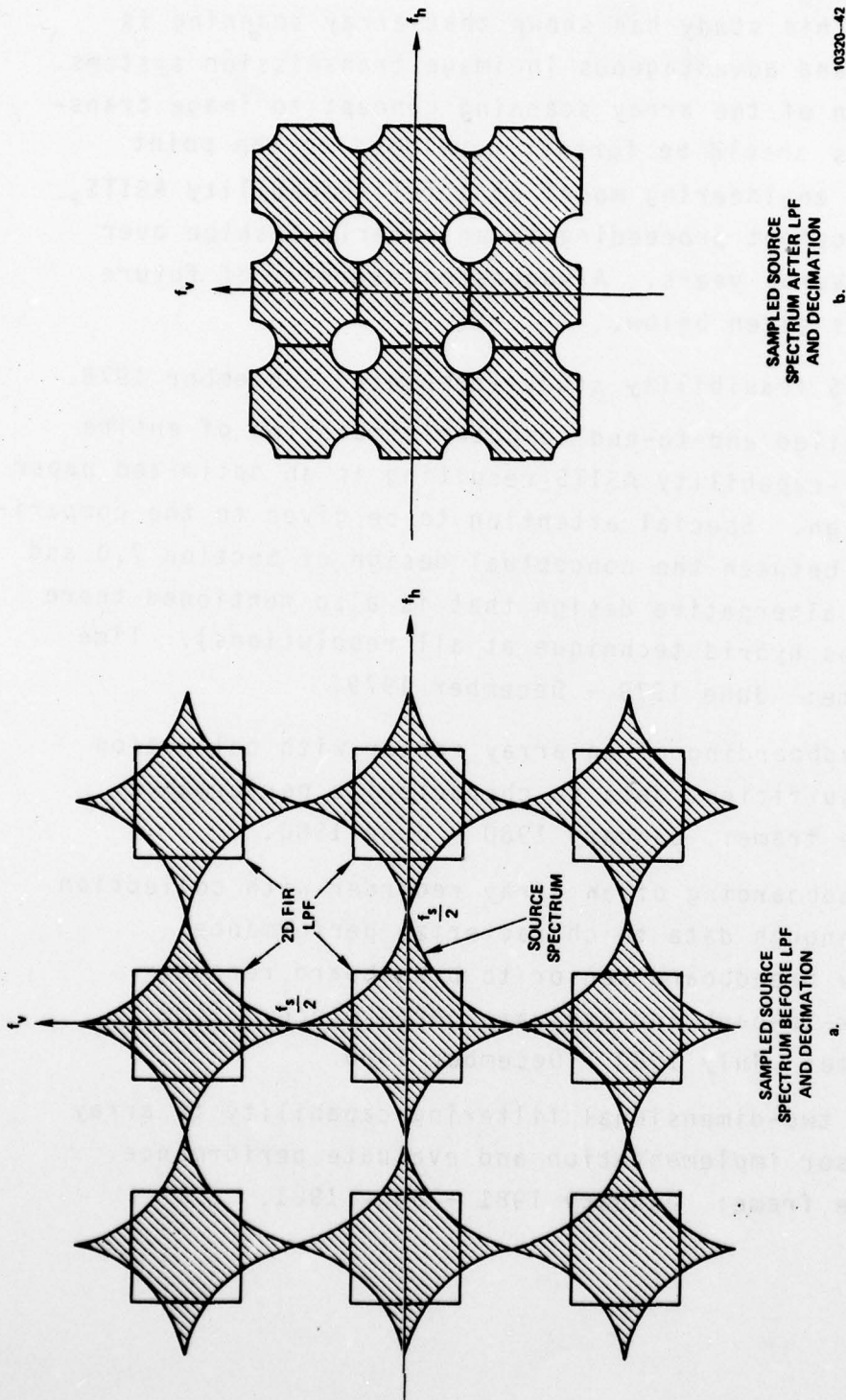
10320–42

Figure 8.1

Graphical Representation of the Two-Dimensional
Decimation Process Applied to a Sampled Image Source

363

8.2   <u>STUDY RECOMMENDATIONS</u>

This study has shown that array scanning is both feasible and advantageous in image transmission systems. The application of the array scanning concept to image transmission systems should be further developed to the point of building an engineering model of a full-capability ASITS, with the development proceeding in an orderly fashion over a period of several years. A suggested sequence of future study phases is given below.

Phase 1: ASITS feasibility study--completed September 1978.

Phase 2: Detailed end-to-end computer simulation of entire full-capability ASITS resulting in an optimized paper design. Special attention to be given to the comparison between the conceptual design of Section 7.0 and the alternative design that is also mentioned there (uses hybrid technique at all resolutions). Time frame: June 1979 - December 1979.

Phase 3: Breadboarding of an array sensor with collection of sufficient data to characterize performance. Time frame: January 1980 - June 1980.

Phase 4: Breadboarding of an array recorder with collection of enough data to characterize performance. Play breadboard sensor to breadboard recorder back-to-back and evaluate performance. Time frame: July 1980 - December 1980.

Phase 5: Add two-dimensional filtering capability to array sensor implementation and evaluate performance. Time frame: January 1981 - June 1981.

Phase 6:   Add hybrid (DCT/DPCM) transformer at transmitter
and hybrid inverse transformer at receiver.
Also include REARCS capability, which implies
various bit assignments for different BWCR's
and resolutions. The required along-scan deci-
mation and interpolation filters are the same as
those used in Phase 5; this reduces the number of
additional R5602's that must be puschased for
this phase. The result of this phase is a full-
capability ASITS. Extensive evaluation and exper-
imentation with this system will help specify the
final design of a production model ASITS. Time
Frame: July 1981 - July 1982.

Two or more of the phases suggested above may be
combined in order to compress the ASITS development schedule
if desired.

REFERENCES

1. J. J. Brady,"Biasing Techniques Improves TAD-32 Performance", Applied Research Laboratories, University of Texas at Austin, ARL-TP-77-13, 3 March, 1977.

2. S. T. Kowel, et al, <u>Direct Electronic Fourier Transforms of Optical Images (DEFT)</u>, RADC-TR-73-254, August, 1973.

3. S.T. Kowel, et al, DEFT: <u>Progress on Direct Electronic Fourier Transforms of Two-Dimensional Images</u>, RADC-TR-74-244, October, 1974.

4. S. T. Kowel, et al, <u>Two-Dimensional Direct Electronic Fourier Transform (DEFT) Devices: Analysis, Fabrication, and Evaluation</u>, Report DAAG53-76-C-0162, 30 June 1977, Dept. of Electrical and Computer Engineering, Syracuse university, Syracuse, N.Y.

5. M. Uchida and N. Niizeki, Proc. IEEE 61, 1073 (1973).

6. H. Eschler and F. Weidinger, J. Appl. Phys. 46, 65 (1975).

7. N. Uchida, J. Appl. Phys. 43, 2915 (1972).

8. T. Yano, A. Fukermoyo and A. Watanale, J. Appl. Phys. 42, 3674 (1971).

9. D. D. Buss, W. H. Bailey, and D. R. Collins, "Analysis and Applications of Analogue CCD Circuits", Proceedings of the 1973 IEEE International Symposium on Circuit Theory, pp. 3-7.

10. R. D. Baertsch, W. E. Engeler, H. S. Goldberg, C. M. Puckette, IV, and J. J. Tiemann, "The Design and Operation of Practical Charge - Transfer Transversal Filters", IEEE Journal of Solid State Circuits, Vol. SC-11, No. 1, February, 1976.

11. J. H. McClellan, T. W. Parks, and L. R. Rabiner, "A Computer Program for Designing Optimum FIR Linear Phase Digital Filters", IEEE Trans. Audio Electroacoustics, Vol. AU-21, pp. 506-526, December, 1973.

12. T. S. Huang, J. W. Burnett, A. G. Deczkey, "The Importance of Phase in Image Processing Filters", IEEE Trans. ASSP, Volume ASSP-23, No. 6, December, 1975, pp. 529-542.

REFERENCES (CONT'D)

13. L. R. Rabiner, J. F. Kaiser, Herrmann, M. T. Dolan, "Some Comparisons Between FIR and IIR Digital Filters", Bell System Technical Journal, Vol. 53, No. 2, February, 1974, pp. 305-331.

14. P. A. Wintz, "Transform Picture Coding", Proc. IEEE, Volume 60, July, 1972, pp. 809-820.

15. H. C. Andrews, Computer Techniques in Image Processing, Academic Press, New York, 1970.

16. A. Habibi, "Hybrid Coding of Pictorial Data," IEEE Transactions on Communications, Volume COM-22, No. 5, May, 1974.

17. J. B. O'Neal, Jr., "A Bound on Signal-to-Quantizing Noise Ratios for Digital Encoding Systems", Proceedings of the IEEE, Vol. 55, No. 3, March, 1967, pp. 287-292.

18. J. B. O'Neal, Jr., "Delta Modulation Quantizing Noise Analytical and Computer Simulation Results for Gaussian and Television Inputs", B.S.T.J., No. 15, Jan., 1966, pp. 117-141.

19. J. B. O'Neal, Jr., "Predictive Quantizing Systems (Differential Pulse Code Modulation) for the Transmission of Television Signals," B.S.T.J., Volume XLV, No. 5, May-June, 1966, pp. 689-721.

20. J. B. O'Neal, Jr., and T. R. Natarajan, "Coding Isotropic Images", IEEE Trans. on Info. Thy., Vol. IT-23, No. 6, November, 1977, pp. 697-707.

21. N. Ahmed, T. Natarajan, K. R. Rao, "Discrete Cosine Transform," IEEE Transaction Computers, January, 1974.

22. J. Essman, D. Hua, G. Papacostas, "Video Data Compression Study for Remote Sensors," (Research conducted at E.E. Dept., Ohio University, for AFAL) Technical Report AFAL-TR-75-173, February, 1976.

23. A. Habibi, G. S. Robinson, "A Survey of Digital Picture Coding, "Computer, May, 1974, pp. 22-34.

24. T. S. Huang, et al, "Image Processing," Proceedings of the IEEE, Vol. 59, No. 11, November, 1971, pp. 1586-1609.

REFERENCES (CONT'D)

25. A. Habibi, and P. Wintz, "Image Coding by Linear Trans-
    formation and Block Quantization," IEEE Transactions on
    Communications Technology, Volume COM-19, No. 1, February,
    1971, pp. 50-62.

26. A. Habibi, "Comparison of nth Order DPCM Encoder with
    Linear Transformations and Block Quantization Techniques,"
    IEEE Trans. Com. Tech., Vol. COM-19, No. 6, December,
    1971, pp. 948-956.

27. M. Paez, and T. Glisson, "Minimum Mean-Squared-Error
    Quantization in Speech PCM and DPCM Systems," IEEE Trans.
    Com., April, 1972, pp. 225-230.

28. W. C. Adams, Jr., and C. E. Giesler, "Quantizing Charact-
    eristics for Signals Having Laplacian Amplitude Probability
    Density Function," IEEE Trans. Comm., COM 8-30, August,
    1978, pp. 1295-1297.

29. L. R. Rabiner, B. Gold, Theory and Applications of Digital
    Signal Processing, Englewood Cliffs, N.J., Prentice-Hall,
    1975.

30. W. B. Schaming, "Digital Image Transform Encoding", RCA
    Corporate Engineering Services, 1973.

31. W. H. Chen, C. H. Smith, and S. C. Fralick, "A Fast
    Computational Algorithm for the Discrete Cosine Transform",
    IEEE Transactions on Communications, Volume COM-25, No. 9,
    September, 1977, pp. 1004-1009.

32. A. Peled and B. Liu, "A New Hardware Realization of
    Digital Filters" IEEE Transactions on Acoustics, Speech,
    and Signal Processing, Volume ASSP-22, No. 6, December,
    1974, pp. 456-462.

33. R. W. Schafer and L. R. Rabiner, "A Digital Signal
    Processing Approach to Interpolation," Proc. IEEE, Vol. 61,
    pp. 692-702, June 1973.

34. J. H. McClellan, "The Design of Two-Dimensional Digital
    Filters by Transformations," Proc. of the 7th Annual
    Princeton Conference on Information Sciences and Systems,
    March, 1973, pp. 247-251.

BIBLIOGRAPHY

1. T. S. Huang, "Two-Dimensional Windows," IEEE Trans. Audio Electroacoust., Vol. AU-20, pp. 88-89, March, 1972, pp. 249-250.

2. L. R. Rabiner and R. E. Crochiere, "A Novel Implementation for Narrow-Band FIR Digital Filters", IEEE Trans. Acoustics, Speech, and Signal Processing, Vol. ASSP-23, No. 5, October, 1975, pp. 457-464.

3. R. E. Crochiere and L. R. Rabiner, "Optimum FIR Digital Filter Implementations for Decimation, Interpolation, and Narrow-Band Filtering", IEEE Trans. Acoustics, Speech, and Signal Processing, Vol. ASSP-23, No. 5, October, 1975. pp. 444-456.

4. A. W. Crooke and J. W. Craig, "Digital Filters for Sample-Rate Reduction", IEEE Trans. Audio and Electroacoustics, Vol. AU-20, No. 4, October, 1972, pp. 308-315

5. R. A. Meyer and C. S. Burrus, "Design and Implementation of Multirate Digital Filters", IEEE Trans. Acoustics, Speech, and Signal Processing, Vol. 1, February, 1976, pp. 53-58.

6. M. G. Bellanger, J. L. Daguet, and G. P. Lepagnol, "Interpolation, Extrapolation, and Reduction of Computation Speed in Digital Filters", IEEE Trans. Acoustics, Speech, and Signal Processing, Vol. ASSP-22, No. 4, August, 1974, pp. 231-235.

7. R. W. Broderson, C. R. Hewes, and D. D. Buss, "A 500-Stage CCD Transversal Filter for Spectral Analysis", IEEE Journal of Solid-State Circuits, Vol. SC-11, No. 1, February, 1976, pp. 75-84.

8. A. Gersho and B. Gopinath, "Multiplexed Filtering with Charge-Transfer Devices", IEEE Journal of Solid-State Circuits, Vol. SC-11, No. 1, February, 1976, pp. 220-224.

9. D. F. Barbe, "Charge-Coupled Device and Charge-Injection Device Imaging", IEEE Journal of Solid-State Circuits, Vol. SC-11, No. 1, February, 1976, pp. 109-114.

LIST OF ABBREVIATIONS

A/D = Analog-to-Digital

AO = Acousto-Optic

AOBD = Acousto-Optic Beam Deflector

AOM = Acousto-Optic Modulator

AOPC = Acousto-Optic Page Composer

ASITS = Array Scanning Image Transmission System

BBD = Bucket Brigade Device

BWC = Bandwidth Compression

BWCR = Bandwidth Compression Ratio

CCD = Charge Coupled Device

CdS = Cadmium Sulfide

CID = Charge-Injected Device

CMD = Command

CTD = Charge Transfer Device

CTI = Charge Transfer Inefficiency

D/A = Digital-to-Analog

DCT = Discrete Cosine Transform

DEFT = Direct Electronic Fourier Transform

DFT = Discrete Fourier Transform

D/I = Decimation/Interpolation

DIP = Dual In-Line Package

DPCM = Differential PCM

LIST OF ABBREVIATIONS (CONT'D)

FFT = Fast Fourier Transform

FIR = Finite Impulse Response

IIR = Infinite Impulse Response

IITS = Intra-Threater Image Transmission System

LED = Light Emitting Diode

LPF = Low Pass Filter

lpi = lines per inch

LSB = Least Significant Bit

MADD = Multiply-and-Add

MSB = Most Significant Bit

MTF = Modulation Transfer Function

NEP = Noise Equivalent Power

PCM = Pulse Code Modulation

PTA = Phototransistor Array

Pixel = Picture Element

PR = Pixel Rate

P/S = parallel-to-serial

PSF = Point Spread Function

RAM = Random Access Memory

REARCS = Redundant Area Coding System

RF = Radio Frequency

ROM = Read-Only Memory

LIST OF ABBREVIATIONS (CONT'D)

SAW = Surface Acoustic Wave

S/P = Serial-to-Parallel

SR = Swath Scanning Rate (inches/sec)

1D = One Dimensional

2D = Two Dimensional

MISSION
of
Rome Air Development Center

RADC plans and conducts research, exploratory and advanced development programs in command, control, and communications (C³) activities, and in the C³ areas of information sciences and intelligence. The principal technical mission areas are communications, electromagnetic guidance and control, surveillance of ground and aerospace objects, intelligence data collection and handling, information system technology, ionospheric propagation, solid state sciences, microwave physics and electronic reliability, maintainability and compatibility.